SOLAR FLARE PARTICLE ACCELERATION IN COLLAPSING MAGNETIC TRAPS

Keith J. Grady

A Thesis Submitted for the Degree of PhD
at the
University of St. Andrews

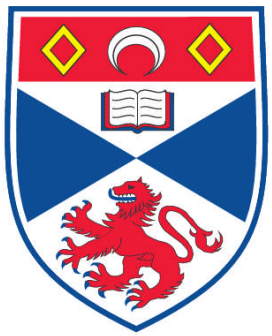

2012

Solar Flare Particle Acceleration in Collapsing Magnetic Traps

Keith J. Grady

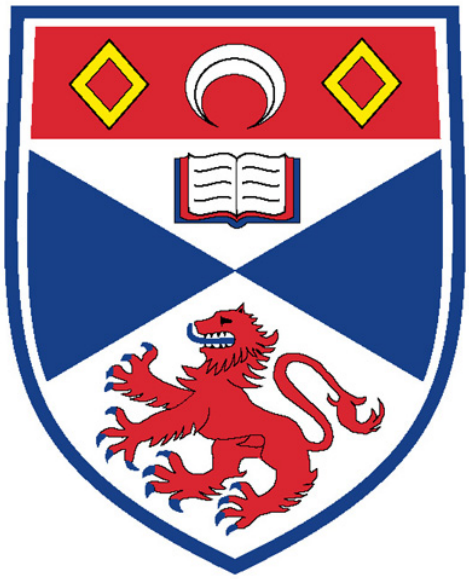

Thesis submitted for the degree of Doctor of Philosophy
of the University of St Andrews

16th April 2012

Abstract

The topic of this thesis is a detailed investigation of different aspects of the particle acceleration mechanisms operating in Collapsing Magnetic Traps (CMTs), which have been suggested as one possible mechanism for particle acceleration during solar flares.

The acceleration processes in CMTs are investigated using guiding centre test particle calculations. Results including terms of different orders in the guiding centre approximation are compared to help identify which of the terms are important for the acceleration of particles. For a basic 2D CMT model the effects of different initial conditions (position, kinetic energy and pitch angle) of particles are investigated in detail. The main result is that the particles that gain most energy are those with initial pitch angles close to 90° and start in weak field regions in the centre of the CMT. The dominant acceleration mechanism for these particles is betatron acceleration, but other particles also show signatures of Fermi acceleration.

The basic CMT model is then extended by (a) including a magnetic field component in the invariant direction and (b) by making it asymmetric. It is found that the addition of a guide field does not change the characteristics of particle acceleration very much, but for the asymmetric models the associated energy gain is found to be much smaller than in symmetric models, because the particles can no longer remain very close to the trap centre throughout their orbit.

The test particle method is then also applied to a CMT model from the literature which contains a magnetic X-line and open and closed field lines and the results are compared with the previous results and the findings in the literature.

Finally, the theoretical framework of CMT models is extended to 2.5D models with shear flow and to fully 3D models, allowing the construction of more realistic CMT models in the future.

Declaration

I, Keith James Grady, hereby certify that this thesis, which is approximately 26,000 words in length, has been written by me, that it is the record of work carried out by me and that it has not been submitted in any previous application for a higher degree.

I was admitted as a research student in October 2007 and as a candidate for the degree of Doctor of Philosophy in October 2007; the higher study for which this is a record was carried out in the University of St Andrews between 2007 and 2011.
date: 16/4/2012 signature of candidate:

I hereby certify that the candidate has fulfilled the conditions of the Resolution and Regulations appropriate for the degree of Doctor of Philosophy in the University of St Andrews and that the candidate is qualified to submit this thesis in application for that degree.
date: 16/4/2012 signature of supervisor:

In submitting this thesis to the University of St Andrews we understand that we are giving permission for it to be made available for use in accordance with the regulations of the University Library for the time being in force, subject to any copyright vested in the work not being affected thereby. We also understand that the title and the abstract will be published, and that a copy of the work may be made and supplied to any bona fide library or research worker, that my thesis will be electronically accessible for personal or research use unless exempt by award of an embargo as requested below, and that the library has the right to migrate my thesis into new electronic forms as required to ensure continued access to the thesis. We have obtained any third-party copyright permissions that may be required in order to allow such access and migration, or have requested the appropriate embargo below.

The following is an agreed request by candidate and supervisor regarding the electronic publication of this thesis:

Access to Printed copy and electronic publication of thesis through the University of St Andrews.

date: 16/4/2012 signature of candidate: signature of supervisor:

Acknowledgements

Firstly, thanks to my Mum and Dad, who have been fantastically supportive throughout my PhD, time at university and whatever I've been doing in life in general! I'm very grateful for the love and support I've always had from you both and the wider families.

Thanks to Thomas for his insight and help throughout my PhD and in the projects I've worked on before with him. I've been very lucky to be able to work for so long with such an expert who is willing to explain anything he knows.

It's been great fun to have breaks with many of the students and postdocs in the group. Thanks for your distractions (and letting me distract you!), meals, music quizzes, balls, cakes,... it's a wonder we do any work at all!

Thanks to my non-maths friends, flatmates and folk I don't see often enough from undergraduate, for (at least pretending to) take an interest in what I'm up to and nagging me to actually get on with it. I'm done now - see?!

Throughout most of my PhD I have had financial assistance from the Science and Technology Facilities Council (STFC). Some conference fees and associated costs were funded by the SOLAIRE Network.

Contents

Chapter 1

Introduction

1.1 The Sun

The most unique thing about the Sun is how close it is to Earth. The distance of the Sun from the Earth has been measured by triangulation of planets motion around it, and more recently with the added help of radar in the 1960's this has been measured more accurately and is now known to be on average 149,598 Mm (Pitjeva and Standish 2009). This distance is called an Astronomical Unit (AU). Being close to Earth means that the Sun can be studied in great detail as an example of a star. The Sun is basically a massive sphere of hot gas. Due to its high temperature, the material of which the Sun consists (about 71% Hydrogen, 27% Helium and 2% heavier elements by mass) is in the plasma state. This is material which consists of free electrons and ions.

The Sun radiates across the whole of the electromagnetic spectrum. The energy firstly comes from the solar core, where hydrogen is converted into helium in a series of nuclear fusion reactions. This gives off some energy and particles called neutrinos. Omitting much detail beyond the scope of this introduction, the reactions are equivalent to

$$4\mathrm{H}_1^1 \rightarrow \mathrm{He}_2^4 + 2e^+ + 2\nu \tag{1.1}$$

i.e. 4 hydrogen atoms become a helium atom, 2 positrons and 2 neutrinos, and 26.73 MeV of energy is released from the reduction of mass. The hydrogen is being consumed in this way at a rate of 5×10^9 kg/s. There is enough hydrogen in the core to keep fuelling the Sun for another 4.5 billion years (Bhatnagar and Livingston 2005).

This process of converting hydrogen into helium and energy is common to all main-sequence stars. The Sun is a type of spectral class G2 star — the G meaning that the dominant emission lines are Ca II (Ca^+) and metals, giving it a yellow colour; and the 2 indicating that it is quite hot for a

G class star (Lang 2001). Stars in the same spectral classes have many properties in common: similar mass, radius, luminance and lifetimes.

The mass of the Sun is 1.9872×10^{30} kg, more than 3 hundred thousand times the mass of Earth. The radius of the Sun (indicated elsewhere as $R_\odot$) is 696 Mm, about 100 times that of the Earth. The Sun's energy output, or luminosity, is 3.8×10^{26} W.

Combining the radius and luminosity, and with the very rough assumption of the Sun as a black body, the surface temperature of the Sun can be calculated using the Stefan-Boltzmann law for black body radiation, $P = \sigma A T^4$, with the constant $\sigma = 5.67 \times 10^{-8}$ J s^{-1} m^{-2} K^{-4}. The area of the photosphere is $A = 4\pi r^2 = 4\pi(6.96 \times 10^8)^2$ m^2 hence the temperature is 5800 K. Considering a sphere with radius 1 AU, the radiation arriving at Earth is approximately 1 kW m^{-2}.

1.1.1 Solar Interior and Atmosphere

In this section is a description of the Sun: its interior and exterior layers; how energy is passed between them; and what makes them different from each other. Figure 1.1 shows a basic diagram of the Sun's layers, with values of the different temperatures and densities.

The centre of the Sun, out to 0.25R$_\odot$, is called the solar core. This region is very hot (1.5×10^7 K) and dense (1.6×10^5 kg m^{-3}), due to the gravity forces inward. Although the hydrogen nuclei repel each other, there is enough pressure in the core to overcome this repulsion. This lets the nuclei fuse together in a nuclear reaction and turn into helium. This reaction converts mass into energy and this is the process that powers the Sun. This is the only part of the Sun dense and hot enough for energy to be produced. The other layers can only transport away energy from the core and do not generate any more.

The energy produced in the core moves towards the outside of the Sun and can be seen as heat, light and magnetic energy on the surface. To get there the energy has to pass through two other layers inside the Sun: the radiative zone, to 0.7 R$_\odot$ and then the convective zone to 1 R$_\odot$. As the names suggest, energy is passed through these regions by radiation and convection respectively.

In the radiative layer the photons that carry this energy collide with the charged particles in this region. Each collision causes the photon to lose some energy. This energy is proportional to the particle's frequency, so photons that start off (e.g.) at gamma-ray frequencies may end up at the surface of the Sun at visible frequencies. Collisions occur about every 0.09 cm, so a photon could take 1.7×10^5 years just to get to the bottom of the convection zone Lang (2001).

The convection region is slightly cooler, about 2×10^6 K. This is cold enough for heavy nuclei to absorb electrons. These can absorb light and heat better than individual particles, so a different

Figure of Layers of the sun, not shown for copyright reasons.

Descriptions: Solar structure indicated by concentric circles

Layer	Radius/ Thickness	Temperature	Density	Other Features
Core		1.5E7	1.6E5	Energy generated
	0.25R	8E6		
Radiative Diffusion				
	0.7R	5E5		
Convection zone				Granulation from convection cells
	1R	6600	8E5	Radiation emitted
Photosphere	0.5Mm	4300		Waves
Chromosphere	2.5Mm			
		1E6	1E-11	Solar wind
Corona				

Figure 1.1: Schematic drawing of solar layers, showing the temperature (in K) and density (in kg/m^3) of the layers and location of some of the major processes (updated from Priest 2000). Between the radiative and convection zones is a tachocline layer, under this the rotation is the same everywhere, above it the rotation is different at the equator to the poles. Reproduced with kind permission of Springer Science and Business Media.

mechanism of energy transport takes over. Convection currents make the hot plasma move outward from the bottom of the convection region, deposit energy in the lower temperature region, then the cooler plasma moves inward to start the process again.

Between the radiative and convective zones is a thin layer called the tachocline. This is thought to be important as part of the dynamo that generates and controls the large scale magnetic fields (e.g. the 11 year solar cycle mentioned later). The outer parts of the Sun rotate faster at the equator than at the poles. The rotation period for the equator is 25.67 days, whereas at a latitude of 75° it takes 33.40 days to rotate (Lang 2001). This differential rotation actually goes as deep as the tachocline between the radiative and convective zones; below this tachocline the rotation is relatively uniform in space, with a rotation period between the two extremes seen at the photosphere (Miesch 2005).

Compared to the solar radius, the photosphere is a very thin layer of the Sun, only about half a megametre thick. The photosphere is not uniform, and even during the quiet stages of the solar cycle, many interesting features are seen on the photosphere. The effects of the convection currents from the plasma below can be seen in photographs of the Sun, as granulation on the photosphere. As could be expected from this scenario, the centre of the cells are rising and are hotter and brighter than the sinking edges. These granules have diameter between 0.7 and 1.5 Mm. Supergranules can also be seen, with diameters around 20 to 54 Mm. These are the tops of the convection cells carrying hot plasma from the region below.

Large dark regions known as sunspots are sometimes noticeable on the surface of the Sun. These sunspots are regions where the magnetic field is stronger than the surrounding area (possibly up to about 0.4 T in the centre of a sunspot). Galileo, and other observers of the time, thought sunspots were clouds above the Sun's surface; then later they were thought to be volcanoes like on a planet's surface (Clark 2009). Sunspots are now known to be cooler regions on the photosphere. Because they are cooler they do not appear as bright as the rest of the photosphere.

The central, darker area of the sunspot is the umbra, usually having diameter around 10 to 20 Mm. An old drawing of a sunspot, surrounded by granulation, is shown in Fig. 1.2. The drawing was published in 1875, but shows many of the same features as modern photographs taken with telescopes. A modern image is shown in Fig. 1.3, where the granulation can been seen more clearly.

The number of sunspots varies on an approximately 11 year cycle, and this matches with the 'activity' of the Sun: the number and intensity of flares, coronal mass ejections (CMEs), prominences etc. all vary with the number of sunspots. Once the global magnetic field has settled down, the sunspot count and activity is at its minimum, then the process continues to the next solar maximum. The time between solar maxima is usually around 11 years, but this can vary considerably, and in some historic times there has been very little solar activity for a very long time, e.g. the Maunder Minimum between 1645 and 1715. Figure 1.4 shows the variation in the number of

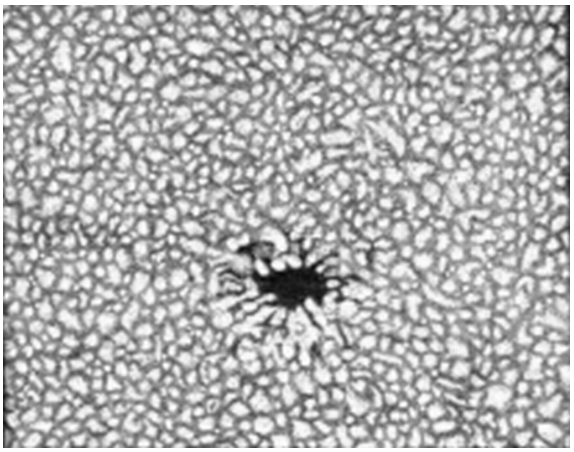

Figure 1.2: Drawing of a sunspot and granulation by Secchi (1875). Book scanned by University of St Andrews Library Special Collections.

sunspots since the 1600's.

Next is the chromosphere, again a thin layer, this time around 2.5 Mm. This is hotter than the photosphere, approximately 10^4 K but far less dense. This means that the spectrum from the chromosphere has emission lines rather than the absorption lines that the photosphere has. The composition is similar to the photosphere so the same lines that are absorbed in the photosphere are emitted from the chromosphere. One feature that can be seen in the chromosphere is narrow jets of gas that last a few minutes each, called spicules.

The temperature is about 6,000 K where the photosphere and chromosphere join, then just further out there is a temperature minimum of about 4,300 K. The temperature increases to become about 30,000 K at the start of the transition region. The transition region is between the chromosphere and corona. In this region the temperature rapidly increases from about 30,000 K to 1,000,000 K over a distance of less than 3 Mm.

Outward from the chromosphere is the corona. During a solar eclipse observed from Earth, the moon blocks out the bright photosphere so the area around can be seen. This looks like a crown, which is where the name corona comes from. Figure 1.5 shows an image of the outer corona. Depending on the amount of activity on the Sun, it may be possible to see coronal streamers that extend far away from the Sun, these are the effects of particles travelling along magnetic field lines that extend far into interplanetary space. Telescopes on the ground and space-based instruments for observations of the corona (e.g. LASCO on SOHO; SECCHI COR 1 and 2 on STEREO) have an occulting disk that block out the bright photosphere like the moon during an eclipse. This allows the corona to be examined constantly. Observations can be made in X-rays, e.g. SXT on Yohkoh and Hinode, or ultraviolet, e.g. EUV on TRACE. The temperature of the corona means that it is the brightest layer observed in soft X-rays.

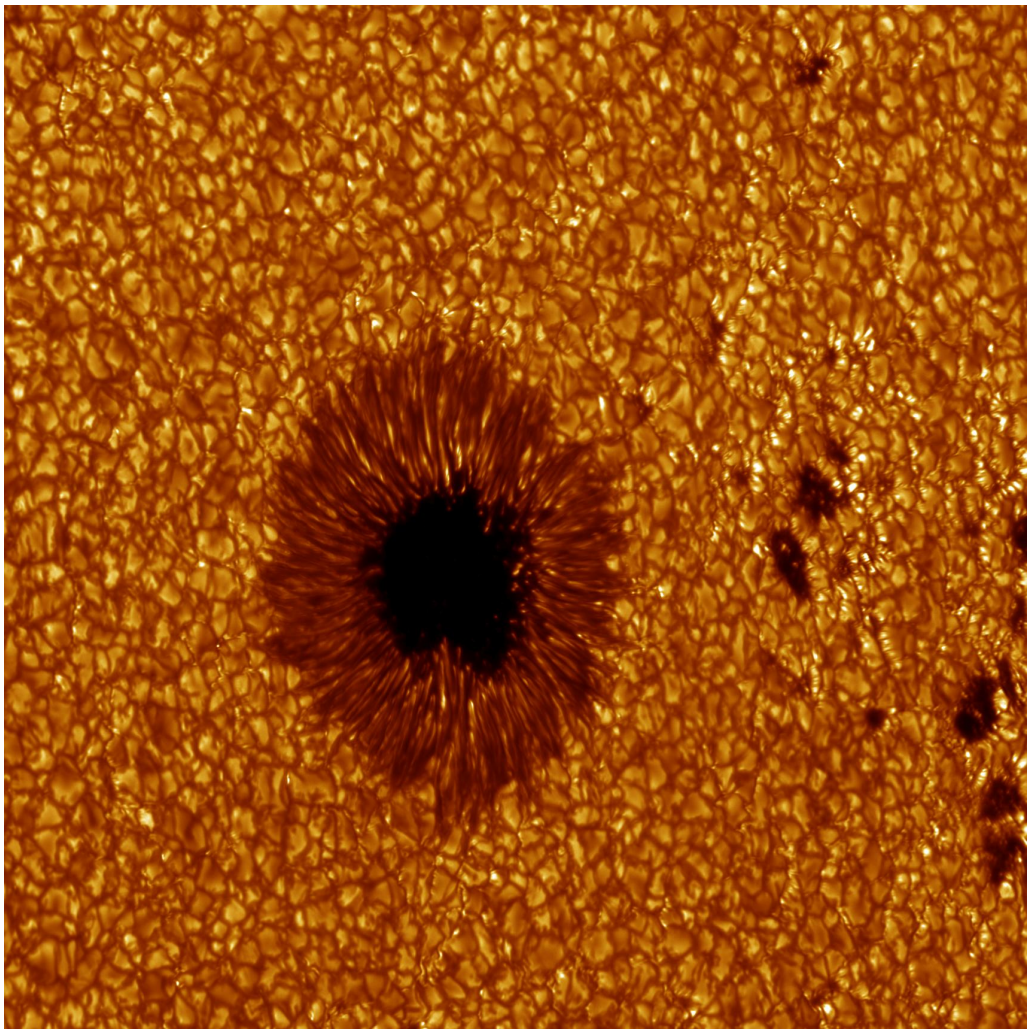

Figure 1.3: Image of a sunspot and granulation taken using the Swedish 1m Solar Telescope on La Palma, Spain. Observed by Scharmer and Langhans (2003) of the Institute for Solar Physics of the Royal Swedish Academy of Sciences, Sweden.

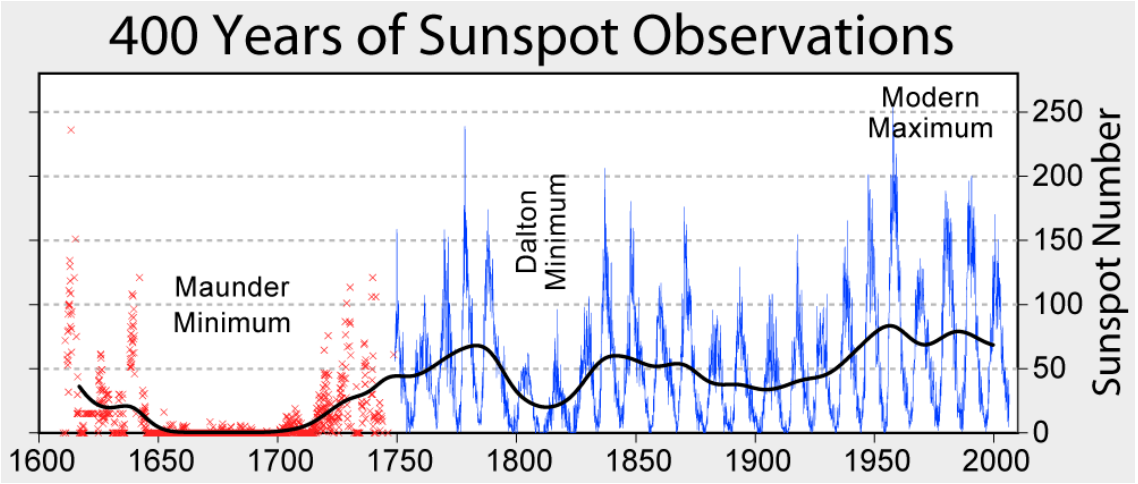

Figure 1.4: Variation in the number of sunspots over the years. The 11 year cycle can be seen as the space between the peaks. The most dramatic change is during the Maunder Minimum from 1645 to 1715. In recent times there has been more solar activity than historically, so the sunspot count is bigger. Image from Rohde (2006).

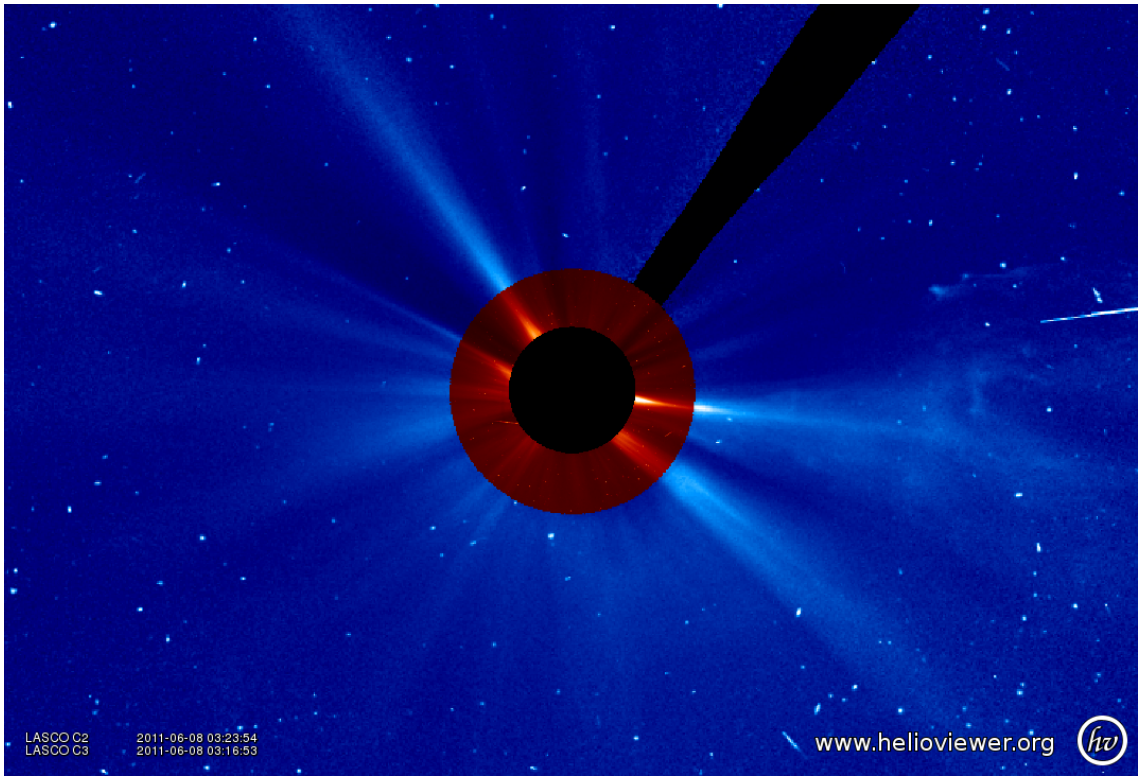

Figure 1.5: White light image of the corona and surrounding heliosphere, out to 32 solar radii. The inner red image is taken by C2, the outer blue image by C3 of LASCO on board SOHO. Images taken around 03:20 on 8th June 2011. Picture from Helioviewer Project (2011).

Magnetic field lines are usually described as open if they do not loop back to the solar surface in a reasonable (measurable) distance. In the corona, plasma can travel along these open field lines, to Earth and far beyond, travelling over distances up to 50 or 100 AU at supersonic speeds. On the open field lines, the hot coronal plasma streams away from the Sun in the form of the solar wind. The solar wind extends throughout the solar system, where it eventually encounters the surrounding interstellar medium (ISM). The region of space where the solar wind dominates is called the heliosphere.

1.1.2 Solar Flares

Flares are sudden increases in emission from the Sun, lasting a few minutes to a few hours. In visible light, very intense flares are often seen as bright patches in Hα emission[1], sometimes called two-ribbon flares. As Hα emission is from the chromosphere, this suggests that the flaring region is in the chromosphere. However, flares can be seen as a brightening over a broad range of wavelengths.

The cause of this brightening is the release of magnetic energy and its conversion into flow energy, thermal energy (heating) and non-thermal energy (accelerated particles). Energies of 10^{19} – 10^{25} J can be released during a flare. The plasma in the flaring region can become much hotter than the average coronal temperature. Flares are the most energetic plasma activity events in the solar system. Flares have also been observed on other stars, so studying them on the Sun may also give insight into other flaring stars.

The Carrington Event, a famous historical example of a flare

The first well-recorded example of a flare is now known as the Carrington event, as it was seen by Richard C. Carrington in his observatory in Surrey on Thursday 1st September 1859. He saw a huge sunspot group, then suddenly two bright spots appeared above the sunspot region. The spots became brighter and changed into more of a kidney shape. After about a minute, the spots had become much dimmer, and eventually went back to being small dots, then to disappear (Carrington 1859). At first Carrington was unsure of what he had really seen, but the flare was also observed by Hodgson (1859) and both presented their independent observations at the Royal Astronomical Society meeting on 11th November 1859 (Clark 2009).

A few days after this flare was seen, it was noticed that strange things were happening on Earth — telegraph machine bells rang mistakenly and sometimes even produced large sparks that started

[1] Hα emission is red light at 656 nm, which is emitted when electrons move from the 3rd to 2nd energy level in a hydrogen atom.

fires in the offices they were in. Aurorae were seen even close to the equator.

The effects seen on Earth around this time would probably have been due to a coronal mass ejection (CME) associated with the flare. A CME distorts the magnetosphere of the Earth and induces electric currents by interacting with the Earth's magnetic field. Nowadays the effects of the accompanying CME might be even more noticeable. In modern times, satellites and electricity power networks have been damaged by the induced currents and the magnetosphere being distorted by high speed blast of charged particles from CMEs.

Modern Views of Solar Flares

Nowadays, there are many instruments, both in space and ground-based, watching the Sun for flares across almost all wavelengths of the electromagnetic spectrum. Observations can show where accelerated particles go, how much they are accelerated and the time this takes, but there is no way to observe directly what acceleration processes are causing this. To try to explain what is seen in these observations, models have to be constructed.

The standard model of a solar flare gives the broad steps of what is happening in a flare. Figure 1.6 shows one of these cartoons and points out areas that have been looked at by observations and theory. In this cartoon, energy powering a flare comes from the magnetic energy released by magnetic reconnection. This energy is converted into other forms of energy such as bulk flows of plasma, thermal energy (plasma heating) and non-thermal energy used to accelerates particles. Accelerated particles can become trapped for some time. Energy is released at the footpoints and loop top/cusp in the form of hard X-rays.

To consider how energy can be stored in the magnetic field then released, it is worth discussing magnetic fields with no free energy. These magnetic fields that have the lowest possible energy for a given boundary condition are called potential fields. There is a unique potential field for a specified set of boundary conditions. There are no currents in this field as $\mathbf{j} \propto \nabla \times \mathbf{B} = \mathbf{0}$. The free energy that can be released by a field can be worked out by subtracting the total energy of the field from the energy of the potential field for the same boundary conditions if there are no further constraints (e.g. the plasma can relax to the potential field).

Magnetic field lines emerging from the chromosphere may be twisted or stretched to make them non-potential; or fields already in the corona may be stressed by motions of the photospheric plasma. The excess energy in these fields can be released during solar eruptions (both flares and CMEs) and converted into heating and other forms of kinetic energy such as particle acceleration and waves.

Observations have been made of flares at many wavelengths, and how much energy is given out

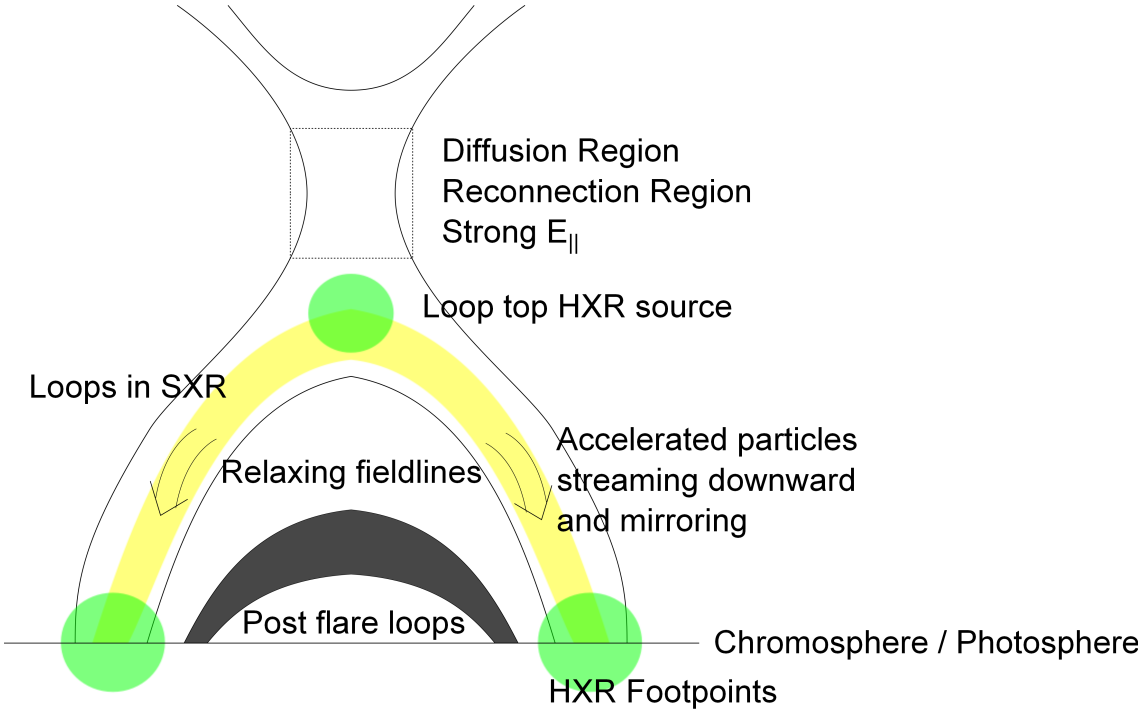

Figure 1.6: Cartoon of the standard flare model showing some of the important features. Footpoint sources in the chromosphere/photosphere and to a lesser extent a loop top source are observable in hard (high energy) X-rays. The heated loops can be seen in soft X-rays. The reconnection region is non-ideal and electric fields parallel to the magnetic field will exist, which could accelerate particles. Reconnected field lines come back into the ideal region from the top and bottom of the diffusion region, bringing hotter plasma with them. Particles can be further accelerated by a collapsing trap forming within the relaxing field lines, or by other mechanisms discussed in this chapter. Particles can be mirrored when they get to the stronger magnetic field regions above the footpoints, where the field lines converge. Particles that are not mirrored above the footpoints penetrate through to the chromosphere and collide with the denser plasma in this region, giving rise to footpoint emission. Flare loops that have already relaxed form a region of stronger magnetic field. This can cause fast shocks to form above it. This cartoon is not to scale, e.g. the reconnection region would be too small to see on this diagram compared to other features.

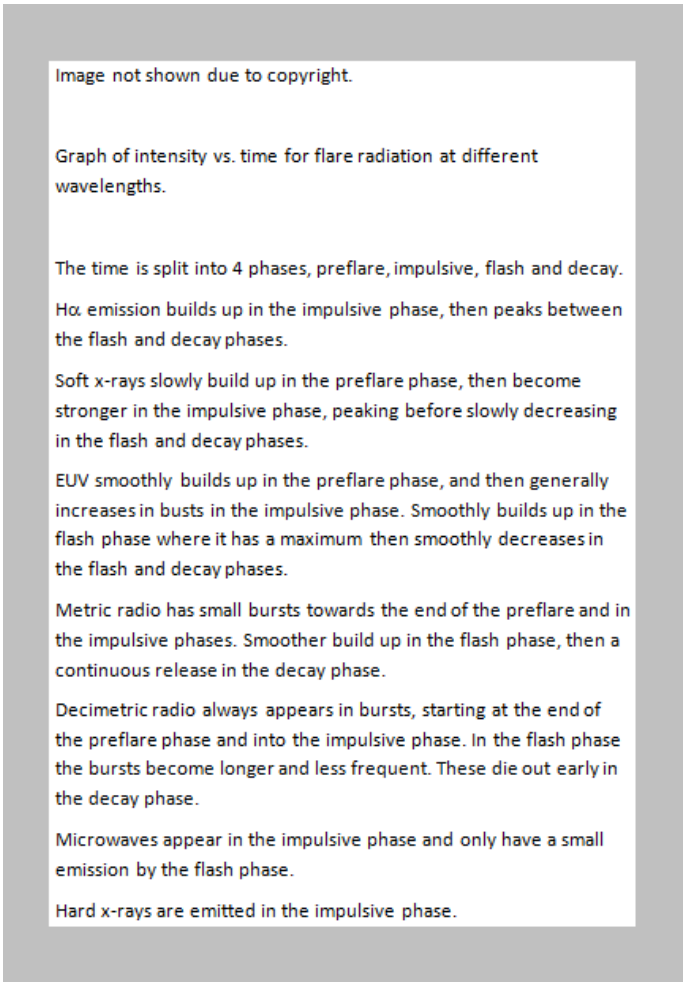

Figure 1.7: Flares in several wavelengths. The different phases of the flare cause emission at different wavelengths. Image from Benz (2002). Copyright Kluwer Academic Publishers, reproduced with kind permission of Springer Science and Business Media.

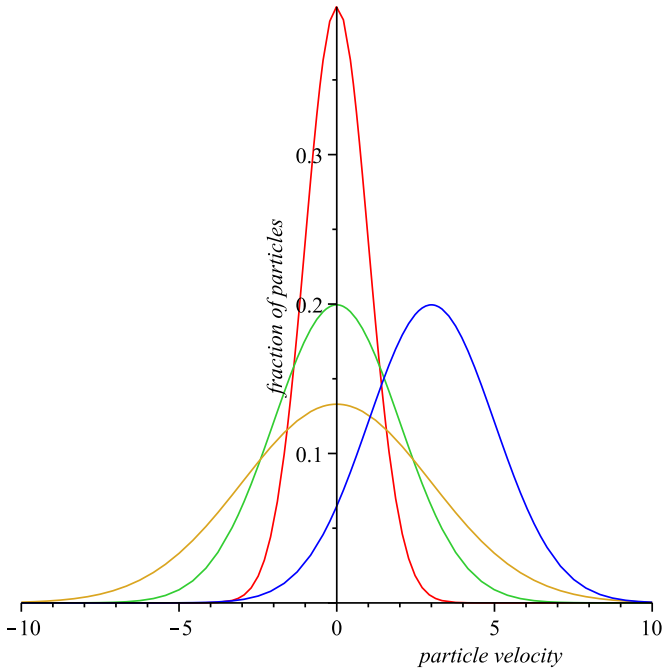

Figure 1.8: Thermal distributions of particle velocity in one dimension. The green and gold lines indicate particle distributions for temperatures that are respectively 2 and 3 times the temperature of the red distribution. Each distribution has the same area under the curve (same number of particles), but higher temperature means that more of the particles have higher energies. The blue line indicates the same thermal distribution as the green line, but there is also a plasma flow at the average velocity (often referred to as the bulk flow velocity).

at the different wavelengths changes throughout the flare. Figure 1.7 shows how the intensities change during the four phases of a flare: In the preflare phase, for approximately the first 10 minutes in a large flare, the plasma begins to heat up and radiates soft X-rays and EUV[2]. Immediately after the preflare phase is the impulsive phase. This phase lasts only a few minutes but is when the majority of the flare's energy is released, mostly to accelerate electrons and ions, causing the hard X-ray footpoints. Some of the particles can be trapped and emit over a longer time at radio and microwave wavelengths. Normally at the same time or just after the impulsive phase is an increase in Hα emission and the glow extending over more wavelengths. This is called the flash phase and lasts up to 20 minutes. In the hours after this the decay phase occurs when most of the plasma has relaxed to how it was before the flare, with the possible exception of the high up coronal plasma (above 10Mm) which may still be reacting to the eruption, the reconfiguring field and accelerating particles (Benz 2002, 2008).

Plasma heating increases the total kinetic energy over all particles, but a Maxwellian distribution of particle speeds is maintained. Figure 1.8 shows the relation between particle velocity distributions

[2]Extreme Ultraviolet. High frequency UV radiation.

(in 1D) at different temperatures and also with a bulk flow. A thermal distribution of particle velocities in 1D is given by:

$$f = \frac{1}{\sqrt{2\pi}v_{th}} \exp\left[\frac{-(v-\bar{v})^2}{(2v_{th}^2)}\right] \tag{1.2}$$

where f is the fraction of particles at that velocity v, $v_{th} = \sqrt{\frac{k_B T}{m}}$ is the thermal speed and $\bar{v}$ is the average velocity (bulk flow velocity) of the plasma. This is a Gaussian distribution with $\int_{v=-\infty}^{\infty} f \mathrm{d}v = 1$. Figure 1.8 shows this for $\bar{v} = 0$ and $T \propto 1, 2, 3$ (in red, green and gold respectively; showing the effect of doubling and tripling the temperature) and also for $\bar{v} = 3, T \propto 2$ (in blue; showing a plasma beam). At higher temperatures the velocity distribution becomes wider. This means that more particles have higher speeds and thus higher energies. The average velocity is still zero if the thermal plasma is not systematically moving on large scales (large in this case being comparable to the MHD scale length). Particle velocity distributions that cannot be described as a single Gaussian are called non-thermal.

The corresponding emissions from thermal and non-thermal distributions can be observed. The non-thermal component is observed by emissions in higher frequency (harder) X-ray emission. The results of observations over a whole flare region are usually considered as thermal spectrum and a non-thermal power law spectrum that can be added together. This is demonstrated in Fig. 1.9.

When high energy particles slow down by coming close to other particles (colliding) they emit Bremsstrahlung radiation. This is seen in the hard X-rays emitted from 'foot points' when accelerated particles reach the denser chromosphere. Observations of the Sun in X-rays can only be made outside the Earth's atmosphere, e.g. using instruments on spacecraft such as RHESSI. Such observations can show where the X-rays are emitted from within the flare. Most of this radiation is emitted at the footpoints. There may also be a source at the loop top but this is usually less bright and the footpoint sources are often so bright that other emission cannot be seen in contrast. However, when a flare erupts just behind the edge of the Sun (known as behind the limb) the emission from the footpoints is occulted by the photosphere and the loop top emission is clearer. There are usually soft X-rays emitted all along the heated magnetic loops and hard X-rays emitted from the loop top, although in the oft-referenced Masuda et al. (1994) flare the hard X-ray source was above the soft X-ray loop top source. X-rays come from the heating of the plasma, as well as bremsstrahlung radiation caused by particles interacting with each other, slowing down and emitting the energy as radiation. Even though the trapping could be going on as discussed in later chapters, the density of the region is very low, so how the particles could be made to give off radiation is not well understood at present.

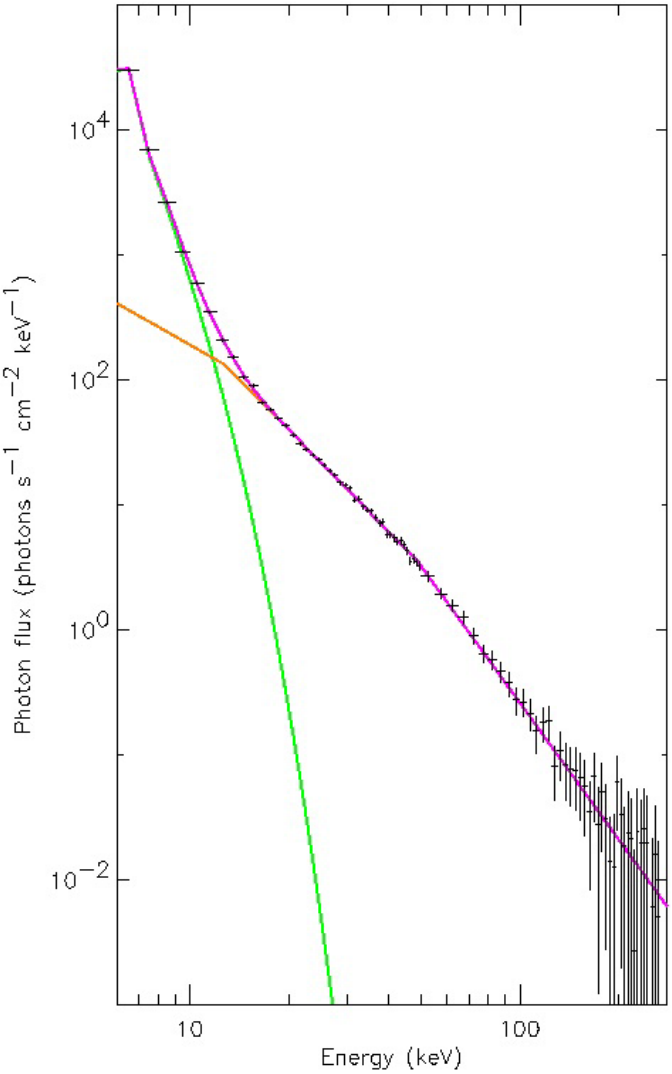

Figure 1.9: Spectrum of X-rays emitted from flares. These are usually considered as a lower energy thermal part in soft X-rays (green), and a higher energy, non thermal part in hard X-rays (orange). The whole spectrum is approximated by adding these two distributions together (purple). From Benz (2008), reproduced with permission under a creative commons licence.

1.2 Maxwell's Equations, Fluid Equations and Magnetohydrodynamics

In this section I discuss the important equations of magnetohydrodynamics. Firstly, it is considered how magnetic and electric forces are related, and then how fluids move with the action of these forces. These are then combined to figure out how conducting fluids behave.

Maxwell's Equations

James Clark Maxwell first found a consistent set of equations describing the connection between electric fields; magnetic fields and electric charges and currents (Maxwell 1861).

In this section, and throughout this thesis, E is the electric field and B is the magnetic induction (commonly called the magnetic field). In this section, Maxwell's equations for electrodynamics are considered.

The first of Maxwell's equations is the Faraday equation. This says that an electric field is created by a magnetic field changing in time:

$$\nabla \times \mathbf{E} = -\frac{\partial \mathbf{B}}{\partial t}. \tag{1.3}$$

Next is Ampere's law, which says that magnetic fields can be generated either by electrical currents ($\mathbf{j}$), or by changing electric field:

$$\nabla \times \mathbf{B} = \mu_0 \mathbf{j} + \frac{1}{c^2}\frac{\partial \mathbf{E}}{\partial t}. \tag{1.4}$$

Gauss's law for the electric field says that current sources generate electric field,

$$\nabla \cdot \mathbf{E} = \frac{1}{\epsilon_0}\rho_D \tag{1.5}$$

where ρ_D is the density of electric charges.

Lastly, the solenoidal constraint is

$$\nabla \cdot \mathbf{B} = 0, \tag{1.6}$$

which means that magnetic monopoles do not exist.

These give the relation between the electric and magnetic fields, but it is also important to consider

the fluid flows. These are discussed in the next section.

Fluid Equations

The equation of motion relies on Newton's 2nd Law. Whereas $\mathbf{F} = m\mathbf{a}$ gives the force required to accelerate a single solid body, here the equation is for a fluid, i.e.

$$\rho \frac{\mathrm{d}\mathbf{v}}{\mathrm{d}t} = \rho \left(\frac{\partial \mathbf{v}}{\partial t} + (\mathbf{v} \cdot \nabla)\, \mathbf{v} \right) = -\nabla P + \mathbf{F} \tag{1.7}$$

where $\mathbf{F}$ is any external forces and ∇P is the pressure gradient. In the cases I will be looking at, these extra forces are mostly the forces due to the Lorentz force. Gravity could also be included here, but is ignored as the effect is too small. The Lorentz force on a single particle is $\mathbf{F} = q\,(\mathbf{E} + \mathbf{v} \times \mathbf{B})$, discussed in more detail later in section 1.5. If this is summed over all the charges, then the $q\mathbf{v}$ can be replaced with the current density, $\mathbf{j}$. This gives the equation of motion,

$$\rho \left(\frac{\partial \mathbf{v}}{\partial t} + (\mathbf{v} \cdot \nabla)\, \mathbf{v} \right) = -\nabla P + \rho_D \mathbf{E} + \mathbf{j} \times \mathbf{B}. \tag{1.8}$$

Ohm's law relates the plasma flow ($\mathbf{v}$) and the electromagnetic fields, giving the current for a moving conductor in the electric field. In ideal MHD the simplest form of Ohm's law is

$$\mathbf{j} = \sigma\,(\mathbf{E} + \mathbf{v} \times \mathbf{B}) \tag{1.9}$$

There are other fluid equations that are not needed for the work in this thesis, but are listed for completeness.

Mass conservation is expressed as

$$\frac{\partial \rho}{\partial t} + \nabla \cdot (\rho \mathbf{v}) = 0. \tag{1.10}$$

If the fluid is is incompressible, i.e. $\frac{\partial \rho}{\partial t} = 0$, then the mass conservation equation is replaced by

$$\nabla \cdot \mathbf{v} = 0. \tag{1.11}$$

The ideal gas law, $P \propto \rho T$, relates the pressure, density and temperature.

If there are no energy losses (e.g. all the changes are slow enough to be adiabatic) then the energy

equation is

$$\frac{\mathrm{d}}{\mathrm{d}t}\left(\frac{P}{\rho^{\gamma}}\right) = 0 \tag{1.12}$$

where γ is the ratio of specific heats, usually taken as $\frac{5}{3}$. This can be manipulated to give the form

$$\frac{\partial P}{\partial t} + (\mathbf{v}\cdot\nabla)\,P + \gamma P \nabla\cdot\mathbf{v} = 0. \tag{1.13}$$

Magnetohydrodynamics

The above equations describe how a plasma can behave if the MHD approximation is valid. Further relations between the quantities can be found by combining these equations.

Firstly, the induction equation can be made from Ohm's law, Ampere's law and Faraday's law:

$$\frac{\partial \mathbf{B}}{\partial t} = \nabla\times(\mathbf{v}\times\mathbf{B}) - \frac{1}{\sigma}\nabla\times\mathbf{j} \tag{1.14}$$

$$= \nabla\times(\mathbf{v}\times\mathbf{B}) + \eta\nabla^2\mathbf{B} \tag{1.15}$$

where $\eta = \frac{1}{\sigma\mu}$ is the magnetic diffusivity, treated as a constant. Here the vector identity $\nabla\times(\nabla\times\mathbf{B}) = -\nabla^2\mathbf{B} + \nabla(\nabla\cdot\mathbf{B})$ and the solenoidal condition (1.6) have been used. If the plasma is perfectly conducting, sometimes called ideal, then only the $\mathbf{v}\times\mathbf{B}$ convection term is important. Similarly, if the fluid is only diffusive, then it is the second term that is important. The relative importance of these two terms is described by a dimensionless quantity called the magnetic Reynolds number,

$$R_m = \frac{L^2}{\eta T} = \frac{LV}{\eta} \tag{1.16}$$

where L, T and V are the scale length, time and speed respectively. In most of the situations considered in the solar corona, $R_m \gg 1$ so the plasma is ideal. The only exception is inside reconnection regions which are usually considered to be very small. Magnetic field lines can enter a reconnection region and be 'split apart' and 'reconnected' together, as shown in Fig. 1.10. The frozen-in condition is not valid inside these regions. This can release energy from the magnetic field, as discussed later. In general, strong currents and an electric field parallel to the magnetic field in and out of the reconnection region would also be expected. Everywhere else, in the ideal regions, the magnetic field is 'frozen-in' to the flow, i.e. the magnetic flux moves with the plasma flow.

In this thesis, the main equations required for modelling the magnetic fields in collapsing magnetic

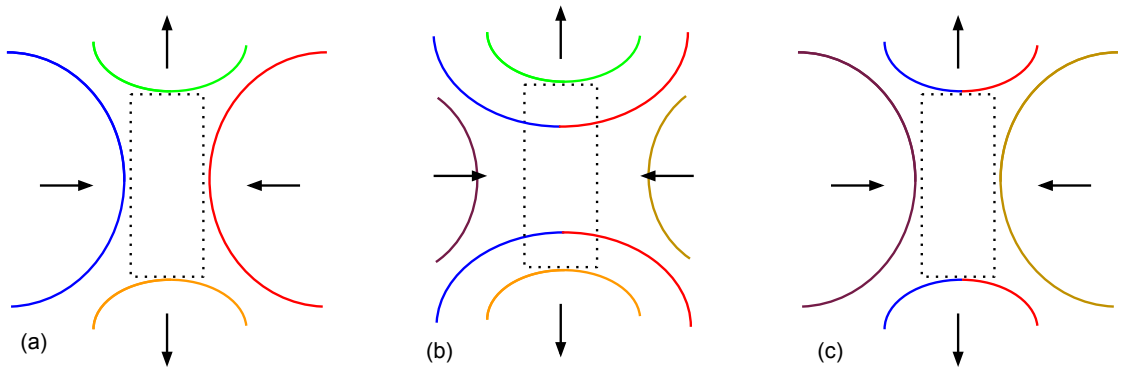

Figure 1.10: Illustration of reconnection of magnetic field lines. (a) Field lines come in to the reconnection region (dotted box) from the sides. (b) Once inside the box, they disconnect and rejoin with another field line. This changes the topology of the magnetic field lines. (c) The newly rejoined field lines leave the reconnection region and the process continues.

traps (CMTs) are Eqs. (1.3), (1.6), (1.9) and (1.15), i.e.,

$$\mathbf{E} + \mathbf{v} \times \mathbf{B} = 0 \tag{1.17}$$

$$\frac{\partial \mathbf{B}}{\partial t} = -\nabla \times \mathbf{E} \tag{1.18}$$

$$\nabla \cdot \mathbf{B} = 0 \tag{1.19}$$

$$\frac{\partial \mathbf{B}}{\partial t} = \nabla \times (\mathbf{v} \times \mathbf{B}) \,. \tag{1.20}$$

For a given velocity field these are called the kinematic MHD equations.

The advantage of kinematic MHD models compared to (e.g.) MHD simulations is that they make it possible to obtain analytical expressions for the electromagnetic fields of the CMT. This makes the integration of particle orbits in these fields more accurate, because there is no need for interpolation of the fields between grid points. Furthermore the investigation of different model features is possible in an easy way by varying model parameters. The major disadvantage of kinematic MHD models is their lack of self-consistency as the magnetic field has already been prescribed, but this is not too critical for the purpose of test particle calculations.

1.3 Particle acceleration mechanisms

In the last sections observations of solar flares were discussed. I now give a very brief summary of the processes that could accelerate particles which in turn causes the emission discussed before. Acceleration of a substantial number of charged particles to high energies is a main feature of solar flares.

The explanation of how this happens is one of the most important open questions in solar physics. There is general agreement that the energy released in solar flares is previously stored in the magnetic field, but the exact physical mechanisms by which this energy is released and converted into bulk flow energy, thermal energy, non-thermal energy and radiation energy are still a matter of discussion (e.g. Miller et al. 1997; Aschwanden 2002; Neukirch 2005; Neukirch et al. 2007; Krucker et al. 2008; Aschwanden 2009). Using observations of non-thermal high-energy (hard X-ray and γ-ray) radiation, it is estimated that a large fraction of the released magnetic energy (up to the order of 50 %) is converted into non-thermal energy in the form of high energy particles (e.g. Emslie et al. 2004, 2005).

As particle acceleration in flares is such a large field, there have been several reviews in the past few years. A variety of possible particle acceleration mechanisms have been suggested including direct acceleration in the parallel electric field associated with the reconnection process, stochastic acceleration by turbulence and/or wave-particle resonance, shock acceleration or acceleration in the inductive electric field of the reconfiguring magnetic field. Aschwanden (2002) gives a very comprehensive review of the recent observational results and the theories and expectations based on the current understanding of the physics. Neukirch et al. (2007) take a more theoretical approach when looking at the mechanisms of flares. Further discussion and references can be found in Miller et al. (1997); Neukirch (2005); Krucker et al. (2008).

1.3.1 Acceleration directly from a parallel electric field

The most obvious possible acceleration method is due to the electric field parallel to the magnetic field. Such an electric field directly accelerates the charged particles. This is usually discussed as two general cases, depending if the energy gained by particles due to the electric field is strong enough to overcome the losses due to collisions. The value of electric field that exactly compensates the losses from Coulomb collisions (particles interacting with each other) for a particular background energy (temperature) is called the Dreicer field. Electric fields both stronger and weaker than the Dreicer field are examined in literature (see reviews by Neukirch et al. 2007; Aschwanden 2002).

In sub-Dreicer models (with electric field weaker than the Dreicer field), only some of the electrons are travelling fast enough to undergo runaway acceleration. These electrons are faster than a fraction of the runaway speed,

$$v_r = v_{Te} \left(\frac{E_D}{E_\parallel} \right)^{1/2} \tag{1.21}$$

where v_{Te} is the electron thermal speed, E_D is the Dreicer field value and $E_\parallel$ is the electric field parallel to the magnetic field experienced by the electron (Holman 1985).

Electrons in a thermal distribution are accelerated up to the runaway speed but leave this distribution once gaining enough speed. The problem with this method of acceleration is that electric fields would need to act on length scales as large as the whole flare; rather than just around the reconnection region where the parallel electric field is localised.

The parallel electric field ($10^2 - 10^3$ V/m) usually associated with magnetic reconnection models is much stronger than the Dreicer field in the corona (around 10^{-3} V/m) (references within Neukirch et al. 2007). These super-Dreicer mechanisms have been modelled with and without a guide field. The guide field keeps electrons inside the acceleration region for longer, so they can gain higher energies (Litvinenko 1996).

As the particles are energised, the collisional friction reduces because the collisional cross section (how far apart the particles need to be to collide/interact) of particles decreases. Therefore as the particle velocity increases, so collisions become rarer. Hence particles with speeds above the runaway speed are accelerated out of the thermal distribution.

The number of particles that could be accelerated due to the electric field alone is significantly less than the number of particles being observed to accelerate. Thus, for a single small reconnection site, this acceleration mechanism is insufficient on its own (Neukirch et al. 2007, and refs. within). Some authors (e.g. Litvinenko 1996; Drake et al. 2005) have argued that this shortcoming might be overcome by either having a very extended current sheet or by having many reconnection regions at the same time. Whether this is possible is an open question.

There are many other acceleration methods suggested for solar flares, as there are lots of possible mechanisms in action within flares. The rest of these are processes where the energy has been transformed from the magnetic energy of reconnection, usually to bulk flow energy.

1.3.2 Shocks and Fermi acceleration

To understand mechanisms such as shock acceleration or stochastic acceleration it is worthwhile to look at what is now called Fermi acceleration. This was what Fermi (1949) suggested as a stochastic acceleration process for cosmic rays. However, it can also be applied to some solar flare models.

Plasma moving out from the reconnection region moves towards the stronger field of the magnetic loops beneath the reconnection region. If the plasma is moving downwards faster than the magnetoacoustic wave speed then information of the loop's field cannot be passed upwards to the approaching outflow. The field continues downward towards the loop, causing a shock (a discontinuity in velocity).

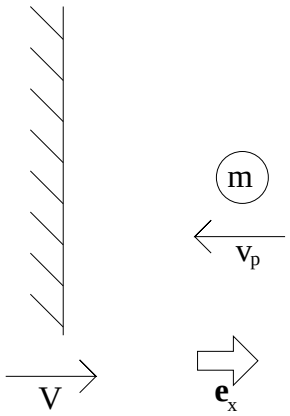

Figure 1.11: Diagram of a particle travelling towards a shock.

Charged particles are reflected at magnetic mirrors, which are stronger regions ('clouds') in the magnetic field. To discuss this in a simplified way, consider the cloud as a shock with a particle travelling normal to it, as shown in Fig. 1.11. In the lab frame (i.e. as a static observer), the particle is travelling at velocity v_p towards a shock travelling at V. In the frame of reference moving with the shock (i.e. so it looks like the shock is stationary), before the collision the particle has momentum

$$-m(v_p + V)\mathbf{e}_x \tag{1.22}$$

where the particle has mass m and $\mathbf{e}_x$ is the direction normal to the shock. After the collision, the particle has the same momentum but is now travelling in the opposite direction,

$$m(v_p + V)\mathbf{e}_x. \tag{1.23}$$

Changing back to the lab frame, the momentum is

$$m(v_p + 2V)\mathbf{e}_x. \tag{1.24}$$

So the particle has gained momentum of $2mV$ from the shock. From this, the energy gained will be:

$$E - E_p = \frac{1}{2}m\left(v_p + 2V\right)^2 - \frac{1}{2}mv_p^2 \tag{1.25}$$

$$= 2m\left(v_pV + V^2\right), \tag{1.26}$$

where E_p is the energy before the collision and E the energy after. The energy gain is first order with the speed of the shock (the lowest power of V is 1); hence is called first order Fermi acceleration. This describes a head-on collision, where the particle and shock are moving in opposite directions when the collision occurs. In this situation the particle gains energy and rebounds in the

direction it came. There is also the possibility of a following, or tail-on, collision, where particle and shock are moving in the same direction. This causes the particle to lose energy. The probability of collisions is proportional to the speed when they occur. So the average energy gain over both types of collisions is

$$\Delta E = \frac{2m(v_p+V)}{(v_p+V)+(v_p-V)}\left[v_pV+4V^2\right]+\frac{2m(v_p-V)}{(v_p+V)+(v_p-V)}\left[-v_pV+4V^2\right] \quad (1.27)$$

$$= \frac{2m}{2v_p}\left[(v_p+V)\left(v_pV+V^2\right)+(v_p-V)\left(-v_pV+V^2\right)\right] \quad (1.28)$$

$$= \frac{m}{v_p}\left[4v_pV^2\right]=4mV^2, \quad (1.29)$$

which is second order in V, so this is known as second order Fermi acceleration (Longair 1981).

The process is more complicated than the simple example that has been worked through here. Longair (1981) goes into more detail by saying that the energy of particles changes stochastically all the time anyway, the energy distribution would be broadened by these random interactions that cause scattering. The root mean square change in energy is first order but the systematic energy increase is only second order — meaning that the nature of the acceleration process must be considered as well as the systematic energy increase.

The particles can hit the shock at any angle but the analysis is the same by taking the component of the particle velocity normal to the shock and leaving the other two components unchanged. Taking account of the collisions at random angles changes the coefficient of the energy gain but it is still second order[3].

Fermi acceleration leads to a power law distribution (Fermi 1949), as is seen in observations of solar flares.

It was suggested by Tsuneta and Naito (1998) that first order Fermi acceleration at a fast shock could be responsible for the large number of high energy electrons in solar flares, however typical thermal energy in the region is less than the injection energy required to produce most of the non-thermal (higher energy) particles, so the particles would be have to be pre-accelerated for the shock acceleration (Neukirch et al. 2007).

1.3.3 Stochastic Acceleration

Stochastic processes both accelerate and decelerate particles, but the total energy gain is more than the total energy loss, so on the whole particles gain energy. In strongly turbulent plasma, where there are non-linear waves, the shock waves can produce Fermi acceleration similarly to above.

[3] e.g. Longair (1981) has particles travelling at velocity v colliding with a shock at angle θ, then works out the mean energy gain by averaging over all θ.

In weakly turbulent cases there can be another form of stochastic acceleration called wave-particle resonance. If there is a background with waves at the particle's cyclotron frequency (or some multiple of it) then the particle can gain energy from them. Because the particle's kinetic energy has changed its resonant frequency will have changed too. This means that there must be a broad spectrum of wave frequencies to enable wave-particle resonance.

Stochastic acceleration can take place within a far larger region than DC electric field models, making it easier to accelerate a greater number of electrons.

Selkowitz and Blackman (2004) say that in a turbulent plasma, the turbulent perturbations (which are fast MHD waves randomly located throughout the plasma produced from the reconnection) reflect particles and gain or lose energy. Miller et al. (1996) explain that particles make head-on or trailing collisions with the perturbation. Head on collisions cause the particles to gain energy and trailing collisions cause the particles to lose energy. Because the particles are travelling faster than the perturbations, most of the collisions will be head on, hence the particles on average gain energy. Miller et al. (1996) say that this is what causes the spikes that have been seen in hard X-ray observations.

1.4 Introduction and Overview of Collapsing Magnetic Traps

There is some observational evidence of post-flare field lines relaxation (field line shrinkage) from Yohkoh (e.g. Forbes and Acton 1996) and Hinode (e.g. Reeves et al. 2008) observations. Forbes and Acton (1996) compare field line shrinkages observed in soft X-ray and Hα loops with predictions from a numerical simulation. Shrinkage was found to be about 20% over 2 hours and 32% over 8 hours in two separate events. This shows that the structure and progression of flares have a shrinking effect on field lines after reconnection. Although this shows that field lines relax slowly, this is in a later phase than when most of the particle acceleration takes place. Earlier stages of a flare are expected to have faster field line shrinkage, but this has yet to be confirmed by observations.

Somov (1992) and Somov and Kosugi (1997) suggested that the reconfiguration of the magnetic field during a flare could contribute to the acceleration of particles. Due to the geometry of the magnetic field charged particles could be trapped while the magnetic field lines relax dynamically. In such a CMT the kinetic energy of the particles could increase due to two effects. Firstly, the betatron effect, as the magnetic field strength in the CMT increases cause the particles to increase in perpendicular velocity to keep the magnetic moment a constant; and secondly due to first-order Fermi acceleration, as the distance between the mirror points of particle orbits decreases due to the shortening of the field lines.

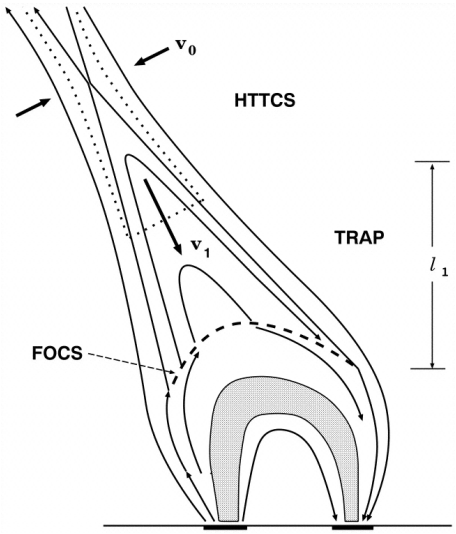

Figure 1.12: Somov and Kosugi (1997) cartoon of a collapsing magnetic trap. Particles are initially accelerated by the current sheet (HTTCS) and go onto the collapsing field line loops. The reconnected field lines relax downwards with speed v_1. Particles on the field lines can be mirrored at the shock (FOCS) or in the regions of stronger magnetic field above the footpoints. Reproduced with permission of the AAS and B. Somov.

Somov and Kosugi (1997) considered CMTs with and without a shock. Figure 1.12 shows a cartoon of this model. They also suggest that field line motions correspond to the shrinkage of X-ray loops seen in soft X-rays.

Somov and Kosugi (1997) suggest that plasma preheated and accelerated in a reconnecting current sheet plays a significant role in the particle acceleration happening in a flare. The particles then stream down the newly-reconnected field lines and are then reflected either at a shock front (if the particles are travelling faster than the magnetoacoustic speed, so can form a fast shock) or as the field lines converge into foot points at the photosphere. After the reconnection, the field lines relax downwards (as the shrinkage mentioned earlier), and the particles become trapped by the collapsing field lines.

Somov and Kosugi (1997) assume that the top of the loops (field lines) move downward with velocity v_1 ≈1400 - 1800 km s^{-1}. The local magnetoacoustic wave speed is approximately 1000 km s^{-1}, so loops travelling toward the magnetic obstacle do not know to slow as 'news' of the obstacle cannot be passed up the loop fast enough (information travels at the magnetoacoustic wave speed). This could cause a shock to form in front of the obstacle. As this is happening, the obstacle gets larger (more field lines have already relaxed to become part of the obstacle) and the shock moves upwards.

If field lines on both sides of the loop go through the shock front then a particle travelling along the loop may be reflected at the points where the loop field lines meet the shock. Alternatively, if

the flow speed is too slow to cause a shock then the particles could be reflected in the converging magnetic field towards the loop legs.

This mechanism can be considered as follows: the particles have been preheated by the current sheet, so Somov and Kosugi (1997) estimate their thermal speed to be around 10^8 m s^{-1}. This means that the particle moves between the reflection points far faster than the trap collapses. Because the environment for the periodic motion changes relatively slowly, the particles may be considered adiabatic. Hence the longitudinal adiabatic invariant is conserved,

$$J = \oint p_{||} \mathrm{d}l \approx \bar{p}_{||}(t) 4l(t) = \text{constant}, \tag{1.30}$$

where $4l$ is the distance the particle travels on a round trip and $\bar{p}_{||}$ is the longitudinal momentum of the particle averaged over one bounce period. Thus,

$$\bar{p}_{||}(t) 4l(t) = \bar{p}_{||}(0) 4l_1. \tag{1.31}$$

If the loop is assumed to be collapsing at an approximately constant velocity,

$$l(t) = v_1(t_1 - t) = \frac{l_1}{t_1}(t_1 - t) = l_1 \left(1 - \frac{t}{t_1}\right) \tag{1.32}$$

thus

$$\bar{p}_{||}(t) = \bar{p}_{||}(0) \frac{l_1}{l(t)} = \frac{1}{\left(1 - \frac{t}{t_1}\right)}. \tag{1.33}$$

so the longitudinal momentum, $\bar{p}_{||}$, increases to infinity as time progresses. This also increases the particle energy, which is given by

$$E(t) = \frac{p^2}{2m} = E(0) \frac{1}{\left(1 - \frac{t}{t_1}\right)^2}. \tag{1.34}$$

Since this Fermi acceleration is non-selective, it accelerates all the plasma, not just the electrons as some other acceleration mechanisms do (Somov and Kosugi 1997).

The betatron effect is also involved, due to the magnetic field becoming stronger as the trap collapses (the 'area' it is spread over is reducing). Because the magnetic moment of the particles $\mu = \frac{mv_\perp^2}{2B}$ is an adiabatic invariant, the perpendicular particle energy, $\frac{1}{2}mv_\perp^2$, must increase.

Somov and Kosugi (1997) also looked at a trap without a shock. In this case the current sheet and the magnetic obstacle are far enough apart that the moving plasma may be able to slow down without causing a discontinuity. This also has been observed in soft X-rays as a 'shrinkage of

X-ray loops' (Somov and Kosugi 1997).

Various fundamental properties of the particle acceleration process in CMTs have been investigated by Somov and co-workers (e.g. Bogachev and Somov 2001, 2005, 2009; Kovalev and Somov 2002, 2003a,b; Somov and Bogachev 2003), including the relative efficiencies of betatron and Fermi acceleration, the effect of collisions, the role of velocity anisotropies and the evolution of the energy distribution function in a CMT. In all cases only a very basic model for CMTs has been used.

Karlický and Kosugi (2004) also investigated particle acceleration, plasma heating and the resulting X-ray emission using a simple CMT model and a simplified equation of motion for the particles. They model particles in a collapsing trap using test particle experiments, with the inclusion of collisions in 2D. They found that acceleration was most efficient whilst particles remain in the centre of the trap (where the magnetic field is highest). This was further studied, and linked with observations when Karlický and Bárta (2006) examined the hard X-ray radiation that would result from 2D test particle experiments. This was done by using CMT-like electromagnetic fields taken from an MHD simulation of a reconnecting current sheet to investigate acceleration using test particle calculations with a view to explain hard X-ray loop-top sources. Some indication that CMTs might be relevant for X-ray loop top sources has been provided by Veronig et al. (2006). A very simple time-dependent trap model was also used by Aschwanden (2004) to explain the pulsed time profile of energetic particle injection during flares.

Bogachev and Somov (2005) give a formula for particle energy at the time of escape from a trap:

$$E_{escape} = E_{initial} \frac{B_{final}}{B_{initial}} \sin^2 \alpha_0, \tag{1.35}$$

where α_0 is the initial pitch angle. However, this requires knowing the magnetic field at the point and time that the particle escapes. In some sections of this thesis, this formula is compared with my results. In general the work in this thesis is more concerned with particles that are trapped and it is found that this formula gives an approximate lower bound on the energy that particles could obtain.

Minoshima et al. (2010) look at a different magnetic field model for a collapsing trap. The magnetic field that they use is a time-dependent series of potential fields. More details are in Chapter 5, where I look at the same field model using test particles. Minoshima et al. (2010) numerically solve the drift-kinetic equation to find the particle distribution function and examine the energy and spatial distribution of trapped particles.

A general theoretical framework for more detailed analytical CMT models based on kinematic MHD, i.e. with given bulk flow profile, in Cartesian coordinates was presented by Giuliani et al. (2005) for 2D and 2.5D magnetic fields, but excluding flow in the invariant direction. Some

examples of model CMTs were given together with a calculation of a particle orbit based on non-relativistic guiding centre theory. They claimed that in the models studied the curvature drift and the gradient-B drift play an important role in the acceleration process. Similar findings have also been made, albeit in systems of a much smaller length, in the investigation of particle acceleration in particle-in-cell simulations of collisionless magnetic reconnection (e.g. Hoshino et al. 2001). I show here that the drifts themselves are not important for the acceleration process, but that the analogous terms in the parallel equation of motion are crucial.

Particle acceleration through rapid reconfiguration of the magnetic field has also been identified as one of the mechanisms for particle energization during magnetospheric substorms in the Earth's magnetotail (e.g. Birn et al. 1997, 1998, 2004). During a substorm the stretched magnetic field of the magnetotail reconnects, leading to a so-called dipolarisation of the near-Earth tail, which is in principle very similar to the evolution of the magnetic field in a CMT associated with a solar flare. Studies of the magnetosphere have the advantage that measurements can be made directly by spacecraft in situ, an impossibility for the study of flares.

1.5 Guiding Centre Approximation

In this section, quantities which are dotted (e.g. $\dot{r}$) represent a full derivative with respect to time. Two dots indicate a second derivative etc.

Newton's second law is that the net force on an object is equal to its mass times its acceleration,

$$\mathbf{F} = m\ddot{\mathbf{r}}. \tag{1.36}$$

In the case of a charged particle in electric and magnetic fields, this force is the Lorentz force:

$$\mathbf{F} = q\left(\mathbf{E} + \dot{\mathbf{r}} \times \mathbf{B}\right). \tag{1.37}$$

These can be combined to give an equation of motion,

$$\ddot{\mathbf{r}} = \frac{q}{m}\left(\mathbf{E} + \dot{\mathbf{r}} \times \mathbf{B}\right). \tag{1.38}$$

The simplest case that can be considered with this equation would be a particle in static electric and magnetic fields. Boyd and Sanderson (1969) use fields

$$\mathbf{B} = (0, 0, B) \qquad \mathbf{E} = \left(0, E_{\perp}, E_{\parallel}\right). \tag{1.39}$$

In this thesis, an electric field parallel to the magnetic field is not considered. In any case, $E_{\parallel}$ must

be small as the plasma will try to counteract it and stay quasineutral. Hence the fields become

$$\mathbf{B} = (0, 0, B) \qquad \mathbf{E} = (0, E_\perp, 0)\,. \tag{1.40}$$

Plugging these fields into Eq. (1.38) gives

$$\ddot{x} = \frac{q}{m} B\dot{y}, \tag{1.41}$$
$$\ddot{y} = \frac{q}{m}\left(E_\perp - B\dot{x}\right). \tag{1.42}$$

where $\mathbf{r} = (x, y, z)$, $\dot{\mathbf{r}} = (\dot{x}, \dot{y}, \dot{z})$, $\ddot{\mathbf{r}} = (\ddot{x}, \ddot{y}, \ddot{z})$.

To solve the coupled equations (1.41) and (1.42), these are differentiated with respect to time:

$$\dddot{x} = \frac{q}{m} B\ddot{y} \tag{1.43}$$
$$= \frac{q^2}{m^2} B\left(E_\perp + B\dot{x}\right) \tag{1.44}$$
$$= \frac{q^2}{m^2} BE_\perp + \frac{q^2}{m^2} B^2\dot{x}, \tag{1.45}$$
$$\dddot{y} = \frac{q}{m} B\ddot{x} \tag{1.46}$$
$$= -\frac{q^2}{m^2} B^2\dot{y}, \tag{1.47}$$

which are second order linear ODEs in $\dot{x}$ and $\dot{y}$. To solve Eq. (1.47), the auxiliary equation $N^2 + \left(\frac{q}{m}B\right)^2 = 0$ is used, so the solution is

$$\dot{y} = -u \sin\left(\frac{q}{m} Bt + \alpha\right) \tag{1.48}$$

and similarly for Eq. (1.45), with the addition of a particular integral due to the inhomogeneity,

$$\dot{x} = -u \cos\left(\frac{q}{m} Bt + \alpha\right) + v_E \tag{1.49}$$

In these equations, u is a constant and $v_E = \frac{E_\perp}{B}$.

Integrating these gives the particle orbit,

$$x = \frac{mu}{qB} \sin\left(\frac{q}{m} Bt + \alpha\right) + x_0 + v_E t \tag{1.50}$$
$$y = \frac{mu}{qB} \cos\left(\frac{q}{m} Bt + \alpha\right) + y_0 \tag{1.51}$$

The sin and cos terms in these equations show that the particle generally moves in a circular orbit. For these fields, the particle moves about a point $(x_0 + v_E t, y_0, z_0)$, more generally called the guiding centre. The coefficients of time in the sin and cos terms include the charge to mass ratio,

$\frac{q}{m} = 1.76 \times 10^{11}$ C/kg for electrons, which is large for the particles being considered. This means that the particle makes its circular gyroorbit far faster than the guiding centre motion.

To compute the particle orbit in more complicated magnetic and electric fields, e.g. in 3 dimensions with time and space dependence, the equation of motion has to be integrated numerically. Because the particle quickly moves around the guiding centre, directly integrating the equation of motion will take many time steps for the particle to move far in space, i.e. for the guiding centre to move. However, by considering how the particle moves, averages can be taken over some timescales and this helps to simplify the equation of motion. The specific method used here is called the guiding centre approximation. The oscillation around the guiding centre point happens much faster than the background magnetic and electric fields change, so over this short time (gyroperiod) they can be assumed to be constant, meaning the particle locally moves in a circle (Larmor circle in some texts) around the guiding centre point. Because the $\mathbf{E} \times \mathbf{B}$ drift is dominant, to a good approximation the guiding centre is always on the same magnetic field line. The rotation around the guiding centre can be ignored, but need to know the speed of the gyroorbit as this contributes to the particle energy. This means that the focus can be on the slightly longer timescales.

The magnetic fields considered in this thesis are between 10 to 500 G, so the longest gyroperiod for an electron would be $\sim 3.6 \times 10^{-8}$ s, far shorter than the scale time of the trap, a few seconds. For the lowest field strength and electron energies of up to 100 keV, the gyroradius would be up to about 0.75 m, much smaller than the scale length of the trap, 10 Mm. These values show that the guiding centre approximation is a good approximation in the cases discussed in this thesis.

There are several ways to derive the guiding centre equation of motion: Boyd and Sanderson (1969) show specific cases with different fields and combine these to build towards a general equation of motion. Northrop (1963) makes the equation non-dimensional then adjusts the coefficients to keep the separation of timescales. Fitzpatrick (2008) splits the orbit into the position of the guiding centre and the offset from the particle position. A summary of this process is given in this section.

The particle position $\mathbf{r}$ is split into the guiding centre, $\mathbf{R}$ and the small offset from this, $\boldsymbol{\rho}$:

$$\mathbf{r}(t) = \mathbf{R}(t) + \boldsymbol{\rho}(t). \tag{1.52}$$

The trajectory of the guiding centre and the actual particle trajectory are illustrated in Fig. 1.13.

The average position over a gyroperiod is the centre of the gyrocircle, $\langle \boldsymbol{\rho} \rangle = 0$, hence called the guiding centre. The gyroradius or Larmor radius is given by $\rho = |\boldsymbol{\rho}|$.

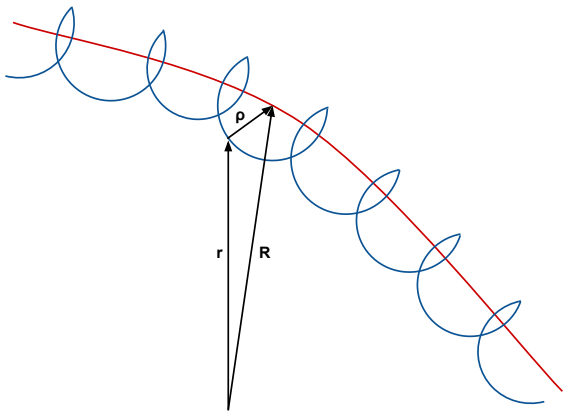

Figure 1.13: Particle trajectory (blue) and guiding centre approximation (red) with vectors defined in Eq. (1.52)*. Not to scale, as ρ is several orders of magnitude smaller than the scale length as discussed elsewhere in the text.*

The vector $\boldsymbol{\rho}$ is defined by Northrop (1963), without much explanation, as:

$$\boldsymbol{\rho} = \frac{m}{qB^2}\mathbf{B} \times \left(\mathbf{v} - \frac{\mathbf{E} \times \mathbf{B}}{B^2}\right) \tag{1.53}$$

where quantities are taken at the particle position. Looking at just the part in brackets shows the particle velocity less the velocity due to the $\mathbf{E} \times \mathbf{B}$ drift — this bracket is equivalent to the perpendicular velocity in the guiding centre ($\mathbf{E} \times \mathbf{B}$) frame. The magnitude of this vector is the gyroradius as above. The field line is perpendicular to the gyrocircle. In this equation this is given by the cross product of $\mathbf{B}$.

To allow for the separation of timescales that leads to the guiding centre approximation, a non-dimensional quantity that is the ratio of the gyrofrequency and MHD frequency is used. The MHD frequency is $\omega = \frac{1}{T}$ where T is the MHD timescale (i.e. the time for the magnetic and electric fields to change significantly). The gyrofrequency is Ω, so the ratio is $\epsilon = \frac{\omega}{\Omega}$. This is a small quantity as the MHD frequency is far slower than the gyrofrequency. Quantities can be described being of order ϵ if they vary with the gyromotion (ρ), order ϵ^0 if they vary with the guiding centre position (electric field, scale length (L) and guiding centre velocity) and order ϵ^{-1} if they vary on the MHD scale (magnetic field). This ordering is imposed by many authors (e.g. Fitzpatrick 2008) to obtain the guiding centre approximation. Cary and Brizard (2009) give tables indicating the significance of each of the quantities used in the guiding centre approximation.

Equation (1.38) can be nondimensionalised by taking

$$\begin{aligned} \tilde{\mathbf{B}} &= \mathbf{B}(\mathbf{r}, t)/B_0 \\ \tilde{\mathbf{E}} &= \mathbf{E}(\mathbf{r}, t)/(v_0 B_0) \end{aligned}$$

$$\begin{aligned}\tilde{t} &= t/(L/v_0)\\ \tilde{\mathbf{r}} &= \mathbf{r}/L.\end{aligned}$$

These make the nondimensional equation of motion

$$\frac{mv_0}{qB_0L}\frac{\mathrm{d}^2\tilde{\mathbf{r}}}{\mathrm{d}\tilde{\mathrm{t}}^2} = \frac{\mathrm{d}\tilde{\mathbf{r}}}{\mathrm{d}\tilde{\mathrm{t}}} \times \tilde{\mathbf{B}}(\tilde{\mathbf{r}},\tilde{t}) + \tilde{\mathbf{E}}\left(\tilde{\mathbf{r}},\tilde{t}\right). \tag{1.54}$$

The ratio of the radius of gyration to the length scale of the fields is contained in $\frac{mv_0}{qB_0L}$ and this is the only scaling in the equation. This is equivalent to the ϵ discussed above. Northrop (1963) claims that this means that the dimensional equation of motion can be used, and $\frac{m}{q}$ can be treated as a dimensional smallness parameter. This is found using a different transformation of variables to get to recover Eq. (1.38):

$$\tilde{\mathbf{B}} \rightarrow \mathbf{B} \tag{1.55}$$
$$\tilde{\mathbf{E}} \rightarrow \mathbf{E} \tag{1.56}$$
$$\tilde{t} \rightarrow t \tag{1.57}$$
$$\tilde{\mathbf{r}} \rightarrow \mathbf{r} \tag{1.58}$$
$$\frac{mv_0}{qB_0L} \rightarrow \frac{m}{q}. \tag{1.59}$$

The magnetic and electric fields at the particle position and guiding centre can be related:

$$\begin{aligned}\mathbf{B}(\mathbf{r}) &= \mathbf{B}(\mathbf{R}) + (\mathbf{r}-\mathbf{R})\cdot\nabla\mathbf{B} &(1.60)\\ &= \mathbf{B}(\mathbf{R}) + \boldsymbol{\rho}\cdot\nabla\mathbf{B} &(1.61)\\ \mathbf{E}(\mathbf{r}) &= \mathbf{E}(\mathbf{R}) + (\mathbf{r}-\mathbf{R})\cdot\nabla\mathbf{E} &(1.62)\\ &= \mathbf{E}(\mathbf{R}) + \boldsymbol{\rho}\cdot\nabla\mathbf{E} &(1.63)\end{aligned}$$

using Eq. (1.52). This is, to first order, the Taylor expansion for $\mathbf{B}$ and $\mathbf{E}$ about the guiding centre. Derivatives of $\mathbf{r}$ can also be written in terms of $\mathbf{R}$ and $\boldsymbol{\rho}$:

$$\frac{\mathrm{d}^\mathrm{n}\mathbf{r}}{\mathrm{dt}^\mathrm{n}} = \frac{\mathrm{d}^\mathrm{n}\mathbf{R}}{\mathrm{dt}^\mathrm{n}} + \frac{\mathrm{d}^\mathrm{n}\boldsymbol{\rho}}{\mathrm{dt}^\mathrm{n}} \tag{1.64}$$

where n is 1 or 2 etc for first, second and higher time derivatives. Putting these into Eq. (1.38) gives an equation of motion using the guiding centre position and gyrovector to order ϵ accuracy:

$$\begin{aligned}&\frac{\mathrm{d}^2\mathbf{R}}{\mathrm{dt}^2} + \frac{\mathrm{d}^2\boldsymbol{\rho}}{\mathrm{dt}^2} =\\ &\quad\frac{q}{m}\left(\mathbf{E}(\mathbf{R},t) + \boldsymbol{\rho}\cdot\nabla\mathbf{E}(\mathbf{R},t) + \left(\frac{\mathrm{d}\mathbf{R}}{\mathrm{dt}} + \frac{\mathrm{d}\boldsymbol{\rho}}{\mathrm{dt}}\right)\times\left[\mathbf{B}(\mathbf{R},t) + \boldsymbol{\rho}\cdot\nabla\mathbf{B}(\mathbf{R},t)\right]\right)\end{aligned} \tag{1.65}$$

The time average of this equation needs to be taken - as mentioned earlier $\boldsymbol{\rho}$ is not important although its derivatives are. The time dependence of $\boldsymbol{\rho}$ must be considered. To do this, the co-ordinate system can be changed so that one of the vectors is along the guiding centre field line, $\mathbf{b} = \frac{\mathbf{B}}{B}$. Two vectors perpendicular to $\mathbf{B}$ and each other are also needed, say, $\hat{\mathbf{e}}_2$ and $\hat{\mathbf{e}}_3$, after the notation of Northrop (1963). These are chosen so that

$$\boldsymbol{\rho} = \rho \left(\hat{\mathbf{e}}_2 \sin(\theta) + \hat{\mathbf{e}}_3 \cos(\theta) \right) \tag{1.66}$$

where $\theta = \int \omega dt$, as $\omega = \frac{qB(R)}{m}$ can be time dependent. This includes the ratio m/e in it, so ω is of order ϵ^{-1}. The equation for $\boldsymbol{\rho}$ can be differentiated, but care needs to be taken as ρ and the vectors, $\hat{\mathbf{e}}_2$ and $\hat{\mathbf{e}}_3$ are time dependent.

$$\frac{\mathrm{d}\boldsymbol{\rho}}{\mathrm{dt}} = \omega\rho \left(\hat{\mathbf{e}}_2 \cos(\theta) - \hat{\mathbf{e}}_3 \sin(\theta) \right) + \frac{\mathrm{d}}{\mathrm{dt}} \left(\rho \hat{\mathbf{e}}_2 \right) \sin(\theta) + \frac{\mathrm{d}}{\mathrm{dt}} \left(\rho \hat{\mathbf{e}}_3 \right) \cos(\theta) \tag{1.67}$$

The first term contains $\omega\rho$, so is of order 1, and the last two terms are of order ϵ as they contain ρ or $\frac{\mathrm{d}\rho}{\mathrm{dt}}$. This is differentiated again and put into Eq. (1.65). After time averaging, so that the changes are averaged over a gyroperiod (integrating θ from 0 to 2π) and some vector manipulation the acceleration of the guiding centre to order 1 is obtained:

$$\frac{\mathrm{d}^2\mathbf{R}}{\mathrm{d}t^2} = \frac{q}{m} \left[E(R) + \frac{\mathrm{d}\mathbf{R}}{\mathrm{d}t} \times \mathbf{B}(\mathbf{R}) \right] - \frac{\mu}{m} \nabla B(\mathbf{R}) \tag{1.68}$$

note that the most significant part of this is order ϵ^{-1}. More details on the process of working out this equation is given in Northrop (1963).

Crossing with $\mathbf{b}$ gives

$$\frac{\mathrm{d}^2\mathbf{R}}{\mathrm{d}t^2} \times \mathbf{b} = \frac{q}{m} \left[\mathbf{E} \times \mathbf{b} + \left(\frac{\mathrm{d}\mathbf{R}}{\mathrm{d}t} \times \mathbf{B}(\mathbf{R}) \right) \times \mathbf{b} \right] - \frac{\mu}{m} \nabla B(\mathbf{R}) \times \mathbf{b}. \tag{1.69}$$

Using $\left(\frac{\mathrm{d}\mathbf{R}}{\mathrm{dt}} \times \mathbf{B}(\mathbf{R}) \right) \times \mathbf{b} = B \left(\frac{\mathrm{d}\mathbf{R}}{\mathrm{dt}} \times \mathbf{b} \right) \times \mathbf{b} = B \left[\left(\mathbf{b} \cdot \frac{\mathrm{d}\mathbf{R}}{\mathrm{dt}} \right) \mathbf{b} - \frac{\mathrm{d}\mathbf{R}}{\mathrm{dt}} \right]$ and rearranging gives the perpendicular velocity for the guiding centre, to order 1:

$$\frac{\mathrm{d}\mathbf{R}_\perp}{\mathrm{d}t} = \frac{\mathrm{d}\mathbf{R}}{\mathrm{d}t} - \left(\mathbf{b} \cdot \frac{\mathrm{d}\mathbf{R}}{\mathrm{d}t} \right) \mathbf{b} = \frac{1}{B} \left(\frac{\mu}{m} \mathbf{b} \times \nabla B(\mathbf{R}) + \mathbf{E} \times \mathbf{b} - \frac{m}{q} \frac{\mathrm{d}^2 R}{\mathrm{d}t^2} \times \mathbf{b} \right) \tag{1.70}$$

This clearly shows three different drifts: Firstly the $\nabla\mathbf{B}$ drift; then the $\mathbf{E} \times \mathbf{B}$; and lastly what Northrop (1963) calls an 'acceleration drift', which includes a combination of the curvature and polarisation drifts. In the form given in Eq. (1.70), the acceleration drift is

$$\mathbf{v}_a = \frac{m}{q} \frac{\frac{\mathrm{d}^2\mathbf{R}}{\mathrm{d}t^2} \times \mathbf{b}}{B} \tag{1.71}$$

which relies on knowing the guiding centre acceleration. This is only needed to $O(1)$ in ϵ, so can be found by differentiating Eq. (1.70), ignoring terms with the $\epsilon = \frac{m}{q}$ factor. To get this, $\frac{\mathrm{d}^2\mathbf{R}}{\mathrm{d}t^2}$ is split into parallel and perpendicular components, where $v_\parallel = \mathbf{b}\left(\frac{\mathrm{d}\mathbf{R}}{\mathrm{d}t}\cdot\mathbf{b}\right)$. This gives

$$\begin{aligned}
\frac{\mathrm{d}^2\mathbf{R}}{\mathrm{d}t^2} &= \frac{\mathrm{d}}{\mathrm{d}t}\left(\frac{\mathrm{d}\mathbf{R}_\perp}{\mathrm{d}t} + \mathbf{b}\left(\frac{\mathrm{d}\mathbf{R}}{\mathrm{d}t}\cdot\mathbf{b}\right)\right) && (1.72)\\
&= \frac{\mathrm{d}}{\mathrm{d}t}\left(\frac{\mathrm{d}\mathbf{R}_\perp}{\mathrm{d}t}\right) + \frac{\mathrm{d}}{\mathrm{d}t}\left(\mathbf{b}v_\parallel\right) && (1.73)\\
&= \frac{\mathrm{d}\mathbf{u}_E}{\mathrm{d}t} + \frac{\mathrm{d}}{\mathrm{d}t}\left(\mathbf{b}v_\parallel\right) && (1.74)\\
&= \frac{\mathrm{d}\mathbf{u}_E}{\mathrm{d}t} + \frac{\mathrm{d}\mathbf{b}}{\mathrm{d}t}v_\parallel + \mathbf{b}\frac{\mathrm{d}v_\parallel}{\mathrm{d}t} && (1.75)
\end{aligned}$$

because to order 1,

$$\frac{\mathrm{d}\mathbf{R}_\perp}{\mathrm{d}t} = \frac{\mathbf{E}\times\mathbf{b}}{B} = \mathbf{u}_E. \tag{1.76}$$

Hence the acceleration drift becomes

$$\begin{aligned}
\mathbf{v}_a &= \frac{m}{q}\frac{\left(\frac{\mathrm{d}\mathbf{u}_E}{\mathrm{d}t} + \frac{\mathrm{d}\mathbf{b}}{\mathrm{d}t}v_\parallel + \mathbf{b}\frac{\mathrm{d}v_\parallel}{\mathrm{d}t}\right)\times\mathbf{b}}{B} && (1.77)\\
&= \frac{m}{q}\frac{\left(\frac{\mathrm{d}\mathbf{u}_E}{\mathrm{d}t} + \frac{\mathrm{d}\mathbf{b}}{\mathrm{d}t}v_\parallel\right)\times\mathbf{b}}{B} && (1.78)
\end{aligned}$$

to make the dependence on space explicit, the full derivatives can be changed into partial derivatives using

$$\frac{\mathrm{d}}{\mathrm{d}t} = \frac{\partial}{\partial t} + \left[\left(\mathbf{b}v_\parallel + \mathbf{u}_E\right)\cdot\nabla\right] = \frac{\partial}{\partial t} + v_\parallel\frac{\partial}{\partial s} + \mathbf{u}_E\cdot\nabla, \tag{1.79}$$

where s is the distance along the guiding centre/field line path.

$$\mathbf{v}_a = \frac{m}{q}\left(\frac{\partial\mathbf{u}_E}{\partial t} + v_\parallel\frac{\partial\mathbf{u}_E}{\partial s} + \mathbf{u}_E\cdot\nabla\mathbf{u}_E + v_\parallel\frac{\partial\mathbf{b}}{\partial t} + v_\parallel^2\frac{\partial\mathbf{b}}{\partial s} + v_\parallel\mathbf{u}_E\cdot\nabla\mathbf{b}\right)\times\frac{\mathbf{b}}{B}. \tag{1.80}$$

These are all partial derivatives so can be calculated in the computer program that is used to model test particles trajectories.

The first three terms are due to the polarisation drift, $\frac{m}{q}\frac{\mathrm{d}\mathbf{u}_\mathrm{E}}{\mathrm{d}t}\times\frac{\mathbf{b}}{B}$.

Next is the curvature drift, $-\frac{v_\parallel^2}{\omega R_c^2}\mathbf{R}_c\times\mathbf{b} = \frac{v_\parallel^2}{\omega}\left(\mathbf{b}\cdot\nabla\right)\mathbf{b}\times\mathbf{b} = \frac{v_\parallel^2}{\omega}\frac{\partial\mathbf{b}}{\partial s}\times\mathbf{b}$, where R_c is the radius of curvature of the field line (see e.g. Freidberg 2008).

The terms involving $\mathbf{u}_E$ and its derivatives are due to the electric field being $O(1)$ rather than small enough to be $O(\epsilon)$ (Northrop 1963). In the cases in this thesis these are included anyway,

but the contribution from these terms is small because the electric field used is small.

Putting all of this together gives the velocity of the guiding centre perpendicular to the magnetic field line.

$$\begin{aligned}\frac{\mathrm{d}\mathbf{R}_\perp}{\mathrm{d}t} &= \frac{\mathbf{b}}{B}\times\Big(\frac{\mu}{m}\nabla B-\mathbf{E}\\ &\quad+\frac{m}{q}\left[\frac{\partial\mathbf{u}_E}{\partial t}+v_\parallel\frac{\partial\mathbf{u}_E}{\partial s}+\mathbf{u}_E\cdot\nabla\mathbf{u}_E+v_\parallel\frac{\partial\mathbf{b}}{\partial t}+v_\parallel^2\frac{\partial\mathbf{b}}{\partial s}+v_\parallel\mathbf{u}_E\cdot\nabla\mathbf{b}\right]\Big)\end{aligned}\tag{1.81}$$

This can be used to calculate part of the energy, $E_\perp=\frac{1}{2}m\left(\frac{\mathrm{d}\mathbf{R}_\perp}{\mathrm{d}t}\right)^2$. The parallel energy and a contribution from the $\mathbf{E}\times\mathbf{B}$ drift still needs to be added.

Next the equation for the motion of the guiding centre along the magnetic field line can be expanded,

$$\frac{\mathrm{d}v_\parallel}{\mathrm{d}t}=\frac{\mathrm{d}}{\mathrm{d}t}\left(\frac{\mathrm{d}\mathbf{R}}{\mathrm{d}t}\cdot\mathbf{b}\right)=\frac{\mathrm{d}^2\mathbf{R}}{\mathrm{d}t^2}\cdot\mathbf{b}+\frac{\mathrm{d}\mathbf{R}}{\mathrm{d}t}\cdot\frac{\mathrm{d}\mathbf{b}}{\mathrm{d}t}.\tag{1.82}$$

From Eq. (1.68), to $O(\epsilon)$,

$$\frac{m}{q}\frac{\mathrm{d}^2\mathbf{R}}{\mathrm{d}t^2}\cdot\mathbf{b}=\mathbf{E}\cdot\mathbf{b}-\mu q\frac{\partial B}{\partial s}.\tag{1.83}$$

Some manipulation gives

$$\frac{\mathrm{d}\mathbf{R}}{\mathrm{d}t}\cdot\mathbf{b}=\big(\mathbf{b}v_\parallel+\mathbf{u}_E\big)\cdot\frac{\mathrm{d}\mathbf{b}}{\mathrm{d}t}=\mathbf{u}_E\cdot\frac{\mathrm{d}\mathbf{b}}{\mathrm{d}t}\tag{1.84}$$

to order 1, as $\mathbf{b}\cdot\frac{\mathrm{d}\mathbf{b}}{\mathrm{d}t}\sim O(\epsilon)$. Using Eq. (1.79) on $\frac{\mathrm{d}\mathbf{b}}{\mathrm{d}t}$ gives

$$\frac{\mathrm{d}\mathbf{R}}{\mathrm{d}t}\cdot\mathbf{b}=\mathbf{u}_E\cdot\left[\frac{\partial\mathbf{b}}{\partial t}+\big(\mathbf{b}v_\parallel+\mathbf{u}_E\big)\cdot\nabla b\right].\tag{1.85}$$

These combine to give the guiding centre equation of motion parallel to the magnetic field line.

$$\frac{m}{q}\frac{\mathrm{d}v_\parallel}{\mathrm{d}t}=E_\parallel-\frac{\mu}{q}\frac{\partial B}{\partial s}+\frac{m}{q}\mathbf{u}_E\cdot\left(\frac{\partial\mathbf{b}}{\partial t}+v_\parallel\frac{\partial\mathbf{b}}{\partial s}+\mathbf{u}_E\cdot\nabla b\right)\tag{1.86}$$

where $E_\parallel=\mathbf{E}\cdot\mathbf{b}$. This, and Eq. (1.81) are numerically integrated to calculate the particle's orbit and energy gain.

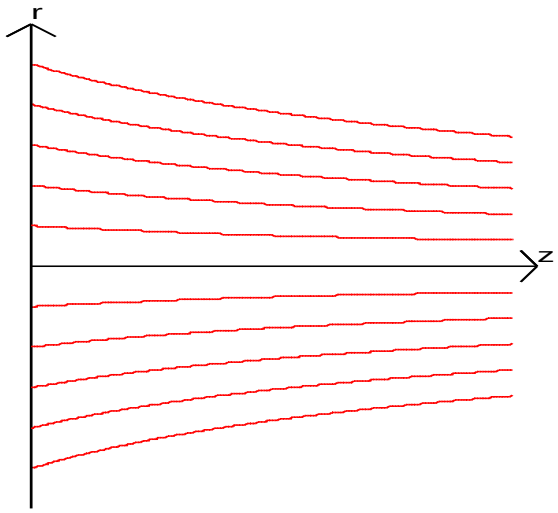

Figure 1.14: Representation of the magnetic field used in the example to show invariance of the magnetic moment.

1.5.1 Invariants of motion

There are more general ways to discuss invariants of motion (e.g. Landau and Lifshitz 1993; Cary and Brizard 2009), but in this section I will follow Boyd and Sanderson (1969).

Using the guiding centre equation with the magnetic field structures chosen brings out some invariants. In particular two of these are good for explaining how particles undergoing motion in a collapsing trap or similar structure could gain energy.

Magnetic moment

The first of these is the magnetic moment,

$$\mu = \frac{mv_\perp^2}{2B} \tag{1.87}$$

This is well conserved in many situations. The conditions for it to be conserved are the same as the requirements for the guiding centre approximation to be valid.

Boyd and Sanderson (1969) and Chamberlain (1964) show this invariance for a particle in a axially symmetric field, where the magnetic field lines converge slowly in the z-direction. This type of field is illustrated in Fig. 1.14.

Using $\nabla \cdot \mathbf{B} = 0$ in cylindrical coordinates,

$$\frac{1}{r}\frac{\partial}{\partial r}(rB_r) + \frac{1}{r}\frac{\partial B_\theta}{\partial \theta} + \frac{\partial B_z}{\partial z} = 0 \tag{1.88}$$

because $B = B(r, z)$ and $B_\theta = 0$ this can be rearranged to

$$\frac{\partial}{\partial r}(rB_r) = -r\frac{\partial B_z}{\partial z} \tag{1.89}$$

$$rB_r = -\int r\frac{\partial B_z}{\partial z}\mathrm{d}r \tag{1.90}$$

The field converges over a long distance, hence in a single gyration, the field will not change much so $\frac{\partial B_z}{\partial z} = \frac{\partial B}{\partial z}$. As a partial derivative, $\frac{\partial B}{\partial z}$ does not depend on r, so can be taken outside the integral. Integrating over a gyroorbit gives

$$B_r \approx -\frac{r_L}{2}\frac{\partial B}{\partial z} \tag{1.91}$$

where $r_L = \frac{mv_\perp}{qB}$ is the gyroradius.

Taking the z component of the equation of motion gives

$$m\frac{\mathrm{d}v_\parallel}{\mathrm{d}t} = qv_\perp B_r = -\frac{1}{2}qr_L v_\perp \frac{\partial B}{\partial z} = -\frac{qmv_\perp^2}{2Bq}\frac{\partial B}{\partial z} = -\mu\frac{\partial B}{\partial z}. \tag{1.92}$$

This can be used to find

$$\frac{\mathrm{d}}{\mathrm{d}t}\left(\frac{mv_\parallel^2}{2}\right) = \frac{m}{2}\left(2v_\parallel\frac{\mathrm{d}v_\parallel}{\mathrm{d}t}\right) = -\mu v_\parallel\frac{\partial B}{\partial z} = -\mu\frac{\mathrm{d}B}{\mathrm{d}t} \tag{1.93}$$

because $v_\parallel = \frac{\mathrm{d}z}{\mathrm{d}t}$. The other part of the energy equation is

$$\frac{\mathrm{d}}{\mathrm{d}t}\left(\frac{1}{2}mv_\perp^2\right) = \frac{\mathrm{d}}{\mathrm{d}t}(\mu B). \tag{1.94}$$

So by conservation of energy,

$$\frac{\mathrm{d}}{\mathrm{d}t}\left(\frac{1}{2}mv_\perp^2 + \frac{1}{2}mv_\parallel^2\right) = \frac{\mathrm{d}}{\mathrm{d}t}(\mu B) - \mu\frac{\mathrm{d}B}{\mathrm{d}t} = \frac{\mathrm{d}\mu}{\mathrm{d}t}B = 0 \tag{1.95}$$

but $\frac{\mathrm{d}}{\mathrm{d}t}(\mu B) = \frac{\mathrm{d}\mu}{\mathrm{d}t}B + \mu\frac{\mathrm{d}B}{\mathrm{d}t}$, so

$$\frac{\mathrm{d}\mu}{\mathrm{d}t} = 0 \tag{1.96}$$

Chamberlain (1964) adds uniform electric field in the z direction. This can be included without

much change to the above, as the effect is cancelled out with the rest of the $\frac{\mathrm{d}}{\mathrm{d}t}v_{\parallel}$ terms.

Invariance of the magnetic moment holds even if the particle energy is not conserved, as in the cases explored in this thesis. In the computer code used to calculate the particle trajectories, the particle magnetic moment is prescribed or calculated initially, then kept as a constant and used to calculate other quantities throughout.

This invariant means that if a particle moves to a region of stronger magnetic field, the particle $v_{\perp}$ is increased proportionally.

Longitudinal invariant

In the last section I dealt with an invariant that came from the periodic motion of the particle around the guiding centre point. In magnetic bottles there is also another periodic motion, the side to side motion between the mirror points. As the particle passes through stronger magnetic fields, $v_{\parallel}$ is reduced then changes sign. The kinetic energy of the particle can be maintained by increasing $v_{\perp}$ when $v_{\parallel}$ reduces and vice-versa. This periodic motion gives rise to the second adiabatic invariant, sometimes called the longitudinal invariant. This is usually denoted as

$$J = \oint m v_{\parallel} \mathrm{ds} \tag{1.97}$$

where s is distance along the field line and the closed integral is taken over a complete orbit back to the same point. Although in the cases considered in this thesis the particle never comes back to exactly the same point, it is very close because of the difference in scale between particle $v_{\parallel}$ and the background velocity.

A proof of this invariant is given in Boyd and Sanderson (1969) and repeated here for completeness: The particle energy is given by $E(t) = \frac{1}{2}mv_{\parallel}^2(t) + \mu B(t, s(t))$, so $v_{\parallel}$ can be substituted out of J:

$$J = \int_{s_1}^{s} \left[\frac{2}{m}\left(E - \mu B\right)\right]^{\frac{1}{2}} \mathrm{ds} \tag{1.98}$$

where the start and end points are now specified as a turning point s_1 and the variable s respectively. The chain rule is used to get the time derivative of J,

$$\frac{\mathrm{d}J}{\mathrm{d}t} = \frac{\partial J}{\partial B}\left(\frac{\partial B}{\partial t} + \frac{\partial B}{\partial s}\frac{\mathrm{d}s}{\mathrm{d}t}\right) + \frac{\partial J}{\partial W}\frac{\mathrm{d}W}{\mathrm{d}t} + \frac{\partial J}{\partial s}\frac{\mathrm{d}s}{\mathrm{d}t} \tag{1.99}$$

where $\frac{\mathrm{d}s}{\mathrm{d}t} = v_\parallel$ and the other quantities are calculated from differentiating (1.98).

$$\begin{aligned}
\frac{\partial J}{\partial B} &= \frac{1}{2}\int_{s1}^{s}\left[\frac{2}{m}\left(E_k-\mu B\right)\right]^{-\frac{1}{2}}\left(\frac{-2}{m}\right)\mu \mathrm{d}s \\
&= -\int_{s1}^{s}\left[\frac{1}{2}\left(E_k-\mu B\right)\right]^{-\frac{1}{2}}\frac{\mu}{m}\mathrm{d}s \qquad (1.100)\\
\frac{\partial J}{\partial E_k} &= \frac{1}{2}\int_{s1}^{s}\left[\frac{2}{m}\left(E_k-\mu B\right)\right]^{-\frac{1}{2}}\frac{2}{m}\mathrm{d}s \\
&= \frac{1}{m}\int_{s1}^{s}\left[\frac{2}{m}\left(E_k-\mu B\right)\right]^{-\frac{1}{2}}\mathrm{d}s \qquad (1.101)\\
\frac{\partial E_k}{\partial t} &= \frac{1}{2}m2v_\parallel\frac{\mathrm{d}v_\parallel}{\mathrm{d}t}+\mu\frac{\partial B}{\partial t}+\mu\frac{\partial B}{\partial t}\frac{\mathrm{d}s}{\mathrm{d}t} \\
&= mv_\parallel\frac{\mathrm{d}v_\parallel}{\mathrm{d}t}+\mu\frac{\partial B}{\partial t}+\mu v_\parallel\frac{\partial B}{\partial s} \qquad (1.102)\\
\frac{\partial J}{\partial s} &= \left[\frac{2}{m}\left(E_k-\mu B\right)\right]^{\frac{1}{2}}. \qquad (1.103)
\end{aligned}$$

At the second turning point, $s = s_2$, $v_\parallel = 0$. Substituting these in to the above gives

$$\begin{aligned}
\frac{\mathrm{d}J(E_k,s_2,t)}{\mathrm{d}t} &= -\int_{s_1}^{s_2}\left[\frac{2}{m}\left(E_k-\mu B\right)\right]^{-\frac{1}{2}}\left(\frac{\mu}{m}\frac{\partial B}{\partial t}\right)\mathrm{d}s \\
&+ \left(\frac{\mu}{m}\frac{\partial B}{\partial t}\right)\int_{s_1}^{s_2}\left[\frac{2}{m}\left(E_k-\mu B\right)\right]^{-\frac{1}{2}}\mathrm{d}s. \qquad (1.104)
\end{aligned}$$

As the magnetic field changes slowly, $\frac{\partial B}{\partial t}$ can be taken outside the integral, so these two terms are opposite and equal so cancel to give

$$\frac{\mathrm{d}J}{\mathrm{d}t} = 0 \qquad (1.105)$$

over the trip from s_1 to s_2.

I calculated how good an invariant this was for some of the particles considered in this thesis. For the particle examined by Giuliani et al. (2005) I calculated J for each of the round trips (e.g. from right mirror point, through left mirror and back to right). For ease in the computer code, I take advantage of the parallel velocity, $v_\parallel = \frac{\mathrm{d}s}{\mathrm{d}t}$; changing the relation to

$$J = m\int_{t_n}^{t_{n+1}} v_\parallel^2 \mathrm{d}t \qquad (1.106)$$

where the integral is over the same closed path in phase space as before, i.e. between the nth and (n+1)th bounce points on the same side.

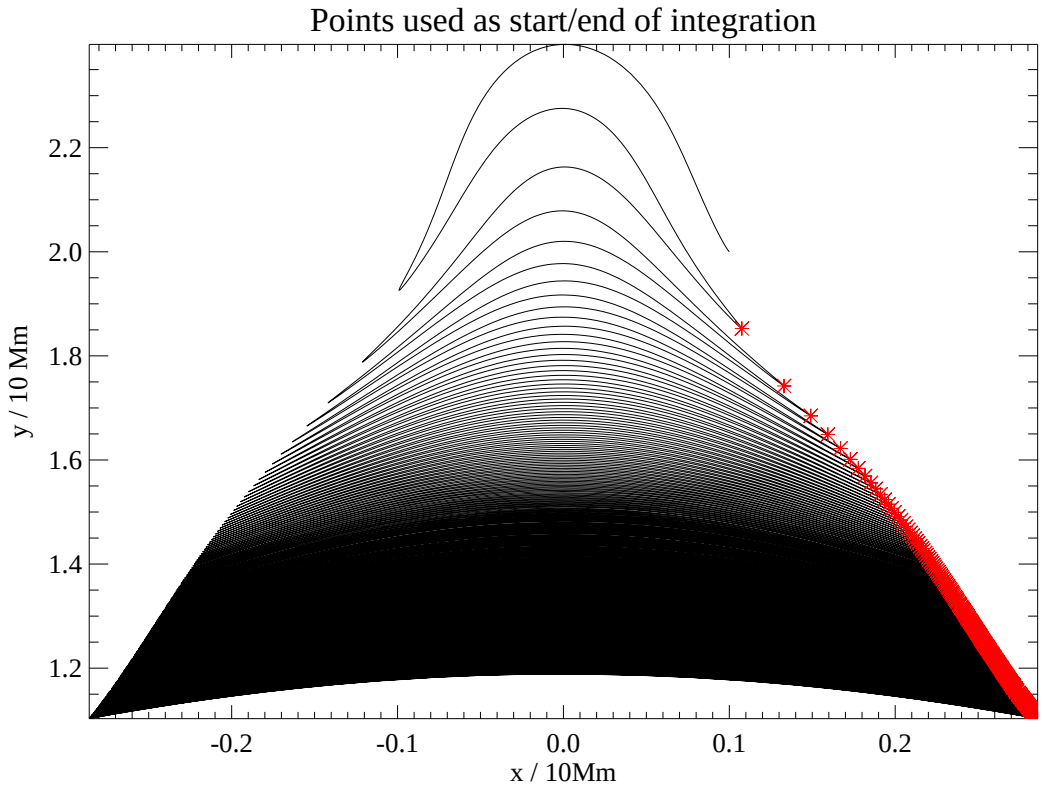

Figure 1.15: Bounce points of the particle orbit, used as the start and end of 'round trips'.

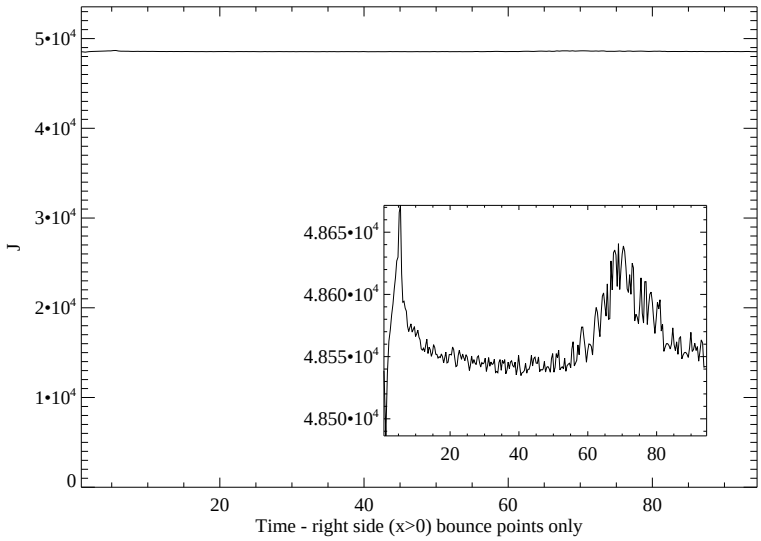

Figure 1.16: Time variation of the longitudinal invariant J for the electron orbit in Giuliani et al. (2005). Inset shows a zoom on the y direction. Maximum deviation is $< 0.4\%$ of the average.

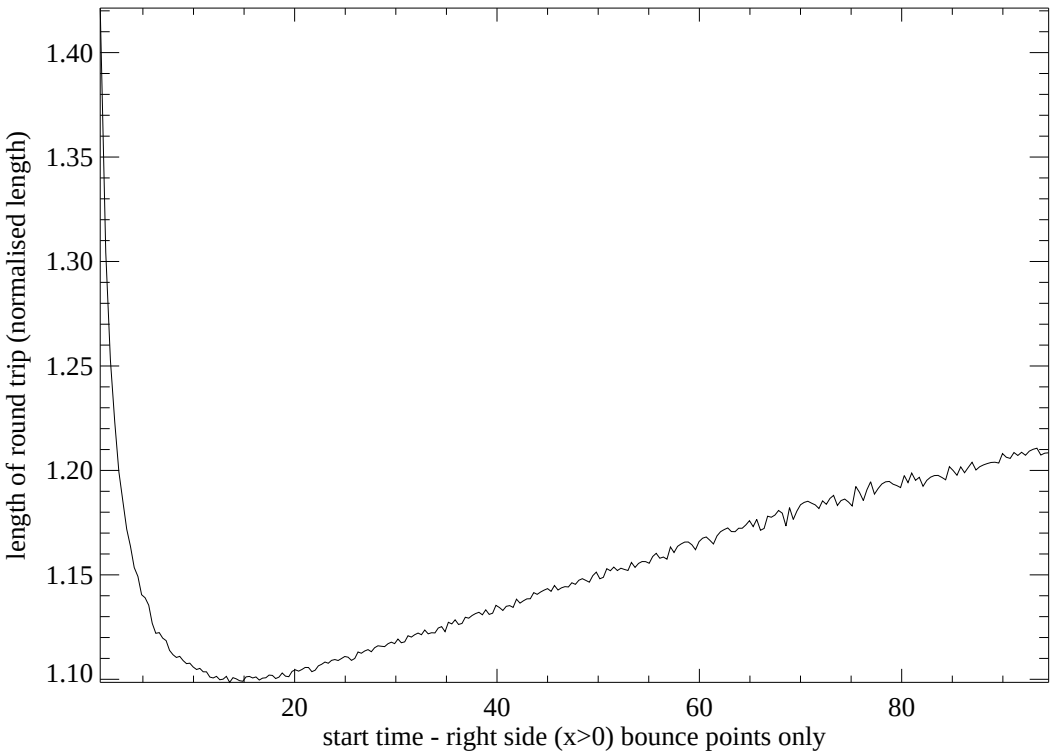

Figure 1.17: Distance particle travels between right side bounce points, equivalent to width of the magnetic bottle.

The code to do this adds up the contribution from each step between the bounce points (bounce points shown in Fig. 1.15). The bounce points are taken as start and end points as the adaptive step size code takes smallest steps here (so $\mathrm{d}t$ and $\mathrm{d}s$ are small) and $v_{\|}$ has its smallest value here, so minimising errors of which of the trips the endpoint should be counted with. The invariant J is more general and any point could be chosen in theory. For the test particles studied by Giuliani et al. (2005), the result can be seen in fig 1.16. There is very little change in the calculated value of J for the trips between the bounce points (less than 0.5%).

Figure 1.17 shows that although J remains constant, the distance between bounce points gets shorter at first. This is not obvious from looking at the particle orbit as the curvature of the field line has to be taken into account. Because of the longitudinal invariant, the particle $v_{\|}$ increases. This is known as Fermi type A acceleration after Fermi (1949) discussed how it might accelerate cosmic-ray particles. This is related to the Fermi acceleration mentioned earlier.

1.6 Computation of test particle orbits

A computer code in Fortran, originally written by Paolo Giuliani and Paul Wood, was used to compute the particle orbits for given fields. This uses an adaptive step size Runge-Kutta method, with a limit on the smallest step size permitted (based on code from Press et al. 1986), to calculate the particle trajectory along the guiding centre using the $\frac{\mathrm{d}\mathbf{R}}{\mathrm{d}t}$ equation earlier in this chapter. The fifth and fourth order Runge-Kutta solutions are calculated and the difference taken as the error. This gives a reasonable trade off between accuracy and computational time. The maximum error can be specified, in all the cases discussed in this thesis the maximum error per step is set to 10^{-15} of the stepsize. Because the maximum number of steps is also limited in the code (an error is produced and the code stops), the maximum total error is kept below 0.001%. The magnetic and velocity fields must be given to the code in nondimensional form. This code was changed by:

- using different magnetic and velocity fields,
- changing which input parameters are specified for test particles (i.e. pitch angle and energy rather than magnetic moment and parallel velocity),
- changing the output from the program to work for many particles rather than being run individually for each particle,
- using a 'minimal' equation of motion to see if the higher order terms are important for particle acceleration.

These were put in place at different points throughout the work as required. Some example code is shown in appendix B.

Most of the data was plotted using IDL, so several file input and plotting codes were also written for this. Some of the plotting and analysis routines are included in Appendix C.

1.7 Outline of thesis

In the rest of this thesis, I investigate how collapsing magnetic traps can cause particle acceleration, mainly based on the theoretical framework by Giuliani et al. (2005). Chapter 2 contains a systematic look at many initial conditions on the particles in the trap model to find out how the initial conditions have an effect on the particles energy gain, trapping time and where particles are trapped.

In chapter 3 a guide field is added to the trap to see the effects of this on the trapped particles. This is looked at by comparing the effects of different guide fields on a single particle in the different

fields. The effects of the guide field on particles with different initial conditions is also briefly discussed.

It is highly unlikely that a solar flare would develop in perfect symmetry, so in chapter 4 a trap that has an asymmetric magnetic field is considered. This is achieved within the general model by simply lowering one of the magnetic charges and adjusting the magnetic field accordingly.

To compare this work with other trap models, in chapter 5 I look at the trap used by Minoshima et al. (2010). This has a different way of defining the magnetic field, but many of the same effects are still present in this trap.

In chapter 6 I extend the theoretical framework of Giuliani et al. (2005), firstly by adding a shearing flow, and secondly making it fully 3D. Examples of both of these types of traps are also shown.

The main body of this thesis is concluded and ideas for future work are presented in chapter 7.

The first appendix shows a different way to a result of chapter 6, namely how to use Euler Potentials to model a 3D magnetic field. Appendix B and C show some of the computer code used for modelling particle orbits.

Chapter 2

Systematic Examination of Particle Motion in the Giuliani et al. Trap Model

2.1 Introduction

In this chapter a systematic investigation of test particle orbits for different initial conditions using the same CMT model as in Giuliani et al. (2005) is presented. As in Giuliani et al. (2005), I will use the first order guiding centre theory (e.g. Northrop 1963). Of particular interest is the dependence of particle energy gain on initial position in the trap, initial energy and initial pitch angle. Another interesting question is whether the energy gain mechanisms predicted using adiabatic invariants can indeed be identified using the full particle orbits. To investigate this question I also consider test particle orbits calculated using guiding centre equations of motion which include terms of different order. Results of using only the lowest order guiding centre equations are compared with the orbits starting with the same initial conditions, but including higher order terms in the equation of motion.

The chapter is structured in the following way. In section 2.2 I summarise the basic theory and the models presented in Giuliani et al. (2005). An overview of the dependence of particle orbits and energy on initial conditions is given in section 2.3. A more detailed look at two particular particle orbits and energy gain mechanisms is given in section 2.4. In the same section I also present calculations for the same sets of initial conditions, but using only lowest order guiding centre theory for comparison. Other aspects of the trap are investigated in the following chapters.

2.2 Basic equations and CMT model

In section 1.2 I discussed the kinematic MHD equations and that they can be used for all the collapsing magnetic trap models considered in this thesis. For ease of reference, the equations are

$$\mathbf{E} + \mathbf{v} \times \mathbf{B} = \mathbf{0}, \tag{2.1}$$

$$\frac{\partial \mathbf{B}}{\partial t} = -\nabla \times \mathbf{E}, \tag{2.2}$$

$$\nabla \cdot \mathbf{B} = 0, \tag{2.3}$$

$$\frac{\partial \mathbf{B}}{\partial t} = \nabla \times (\mathbf{v} \times \mathbf{B}). \tag{2.4}$$

In this chapter I shall take advantage of the translationally invariant 2.5D kinematic MHD theory of CMTs developed by Giuliani et al. (2005). This does not include a velocity component in the invariant direction. I will use the same coordinate system as used by Giuliani et al. (2005), i.e. all physical quantities depend only upon x and y, with x being the coordinate parallel to the solar surface (photosphere) and y being the height above the solar surface. The invariant direction is the z-direction, also along the photosphere.

Under the assumption that all z-derivatives vanish, one can write the magnetic field in the form

$$\mathbf{B}(x, y, t) = \mathbf{B}_p + B_z \mathbf{e}_z = \nabla A(x, y, t) \times \mathbf{e}_z + B_z(x, y, t)\mathbf{e}_z, \tag{2.5}$$

where $\mathbf{B}_p = (B_x(x, y, t), B_y(x, y, t), 0)$, $B_z(x, y, t)$ is the z-component of the magnetic field and $A(x, y, t)$ is the magnetic flux function. This form of the magnetic field automatically satisfies the solenoidal condition, Eq. (2.3).

Following Giuliani et al. (2005), in this chapter no flow will be assumed in the invariant direction, i.e.

$$\mathbf{v}(x, y, t) = (v_x(x, y, t), v_y(x, y, t), 0). \tag{2.6}$$

This restriction is removed with an extension of the theory to 3D, given in Sect. 6.2.3.

Using the above, and that $E_z = -\frac{\partial A}{\partial t}$, as discussed in Giuliani et al. (2005), the z component of the ideal Ohm's law (2.1) then takes the form

$$\frac{\partial A}{\partial t} + \mathbf{v} \cdot \nabla A = \frac{\mathrm{d}A}{\mathrm{d}t} = 0, \tag{2.7}$$

the time evolution of the flux function A. For the time evolution of B_z it is better to use the

z-component of the induction equation (2.4),

$$\frac{\partial B_z}{\partial t} + \nabla \cdot (\mathbf{v}_2 B_z) = 0. \tag{2.8}$$

Equations (2.7) and (2.8) simply express the conservation of magnetic flux. In the case with vanishing shear velocity ($v_z = 0$) the magnetic flux $\int B_z \mathrm{d}x\mathrm{d}y$ over arbitrary areas is conserved independently.

A CMT model is then defined by specifying the flux function A at a specific time and a velocity field $\mathbf{v}(x, y, t)$. In Giuliani et al. (2005) the flux function defines the magnetic field as $t \to \infty$, i.e. the field that the trap will relax into.

To solve Eqs. (2.7) and (2.8) for $A(x, y, t)$ and $B_z(x, y, t)$, Giuliani et al. (2005) prescribe a time-dependent transformation between Lagrangian coordinates X, Y and Eulerian coordinates x, y:

$$X = X(x, y, t), \qquad Y = Y(x, y, t), \tag{2.9}$$

instead of a time-dependent velocity field $v_x(x, y, t)$, $v_y(x, y, t)$.

Giuliani et al. (2005) show that the transformation equations can be found by setting the total time derivative of (2.9) to zero:

$$\frac{\mathrm{d}X}{\mathrm{d}t} = \frac{\partial X}{\partial x}\frac{\mathrm{d}x}{\mathrm{d}t} + \frac{\partial X}{\partial y}\frac{\mathrm{d}y}{\mathrm{d}t} + \frac{\partial X}{\partial t} = 0 \tag{2.10}$$

$$\frac{\mathrm{d}Y}{\mathrm{d}t} = \frac{\partial Y}{\partial x}\frac{\mathrm{d}x}{\mathrm{d}t} + \frac{\partial Y}{\partial y}\frac{\mathrm{d}y}{\mathrm{d}t} + \frac{\partial Y}{\partial t} = 0 \tag{2.11}$$

and these can be solved to give the plasma velocity field:

$$v_x = \frac{\mathrm{d}x}{\mathrm{d}t} = \left(-\frac{\partial X}{\partial t}\frac{\partial Y}{\partial y} + \frac{\partial X}{\partial y}\frac{\partial Y}{\partial t}\right)\left(\frac{\partial X}{\partial x}\frac{\partial Y}{\partial y} - \frac{\partial X}{\partial y}\frac{\partial Y}{\partial x}\right)^{-1} \tag{2.12}$$

$$v_y = \frac{\mathrm{d}y}{\mathrm{d}t} = \left(-\frac{\partial Y}{\partial t}\frac{\partial X}{\partial x} + \frac{\partial Y}{\partial x}\frac{\partial X}{\partial t}\right)\left(\frac{\partial X}{\partial x}\frac{\partial Y}{\partial y} - \frac{\partial X}{\partial y}\frac{\partial Y}{\partial x}\right)^{-1}. \tag{2.13}$$

The solution for the magnetic flux function $A(x, y, t)$ is then trivially given by

$$A(x, y, t) = A_0(X(x, y, t), Y(x, y, t)), \tag{2.14}$$

where $A_0(X, Y)$ is the flux function at some reference time $t = t_0$. The B_x- and B_y-components of the magnetic field can be calculated from Eq. (2.5) by differentiation.

Equation (2.8) has the form of a continuity equation for B_z with the solution

$$B_z(x, y, t) = JB_{0z}(X(x, y, t), Y(x, y, t)), \tag{2.15}$$

where $B_{0z}(X, Y)$ is again the B_z at a reference time $t = t_0$ and J is the Jacobian determinant of the transformation between the Lagrangian and Eulerian coordinates, here written as

$$J = \frac{\partial X}{\partial x}\frac{\partial Y}{\partial y} - \frac{\partial Y}{\partial x}\frac{\partial X}{\partial y}. \tag{2.16}$$

The Jacobian determinant basically expresses the deformation of infinitesimal area elements, i.e. a change of cross section, in the x-y-plane during the time evolution of the system. Because the magnetic flux associated with B_z is conserved independently in the case discussed in this section, any decrease in area must be compensated by a matching increase in B_z and vice versa.

Finally, the electric field can be determined from Ohm's law (2.1) once the velocity field $\mathbf{v}$ and the magnetic field $\mathbf{B}$ are known.

Until this point the theory is quite general, but to continue, a specific flux function and a coordinate transformation must be chosen. I use the same CMT model as used by Giuliani et al. (2005). The final magnetic field is determined by the flux function

$$A_0 = c_1 \arctan\left(\frac{y_0 + d/L}{x_0 + 1/2}\right) - c_1 \arctan\left(\frac{y_0 + d/L}{x_0 - 1/2}\right), \tag{2.17}$$

where c_1 is used to control the strength of the magnetic field.

The corresponding magnetic field is a loop between two 2D magnetic sources (line currents) separated by a distance L and placed at a distance $y_0 = -d$ below the photosphere at $x_0 = \pm L/2$. The magnetic field generated by the flux function (2.17) is potential if regarded as a function of x_0 and y_0. This potential field is the final field to which the CMT relaxes as $t \to \infty$.

The coordinate transformation used by Giuliani et al. (2005) is given by

$$x_0 = x, \tag{2.18}$$

$$y_0 = (at)^b \ln\left[1 + \frac{y}{(at)^b}\right]\left\{\frac{1 + \tanh[(y - L_v/L)a_1]}{2}\right\} + \left\{\frac{1 + \tanh[(y - L_v/L)a_1]}{2}\right\} y. \tag{2.19}$$

This transformation stretches the magnetic field in the y-direction above a height given by L_v/L, where the transition between unstretched and stretched field is controlled by the parameter a_1. In this chapter I will use the same parameter values as Giuliani et al. (2005), namely $a = 0.4$, $b = 1.0$, $L_v/L = 1$ and $a_1 = 0.9$. For simplicity, the transformation depends on time only through the

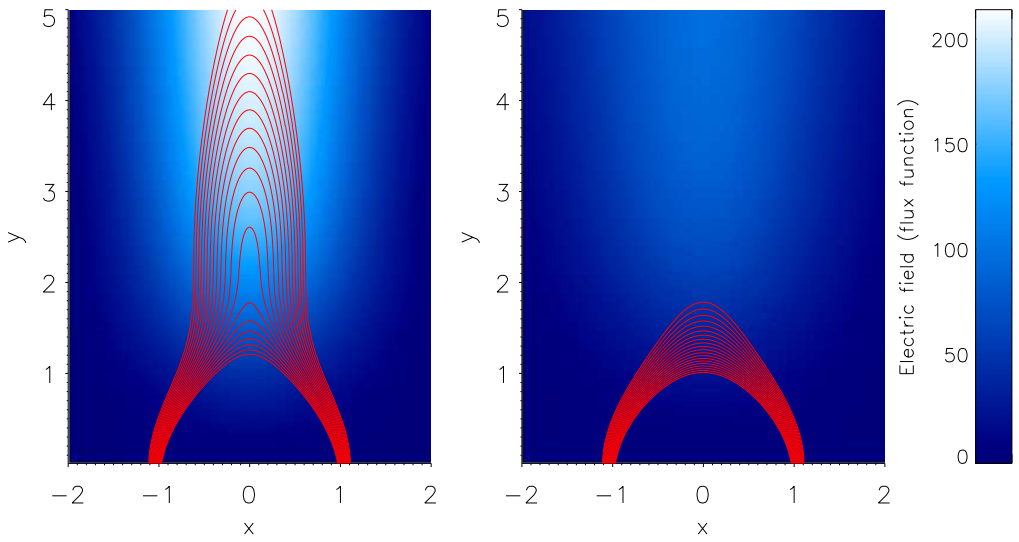

Figure 2.1: The magnetic field lines (red) and the electric field (blue colour scale) of the CMT model by Giuliani et al. (2005) at the beginning (left panel) and at the end (right panel) of the collapse, corresponding to 95 *s in the simulation.*

function $y_0(y,t)$. This time-dependence lets the field collapse to the final field described above as for $t \to \infty$, y_0 tends to y. An important feature of the transformation is that the foot points of magnetic field lines do not move during the collapse as for $y = 0$, $y_0 = 0$ for all t. Figure 2.1 shows a plot of the magnetic field lines, and the electric field, at the start and at the end of the collapse.

For reasons of comparability, I also use the same normalisation as used by Giuliani et al. (2005), i.e. the typical length scale of the trap is $L = 10^7$ m, the magnetic field is normalised by 0.01 T (100 G) and the time scale for the collapse of the trap is 100 s. These are rather conservative values, giving, for example, a typical field strength of $2 \cdot 10^{-3}$ T (20 G) and below at the initial positions of the particles. Stronger magnetic fields and smaller time-scales of CMT collapse are possible for solar flares and the consequences of varying the CMT parameters, and also the CMT model itself should be investigated in more detail in the future.

The particle orbits are calculated using first order non-relativistic guiding centre theory as discussed in Sect. 1.5.

$$\left(\frac{m}{q}\right)\frac{dv_\parallel}{dt} = E_\parallel - \frac{\mu}{q}\frac{\partial B}{\partial s} + \left(\frac{m}{q}\right)\mathbf{u}_E \cdot \left(\frac{\partial \mathbf{b}}{\partial t} + v_\parallel \frac{\partial \mathbf{b}}{\partial s} + \mathbf{u}_E \cdot \nabla \mathbf{b}\right)$$

$$\dot{\mathbf{R}}_\perp = \frac{\mathbf{b}}{B} \times \left\{-\mathbf{E} + \frac{\mu}{q}\nabla B + \frac{m}{q}\left[\right.\right.$$

$$v_{\|}\frac{\partial \mathbf{b}}{\partial t} + v_{\|}^2\frac{\partial \mathbf{b}}{\partial s} + v_{\|}\mathbf{u}_E\cdot\nabla\mathbf{b} + \frac{\partial \mathbf{u}_E}{\partial t} + v_{\|}\frac{\partial \mathbf{u}_E}{\partial s} + \mathbf{u}_E\cdot\nabla\mathbf{u}_E\Bigg]\Bigg\}$$

where $\mu = (1/2)mv_g^2/B$, is the magnetic moment, v_g is the gyro-velocity, $\mathbf{u}_E = (\mathbf{E}\times\mathbf{b})/B$, $\mathbf{b} = \mathbf{B}/B$, $\mathbf{R}$ is the vector location of the guiding centre, $v_{\|} = \mathbf{b}\cdot\dot{\mathbf{R}}$ and $\dot{\mathbf{R}}_{\perp} = \dot{\mathbf{R}} - v_{\|}\mathbf{b}$.

Throughout this thesis, I deal with the orbits of electrons only. For all electron orbits presented in this chapter the use of the guiding centre approximation is well justified, as, for example, the typical ratio between the gyration timescale for electrons and the time-scale for the variation of the magnetic field of the CMT is of the order 10^{-3} – 10^{-4}, and the differences between typical gyroradii and the MHD lengths scale of the CMT are also of this order.

2.3 Electron energy gains for varying initial conditions

2.3.1 Discussion of initial conditions

In this section I investigate the influence of initial conditions on the energy gain of electrons in the CMT model of Giuliani et al. (2005). Generally, the initial position and initial velocity are varied. Regarding the initial position, only the initial x and y-values need be varied, because the CMT model is invariant in the z-direction. Due to the use of guiding centre theory, the complete initial velocity vector does not need to be specified. In the present chapter, I choose to specify the total initial kinetic energy and the initial pitch angle (α) of the particles. Together with the initial position, this fixes the magnetic moment (μ) of the particles. It also implicitly fixes the initial parallel and perpendicular energies of the particle.

In the following I distinguish between particle orbits that have $y > 0$ for all times (trapped particles) and particle orbits that eventually cross the lower boundary ($y = 0$; escaping particles). For escaping particles, the final energy and other quantities are recorded at the time of escape, i.e. when their orbit first reaches a value $y < 0$, whereas for particles which remain trapped the corresponding values are recorded at the final time of the calculation, i.e. when the trap is sufficiently relaxed.

To study the effects of varying the initial conditions, I use a grid of 11 by 11 equidistantly spaced initial positions for $-0.5L \leq x \leq 0.5L$ and $1L \leq y \leq 5L$ (see diamond shaped symbols in Fig. 2.2). For each initial position I calculate particle orbits for 11 equally spaced values between 5 keV and 6 keV for the initial energy and 10 values for the initial pitch angle between 13° and 163°. In Fig. 2.2 the final positions of the particles remaining in the trap as dots are also shown. Particles which start at positions further away from the centre of the trap ($x = 0$) are more likely to escape quickly even for initial pitch angles relatively close to 90°, often without mirroring,

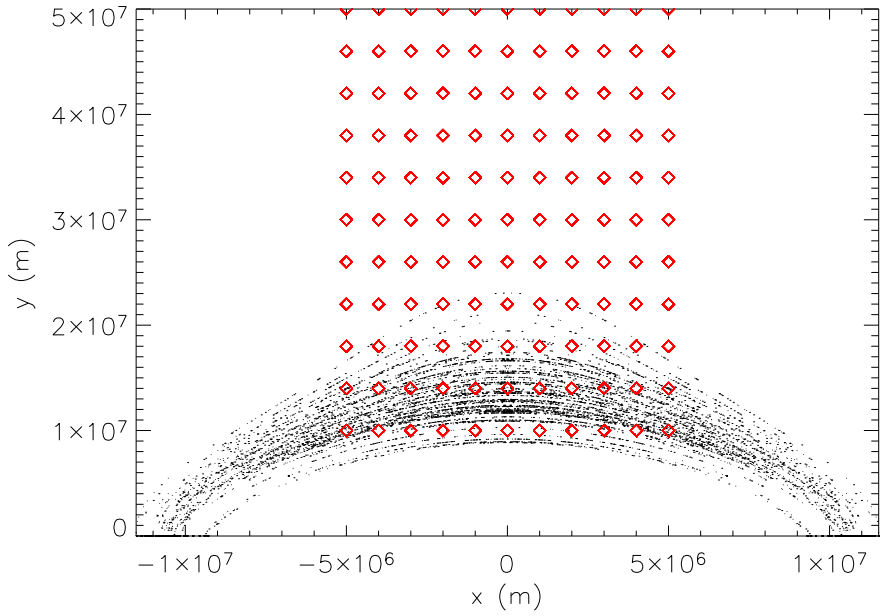

Figure 2.2: Initial (diamond) and final (dot) positions for test particles.

whereas particles starting close to the centre are more likely to remain trapped. The reason is that outside the main region of the CMT the magnetic field strength does not vary as much as inside the CMT and mirroring is less likely to occur. At the final time, once the trap has collapsed, the particle that are still in the trap with the highest energies are trapped in the centre at the top of loops.

2.3.2 Dependence of energy gain on initial position

Figure 2.3 shows the energy gain of particles as the ratio between the final and initial energy. The values of initial energies chosen can be identified as the vertical bands on the graph. For the initial conditions investigated here, the final energy can be up to 53 times the initial energy (top boundary of Fig. 2.3). Most particles (98.5 % of the initial conditions shown) have modest energy gains of up to a factor of 10.

Furthermore, for 2 % of the initial conditions shown, the particles lose energy compared to the initial state, but these are all particles which escape the trap almost immediately (within 1.5 s in the normalisation discussed above). These particles all start outwith the central region of the CMT and usually have parallel velocities which take them directly to the nearest foot point of the field line they start on. Even some of the particles staying longer within the CMT are actually never really trapped, i.e. they do not mirror before crossing the lower boundary ($y = 0$). These

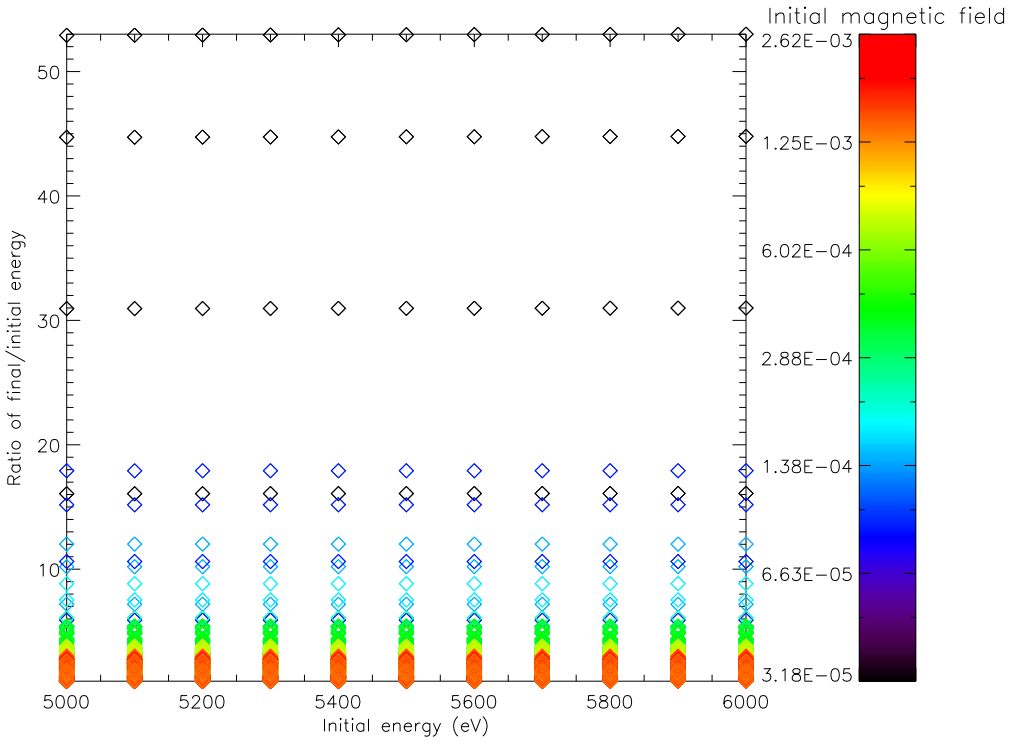

Figure 2.3: Ratio of final to initial energy. Each point indicates a different test particle. Colours show, on logarithmic scale, the magnetic field strength at the initial positions of the orbits. One can see a clear trend that higher energy gains are correlated with initial positions in weak field regions. The energy gain does, however, also depend on the initial pitch angle, with orbits with initial pitch angles close to 90° *gaining more energy, up to 53 times the initial energy.*

particles usually have an initial parallel velocity which takes them in the direction of the foot point further away from their starting position, which means they simply take longer to reach the lower boundary. It is interesting that, despite not being trapped, even some of these particles gain energy because they encounter stronger magnetic field values while travelling to the point where they leave the CMT.

A closer investigation shows that the ratio between final and initial energy is determined very strongly by the initial position and the initial pitch angle, and only to a much lesser extent by the initial energy, at least over the range of initial energies studied in the present chapter. In particular, the initial position determines the initial magnetic field strength that the particle experiences. In Fig. 2.3 the magnetic field strength at the initial position of the particles is indicated by the colour of the symbols, with the values being shown by the colour bar. As a general trend, particles starting in regions of lower magnetic field have the higher energy gains. Although the initial pitch angle is not indicated in Fig. 2.3, it was found that apart from starting in a region with lower magnetic field strength, the orbits with the highest energy gains also have initial pitch angles which are closest to $90°$, i.e. the particles have small initial parallel energies. The nearly horizontal bands seen in Fig. 2.3 are actually made up of particle orbits which start at the same initial position with the same initial pitch angle, but different total initial energies. The particles with the largest energy gain ratio (above 30) start in the centre of the trap (at $x = 0$, $y = 2.2$ L for those plotted here) with a pitch angle close to $90°$. These findings indicate that the betatron effect plays a major role for particles with the highest energy gains.

Particles that end up with the highest energy gain are kept close to the trap centre and are trapped at the top of the magnetic loops. The final positions of particle are shown in Fig. 2.4, where the colour represents the ratio of final to initial particle kinetic energy. The colour bar has a log scale to emphasise the particles with high energy gain.

2.3.3 Estimating the final energy of particles using the equation from Bogachev & Somov (2005)

Bogachev and Somov (2005) suggest that the final energy of an escaping particle can be found by knowing only the initial energy and pitch angle and initial and final magnetic field strengths. The formula for particle energy at the time of escape from a trap:

$$E_{final} = E_{initial} \frac{B_{final}}{B_{initial}} \sin^2 \alpha_0, \tag{2.20}$$

where α_0 is the initial pitch angle. As was mentioned in the previous chapter, this requires knowing the magnetic field strength where the particle escapes. However, it is possible to work backwards once the particle orbits have been calculated and test this formula. The final values are considered

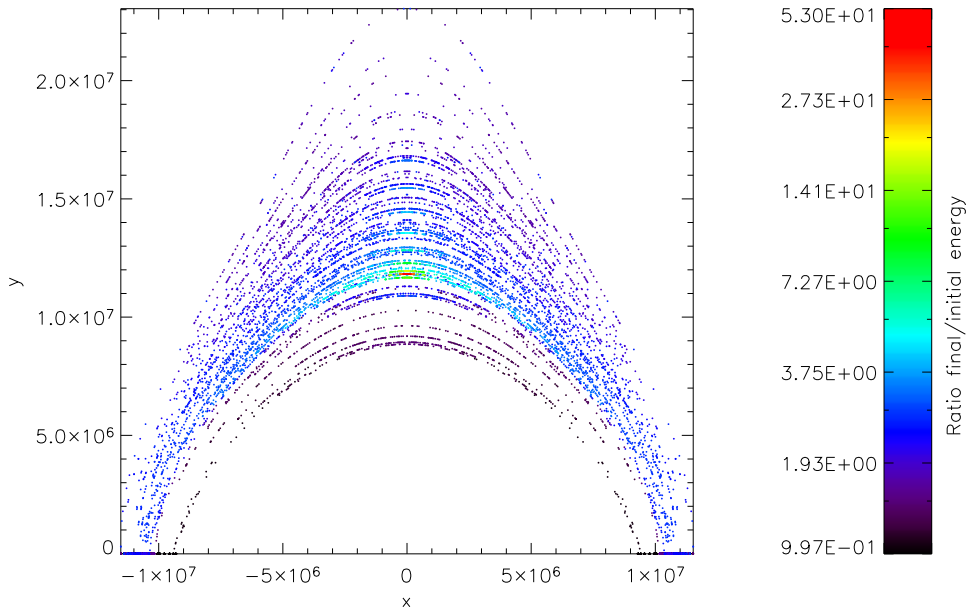

Figure 2.4: Final positions of particles in the trap, with colour indicating the energy gain on a logarithmic scale.

to be at the point of escape, or for those particles that are trapped, the values at the point when the code stops measuring and assume the trap has collapsed.

Figure 2.5 shows the estimated final energy from Eq. 2.20 plotted against the final energy calculated from the particle orbit code. The blue line indicates where these values are equal. Red indicates the particles that have escaped the trap. Almost all of the particles have a higher energy than Eq. 2.20 says they should have.

For the few particles that have a lower final energy than the estimate (274 of 13310), the final energy is within 1.05% of the value estimated by the formula. These have a *final* pitch angle close to 90° (between 84.8° and 95.2°; compared with 15.2° to 164.8° for all particles) but there is no systematic link to the initial conditions. Figure 2.6 shows the initial and some final conditions of the particles examined, with the particles that have final energy less than the estimate shown by red plus symbols. In general, the formula for estimating the final energy seems to give a reasonable lower bound on the final energy of the particles.

2.3.4 The effect of the initial pitch angle

To investigate more closely the effect of the initial pitch angle on the energy gain, Fig. 2.7 shows the final energies (colour contours) for particle orbits starting at the same position ($x = 0.1L, y =$

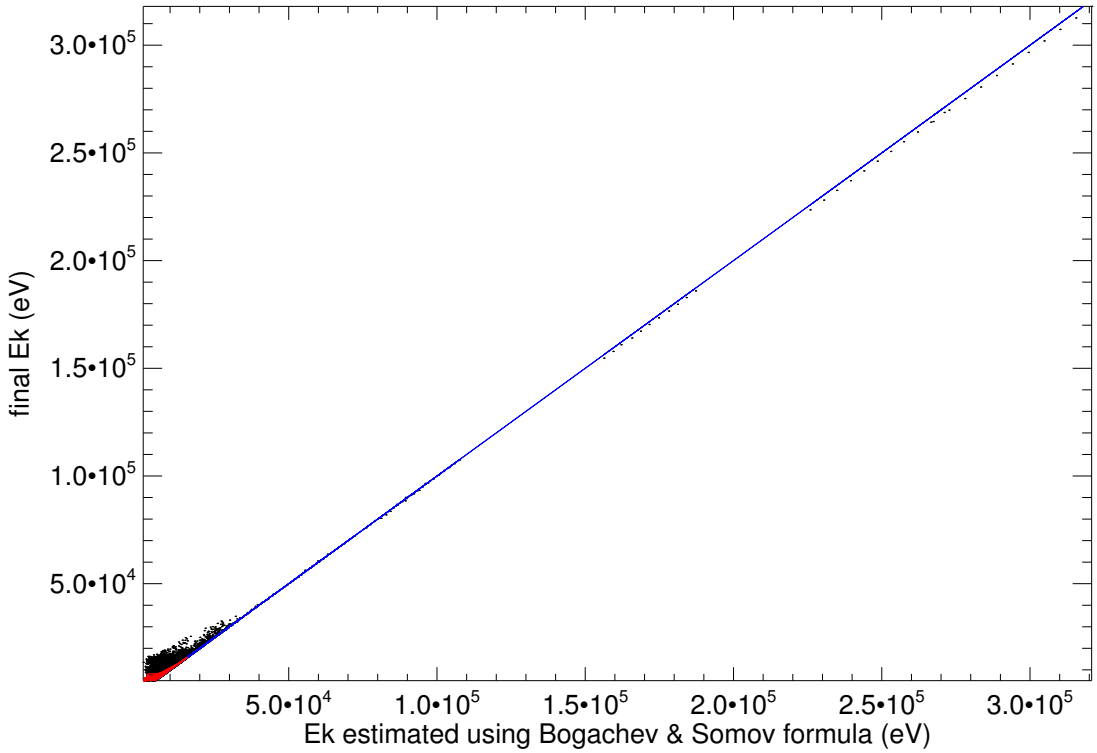

Figure 2.5: Estimate of the final particle energy vs the energy calculated using the particle orbit. Red points indicate particles that escape the trap, so the value at the time of escape is used as the final. The blue line shows where the estimate and final energy are equal.

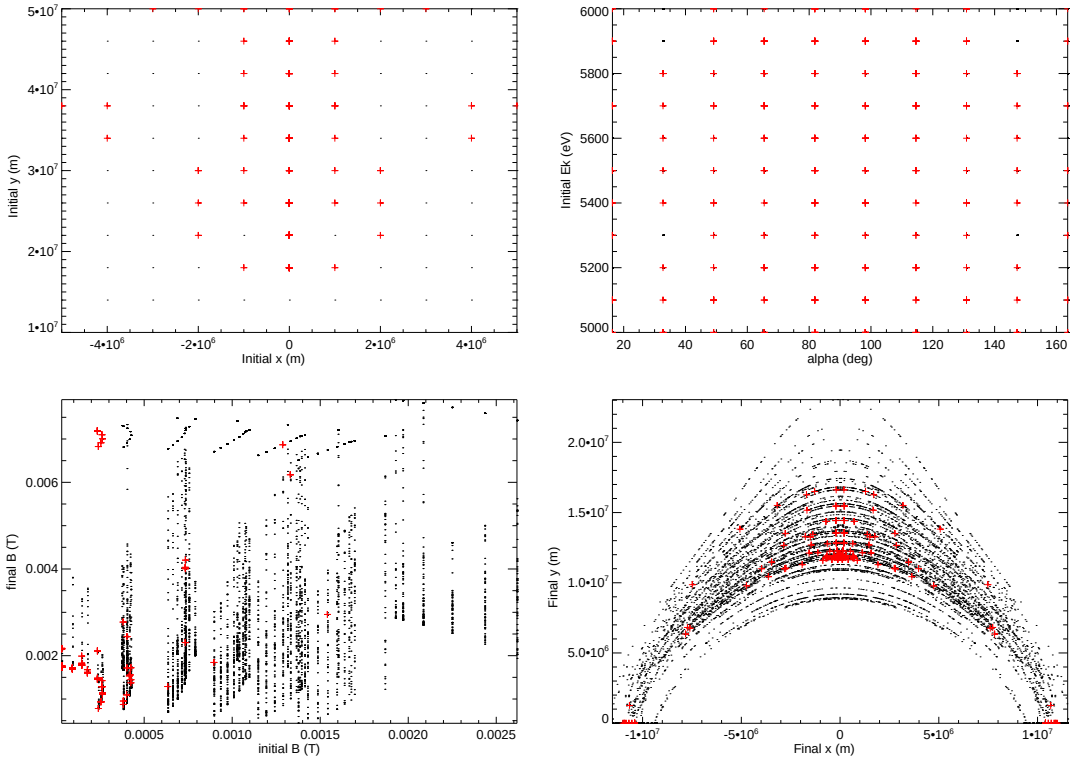

Figure 2.6: Initial and final conditions for the particles discussed in this chapter. Conditions that produce particles with final energy less than the Bogachev and Somov (2005) estimate are shown as red plus symbols. Upper left panel shows initial position; upper right initial pitch angle and energy; lower left magnetic field experienced initially and finally; lower right final positions (note particles that have escaped are shown at $x = 0$).

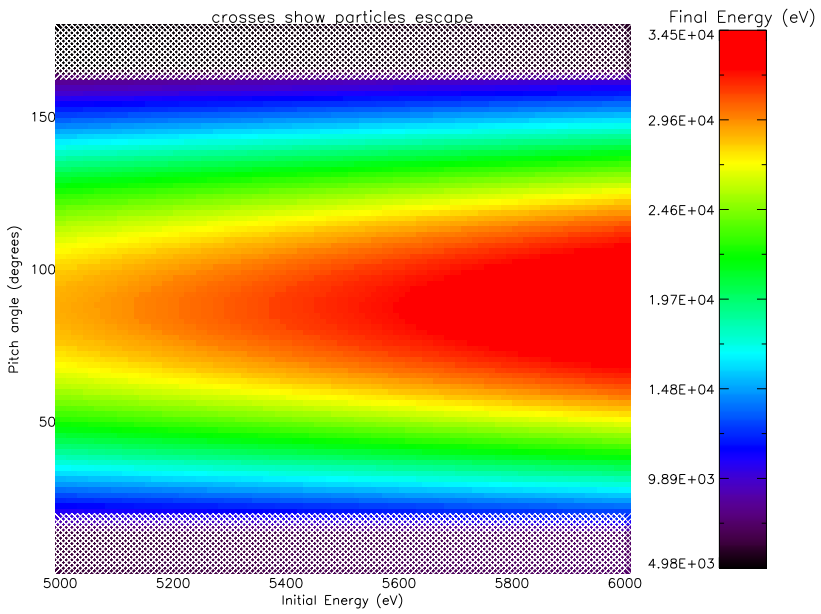

Figure 2.7: Final energy (colour contours) of test particles with the same initial position ($x = 0.1L$, $y = 2.0L$), but different initial energies (y-axis) and pitch angles (x-axis). Crossed squares indicate particles that escape before the trap has collapsed. For this initial position the highest energy particles have pitch angles closest to $90°$.

$2.0L$), but with different initial energy (x-axis) and pitch angle (y-axis). For these orbits the initial pitch angle varies between $1.8°$ and $178.2°$, and energy varies between 5keV and 6keV as shown. Particles that remain in the trap until the final time have initial pitch angles between $19.6°$ and $162.2°$. Particles that escape the trap had pitch angles $\leq 17.8°$ or $\geq 164.0°$. Escaping particles are indicated by crossed squares in Fig. 2.7. The particles ending up with the highest final energy (about 34.5 keV) have pitch angle closest to $90°$ and start with the highest initial energy, consistent with the conclusions of the previous section.

The effect of varying the initial pitch angle at different initial positions, for a fixed initial energy of 5.5 keV, is shown in Fig. 2.8. The plots show final energy distributions versus initial pitch angle for any combination of initial positions out of $x = 0.0L$, $0.12L$, $0.24L$, $0.36L$, $0.48L$ and $0.6L$ with $y = 1.0L$, $1.8L$, $2.6L$, $3.4L$, $4.2L$ and $5.0L$. Basically, every plot shown in Fig. 2.8 can be considered as a vertical cut through a figure similar to Fig. 2.7 at 5.5 keV for each of the initial positions. In Fig. 2.8, black dots indicate particles which remain trapped, whereas red dots indicate escaping particles. It is obvious that particles with pitch angles deviating substantially from $90°$ escape from the trap more easily. It can also be easily seen that for initial positions further away from the centre of the trap in the horizontal direction (x-direction), the range of initial pitch angles leading to escaping particle orbits becomes larger.

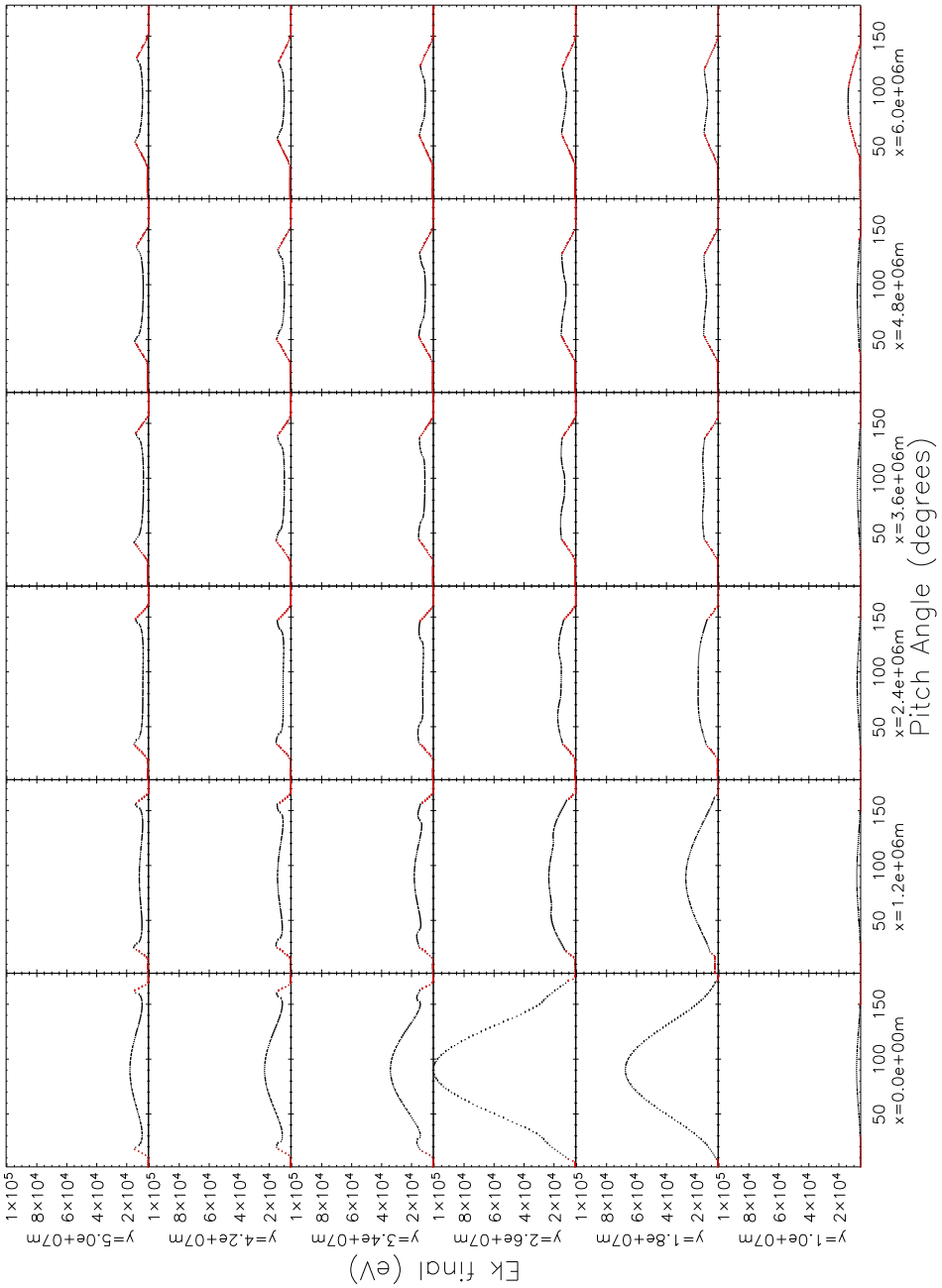

Figure 2.8: Final energy vs. pitch angle for different initial positions. All particles start with the same initial kinetic energy (5.5 keV). Each plot is similar to a vertical cut through Fig. 2.7. Red points indicate which particles escape. Note that the initial pitch angle leading to the maximum energy gain is not always 90°, but depends on initial position.

One can also see again that the particles with the highest final energy start with pitch angles close to 90° in the centre of the CMT ($x = 0.0L$) and within the region of weak magnetic field (see e.g. $y = 2.6L$). While there is still a maximum of the final energy distribution around a pitch angle of 90° in the CMT centre for other values of the initial height y, the value of the maximum energy is reduced compared to $y = 2.6L$. Another feature of the final energy as a function of pitch angle for increasing initial height y is the development of secondary maxima at small and large pitch angles. A first indication is already visible for $y = 2.6L$, but becomes increasingly clearer for larger initial y values. The largest energy values of the secondary maxima occur close to the point of transition from trapped to escaping particle orbits. Similar trends as for the CMT centre at $x = 0L$ are also seen for the other values of x, although the final energies drop strongly in value. The maximum energy around the pitch angle of 90° actually turns into a local minimum, with the secondary maxima for small / large pitch angle becoming the highest energies as one moves away from $x = 0$ at constant initial height y. An explanation for these features is that the largest energy gains at the CMT centre are caused by the betatron effect, because the largest increase in magnetic field with time occurs at the centre of the CMT. Particles starting close to the CMT centre with a pitch angle around 90° stay very close to the CMT centre and thus basically gain all their energy through the betatron effect. Particles with small or large pitch angle have larger oscillation amplitudes inside the trap. While the trap collapses, the particles move on field lines which shorten and the distance between successive bounces becomes shorter. These particles could therefore be mainly accelerated by the first order Fermi effect. This would explain the secondary peaks for smaller and larger pitch angles.

Particles starting away from the centre of the CMT do not experience the same large difference between initial and final magnetic field strength as the particles at the centre of the CMT, and thus the betatron effect becomes less efficient as the initial position moves away from the CMT centre. For small or large pitch angles, however, the Fermi effect could still operate, but only for particles outside the loss cone. This would explain the final energy minimum and the secondary maxima for initial positions outside the centre of the CMT.

2.4 Comparison of two particle orbits with different initial pitch angles

To gain a better understanding of the different acceleration processes described above and how they depend on the initial pitch angle, I investigated in detail two particle orbits with the same initial position ($x = 0L, y = 4.2L$) and energy (5.5 keV), but with different initial pitch angles. Particle orbit 1 has an initial pitch angle of 160.4°, i.e. the particle is moving initially mainly in the direction opposite to the field line. Particle orbit 2 has a pitch angle of 87.3°, so most of its initial energy is associated with the gyrational motion perpendicular rather than parallel to the field line.

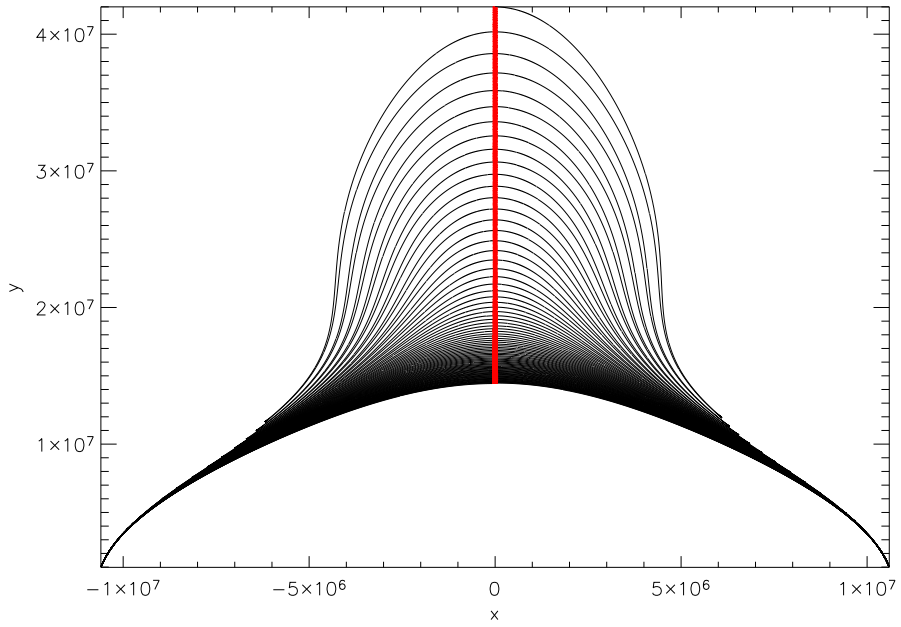

Figure 2.9: The two test particle orbits. Particle orbit 1 with initial pitch angle 160.4° *is shown in black, particle orbit 2 with initial pitch angle close to* 87.3° *is shown in red.*

Both particle orbits are shown in Fig. 2.9. As is to be expected, particle orbit 1 extends far along the field line, well into the legs of the trap, whereas particle orbit 2 remains close to the centre and mirrors more frequently. Particles orbit the same field line and hence in the guiding centre approximation could be described as being on the same field line at all times.

2.4.1 Time evolution of particle energies

The upper left panel of Fig. 2.10 shows the time evolution of the total kinetic energy for orbit 1. The time evolution of the total energy for this orbit shows features which are very similar to the energy evolution of the particle orbit investigated by Giuliani et al. (2005). The energy increases in steps when the guiding centre moves along the top of the field line it is on, and it decreases slightly closer to the mirror points. As shown by Giuliani et al. (2005), the steps are caused by the curvature in the parallel equation of motion and this gives rise to an initial average increase in parallel energy ($mv_{\parallel}^2/2$). This is confirmed for particle orbit 1 by the plot of the parallel energy shown in the upper right panel of Fig. 2.10. A clear increase is visible when looking at the envelope of maxima of the parallel energy. These maxima occur when the particle passes through the centre of the trap ($x = 0$), which is consistent with the findings of Giuliani et al. (2005). Obviously, for every trapped particle the minimum value of the parallel energy is zero (at the mirror points), but on average the parallel energy increases with time.

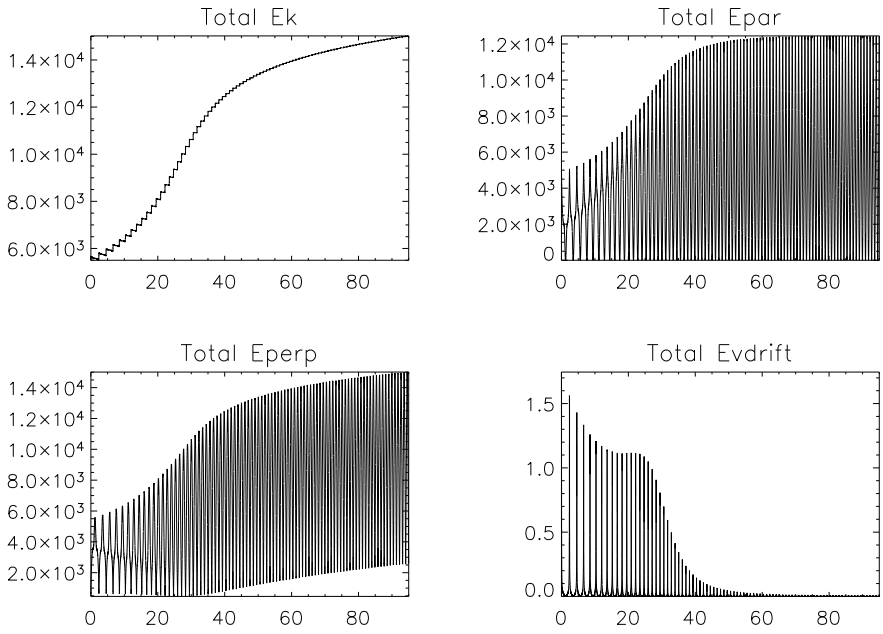

Figure 2.10: Plots of time evolution of energy for particle orbit 1 (initial pitch angle $160.4°$*). Shown are the total kinetic energy (upper left panel), the parallel energy (upper right panel), the perpendicular energy (lower left panel), and the energy associated with the* $\mathbf{E} \times \mathbf{B}$*-drift motion (lower right panel). In the normalisation discussed in the text, the numbers on the* x*-axis can be interpreted as seconds and the numbers on the* y*-axis as electron volts.*

At the same time the perpendicular energy associated with gyrational motion of the particle (μB) also increases on average, as shown in the lower left panel of Fig. 2.10. The perpendicular energy has its maximum values at the mirror points and its minimum when passing through the centre of the CMT. However, even at the centre of the CMT, the perpendicular energy is increasing with time. The increase of the perpendicular energy is clearly a consequence of the collapse of the magnetic field and the corresponding increase in magnetic field strength along the particle orbit.

For comparison, the lower right panel of Fig. 2.10 shows the energy associated with the $\mathbf{E}\times\mathbf{B}$-drift motion, $m\mathbf{u}_E^2/2$, where

$$\mathbf{u}_E = \frac{1}{B^2}\mathbf{E}\times\mathbf{B}. \tag{2.21}$$

Compared to the other parallel and perpendicular energies, the energy of the $\mathbf{E}\times\mathbf{B}$-drift motion is insignificant (here it is smaller by a factor of about 10^{-4}). Even at the initial time, the energy due to this drift is not significant when compared to the others, contributing 0.1% at most. As the CMT collapses the energy associated with $\mathbf{E}\times\mathbf{B}$-drift generally decreases to zero.

Obviously, due to the nature of trapped particle motion there is a constant interchange between parallel and perpendicular energy along any trapped particle orbit and the two energy forms show the corresponding oscillations between maximum and minimum values. Naturally, these oscillations are out of phase and if added up lead to the total energy not having any oscillation apart from the step-like behaviour discussed above. The average perpendicular energy and the average parallel energy are comparable for this orbit.

For particle orbit 2, the energy shows a very different behaviour (see Fig. 2.11) The total energy (upper left panel) again shows an overall gain, but only after some energy decrease at the beginning. The step-like behaviour, seen in the total energy for orbit 1, is not visible for orbit 2. The parallel energy (shown in the upper right panel) is again periodic, but this is more difficult to see as there are far more bounces due to the particle being trapped with mirror points very close to the centre of the CMT. It should also be noted that the parallel energy for this particle orbit is three orders of magnitude smaller than the total energy. This explains why the step-like behaviour seen for orbit 1 is not seen here, as it is simply too small to see on the scale of the total energy, although a closer investigation shows that it is still present, but with a much smaller amplitude than for orbit 1. Another remark is that the peak seen in the parallel energy at about 28 s corresponds to the minimum in total energy around the same time.

As the parallel energy is so much smaller than the total energy, it is clear that the perpendicular energy must be the dominating contribution to the total energy, and the two are indeed almost identical (see lower left panel; as for particle orbit 1, the energy associated with the $\mathbf{E}\times\mathbf{B}$-drift motion is negligible, see lower right panel). However, a closer investigation shows, similar to the case of orbit 1, there are still small periodic variations in the perpendicular energy, although they

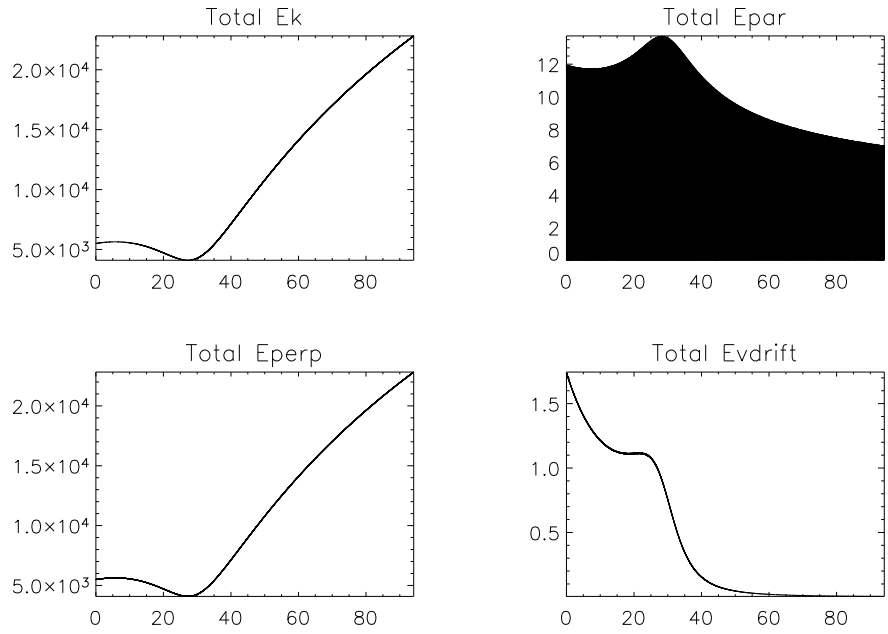

Figure 2.11: Plots of time evolution of energy for particle orbit 2 (initial pitch angle $87.3°$). Shown are the total kinetic energy (upper left panel), the parallel energy (upper right panel), the perpendicular energy (lower left panel), and the energy associated with the $\mathbf{E} \times \mathbf{B}$-drift motion (lower right panel). Using the normalisation discussed in the text, the numbers on the x-axis can be interpreted as seconds and the numbers on the y-axis as electron volts.

are not visible on the scale shown here. Because the bounce points are close to the centre of the CMT, the magnetic field does not change much over the period of a single particle oscillation, and thus $E_\perp = \mu B$ does not change much either. An interesting feature of the perpendicular and the total energy time evolution is that there is an energy decrease to start with and that both energies increase only after they have gone through a minimum. This feature can be explained quite easily by looking at the magnetic field structure of the CMT model. The CMT magnetic field strength has its minimum in the centre of the CMT at a height of about $y = 2L$ at the beginning. Although the magnetic field evolves in time and the minimum in magnetic field strength eventually disappears, particles initially situated above this minimum and moving mainly downwards with collapsing field lines in the centre of the CMT will pass through this minimum magnetic field strength region and their perpendicular energy will decrease accordingly. Once they have passed through that region the magnetic field will increase again and the perpendicular energy will increase as well, which is exactly what is seen in the two left panels of Fig. 2.11. Generally, it can be concluded that for particle orbits like orbit 2, the betatron effect is the dominating mechanism of energy gain.

As orbits 1 and 2 start at the same initial position, they must both pass through the field strength minimum, although orbit 1 will only pass through it when in the centre of the CMT, i.e. when its perpendicular energy is at its minimum. A closer investigation does show that the graph of the perpendicular energy for orbit 2 has the same shape as the lower envelope of the perpendicular energy plot for orbit 1. An indication of this can be found in the lower left panel of Fig. 2.10. More generally, any other particle orbit starting at the same position should have a perpendicular energy graph with a lower envelope of the same shape. This shape is determined by variation of the magnetic field strength B with height at the centre of the CMT ($x = 0L$). The perpendicular energy graph for any particle is given by the product of B and the magnetic moment. The magnetic moment is a constant in guiding centre theory, and thus the minima of the perpendicular energy correspond to the minima in B along an orbit.

2.4.2 Longitudinal invariant and bounce length

In section 1.5.1 I showed that the longitudinal invariant J is very well conserved for the particle orbit investigated in Giuliani et al. (2005). This is also the case for the two orbits discussed above. For particle orbit 1 the maximum value is only 0.037% larger than the minimum, and for particle 2 the maximum is only 0.062% larger than its minimum. Given that J is a good invariant for the two orbits, an interesting question to investigate is in which way the distance between consecutive bounce points changes during the evolution of the trap, because that could indicate the presence of the first order Fermi mechanism (see e.g. Somov and Kosugi 1997). The bounce lengths for the two orbits are shown in Fig. 2.12. For particle orbit 1 the length decreases all the time while the trap is collapsing. This would be consistent with interpreting at least part of the energy gain as

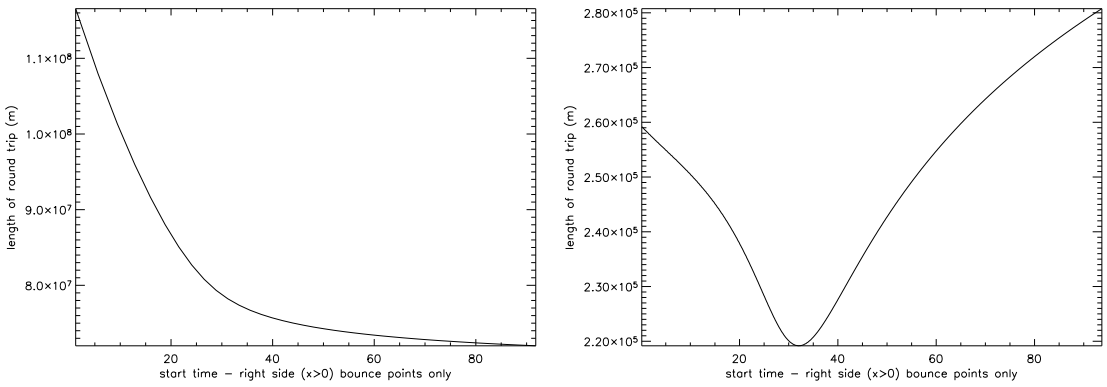

Figure 2.12: Bounce length as a function of time for particle orbit 1 (left panel) and 2 (right panel).

related to the first order Fermi mechanism. One should, however, bear in mind that, as discussed in detail by Giuliani et al. (2005), the parallel energy increases mainly at the loop top due to the field line curvature, as this gives rise to a source term in the parallel energy equation (e.g. Northrop 1963). For particle orbit 2 the bounce length decreases to a minimum and then increases again. This is consistent with the increase of average parallel energy at the beginning and decrease of the average parallel energy in the later stages of the collapse, as shown in the upper right panel of Fig. 2.11.

2.4.3 The orbits using different orders of guiding centre theory

Both in Giuliani et al. (2005) and earlier in this chapter it was found that the higher order terms of the guiding centre theory, in particular the curvature term in the parallel equation of motion, play an important role in the energization process of trapped particles in a CMT. On the other hand, if the two main energization processes can be simply understood as either betatron effect or first order Fermi acceleration due to a shortening of the bounce length, the higher order terms should not be important.

To gain more insight into this issue I have calculated particle orbits for the same initial conditions as just described, but using only the lowest order guiding centre theory, i.e. neglecting higher order drift terms such as the grad B drift and the curvature drift, only including the $\mathbf{E} \times \mathbf{B}$-drift and the mirror term. Because there is no electric field parallel to the magnetic field in the models considered, this term can also be dropped and the equations become

$$\dot{R}_\perp = \frac{\mathbf{b}}{B} \times \mathbf{E} + v_\parallel \mathbf{b}, \tag{2.22}$$

$$\frac{m}{q}\frac{dv_\parallel}{dt} = -\frac{\mu}{q}\frac{\partial B}{\partial s}. \tag{2.23}$$

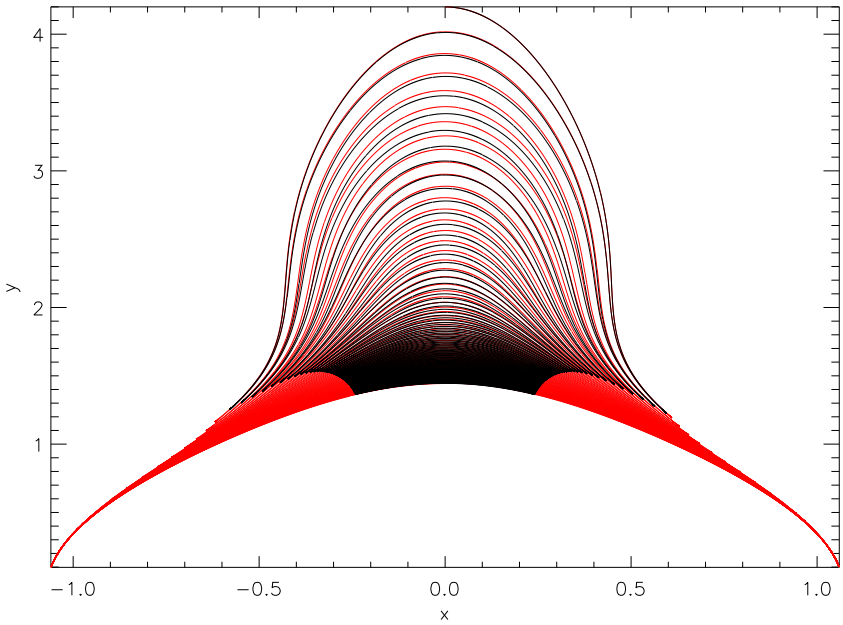

Figure 2.13: Orbit of particle 1, calculated including lowest order terms only (black) and the fully first order equations (red).

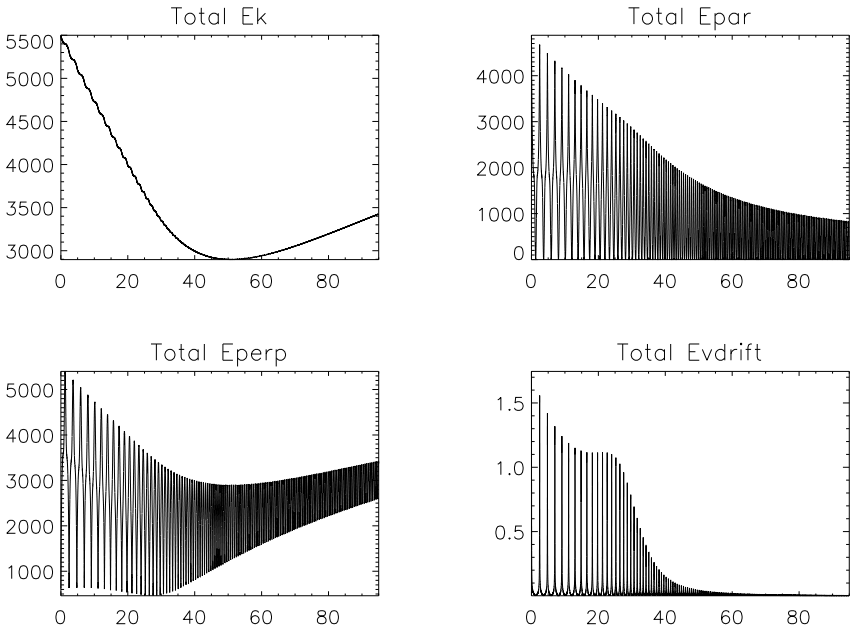

Figure 2.14: Energy for particle 1, using lowest order guiding centre theory. Shown are the total kinetic energy (upper left panel), the parallel energy (upper right panel), the perpendicular energy (lower left panel), and the energy associated with the $\mathbf{E} \times \mathbf{B}$*-drift motion (lower right panel).*

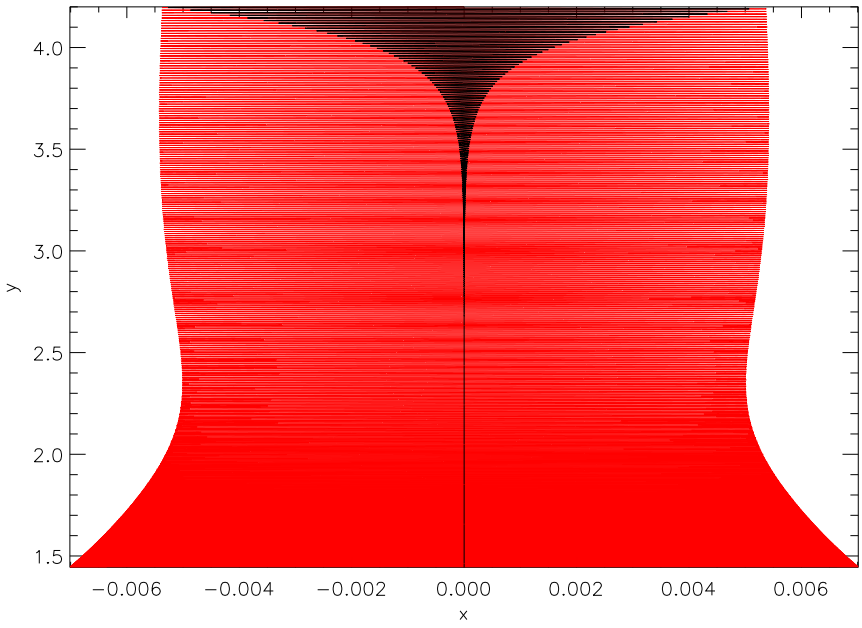

Figure 2.15: Orbit of particle 2, calculated including first order terms (red) and lowest order terms only (black).

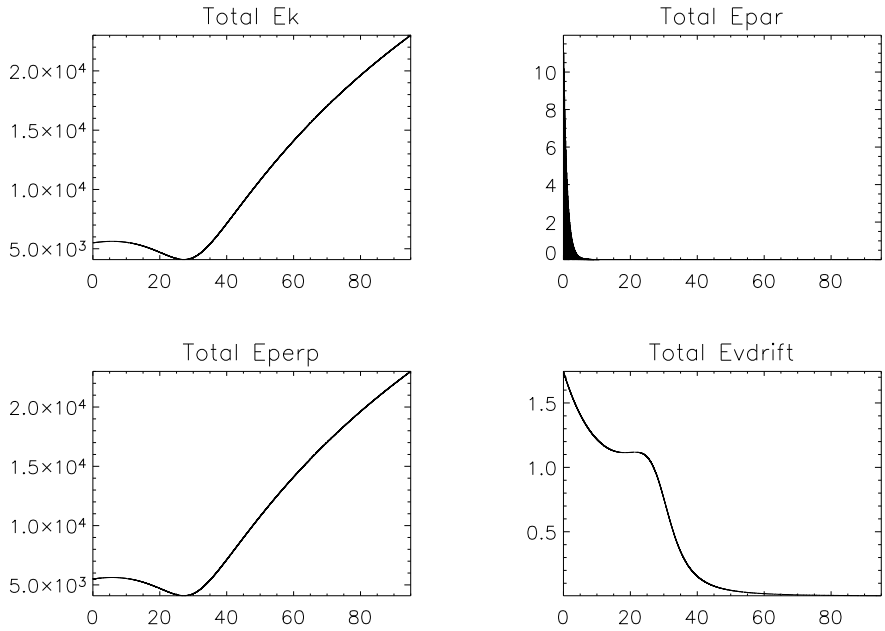

Figure 2.16: Energy for particle 2, using lowest order guiding centre theory. Shown are the total kinetic energy (upper left panel), the parallel energy (upper right panel), the perpendicular energy (lower left panel), and the energy associated with the $\mathbf{E} \times \mathbf{B}$*-drift motion (lower right panel).*

The results for the initial condition of orbit 1 are shown in Fig. 2.13, where the orbit calculated previously is shown in red and the orbit calculated with Eqs. (2.22) and (2.23) is overlaid in black. It is immediately clear from Fig. 2.13 that there is a substantial difference between the two orbits. For the orbit calculated using the lowest order guiding centre theory, the mirror points are much closer to the trap centre and the particle does not go as far down the loop legs as when the first order terms are included. Due to the smaller distance between the mirror points the orbit calculated with the lowest order guiding centre theory mirrors more times than the orbit calculated with the first order terms (135 compared to 86). Additionally, as the trap collapses, the mirror points of the orbit calculated with the lowest order guiding centre theory approach each other in the later stages of the CMT collapse.

Figure 2.14 shows the same energy plots as in Fig. 2.10, but now for the orbit calculated with the lowest order guiding centre theory. The only plot in Fig. 2.14 which is similar to the corresponding plot in Fig. 2.10 is the plot of the energy associated with the $\mathbf{E} \times \mathbf{B}$-drift (lower right panel). The plots for the total energy, the parallel energy and the perpendicular energy are all vastly different from Fig. 2.10. The total energy decreases to almost half of its starting value before rising, but it does not even return to its value at the start within the trap collapse time, so overall energy is lost. The individual components of the energy also reflect this. The upper envelope of the parallel energy (upper right panel in Fig. 2.14) decreases all the time during the collapse, despite the fact that the mirror points are moving towards each other. (This is to be compared to the increase in average parallel energy found when using first order guiding centre theory.) This can be understood by the absence of the curvature term from the parallel equation of motion. As already explained above, Giuliani et al. (2005) found that the curvature term in the parallel velocity equation is the most important source term of the parallel energy, at least in the initial phase of the CMT collapse. It seems that in the absence of that term the parallel energy cannot increase for the particle orbit, despite the fact that the mirror points are approaching each other. This indicates that a naive interpretation of an increase of the average parallel energy should be avoided.

In the perpendicular energy graph (lower left panel in Fig. 2.14) the upper envelope is almost identical to the total energy graph. Perpendicular energy is first lost and then gained again in the later stages, but as it does not reach the initial energy level at the final time there is an overall loss of perpendicular energy.

For particle 2, the orbit again looks different depending on the set of equations used (see Fig. 2.15). Using lowest order guiding centre theory, the orbits mirrors closer and closer to the centre of the CMT, basically remaining at $x = 0$ (to within numerical accuracy) towards the end. As in the case of orbit 1 this can be explained by the decrease in parallel energy due to the lack of the curvature term in the parallel equation of motion.

Figure 2.16 again shows the energy plots for orbit 2 as calculated with lowest order guiding centre

theory. The energy due to the u_E drift (lower right panel of Fig. 2.16) is again very similar in both cases and it makes a negligible contribution to the total energy. The total energy (upper left panel in Fig. 2.16) for particle orbit 2 looks very similar to the corresponding plot in Fig. 2.11. This is due to the fact that for this orbit the total energy is dominated by the contribution of the perpendicular energy, as discussed below. The upper envelope of the parallel energy (upper right panel in Fig. 2.16) decreases quickly with time. This is consistent with the orbit basically stopping in the centre of the CMT, i.e. the parallel motion getting smaller and smaller in amplitude. As for orbit 1, the loss in parallel energy can be explained by the absence of the curvature term from the lowest order guiding centre parallel equation of motion. Bearing in mind that the perpendicular energy is much larger than the parallel energy for orbit 2, it is not surprising that the perpendicular energy plot (lower left panel of Fig. 2.16) is also similar for both sets of equations, i.e. the equations with only the lowest order terms are fine for particles with inital pitch angles close to 90°. The main reason for the similarity between energy graphs in the two cases, despite the difference in the orbits, is that the time evolution of the energy is dominated by the betatron effect, which in turn is determined only by the variation of the magnetic field strength along the particle orbit. As both orbits do not move far away from the centre of the CMT, they both experience approximately the same magnetic field strength and thus the perpendicular energies are almost identical.

A 'mixed order' guiding centre approximation would be to use only the lowest order terms in the perpendicular equation, but include higher order terms in the parallel equation. So in this case the equations used are:

$$\begin{aligned} \frac{m}{q}\frac{\mathrm{d}v_\parallel}{\mathrm{d}t} &= E_\parallel - \frac{\mu}{q}\frac{\partial B}{\partial s} + \frac{m}{q}\mathbf{u}_E \cdot \left(\frac{\partial \mathbf{b}}{\partial t} + v_\parallel \frac{\partial \mathbf{b}}{\partial s} + \mathbf{u}_E \cdot \nabla b\right) \\ \dot{R}_\perp &= \frac{\mathbf{b}}{B} \times \mathbf{E} + v_\parallel \mathbf{b} \end{aligned}$$

i.e. Eqs. (1.86) and (2.22). Energy plots for these cases are shown in Figures 2.17 and 2.18, for particles 1 and 2 respectively. These have been overplotted on the results from the fully first order equation of motion in red, but are such a good match that these cannot be seen. Similarly, the orbits using the mixed order equations have been plotted on the orbits from the fully first order equations in Figs. 2.19 and 2.20, again for particles 1 and 2 respectively.

It is difficult to quantify this difference between the full first order and the mixed order equations of motion, but table 2.1 shows the differences between the mixed order and lowest order only cases compared to the full first order equations. The first column is the difference between the minimum and maximum values of the variable (calculated using the first order equations). This is helpful to give an idea of the scale of the variable. The next column shows the absolute difference between the mixed/lowest order cases and using the full equations, interpolated to the same times. The third column shows the ratio of the last two as a percentage. The units for the scale and absolute difference are the scale length (10Mm) for x and y and eV for the energies. Like the graphs, the

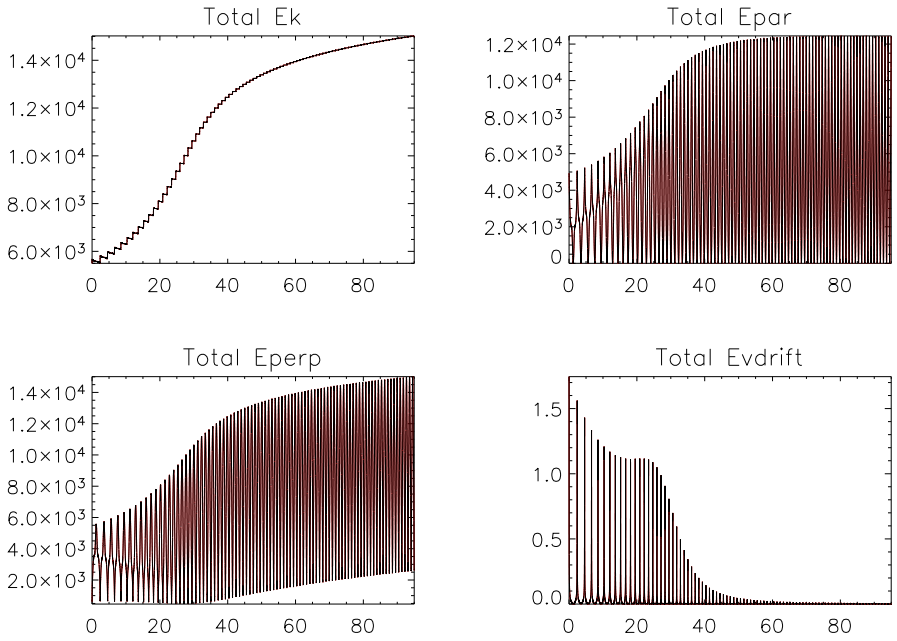

Figure 2.17: Total kinetic energy, parallel energy, perpendicular energy and energy due to the $E \times B$ drift when calculated using the mixed order equations of motion for particle 1. Same calculated with fully first order equations of motion plotted underneath but not visible as values so similar.

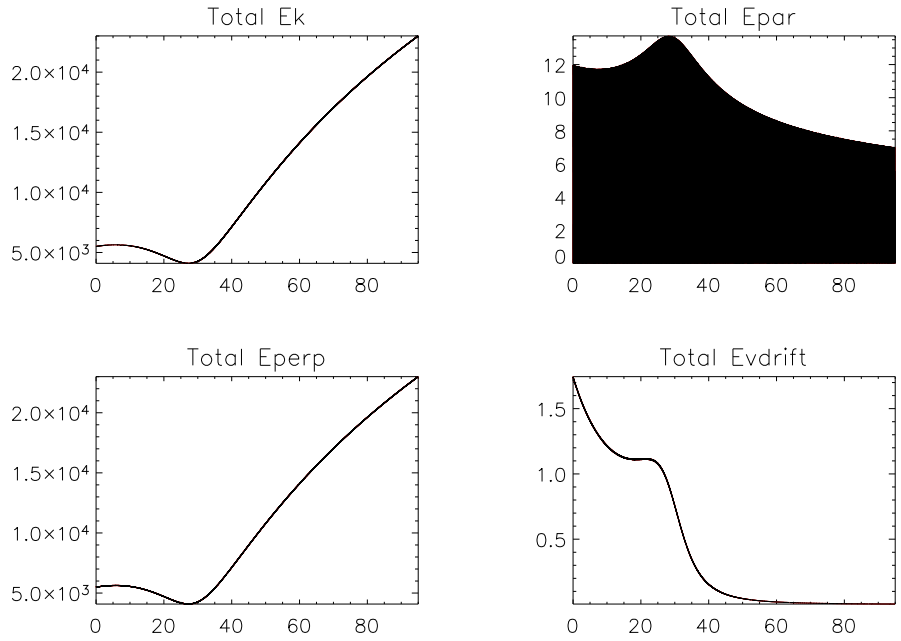

Figure 2.18: Total kinetic energy, parallel energy, perpendicular energy and energy due to the $E \times B$ drift when calculated using the mixed order equations of motion for particle 2. Same calculated with fully first order equations of motion plotted underneath but not visible as values so similar.

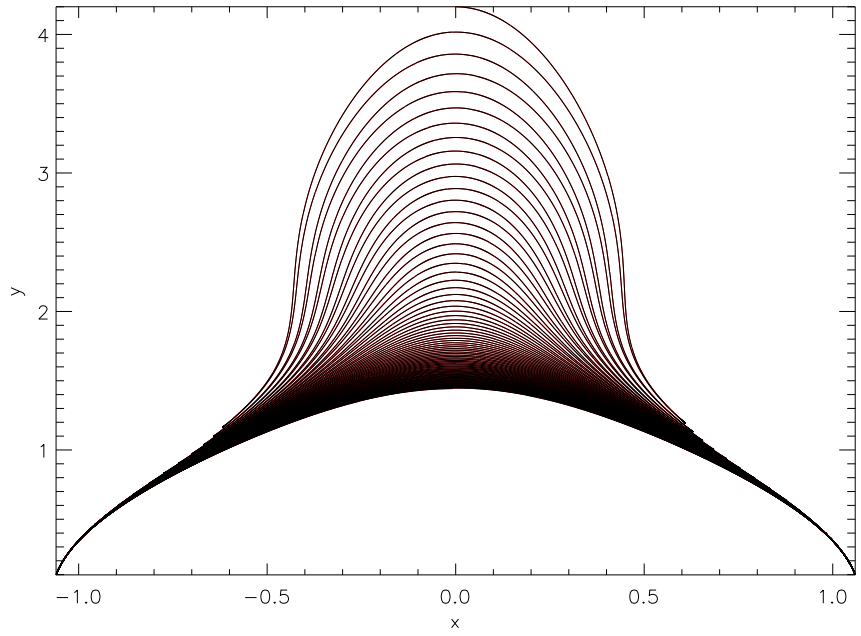

Figure 2.19: Particle orbit calculated using the mixed order equations of motion for particle 1. Same calculated with fully first order equations of motion plotted underneath but not visible as values so similar.

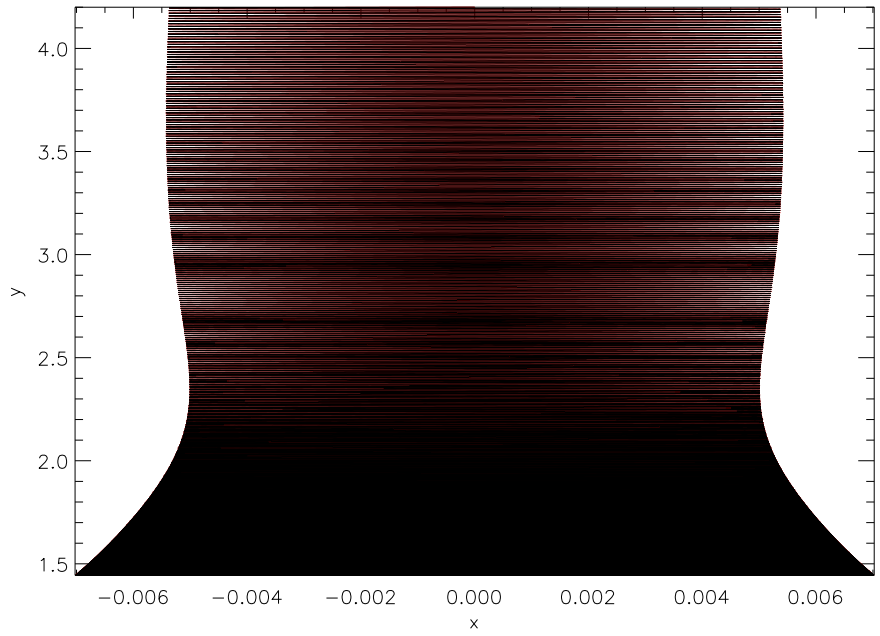

Figure 2.20: Particle orbit calculated using the mixed order equations of motion for particle 2. Same calculated with fully first order equations of motion plotted underneath but not visible as values so similar.

variable	range†	max. absolute difference	max. percentage difference
Particle 1 - Mixed order equations			
x	2.119554	1.428475E-06	0.000067
y	4.101746	0.006282639	0.000054
Total E_K	9519.905	0.0007897472	0.000008
$E_{\parallel}$	12447.03	0.01873195	0.000150
$E_{\perp}$	14549.78	0.01873235	0.000129
E_{u_E}	1.745160	5.186175E-06	0.000297
Particle 2 - Mixed order equations			
x	0.01404837	2.605181E-08	0.000185
y	2.755860	1.698628E-05	0.000000
Total E_K	18911.11	5.094081E-06	0.000000
$E_{\parallel}$	13.73002	0.0008533907	0.006216
$E_{\perp}$	18919.91	0.0008513910	0.000004
E_{u_E}	1.741933	4.491764E-07	0.000026
Particle 1 - Lowest order equations			
x	1.175278	1.333914	113.497741
y	2.975070	2.434909	79.079498
Total E_K	2603.408	11597.12	445.459284
$E_{\parallel}$	4879.308	12445.83	255.073553
$E_{\perp}$	4937.915	12433.45	251.795471
E_{u_E}	1.743984	1.351568	77.498898
Particle 2 - Lowest order equations			
x	0.01033359	0.007017182	67.906540
y	2.755846	1.849363	0.007585
Total E_K	18917.51	14.01689	0.074095
$E_{\parallel}$	11.96050	13.72675	114.767405
$E_{\perp}$	18918.49	13.72367	0.072541
E_{u_E}	1.741932	0.007129351	0.409278

† range is (max - min) for full first order equation

Table 2.1: Maximum size of errors using the different equations of motion.

table shows that the lowest order equations are inadequate, but the difference between using the fully first order and the mixed order equations is negligible.

From the comparison presented in this section it can be concluded that studying the acceleration mechanisms operating in a CMT using only the lowest order terms in the guiding centre theory is not justified, as it leads to incorrect results. Despite being of higher order, terms that are related to the curvature term play an important role in the energization process and should not be neglected in the equation for the parallel velocity. However, the higher order terms in the perpendicular equation are not as important and can be safely discarded.

2.5 Summary and Discussion

In this chapter I have presented a detailed study of the particle energization processes in CMTs, using specifically the CMT model of Giuliani et al. (2005). It was found that particle energies can increase by factors of up to approximately 50, but that most particles experience a more modest energy increase. While the energy increase does not depend strongly on initial energy, it does depend on the initial position of particles in the CMT and on the initial pitch angle. Particles with the highest increase in energy start in the region of the CMT which initially has the smallest magnetic field strength and usually have pitch angles close to $90°$. The energy increase for these particles is caused mainly by the betatron effect as the trap collapses and the magnetic field strength along the orbit increases. Due to their pitch angle these particles remain trapped close to the centre of the trap, which means that at the end of the CMT collapse the highest energy population of particles is confined in a region at the top of the most collapsed magnetic loop. This is consistent with previous results using other CMT models (e.g. Karlický and Kosugi 2004).

I also found that for particles with initial pitch angles differing substantially from $90°$, but outside the loss cone at any time during the collapse of the CMT, a substantial increase in parallel energy is possible. On a superficial level this could be interpreted as first order Fermi acceleration as usually the distance between mirror points is decreasing during the CMT evolution. A more careful investigation, however, corroborates the finding of Giuliani et al. (2005) that the parallel energy increase is mainly due to the curvature term in the equation for the parallel velocity. This effect is actually strongest when the orbits cross the centre of the CMT. Further support for this interpretation is found by comparing particle orbits calculated with and without including the first order drifts. In the minimal case without including the first order drifts the parallel energy decreases despite a decreasing distance between the mirror points, which contradicts a simple interpretation in terms of first order Fermi acceleration. Adding first order terms back in to the parallel equation of motion but still omitting them from the perpendicular equation gives a very similar result to having the higher order terms in both equations. Again this confirms the importance of the higher order terms (associated with the field line curvature) in the parallel equation of motion. This is consistent with previous findings by other authors for different CMT models (e.g. Karlický and Bárta 2006).

In view of recent findings that high energy radiation from loop tops or above loop tops (Masuda et al. 1994) is more common during solar flares than previously thought (see e.g. Krucker et al. 2008, for an excellent review), it is tempting to associate the fact that the highest energy particles are trapped at the top of the loop with hard X-ray loop top sources. This has been suggested in the past by other authors (e.g. Somov and Kosugi 1997; Karlický and Kosugi 2004; Karlický and Bárta 2006; Minoshima et al. 2010) and attempts have been made at calculating the characteristics of the hard X-ray emission expected from CMT models (e.g. Karlický and Bárta 2006). In order

to assess this properly, the present CMT models should be amended to include collisions with a background plasma along the lines of previous models for hard X-ray loop top emission using static loop models (e.g. Fletcher 1995; Fletcher and Martens 1998). Apart from being a possible explanation for sources of coronal high energy radiation, the trapping of high energy particles in the corona can also contribute to the explanation of observations of microwave emission from flaring loops (e.g. Melnikov et al. 2002).

In this chapter I have shown that some of the higher order drifts must be considered when looking at particle acceleration. For any 2D CMT model, some higher order drifts such as the curvature drift and the gradient-B drift are actually directed into the invariant direction (i.e. along the z-direction). It turns out that the particle orbits do not move too far in the z-direction compared to their motion in the x-y-plane, but it nevertheless raises the question whether the results would change for a 3D CMT model. This is considered in chapter 6 where I present a generalised theory allowing for 3D CMT models including both 3D magnetic fields and 3D flows.

In the next chapter, the fields in the Giuliani et al. (2005) model are extended to include a guide field ($B_z \neq 0$) in the invariant direction. In later chapters the fields are further modified to include an asymmetry in the magnetic field (chapter 4) and the velocity and magnetic fields made fully dependent on all three dimensions (chapter 6).

Chapter 3

Addition of a guide field

None of the models in the literature has investigated the effects of a guide field. The addition of a guide field to a spatially invariant model is the first step towards a three-dimensional trap model. In this chapter, I will briefly discuss the effects of adding a guide field to the Giuliani et al. (2005) mode, but without adding flow in the invariant direction. The extension of the theoretical framework to include flows in the invariant direction will be discussed in chapter 6.

3.1 Including a guide field in the Giuliani et al. model

The inclusion of a guide field can be done with a straightforward change to the Giuliani et al. (2005) model. Only the B_z needs to be changed, but in such a way that the MHD equations are maintained. The B_z should be localised in y and get stronger as time progresses. At the photosphere, $y = 0$, the B_z should be constant for all time (i.e. $\frac{\mathrm{d}B_z}{\mathrm{d}t}(y = 0) = 0$), as the footpoints should not move. The $\frac{dY_0}{dy}$ function used previously has all these properties, so can be taken advantage of by setting

$$B_z(x, y, t) = \left| \frac{\partial Y_0}{\partial y}(x, y, t) \right| B_{z_{final}} \tag{3.1}$$

where

$$\begin{aligned} \frac{\partial Y_0}{\partial y} &= \frac{1}{2}\left(1 + \tanh\left(\left(y - \frac{L_v}{L}\right)a_1\right)\right)\left(1 + \frac{y}{(at)^b}\right)^{-1} \\ &\quad + \frac{1}{2}a_1\left[(at)^b \ln\left(1 + \frac{y}{(at)^b}\right) - y\right]\left(1 - \left\{\tanh\left(\left[y - \frac{L_v}{L}\right]a_1\right)\right\}^2\right) \end{aligned}$$

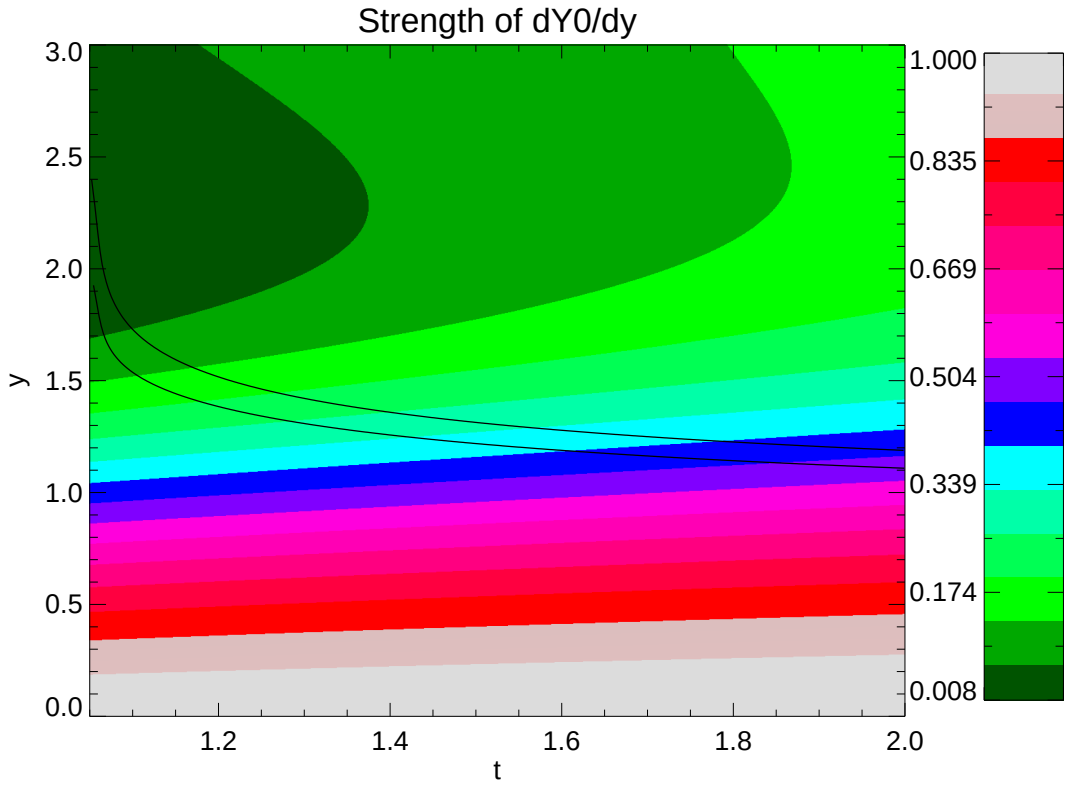

Figure 3.1: Values of $\frac{\partial Y_0}{\partial y}$ for reasonable values of t and y. The black lines show the envelope of a particle trajectory. Because of the time and position of the particle, the $\frac{\partial Y_0}{\partial y}$ experienced increases. All values are shown normalised for use in computer code: t goes from 1.05 to 2.00, representing 95 seconds; y is in units of 10 Mm.

$$+\frac{1}{2}\left(1-\tanh\left(\left(y-\frac{L_v}{L}\right)a_1\right)\right),$$

the derivative of the transformation used previously, Eq. (2.19). This is always positive so the absolute value is not actually required. This function is illustrated in Fig. 3.1, where the value of $\frac{\partial Y_0}{\partial y}(t,y)$ is shown in the colour scale for values of t and y. The black lines indicate the values of t and y for a particle (specifically, particle 1 with $\beta = 1$, the meaning of this is discussed later). Because the particle bounces back and forth in the y direction, only the envelope of its trajectory is shown. $B_{z_{final}}$ is a constant for each run, varied to examine the effect of the guide field strength. Values of $B_{z_{final}}$ were chosen to be of a similar order as the magnetic field already used. The previous expression is reused for convenience only, as any other suitable functions could be used instead. This B_z model is of course not the only possible model, but is simple enough to make a first investigation.

The continuity equation for B_z, Eq. (2.8),

$$\frac{\partial B_z}{\partial t} = -\nabla \cdot (\mathbf{v} B_z) \tag{3.2}$$

can be written as

$$B_z = B_{z_0} J \tag{3.3}$$

where J is the Jacobian determinant of the coordinate transformation. This determinant is given by

$$J = \begin{vmatrix} \frac{\partial X}{\partial x} & \frac{\partial X}{\partial y} \\ \frac{\partial Y}{\partial x} & \frac{\partial Y}{\partial y} \end{vmatrix} = \begin{vmatrix} 1 & 0 \\ 1 & \frac{\partial Y}{\partial y} \end{vmatrix} = \left| \frac{\partial Y}{\partial y} \right| \tag{3.4}$$

so the continuity equation is satisfied for the choice of $B_z \propto \left| \frac{\partial Y}{\partial y} \right|$ above. As a starting point for $B_{z_{final}}$ values, the final magnetic field experienced by a particle travelling in the previous trap with no guide field is used. This gives a value for B of 1.717×10^{-3} T which I shall call B_{00}. To study the effect of different guide field strengths I use $B_{z_{final}} = \beta B_{00}$ with values for β of $0.05, 0.1, 0.5, 1.0$ and 2.0. This lets the guide field be significant compared to the magnetic field as used before, e.g. with $\beta = 1$, the guide field B_z contributes up to 44% of the total magnetic field experienced by the particle at all times. The local maxia in B_z/B happen as the particle goes past the loop top, where B_x and B_y are weaker.

The guide field affects different particles in the trap differently. An example of this can be found by looking at two particles with the same properties as in Sect. 2.4.

The problem of choosing particles with comparable initial conditions is deciding which of the initial conditions should stay the same between particles. If the magnetic moment and pitch angle are kept the same then the total energy will be different due to the perpendicular velocity's dependence on the magnetic field strength.

The particles are chosen to have the same starting position ($x = 0L, y = 4.2L$) and the same energy (5.5 keV), but one particle has parallel velocity -4.14×10^7 m/s (referred to later as particle 1) and the other has parallel velocity 2.05×10^6 m/s (particle 2). These values are chosen so that the pitch angles are 160.40° and 87.33° respectively. As the particles have the same total initial energy and parallel energy (by setting $v_\parallel$), they also have the same pitch angle and perpendicular energy. To account for this, the particles have to have different magnetic moments.

In both cases the particle orbits are changed by the guide field, as it causes more motion in the z direction. This effect is far more noticeable for particle 1. Figures 3.2 and 3.3 show particle orbits in fields with $\beta = 0, 1, 2$ for particles 1 and 2 respectively. As could be expected, the motion in

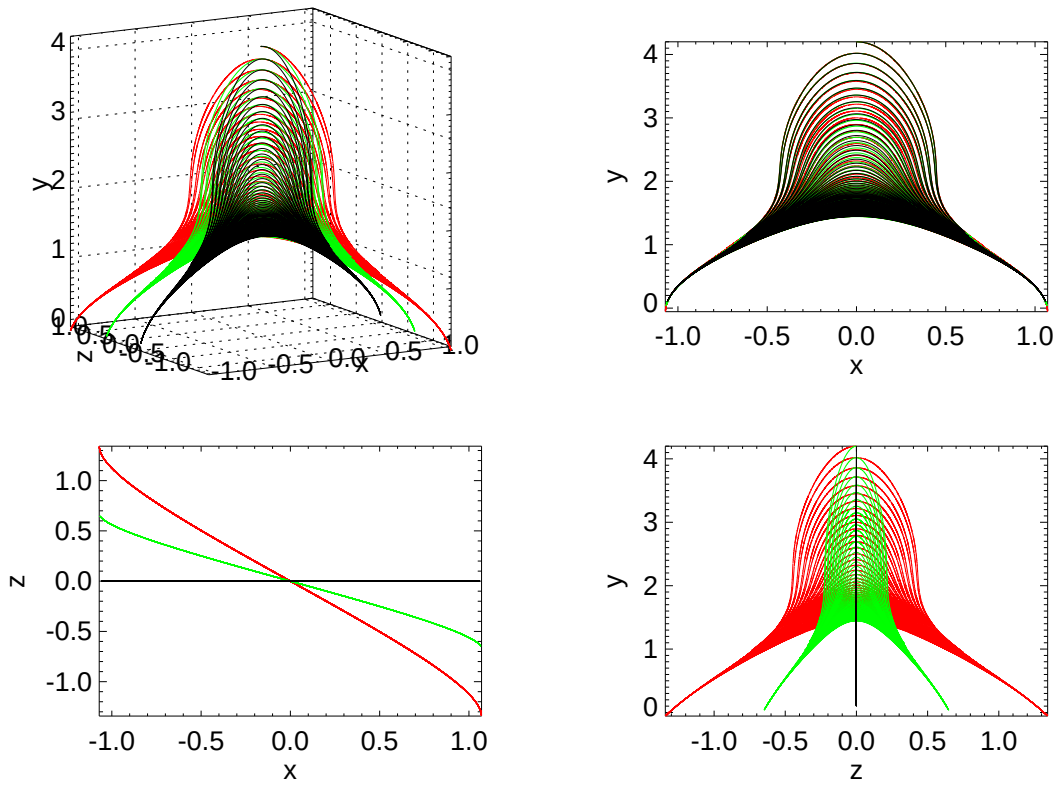

Figure 3.2: Orbit of particle 1 in the traps with $\beta = 0$ (black), $\beta = 1$ (green), $\beta = 2$ (red). Top left is a 3D view, bottom left is looking down on the trajectories, and two side views on the right.

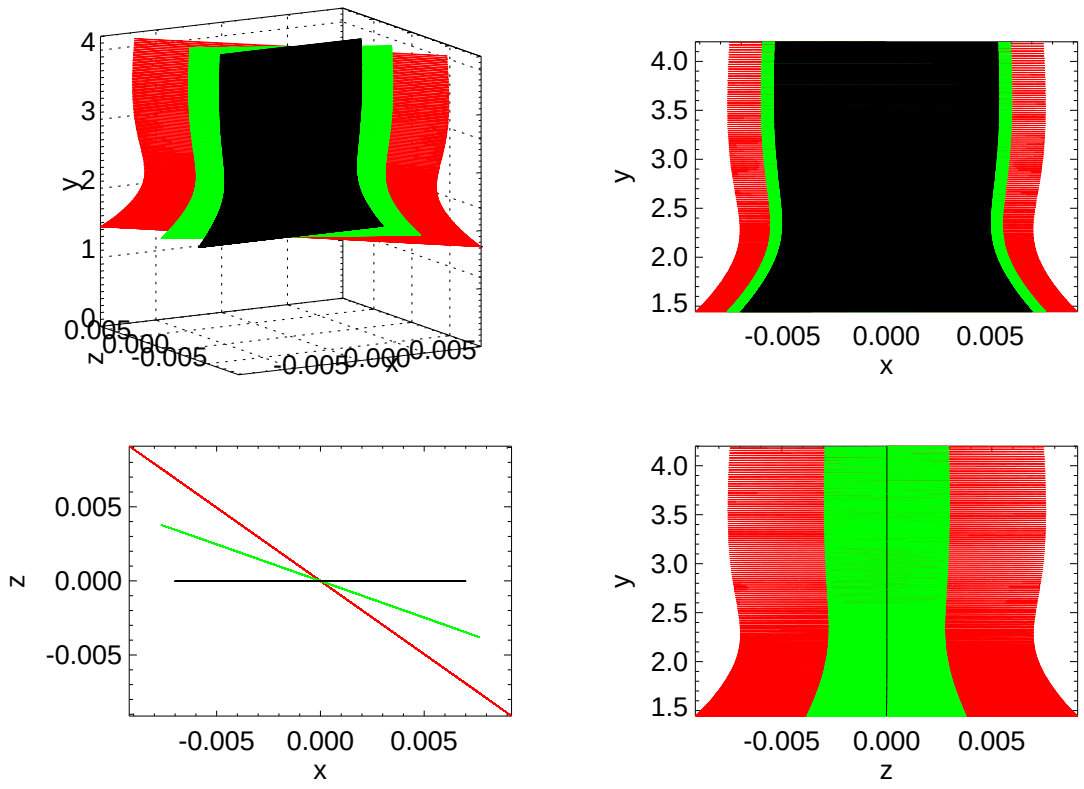

Figure 3.3: Orbit of particle 2 in the traps with $\beta = 0$ (black), $\beta = 1$ (green), $\beta = 2$ (red) as in Fig. 3.2. Note that this particle moves much less in the x and z directions compared to particle 1.

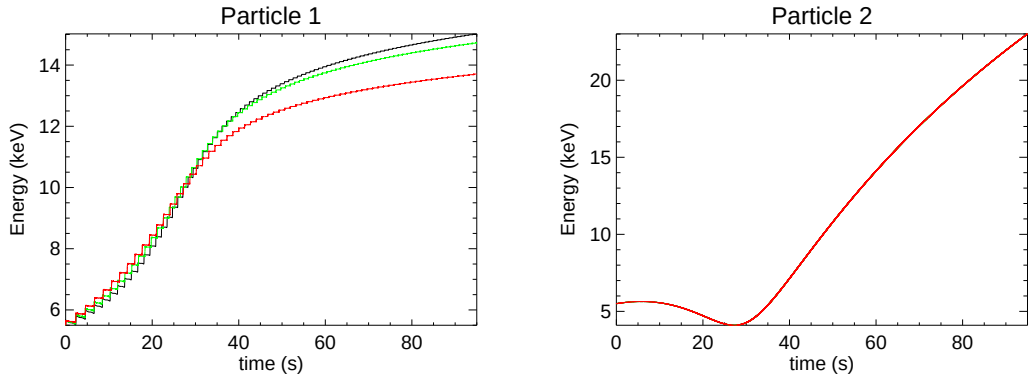

Figure 3.4: Energy of particles in fields with guide fields. Colours indicate the β of 0 (black), 1 (green) and 2 (red). Particle 2 (right) is not affected much by the different fields, so the lines overlap.

the z direction is more dramatic with a stronger B_z.

An interesting question is how the energy of the particle is affected by the guide field. Addition of a guide field does not affect the energy of particle 2 ($\alpha \approx 90°$). The final energy differs by less than 2 eV, even comparing the cases with strongest guide field and no guide field. However, particle 1 is quite different. The guide field causes particle 1 to gain less energy by the end time. This is not the case throughout, as initially the particle in the guide field may gain more energy. As there is not a constant factor between the energies of the particles in different traps this effect cannot be solely due to the particles having different magnetic moments. Figure 3.4 shows the energy of particles in the different guide fields. For particle 1, initially particles in stronger guide fields gain more energy, but this levels off later on, and the particle in the field with no guide field ends up having gained most energy. The final energy of these particles are listed in tables 3.1 and 3.2 for particles 1 and 2 respectively. This table also lists the ratio of final to initial magnetic field. For particle 1, this does not show the same trend as seen for the final energy, suggesting that the energy gain is not just straightforward betatron acceleration. Because the particles with pitch angle close to 180° bounce far from the trap centre, it is worth measuring quantities as the particle passes the trap centre for the last time. Apart from the particle in the trap with $\beta = 8$, all of these occur within the last second of the trap. The B_f/B_i and E_k columns not having the same trend suggest that this is not purely betatron acceleration. For particle 2 the change in magnetic field is the same in all cases. As particle 2 remains close to the trap centre it is not necessary to calculate values at the last pass of the trap centre; nor is it worthwhile to count the number of bounces, as the orbit code only outputs every 50th step it takes so bounces could be missed. The results found here are consistent with the results of particles in fields without a guide field discussed in Sect. 2.4.

The energy gains of particle 2 seem to be related to the betatron effect, as the increase in energy

Particle with $\alpha \approx 180°$ (Particle 1)							
	Final	close to last pass of $x = 0$					no of
β	E_k (eV)	t (s)	x ($\times 10^7$m)	B (T)	B_f/B_i	E_k (eV)	bounces
0	15019	94.08689	4.342033E-3	1.094313E-3	4.16	15001	86
0.05	15016	94.10295	-2.761382E-3	1.094732E-3	3.93	15001	86
0.1	15011	94.14875	-8.556418E-3	1.096646E-3	3.71	15000	86
0.5	14960	94.63730	-3.465442E-3	1.132892E-3	3.00	14950	84
1	14732	94.93368	3.676825E-3	1.230132E-3	2.79	14725	80
2	13705	94.37519	3.984482E-4	1.542674E-3	4.17	13696	68
8	9039	91.53292	-1.383723E-4	4.356385E-3	3.00	9018	24

Table 3.1: Effect of guide field strength on energy gain by the final time. Particle energy at the last pass of the central point and the ratio of the strength of the magnetic field here to at the particle starting point. Last column shows the number of times the particle was reflected during the orbit.

Particle with $\alpha \approx 90°$ (Particle 2)		
$B_{z_{final}}$	Final Energy (eV)	$B_{final}/B_{initial}$
0	23010	4.19
0.05	23010	4.19
0.1	23010	4.19
0.5	23010	4.19
1	23010	4.19
2	23011	4.19

Table 3.2: Effect of guide field strength on energy gain. As the particle remains close to the centre and bounces many times to achieve this, the extra columns in Table 3.1 are not calculated for particle 2.

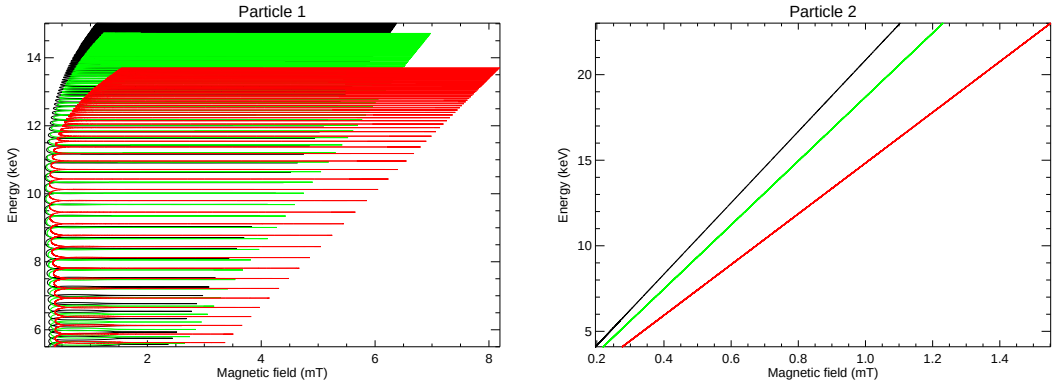

Figure 3.5: Energy of particles in relation to magnetic field. Colours indicate the β of 0 (black), 1 (green) and 2 (red). Particle 2 is accelerated by the betatron effect, so energy is proportional to magnetic field.

is proportional to the gain in magnetic field encountered. This is not the case for particle 1, but as seen previously for cases without the guide field this can still give an contribution to the kinetic energy. Figure 3.5 shows the relation between the magnetic field encountered and the particle kinetic energy.

Although the scales for the magnetic field in Fig. 3.5 look different, particles all start at the same position, so experience the same magnetic field initially. As the particles take different orbits, it is not surprising that they experience different magnetic fields later on. As an illustration of this, Fig. 3.6 shows the magnetic field experienced by particles 1 and 2 in the $\beta = 1$ field. The energy gain of the particles is also very different, shown by plotting the magnetic field experienced and the energy of particles 1 and 2 in the field with $\beta = 1$ in Fig. 3.7. Similar graphs would be produced by plotting other pairs of particles.

For completeness, the distance the particles travel between bounce points in each of the traps can be examined. Figure 3.8 shows this for particle 1. A stronger guide field means fewer trips that are longer and take more time.

3.2 Particles with different initial conditions in guide fields

In this section I compare a large number of particles with the same initial conditions in different fields. For simplicity the same initial energy and pitch angle for each of the sets of initial conditions are chosen. As mentioned previously, this means that 'equivalent' particles can have different magnetic moments. 'Equivalent' particles will have different trajectories in the different fields because the field line structure will be different. Similarly to previous chapters there is a grid of initial conditions for particles. In this case equally spaced initial conditions are considered

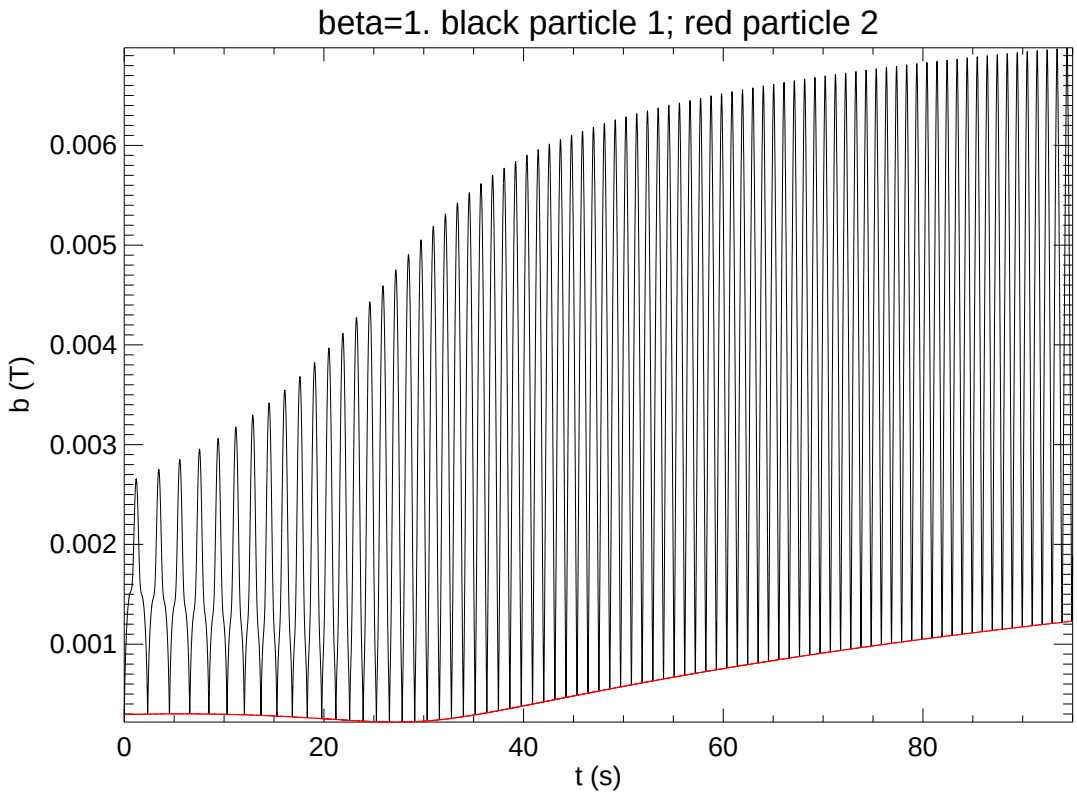

Figure 3.6: Magnetic field experienced in time by particles 1 (black) and 2 (red) in the field with $\beta = 1$.

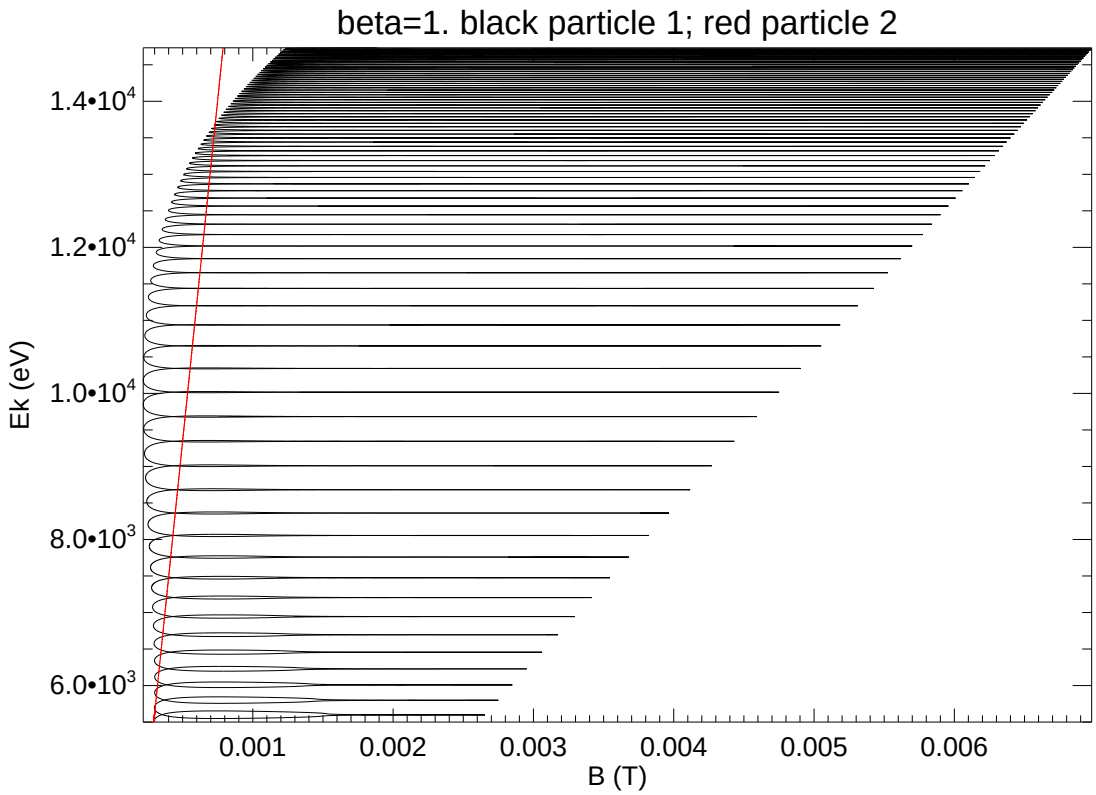

Figure 3.7: Energy of particles 1 (black) and 2 (red) and the magnetic field they experienced in the field with $\beta = 1$.

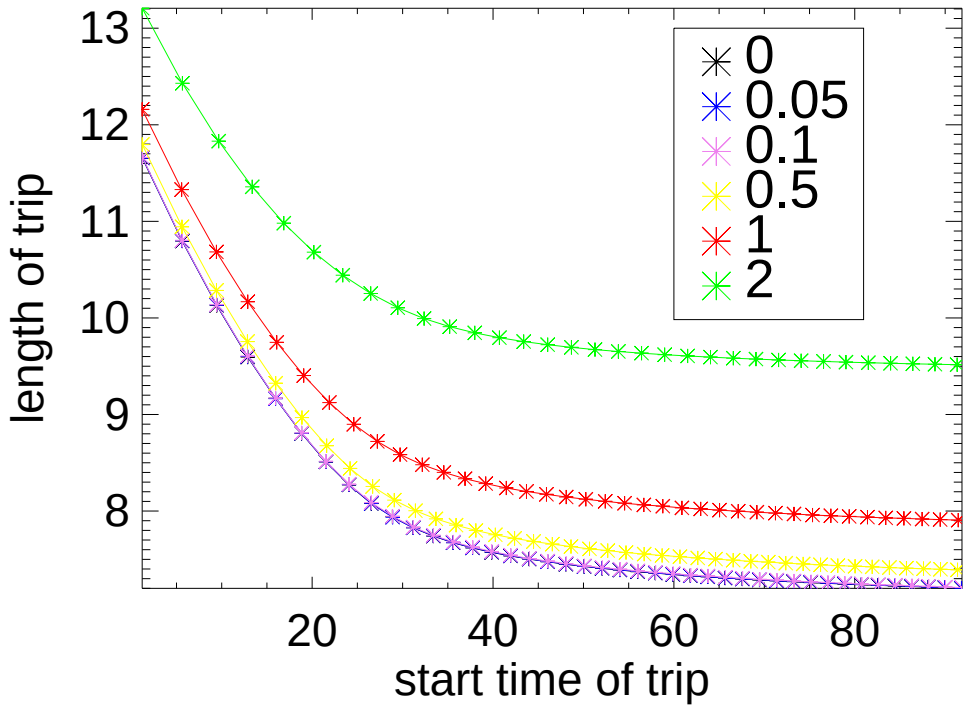

Figure 3.8: 'Trip lengths' for particle 1 in fields with different values of guide field.

(inclusive):

- Kinetic energy: 11 values between 5keV and 6keV;
- Pitch Angle: 10 values between 16.36° and 163.6°;
- Positions: 11 values of x between $-0.5L$ and $0.5L$ and 11 values of y between $1L$ and $5L$;
- z is $1.25 \times 10^{-6}L$ as before.

This gives a total of 13310 particles in each trap.

These were tried in several fields, with $\beta = 0, 0.05, 0.1, 0.5, 1, 2$. The effect of changing the field is small. The energy gained for an equivalent particle is very similar even in fields with $\beta = 0$ and $\beta = 20$. As before, the maximum energy gain is about 53 times the initial energy.

Looking in the x-y-plane, the positions of the particles at the final time is also similar. The highest energy particles are still trapped in the centre. This is shown for $\beta = 2$ in Fig. 3.9, with a colour scale showing the energy gain. Plotting the same for the other guide fields that are considered here would give an almost identical image.

The difference can be seen looking along the z direction. Particles travel in this direction proportionally to the value of $B_{z_{final}}$. Figure 3.10 shows a top down view for $\beta = 2$. The difference between this figure and one from particles in a field with different $B_{z_{final}}$ is only the scaling of the z axis.

Field lines that are higher up in the trap have footpoints further along the x axis. Thus, they are sheared more by the guide field. The effect of this can be seen quite clearly in 3D images of the final particle positions, as shown in Fig. 3.11.

Because of the nature of the transformation, field lines (and thus particles) that are higher up in the trap are pushed further into the z direction.

The number of particles escaping from the trap before it has collapsed (at 95 s in this normalisation) is similar in most cases. Fig. 3.12 shows histograms of the time particles escape from the traps with the different guide fields. Stronger guide fields may cause less particles to escape, as in the $\beta = 2$ case 6% less particles escape compared to no guide field. To corroborate this, a trial was done with $\beta = 8$, which found 40% less particles escape. The histogram for the $\beta = 8$ case is shown in Fig. 3.13. These multiple particle studies can take many days to run, so this was not investigated in great detail. A plausible explanation of this effect would be that the stronger total magnetic field causes more particles to mirror before reaching the lower boundary, although further calculations would be needed to confirm this suggestion.

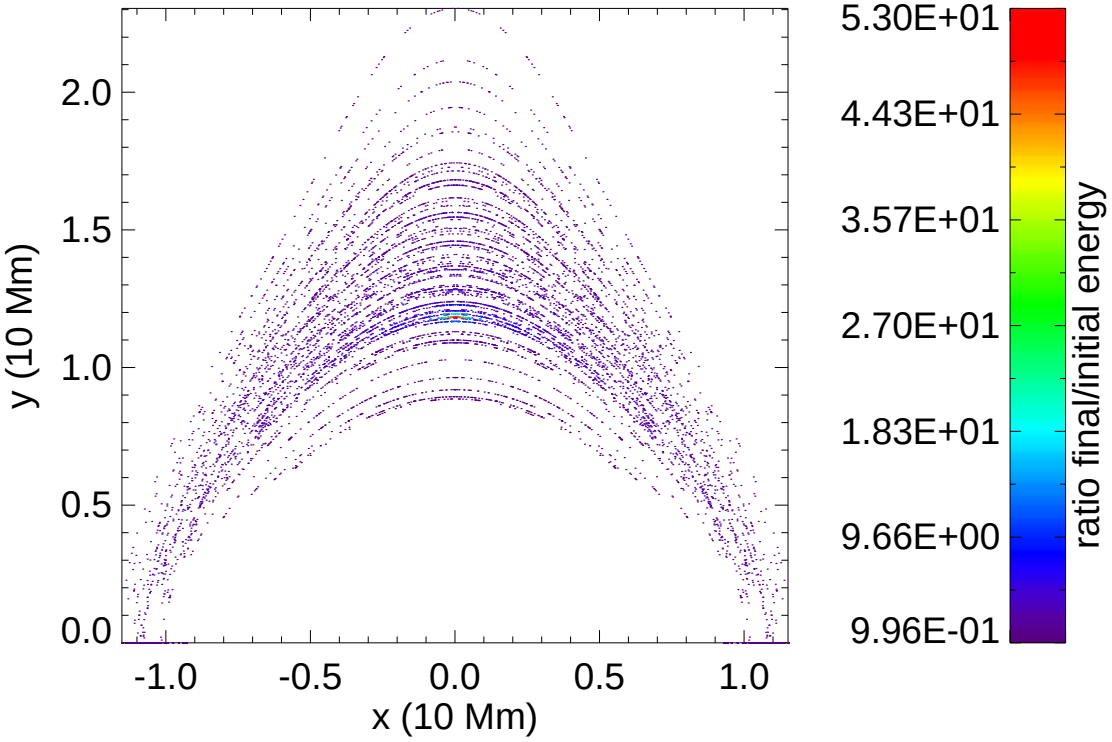

Figure 3.9: Final positions of the particles in the field with guide field due to $\beta = 2$. The colour scale shows the energy gain, the final energy can be up to 53 times the initial energy. This figure would be very similar for any of the guide field cases considered here.

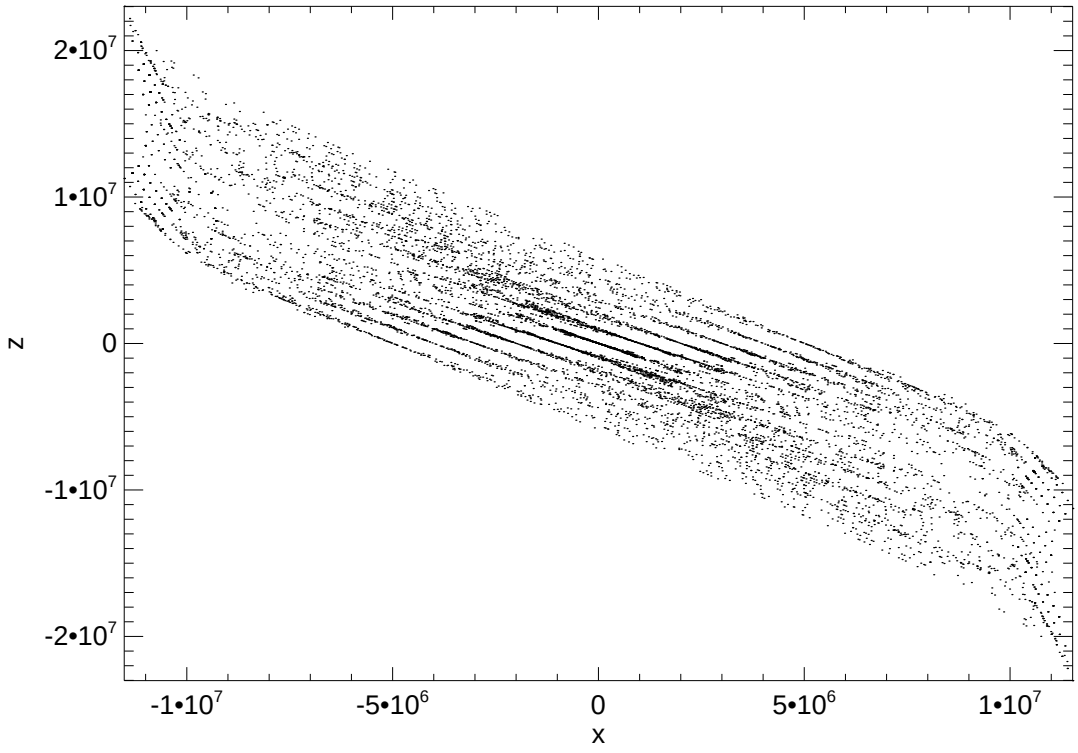

Figure 3.10: Top down plot of particles in final position in a magnetic field with a guide field. Positions shown in meters.

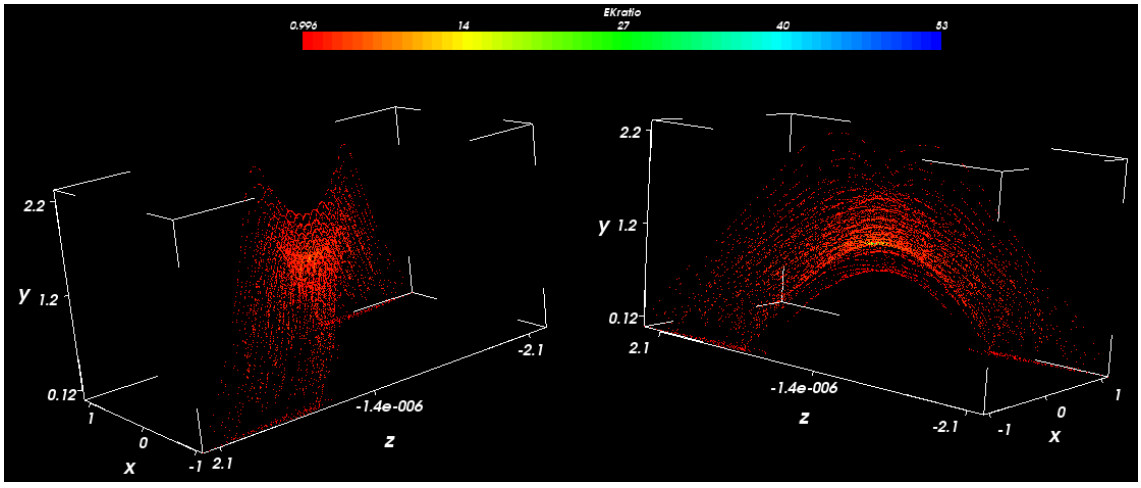

Figure 3.11: Two views of the final positions of particles in a trap with a guide field ($\beta = 2$). Particles that started higher up have been spread out in the z direction along the guide field. Colour scale indicates the energy gained by the particles. Image produced with VisIVO software.

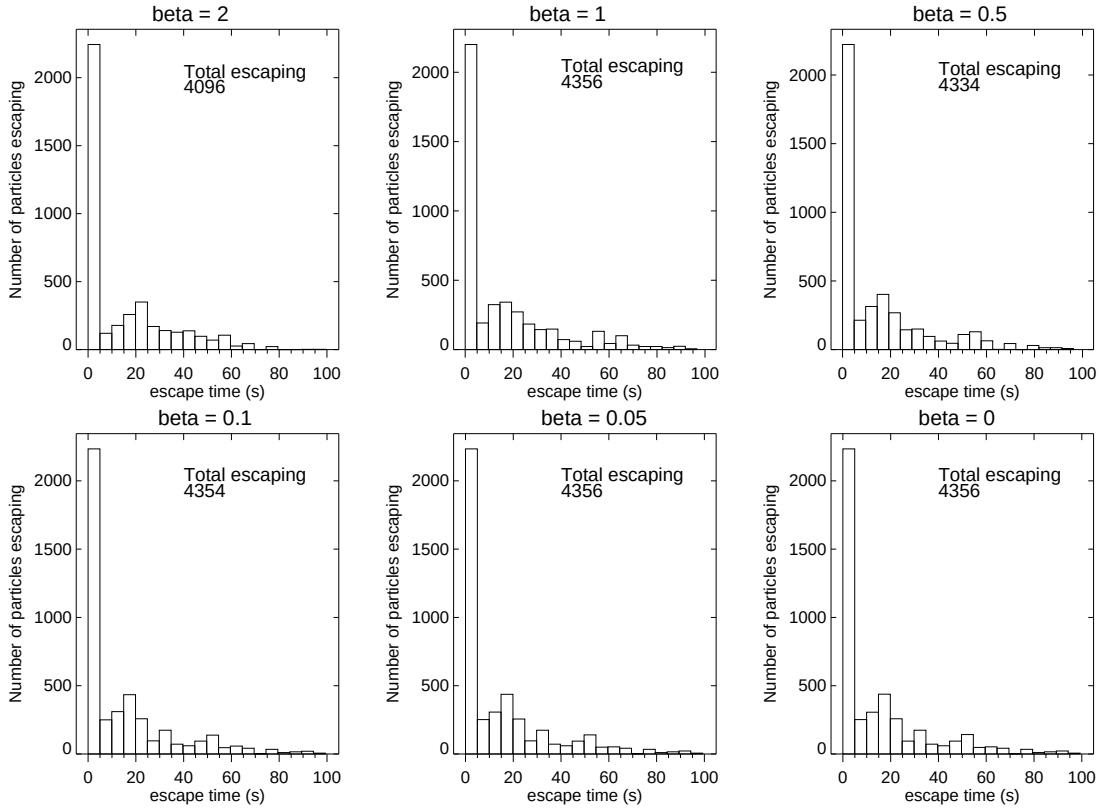

Figure 3.12: Histograms showing when particles escape from the traps with guide fields. The total number of particles starting in each trap is 13310. Particles still in the trap at the final time, $t = 95$ s are considered trapped.

In the following chapters I look at other ways of changing the CMT field from Giuliani et al. (2005). In the next chapter I discuss a trap where the magnetic field has been made asymmetric.

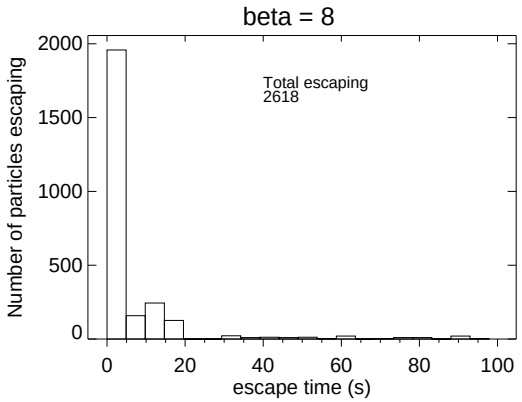

Figure 3.13: Histograms showing when particles escape from the traps with a strong guide field.

Chapter 4

An Asymmetric Trap Model

It is very unlikely that a solar flare would develop in perfect symmetry as has been assumed in the previous models. A simple modification to make the trap model more realistic would be to make the magnetic field asymmetric. This would allow differences between the acceleration processes in traps that are symmetric or asymmetric to be examined. A straightforward way to make the magnetic field asymmetric is to change the equation for the final magnetic field slightly so that the magnetic monopoles are placed at different heights. Thus equation (6.31) becomes:

$$A_0 = c_1 \arctan\left(\frac{y_0 + d_1/L}{x_0 + 1/2}\right) - c_1 \arctan\left(\frac{y_0 + d_2/L}{x_0 - 1/2}\right), \tag{4.1}$$

where d_1 controls the depth of the left magnetic charge and d_2 the right. Equation (6.31) can be easily recovered by setting $d_1 = d_2 = d$.

4.1 Effects of trap asymmetry

The same values as before are reused in this model. Some experimentation showed that a value of $d_1 = L$ and $d_2 = 1.5L$ illustrates the asymmetric trap nicely, but this choice is reasonably arbitrary. Using a larger value for d_2 means that the charge on the right is further from $y = 0$ so the magnetic field above it at $y = 0$ will be weaker than above the left charge. The trap centre is difficult to define because of the asymmetry, but will move to the right when compared to previous traps. The particles would be expected to penetrate deeper into the side with the weaker magnetic field. Figure 4.1 shows some magnetic field lines of the trap at the start and end of its time evolution.

Figure 4.2 shows the trap with particles starting in the same position as in chapter 2. More particles

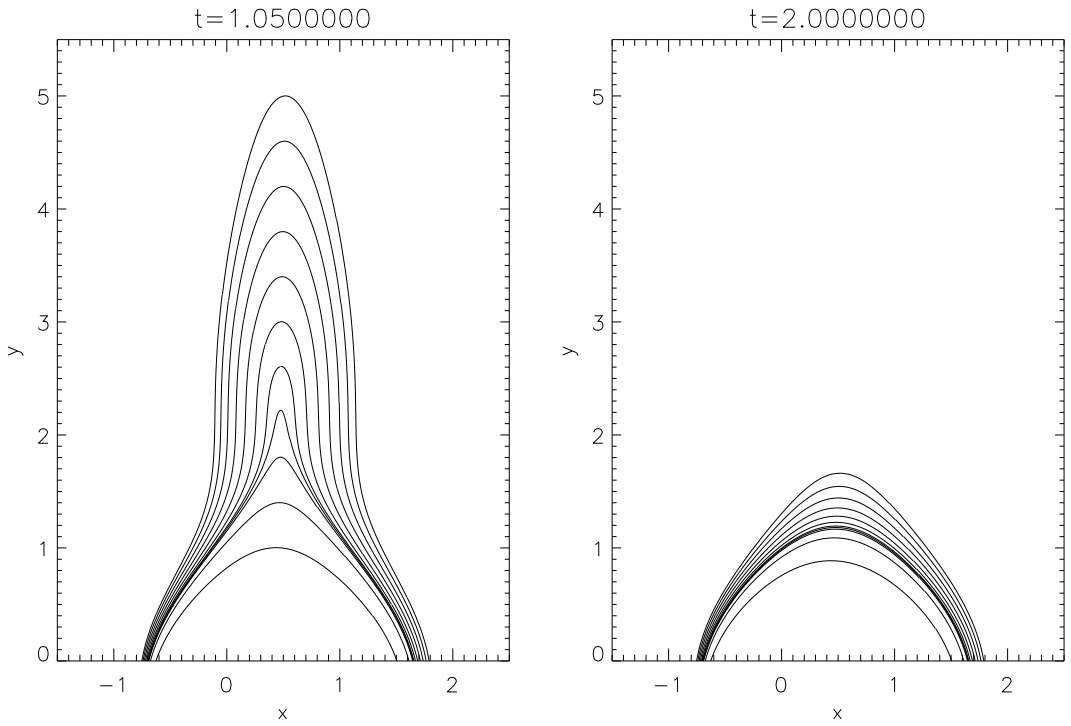

Figure 4.1: Field lines at the start and end of the trap collapse in the asymmetric trap discussed in this chapter. Note that the field lines on the left are closer than those on the right, indicating a stronger magnetic field at the left footpoint.

escape than before because this region is not close to the trap centre, so particles start on field lines outside the trap or in weak field regions. The asymmetry is very clear: on the left, where the field is stronger, particles mirror higher up and on the right more particles escape below the x axis. More particles escape to the photosphere on the right (7938 particles) rather than the left (1188). Also, the particles escaping on the right cover a larger region of the x axis. This is not surprising as the field lines here will be further apart than on the left.

The image also shows, for each of the starting positions, if any of the particles starting there are trapped. The result also fits with expectations, as particles starting at points far from the trap centre are not trapped.

These effects become more extreme with a larger asymmetry. Figure 4.3 shows particles starting in the same positions as above for a field where the right side charge has been moved to $d_2 = 2L$. In this case even less of the particles are trapped for the full time (220 particles), and the difference between the number escaping on the left (1782) and right (11308) is larger. Throughout the rest of this chapter only the asymmetric trap with $d_2 = 1.5L$ will be considered.

Because of the asymmetry, defining the trap centre accurately is more difficult. To compensate for this, there are more initial positions in the x direction. The other initial condition ranges are kept the same as the symmetric trap. A grid of 22 by 11 equidistantly spaced initial positions for $-0.5L \leq x \leq 1.6L$ and $1L \leq y \leq 5L$ is used (see diamond shaped symbols in Fig. 4.4). As in the symmetric trap, for each initial position particle orbits are calculated for 11 equally spaced values between 5 keV and 6 keV for the initial energy and 10 values for the initial pitch angle between 16° and 163°. In Fig. 4.4 the final positions of the particles remaining in the trap are shown as dots, with the colour bar showing the energy gain. Similarly to the symmetric trap this is based on, the highest energy particles are trapped in the loop top close to the trap centre. Again, many of the particles starting far away from the trap centre escape quickly. In Fig. 4.4 the red diamonds show that all the particles starting at that position escaped the trap before the trap collapsed. Although the final positions of particles look higher up in Fig. 4.4 compared to Fig. 2.2, this is really because the region of starting positions has been extended, hence particles starting further out are on field lines that are higher up at the trap centre.

In this asymmetric trap the particles go closer to the footpoint where the field is weaker (right side in Fig. 4.4). Also, for the particles that do escape (those on the x axis in the figure), the area they spread over is wider on the weaker right hand side. This is because the field lines they are on are further apart here.

Another way to look at how the initial conditions effect particle acceleration is to start particles with different pitch angles but all having the same initial energy from each position. This is shown in Figs. 4.5 and 4.6. Each box shows particles starting at different positions in the trap. The ratio of final/initial energy is plotted at the final trap time or at the time of escape. Red points indicate

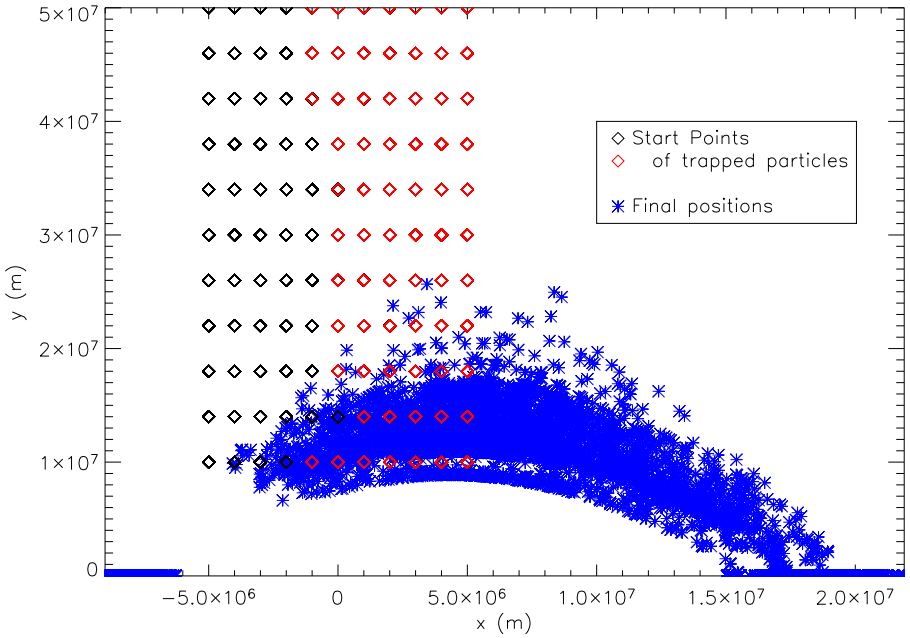

Figure 4.2: Particles starting in the same positions as in previous traps in the asymmetric trap with $d_2 = 1.5L$. Blue asterisks show where particles are after trap collapse.

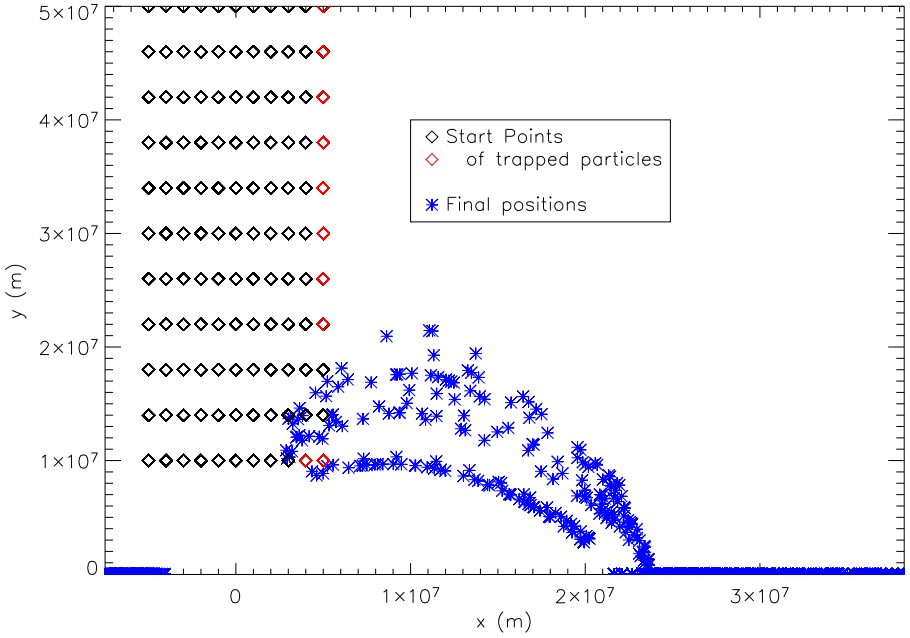

Figure 4.3: Particles in the trap with a large asymmetry in the magnetic field, given by moving the magnetic charge on the right further down to $d_2 = 2L$.

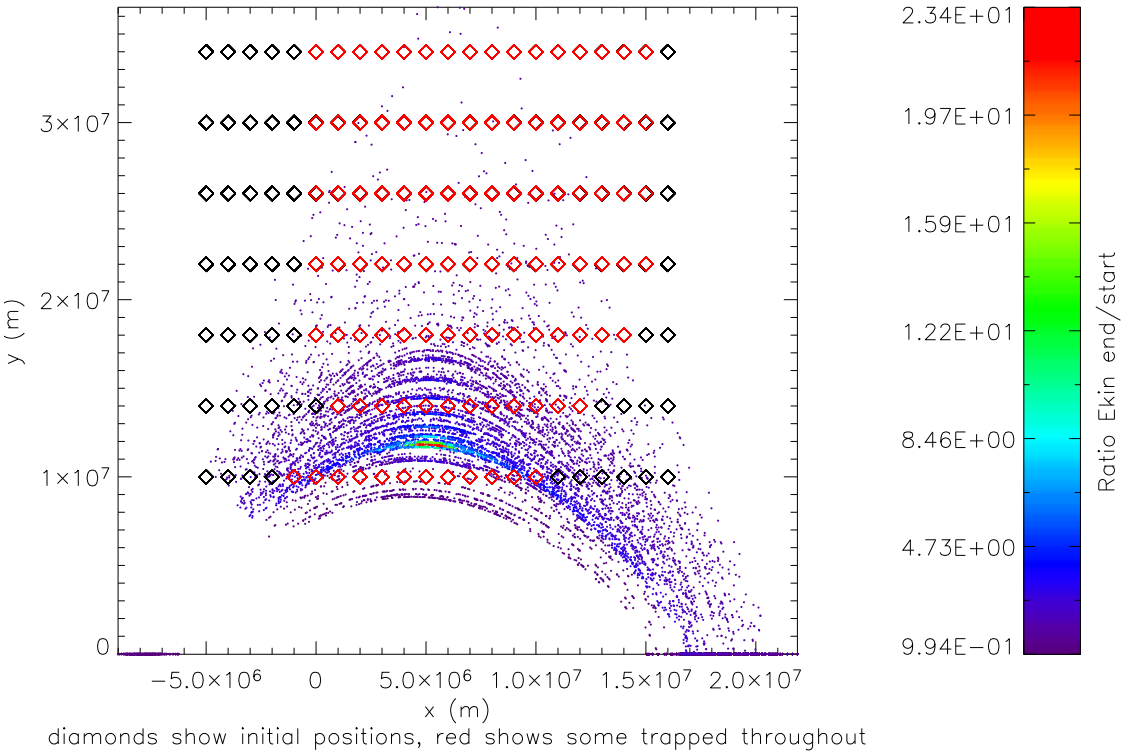

Figure 4.4: Positions of particles starting in the trap and their eventual positions once the trap collapses. Diamonds indicate particle injection points, red shows that at least one of the particles starting there with different initial conditions remains in the trap throughout. Final positions show the particles energy gain according to the colour scale.

escape from the trap. As with the symmetric trap, the maximum energy ratio is for particles starting near the trap centre with pitch angles close to 90°. Also as in the symmetric trap case, there is a secondary effect with 'wings' on these graphs when the pitch angle is more field aligned and the starting position is further from the trap centre. For these particles shown, the maximum ratio between final and initial energy is 24, giving a maximum final energy of 131keV.

4.2 Comparison between single particles in symmetric and asymmetric traps

It can be difficult to compare particle orbits between different trap models as the magnetic field strengths are of course different. In this section a particle that gains a high amount of energy in both traps is considered. In the asymmetric trap mentioned, the particle starts at $x = 0.5L, y = 2.2L, z = 1.25 \times 10^{-6}L$. This position corresponds to the highest energy gain shown in Fig. 4.5. At this point the contribution of the $\mathbf{E} \times \mathbf{B}$ drift to the energy is 9.8 eV. The particle is chosen to start with energy 5.5 keV and pitch angle 88.8°. The energy of this particle is shown in Fig. 4.7. This shows the final energy is about 130 keV. A close up of the first 0.2 s is shown in Fig. 4.8. This shows that the energy jumps up and is lost slowly - as seen to a greater extent with the previous symmetric trap - and that overall this causes the particle to gain energy. As in the symmetric trap, this is most noticeable at the start of the orbit.

For comparison, a particle from the symmetric trap studied in chapter 2 and by Giuliani et al. (2005) with a similar energy and pitch angle was also examined. This particle starts at position $x = 0L, y = 2.6L, z = 1.25 \times 10^{-6}L$ where the energy from the $\mathbf{E} \times \mathbf{B}$ drift is 8.5 eV. This particle has initial energy 5.5 keV and pitch angle 88.8°. In this case, on macroscopic timescales the particle loses energy to begin with, but after a short while gains again and ends up just short of 100 keV as shown in Fig. 4.9. The zoomed in image of energy until 0.2 seconds (Fig. 4.10) shows that energy is mostly lost over this time, but there is at least a periodic flattening in the graph, if not an increase, lasting for a short time in each bounce. Once the particle energy has passed its minimum both graphs of particles in symmetric and asymmetric traps have similar shapes.

There are also clear differences with individual particles trajectories and energy gains over time when compared to particles in a symmetric trap. Figure 4.11 shows the trajectory of the particle in the asymmetric trap. The particle goes far further towards the right footpoint than the left. This is not surprising as the field is weaker on the right, so it will need to travel further to get to the same strength of magnetic field. This effect causes the trap centre to move to the side as well as downward. For comparison, the orbit of the particle in the symmetric field is shown in figure 4.13. This orbit looks far more symmetric. Another difference between these two graphs is that the particle in the symmetric field moves far less along the x direction, even though both particles

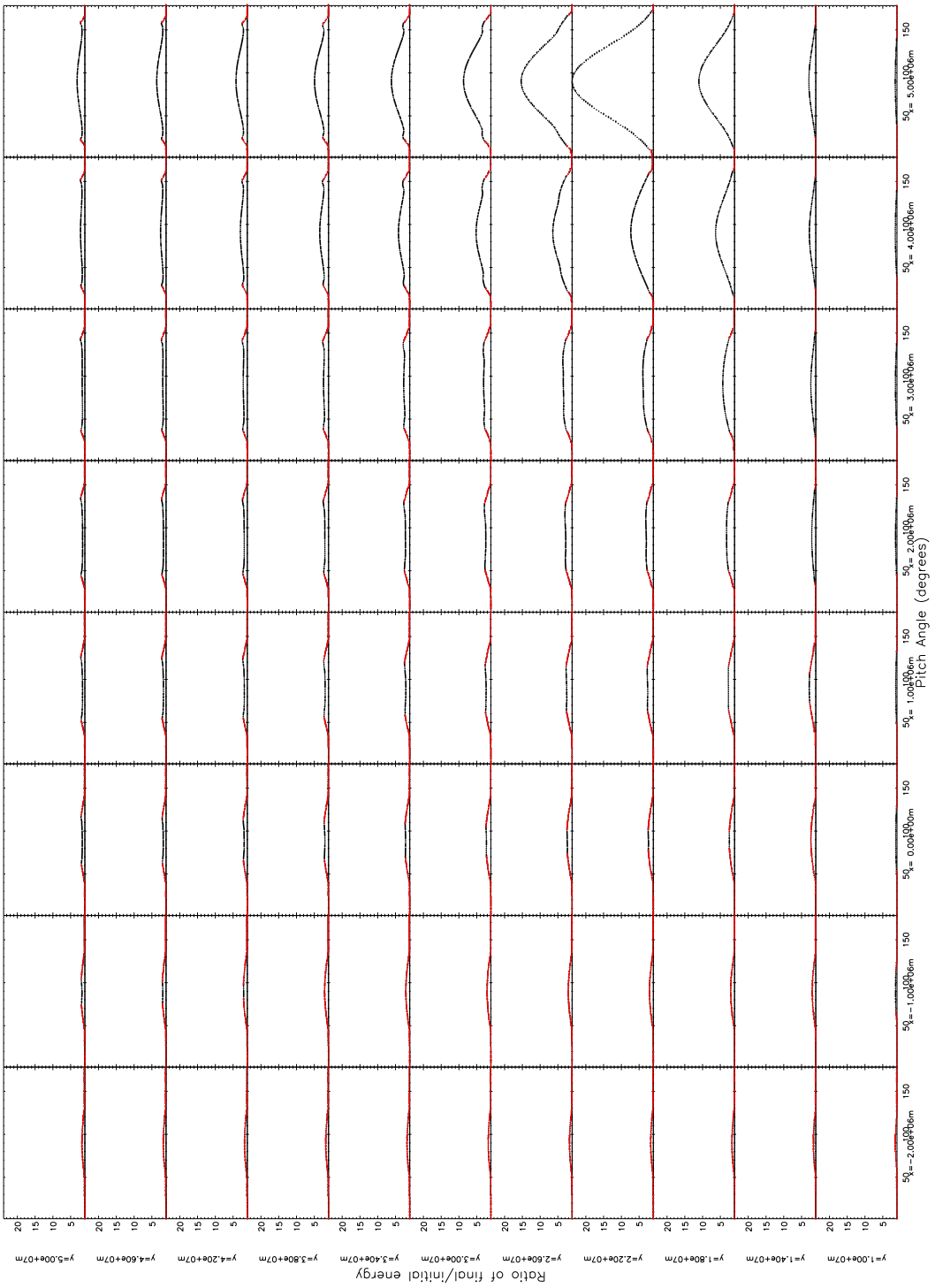

Figure 4.5: Each graph shows particles starting at a different position in x (from $-0.2L = -2 \times 10^6$ m to $0.5L = 0.5 \times 10^6$ m) and y ($1L = 10^7$ m to $5L = 5 \times 10^7$ m). At each of these positions, particles are started with different pitch angles and the energy gain of the particle (as a multiple of its initial energy) has either at its escape or after the trap collapses is shown. Particles that escape are shown in red. All particles have initial energy 5.5 keV. Particles starting further right are shown in Fig. 4.6.

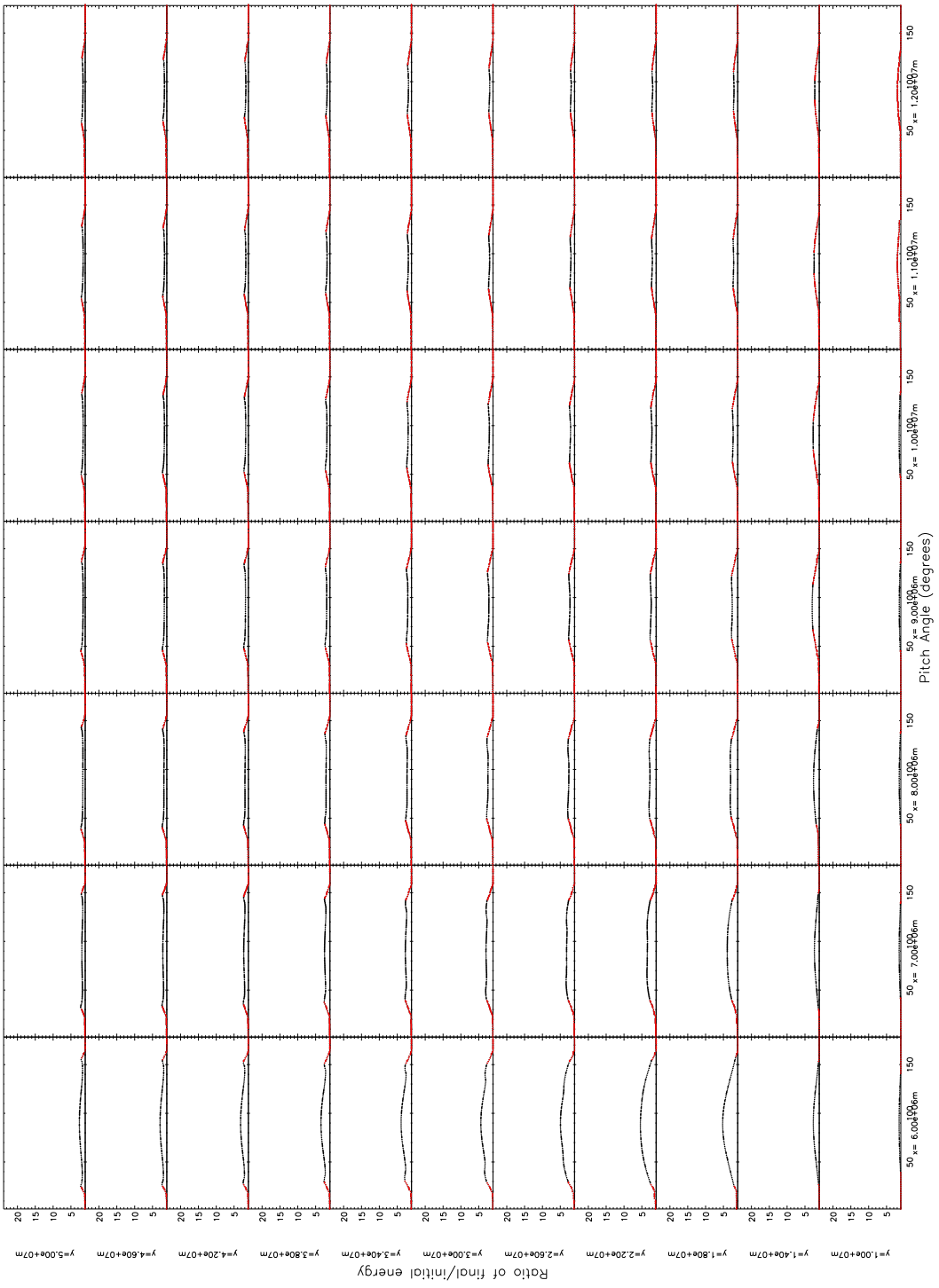

Figure 4.6: Graph showing energy gain of particles with different starting positions and pitch angles, for positions on the right of those in Fig. 4.5, this time the x range is from $0.6L = 6\times10^6$ m to $1.2L = 1.2 \times 10^7$ m.

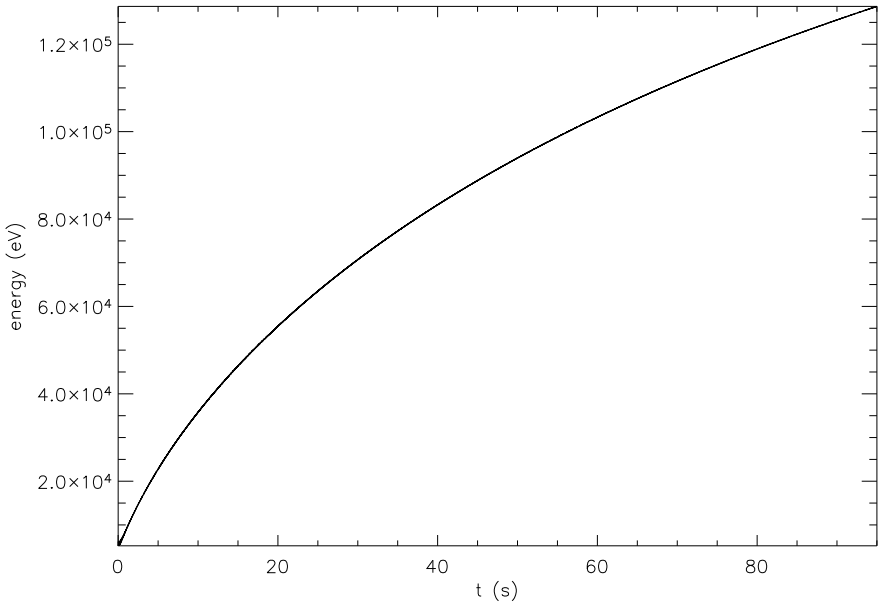

Figure 4.7: Energy of a particle in the asymmetric trap.

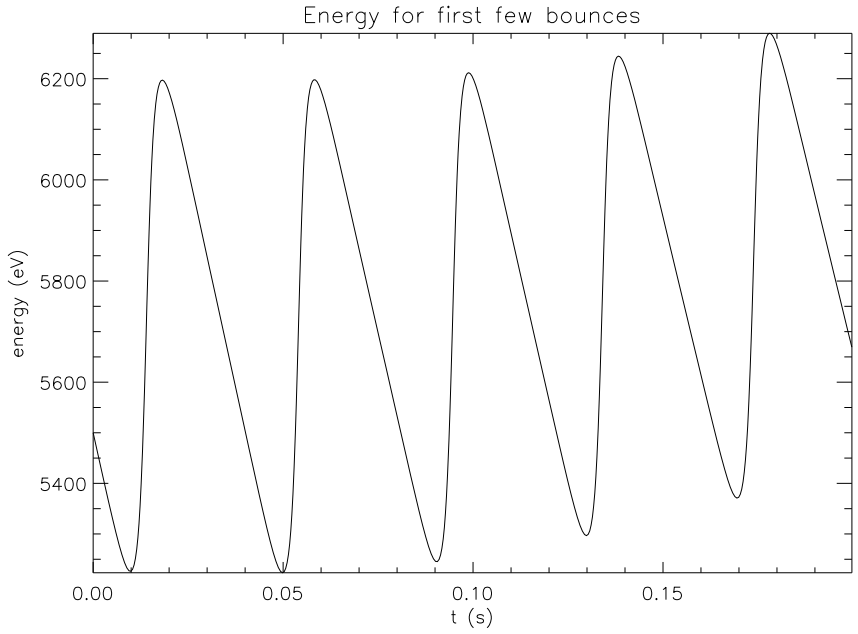

Figure 4.8: Energy of a particle in the asymmetric trap for the first 0.2 s of the trajectory showing energy gains are similar to the symmetric case investigated by Giuliani et al. (2005).

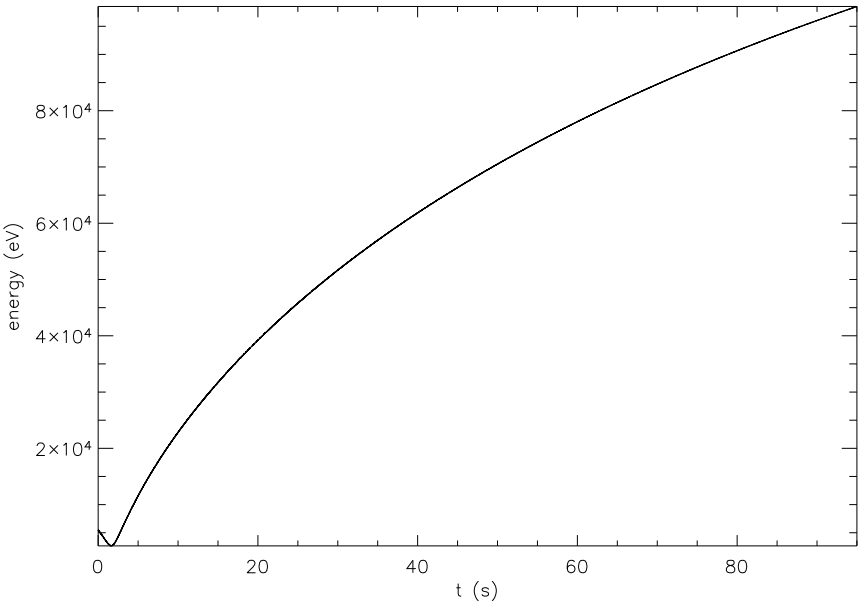

Figure 4.9: Energy of a particle in a symmetric trap.

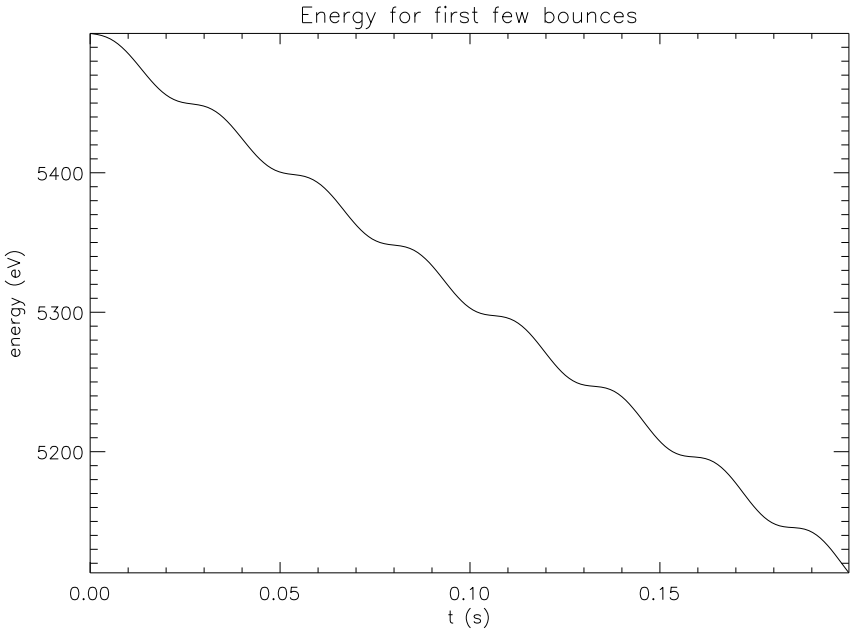

Figure 4.10: Energy of a particle in a symmetric trap for the first 0.2 s of the trajectory.

start with the same pitch angle. Another cause of the distance between bounce points being further apart in the asymmetric trap is that the orbit is more curved, due to a combination of the field line shape and the particle orbit going further to the left and right so covering more of the field line. This is shown more clearly in figures 4.12 and 4.14, which show only the first 0.2 seconds of the orbit for particle in the asymmetric and symmetric trap respectively.

4.3 Energy gain in the asymmetric trap

Asymmetries are also noticeable in the energy graph of individual particles in the trap. The right panel of Fig. 4.15 shows the energy of a particle in the asymmetric trap for the first 35 seconds. This specific particle has initial energy 5 keV and pitch angle $81.8°$, starting position $x = 0.1L, y = 3.8L$, although the results discussed in this section apply to many of the test particles that have been looked at.

To illustrate the energy gain processes, the graph is split into regions where the particle suddenly gains energy, shown in red and blue, and regions where the energy is slowly lost, shown in green and magenta. Only the first 35 seconds are shown as the energy gain and loss in this step like fashion is reduced and it is more difficult to pick out the different regions. The boundaries of the different sections are set to be the local minima and maxima in the energy. Looking at the sections where energy is lost, more energy is lost in the magenta sections than the green sections (ignoring the initial magenta region which the particle starts partway through) even though the green sections last for a longer time. The left panel of Fig. 4.15 can give some insight into this. Here it can be seen that the energy losses happen on the outer edges of the trap. The particle goes further towards the footpoint on the right which has a lower magnetic strength than the footpoint on the right. Travelling near the right mirror point corresponds to the green section in the energy graph which lasts longer than, and reduces the energy by less than, the magenta section on the left. The only time the particle gains energy is when it is in the centre of the orbit, again shown in blue and red. Having energy gain in this region only is difficult to interpret in the Fermi acceleration model, which would suggest that energy gain should be happening at the turning points if one takes the analogy of with the “moving walls” picture literally. Obviously, if this energy gain process really is to be interpreted as Fermi acceleration, one can only do this by averaging over a complete bounce period. Finally, the rest of the orbit of the particle in the trap is indicated in black, for completeness.

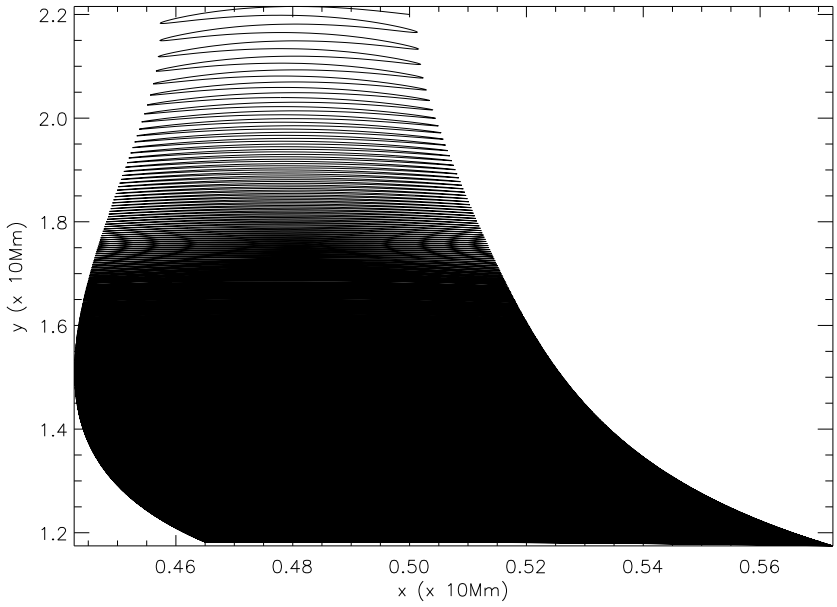

Figure 4.11: Particle motion in the asymmetric trap.

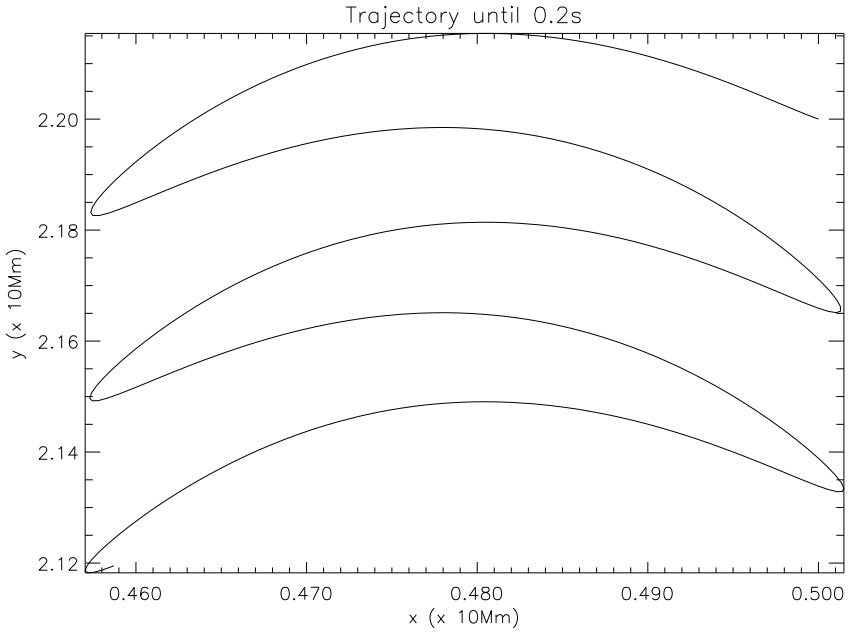

Figure 4.12: Particle motion in the asymmetric trap, first 0.2 seconds.

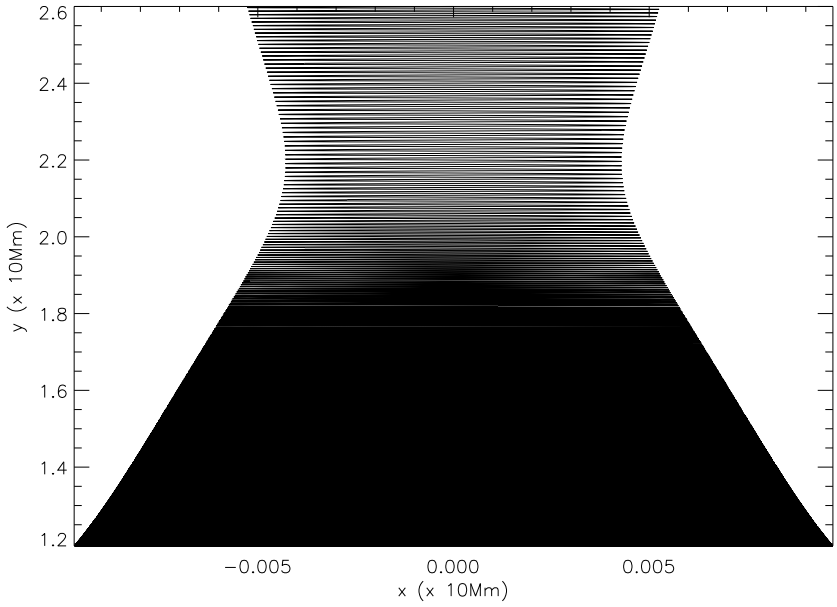

Figure 4.13: Particle motion in the symmetric trap.

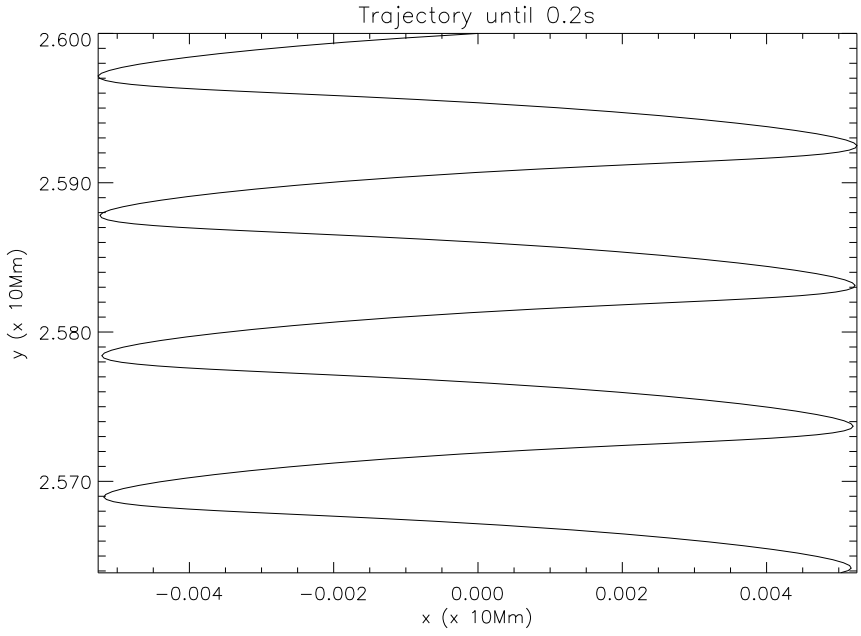

Figure 4.14: Particle motion in the symmetric trap, first 0.2 seconds.

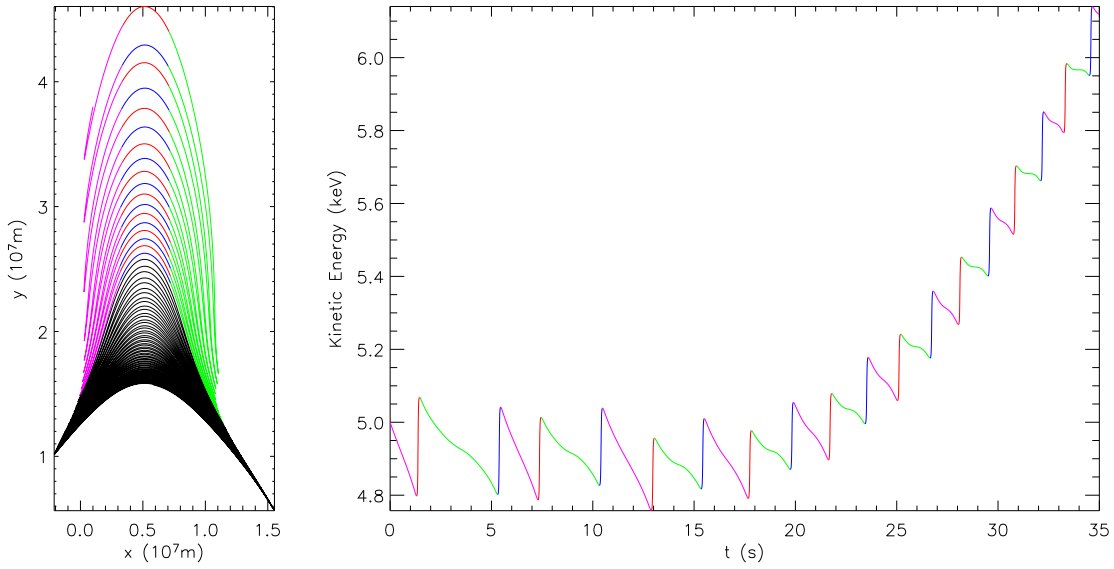

Figure 4.15: Particle motion and energy gain in an asymmetric trap. Red and blue sections are where the particle gains energy, green and magenta where energy is lost. See text for more details.

Chapter 5

Other collapsing trap magnetic field and flow models

All the field models considered so far are based on the magnetic field and velocity transformation from Giuliani et al. (2005). In this section a different way to construct the magnetic and velocity fields of a collapsing trap is considered. This will be used to demonstrate the general ability of CMTs to accelerate particles while highlighting possible differences in the physical operation of different CMT models.

In the previous chapters a magnetic field was given at a specified time and a time dependent transformation used to generate the time dependent velocity and magnetic fields. An alternative is to use a time-dependent flux function to define the electric and magnetic fields, calculating the velocity using the ideal Ohm's Law. This method was used by Minoshima et al. (2010) for a flare particle acceleration model.

5.1 Test particles in the Minoshima et al. magnetic field

Minoshima et al. (2010) consider a series of potential magnetic fields, rescaled as time progresses. It is worth noting here that because the field is always potential there is no excess energy in the magnetic field that could be transformed into the kinetic energy of particles. This is possible because the models are not self-consistent — the effect of single particle motion on the large scale flows is not considered, so the energy of all the particles is not directly related to the change in energy stored in the magnetic field.

The magnetic field used by Minoshima et al. (2010) is a two dimensional field with an X-type neutral line at height $z = a$. The field model was originally suggested as an analytical model of a

flare by Lin et al. (1995). The flux function for the field is given by

$$A_z(x,y) = \left[\frac{x+d}{x^2+(y+d)^2} + \frac{y}{(a+d)^3}\right] \tag{5.1}$$

in normalised form, which gives the magnetic field:

$$B_x(x,y) = -\frac{\partial A_z}{\partial y} = -\left[\frac{x^2-(y+d)^2}{\{x^2+(y+d)^2\}^2} + \frac{1}{(a+d)^2}\right], \tag{5.2}$$

$$B_y(x,y) = -\frac{\partial A_z}{\partial x} = -\frac{2x(y+d)}{\{x^2+(y+d)^2\}^2} \tag{5.3}$$

with d the depth of a dipole moment and a the height of the X-point on the y axis. This is shown in Fig. 5.1. The height a is assumed to be time dependent, allowing for the X-point to move upward. This mimics reconnection at the X-point. The field lines that were in the open regions on the sides change connectivity so more field lines are in the closed region. The equation of the separatrix can be worked out by equating $A_z(x,y) = A_z(0,a)$ and solving algebraically using a computer package. The actual solution is rather lengthy and adds little to the understanding, so it omitted here. The movement of the magnetic field lines makes the intersection of the separatrix with the photosphere appear to move. In the original paper by Lin et al. (1995) this was used to model the motion of Hα ribbons in a two-ribbon flare. The separatrix footpoints are at $x = \pm x_f$ and must be on the same field line as the X-point, hence $A_z(x_f,0) = A_z(0,a)$. Substituting these values into Eq. (5.1) gives

$$\frac{a}{d} = \left(\frac{x_f}{d} + \sqrt{\left(\frac{x_f}{d}\right)^2 + 1}\right)\frac{x_f}{d}. \tag{5.4}$$

The initial value of x_f is chosen so that $R = a/x_f = 1.7$ to correspond with observations. R is related to x_f by the equation

$$\frac{x_f}{d} = \frac{R^2-1}{2R}. \tag{5.5}$$

Time dependence is introduced to x_f and thus the magnetic fields by giving the apparent velocity of the footpoint positions a Gaussian profile,

$$\frac{\mathrm{d}x_f}{\mathrm{d}t} = v_p \exp\left[-\frac{1}{2}\left(\frac{t-t_p}{\tau}\right)^2\right]. \tag{5.6}$$

Because the magnetic field is time dependent, this can be used to calculate the associated electric field. As the electric field is perpendicular to the two-dimensional magnetic field, the electric field

is only

$$E_z(x,y) = -\frac{\partial A_z}{\partial t} = -\frac{\mathrm{d}x_f}{\mathrm{d}t}\frac{\partial a}{\partial x_f}\frac{\partial A_z}{\partial a} \tag{5.7}$$

The electric field gets stronger when $t < t_p$ (footpoint motion getting faster) and weaker when $t > t_p$ (when footpoint motion is slowing). I use the values for constants given by Minoshima et al. (2010), $\tau = 1.77$ s, $v_p = 6 \times 10^4$ m s^{-1} and $t_p = 5$ s with a total experiment time of 10 seconds.

Unlike Minoshima et al. (2010) I use the non-relativistic equations for particle motion. This is still reasonable as the maximum energy of test particles is of the order of 100 keV, much less than the rest mass of electrons, 511 keV. Minoshima et al. (2010) have initial conditions in the region below the X point, including open field lines. I only consider particles in the region of closed field lines – under the separatrix in Fig. 5.1.

For completeness, Fig. 5.2 shows an example particle orbit for a particle starting on an open field line which then reconnects, and becomes closed. The particle orbit is calculated in the same way as for all the other particles. This started at $x = 3.15, y = 12.15, z = 10$ Mm with energy 20.8 keV and pitch angle $90°$ (more precisely, $E_\parallel/E_\perp < 10^{-20}$). The energy of this particle jumps up as it crosses the separatrix at around $x = 0.0030, y = 14.44$Mm (in normalised units $x = 2.0587 \times 10^{-4}, y = 0.9631$; shown as the blue star in Fig. 5.2), where the field line reconnects. Another interesting point is that the particle goes below $y = 0$, so would escape into the photosphere.

Although Minoshima et al. (2010) mostly refer to solving the drift-kinetic Vlasov equation, many of their results can be found using test particles. To recreate the orbits of particles in the Minoshima et al. (2010) paper, particles are started at 11 equally spaced positions between $x = 0$ to 10.5 Mm and 11 equally spaced positions $y = 0$ to 13.5 Mm, all inclusive. Positions outside the closed field region are ignored, i.e. particles starting above the separatrix are not included. To do this, the equation for the separatrix was numerically calculated using Maple. The y position of the separatrix for the given x position of the particle is calculated and then compared to the y position of the particle.

At each initial point, particles start with 101 values for the pitch angle (between $0°$ and $180°$ exclusive), and 101 values of energy, linearly spaced between 0.5 keV and 102.2 keV inclusive.

As in Minoshima et al. (2010), particle orbits are calculated for 10 seconds, or until they have left the region by passing below $y = 0$.

The energy gain of particles (as a ratio between final and initial energy) in this trap seems not to be affected by the initial energy – the ratio between the final and initial energy depends only on the initial position and pitch angle. Figure 5.3 shows how different starting points and pitch angles

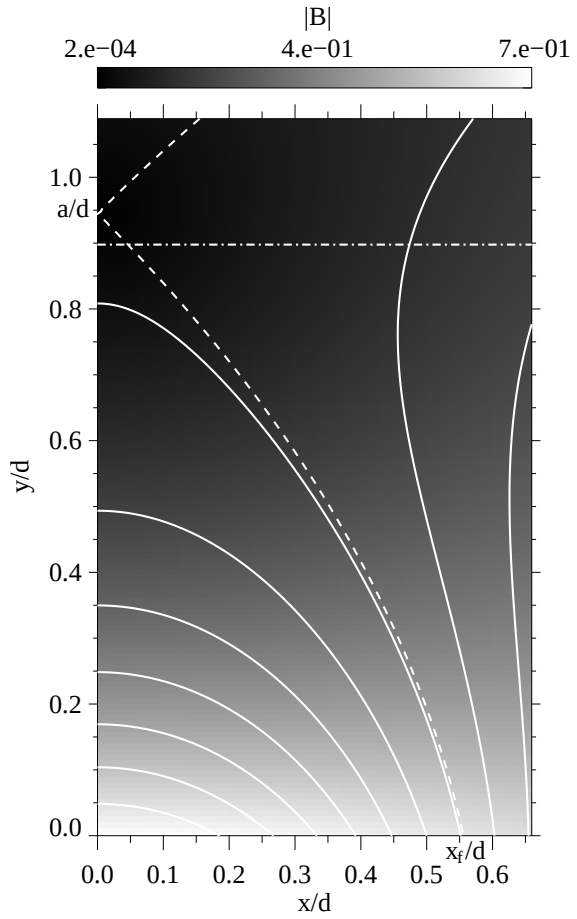

Figure 5.1: Magnetic field lines of the Minoshima model for time $t = 0$. Gray scale shows the magnetic field strength and the dashed line indicates the separatrices. Only one half of the configuration is shown due to symmetry. Minoshima et al. experiment in the region everywhere below the dot-dashed line. In this section only particles starting in the closed field region, below the dashed and dot-dashed lines, are considered. Image from Minoshima et al. (2010). Reproduced by permission of the AAS and T. Minoshima.

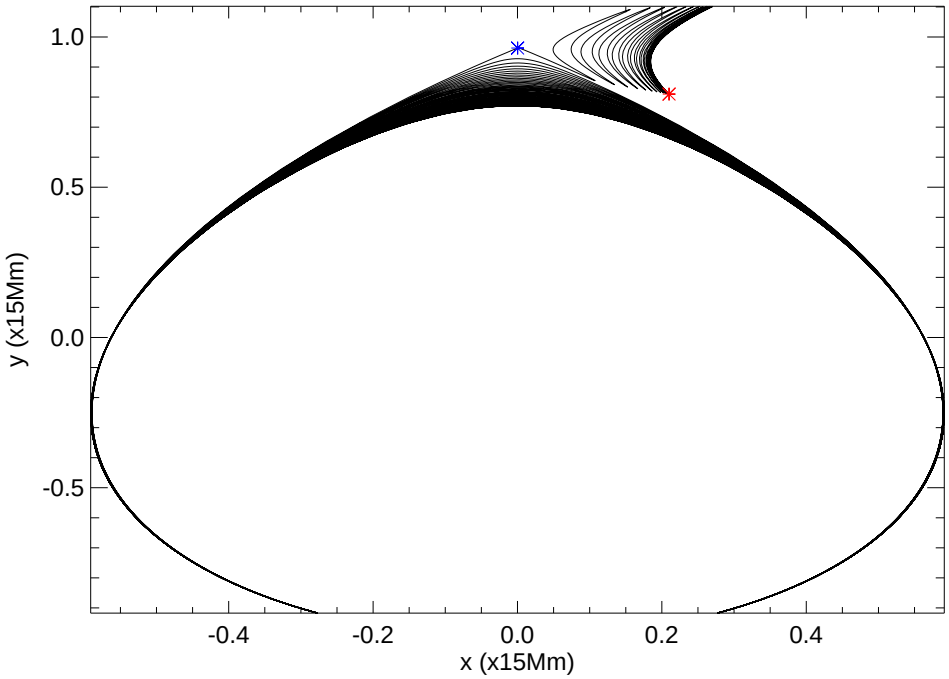

Figure 5.2: Orbit of a particle in the Minoshima et al. model. The initial position is shown in red. The particle starts on an open field line, which is brought inward and reconnects. This can be seen by the particle changing direction at the separatrix between the open and closed field line regions (shown in blue).

affect this energy ratio. Particles with initial pitch angles close to 90° are accelerated more than those with pitch angles close to 0° or 180°. Particles starting close to the centre and high up in the trap, in a weaker magnetic field and closer to the neutral line, are also accelerated more than elsewhere. For the particles studied, the maximum ratio between final and initial energy is 7.12.

However, I still do not find the straightforward relation between these quantities that Bogachev and Somov (2005) describe, i.e. that energy at escape time is given by the equation

$$E_{final} = E_0(B_m/B_0)\sin^2\alpha_0 \tag{5.8}$$

where E_0 is the initial energy, α_0 is the initial pitch angle and B_m and B_0 are the magnetic fields at the mirror/escape points and initially, respectively. (See introduction and section 2.3.3 for more details.) To examine this I use the magnetic field at the final time (either escape or at 10 seconds) as B_m and all other quantities as described. This gives an estimated value for the final energy, which appears as a lower bound when plotted with the energy calculated by the particle orbit as in Fig. 5.4

Particles that remain in the trap gain more energy than those escaping. After 10 s, the particles with the highest energy gain in the trap are on field lines that are high up in the region, towards the centre. This is shown in figure 5.5.

The general model presented by Giuliani et al. (2005) allows for more control than the Minoshima et al. (2010) model. With the Giuliani et al. (2005) model, the magnetic and velocity fields can be chosen, then the electric field is calculated using the ideal Ohm's law. The Minoshima et al. (2010) model requires only a time dependent flux function and the magnetic and electric fields follow automatically as spatial (for magnetic field) and temporal (for electric field) derivatives of the flux function.

A shortcoming of the Minoshima et al. (2010) model is that the resulting velocity field is singular at the X-point at $x = 0, y = a$. This is justified by Minoshima et al. (2010) by only examining a region below the X-point where the $\mathbf{E}\times\mathbf{B}$ drift is less than 2000 km s^{-1} (a typical Alfvén velocity in the corona).

In both Minoshima et al. (2010) and this chapter, higher energy particles are found at the top of the closed loops (under the X-point). This is similar to the other traps examined in this thesis where the higher energy particles are trapped at the loop top by the time the trap collapses.

By comparing the magnetic field at the loop top at the final and initial times, the compression ratio for this trap was found to be ~ 6 by Minoshima et al. (2010). This corresponds well with the maximum energy gain of around 7 that I find for particles with pitch angle $\sim 90°$ at the loop top. In the traps discussed elsewhere in this thesis the compression ratio is much larger (~ 50), and the

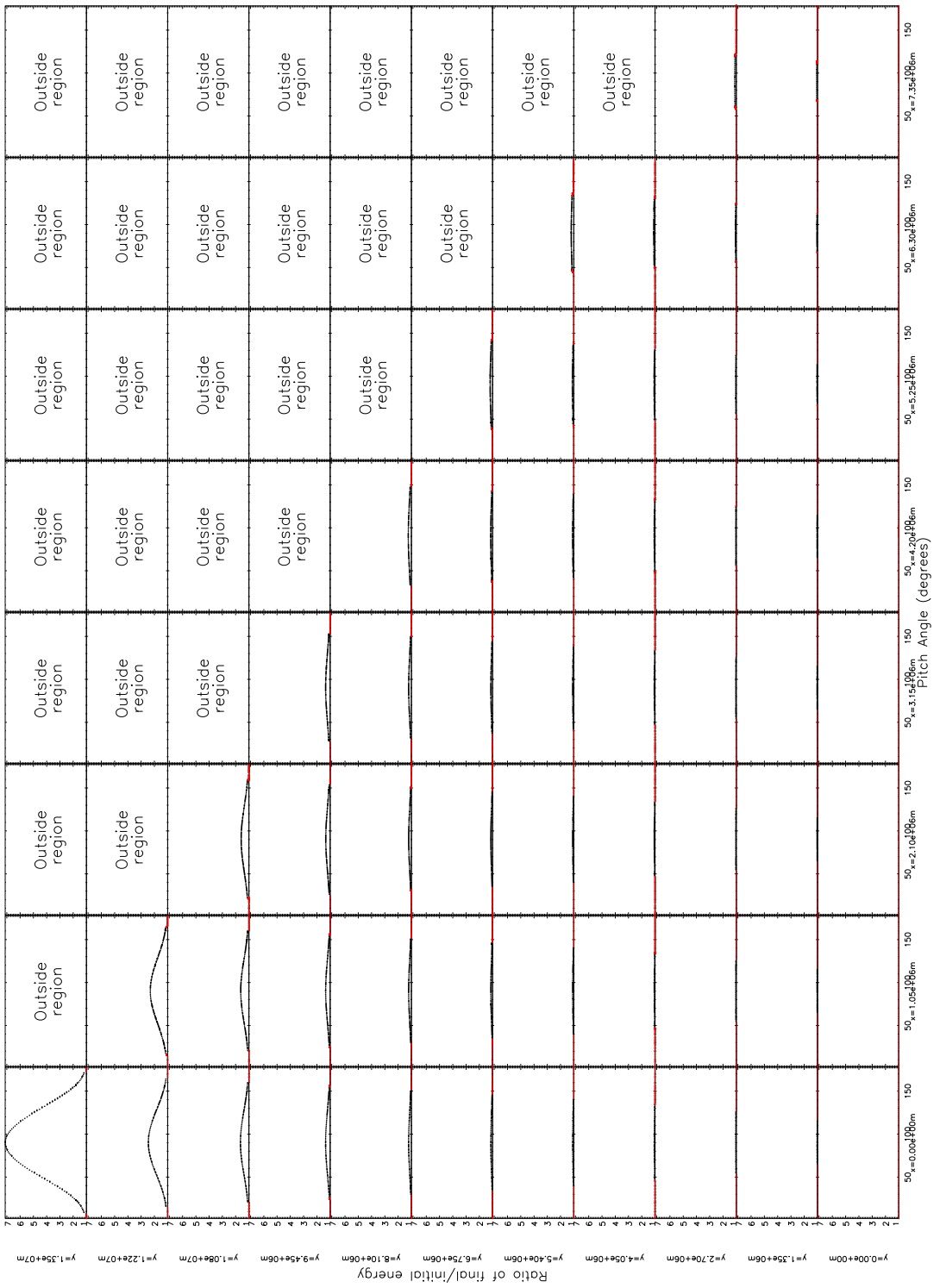

Figure 5.3: Each graph shows the energy gain ratio (final/initial kinetic energy) as a function of pitch angle for particles starting at a specific point. Particles with pitch angles close to 90° gain more energy, as do particles starting higher and more central to the trap. The maximum energy ratio achieved was 7.12.

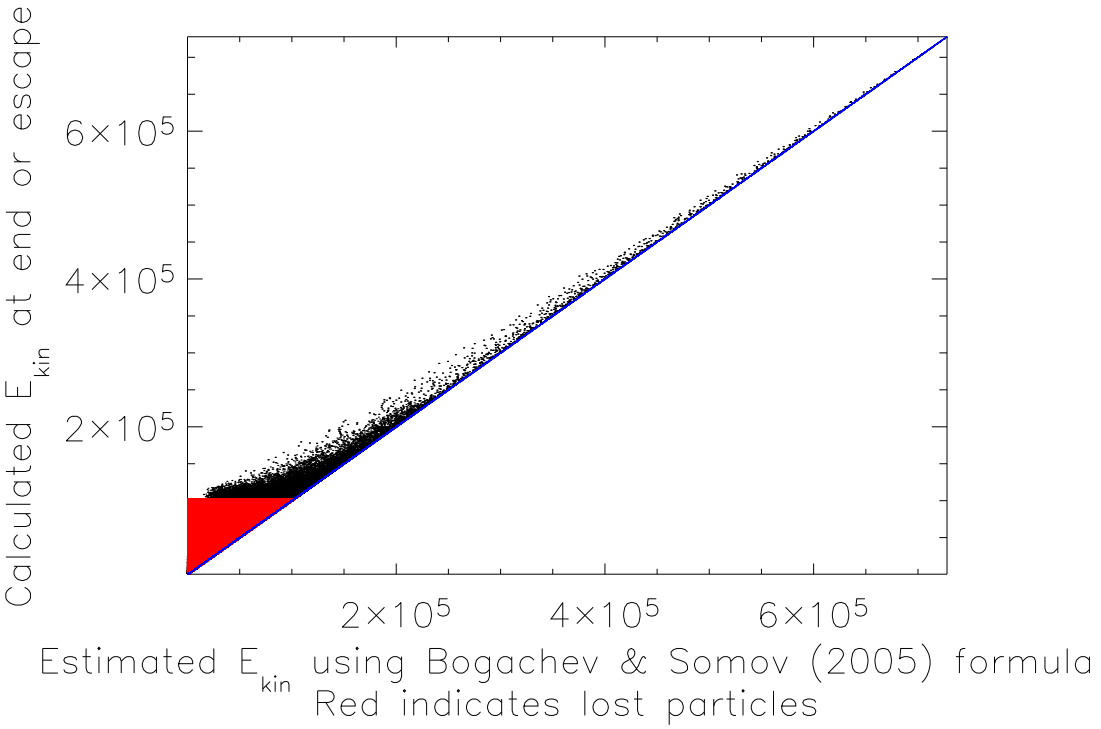

Figure 5.4: Estimated final energy, as calculated using the formula in Bogachev and Somov (2005) and final energy as calculated by the particle orbit. Red points indicate particles that escape before 10 s, so are measured at escape time. The blue line shows where the estimated and actual energies are the same, and shows that the actual energy is greater than or equal to the estimate.

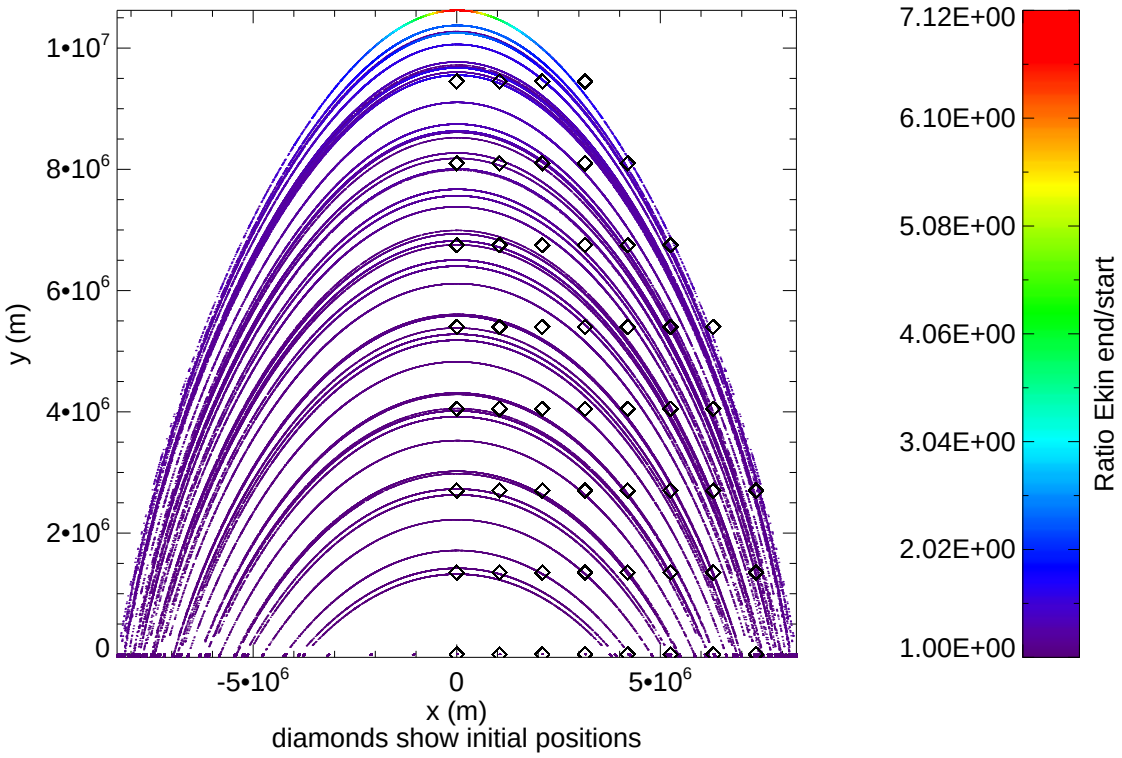

Figure 5.5: Final positions of particles in the Minoshima et al. trap. The colour scale indicates the ratio of final to initial energy. Particles that have the highest energy gains remain in the trap and on higher up field lines towards the centre. Diamonds show the initial positions of particles.

particle energy gain roughly scales with this, as would be expected for the betatron effect.

Until this point all the velocity fields have had components in only two directions. In the next chapter I look at collapsing traps with velocity fields that are fully three dimensional.

Chapter 6

Extending CMT models to 2.5 and 3D

This chapter is based on work published in Astronomy and Astrophysics, Volume 508, Issue 3, 2009, pp.1461-1468 (Grady and Neukirch 2009).

6.1 Introduction

The purpose of this chapter is to extend the theoretical framework for kinematic MHD CMT models given by Giuliani et al. (2005) to 2.5D models with flow in the invariant direction and to fully three-dimensional models. This is necessary for a number of reasons:

1. The theory of kinematic MHD CMTs as developed so far by Giuliani et al. (2005) only allows for a magnetic field component in the invariant direction, but not for a component of the flow velocity in this direction. Without this component of the flow velocity the magnetic field component in the invariant direction can only increase in a CMT due to magnetic flux conservation. It is, however, to be expected that during a flare magnetic shear will be reduced rather than increased and therefore the introduction of a component of the flow velocity in the invariant direction is a necessary extension to be able to make the 2.5D models more realistic.

2. In the 2D cases investigated earlier in this thesis and by Giuliani et al. (2005), due to the spatial symmetry, the electric field does not vary in the invariant direction and this may have an influence on the acceleration process. It is therefore important to investigate the differences of the acceleration process between 2D models and non-symmetric 3D CMT models in the future.

3. Giuliani et al. (2005) have already discussed a possible way of extending the 2D theory to

three dimensions using Euler potentials. While Euler potentials allow a relatively straightforward extension of the theory to 3D by simple analogy to the 2D case, they are not easy to use in the modelling process, which is already intrinsically more difficult in three dimensions. I therefore present in this chapter an extension to the theory which makes it possible to avoid the explicit calculation of Euler potentials and uses the magnetic field directly.

This chapter is organised as follows. In Sect. 6.2 I briefly summarise again the present state of the kinematic MHD theory of CMTs, before presenting its extensions to 2.5D with shear flow and to 3D. In Sect. 6.3 a couple of illustrative examples of CMT models based on the new theoretical descriptions are shown, followed by examples of test particle calculations in Sect. 6.4. A summary and some conclusions are given in Sect. 6.5 with a summary and conclusions. Lastly, to link with work by Giuliani et al. (2005) on Euler Potentials, Appendix A gives more detail of the calculation of the 3D field using Euler Potentials.

6.2 Basic Theory

6.2.1 Kinematic MHD Models of CMTs in 2.5D without shear flow

The theory of CMT models in 2.5D without shear flow is discussed by Giuliani et al. (2005) and reviewed in Sect. 2.2 of this thesis. As this theory is a basis for the extensions to 2.5D with shear flow and fully 3D models, some of the points are reiterated here.

The ideal kinematic MHD equations may be used to describe the evolution of the electromagnetic field

$$\mathbf{E} + \mathbf{v} \times \mathbf{B} = \mathbf{0}, \tag{6.1}$$

$$\frac{\partial \mathbf{B}}{\partial t} = -\nabla \times \mathbf{E}, \tag{6.2}$$

$$\nabla \cdot \mathbf{B} = 0, \tag{6.3}$$

with the MHD velocity $\mathbf{v}$ assumed to be given as a function of space and time. I will also make occasional use of the ideal induction equation

$$\frac{\partial \mathbf{B}}{\partial t} = \nabla \times (\mathbf{v} \times \mathbf{B}), \tag{6.4}$$

which results from combining Eqs. (6.1) and (6.2).

For the 2.5D cases, the magnetic field can be written in terms of a flux function, A,

$$\mathbf{B} = \mathbf{B}_p + B_z \mathbf{e}_z = \nabla A \times \mathbf{e}_z + B_z \mathbf{e}_z. \tag{6.5}$$

There is no flow in the invariant direction in this case, so

$$\mathbf{v}_2(x, y, t) = (v_x(x, y, t), v_y(x, y, t), 0). \tag{6.6}$$

As I will make use of this particular velocity field later on, I use the index 2 to distinguish it from the full velocity field with non-zero v_z. The time evolution of B_z can be found using the induction equation (6.4).

$$\frac{\partial B_z}{\partial t} + \nabla \cdot (\mathbf{v}_2 B_z) = 0, \tag{6.7}$$

i.e., conservation of the magnetic flux.

Rather than directly specifying a velocity field I use a transformation between Lagrangian coordinates X, Y and Eulerian coordinates x, y:

$$X = X(x, y, t), \qquad Y = Y(x, y, t), \tag{6.8}$$

The flux function A_0 can be given at a specified time, $t = t_0$ and the flux function for all other times calculated using

$$A(x, y, t) = A_0(X(x, y, t), Y(x, y, t)). \tag{6.9}$$

The B_x and B_y follow from Eq. (6.5). Using the Jacobian determinant J for the coordinate transformation, the B_z equation can be written in the form

$$B_z(x, y, t) = JB_{0z}(X(x, y, t), Y(x, y, t)), \tag{6.10}$$

where $B_{0z}(X, Y)$ is B_z at the same reference time $t = t_0$.

6.2.2 Extension to 2.5D with shear flow

To allow the effect of shearing and unshearing of the magnetic field to be taken into account it is necessary to have a non-zero $v_z(x, y, t)$. The basic effect of a non-zero v_z is to add a source term to equation (6.7)

$$\frac{\partial B_z}{\partial t} + \nabla \cdot (\mathbf{v}_2 B_z) = \nabla \cdot (v_z \mathbf{B}_p)\,. \tag{6.11}$$

The source term on the right-hand-side of Eq. (6.11) destroys the separate conservation of magnetic flux in the z-direction, because a non-zero v_z allows B_x and B_y to by turned into B_z and vice versa. In addition to the transformation equations for the x- and y-coordinates one has to add a

transformation equation for the z-coordinate of the form

$$Z = z + \bar{Z}(x, y, t). \tag{6.12}$$

The general solution for the flux function remains the same, but the solution for B_z becomes more complicated. As it is much easier to deduce the solution for B_z as a special case from the 3D case discussed next, I will give the appropriate expressions for B_z and the velocity field after discussing the general theory for three dimensions.

6.2.3 Extension to 3D

As already pointed out by Giuliani et al. (2005), one can in principle use a similar approach as for 2D to generalise the theory to 3D. Instead of writing the magnetic field in terms of a flux function A, I use Euler Potentials to satisfy the solenoidal condition (6.3) (see e.g. Stern 1970, 1987):

$$\mathbf{B} = \nabla\alpha \times \nabla\beta. \tag{6.13}$$

When using Euler potentials one has to assume that the magnetic topology of the CMT is sufficiently simple to allow the global existence of a set of Euler potentials satisfying Eq. (6.13) for all positions and times (see e.g. Moffatt 1978, for a discussion). Using Euler potentials in an appropriate gauge, Ohm's law (6.1) can be written as (e.g. Stern 1970)

$$\frac{\partial\alpha}{\partial t} + \mathbf{v}\cdot\nabla\alpha = 0, \tag{6.14}$$

$$\frac{\partial\beta}{\partial t} + \mathbf{v}\cdot\nabla\beta = 0, \tag{6.15}$$

and the solutions of Eqs. (6.14) and (6.15) are given by

$$\alpha(\mathbf{x}, t) = \bar{\alpha}(\mathbf{X}(\mathbf{x}, t)), \tag{6.16}$$

$$\beta(\mathbf{x}, t) = \bar{\beta}(\mathbf{X}(\mathbf{x}, t)), \tag{6.17}$$

where, as in the 2D solution $\bar{\alpha}(\mathbf{X})$ and $\bar{\beta}(\mathbf{X})$ are the Euler potentials at a reference time $t = t_0$. This need not be the initial time, Giuliani et al. (2005) use the final time as reference time and I shall also use this. As in the 2D case a transformation between Eulerian ($\mathbf{x}$) coordinates and Lagrangian ($\mathbf{X}$) coordinates is assumed as given in the form

$$\mathbf{X} = \mathbf{X}(x, y, z, t), \tag{6.18}$$

where the transformation equations for the three coordinates have been combined into a vector

$$\mathbf{X} = (X(x, y, z, t), Y(x, y, z, t), Z(x, y, z, t))$$

for ease of reference. For completeness, the full derivation of the expression for the magnetic field using Eqs. (6.16) and (6.17) is shown in Appendix A. The result is given by the equations

$$B_x = \left(\frac{\partial \mathbf{X}}{\partial y} \times \frac{\partial \mathbf{X}}{\partial z}\right) \cdot \mathbf{B}_0\left(\mathbf{X}\right), \tag{6.19}$$

$$B_y = \left(\frac{\partial \mathbf{X}}{\partial z} \times \frac{\partial \mathbf{X}}{\partial x}\right) \cdot \mathbf{B}_0\left(\mathbf{X}\right), \tag{6.20}$$

$$B_z = \left(\frac{\partial \mathbf{X}}{\partial x} \times \frac{\partial \mathbf{X}}{\partial y}\right) \cdot \mathbf{B}_0\left(\mathbf{X}\right). \tag{6.21}$$

It is important to note that this result is expressed completely in terms of derivatives of the transformation equations and the magnetic field at the reference time $t = t_0$,

$$\mathbf{B}_0 = \mathbf{B}_0\left(x, y, z\right), \tag{6.22}$$

i.e. no reference to Euler potentials has to be made when modelling CMTs in 3D. This is no surprise as the same result can also be found without the use of Euler potentials (see e.g. Moffatt 1978, p. 44), but using Euler potentials makes the transition from 2D to 3D a bit more obvious. While Euler potentials are often very useful for gaining better theoretical insight (e.g. Stern 1970; Hesse and Schindler 1988; Hesse et al. 2005), they are usually quite difficult to use for modelling purposes (e.g. Platt and Neukirch 1994; Romeou and Neukirch 1999, 2002). Also, due to this result the conditions for the global existence of Euler potentials do not apply for the modelling of 3D CMTs and the modelling process is thus much less restrictive. It is therefore very beneficial to have a formulation which is based purely on the magnetic field at the reference time and on the transformation equation (6.18), both of which can be chosen freely.

From the transformation equation (6.18), one can calculate the flow velocity by using that

$$\frac{d\mathbf{X}}{dt} = \frac{\partial \mathbf{X}}{\partial t} + \left(\mathbf{v} \cdot \nabla\right) \mathbf{X} = \mathbf{0}, \tag{6.23}$$

from which one can calculate the velocity $\mathbf{v}$ by inversion of the non-singular 3×3 matrix $\nabla \mathbf{X}$, giving

$$\mathbf{v}(x, y, z, t) = -(\nabla \mathbf{X})^{-1} \cdot \frac{\partial \mathbf{X}}{\partial t}. \tag{6.24}$$

I refrain from giving the complete explicit form of the velocity field here, as it is rather lengthy and not too instructive. Finally, knowledge of the flow velocity and the magnetic field allows the calculation of the electric field from Ohm's law (6.1).

6.2.4 Derivation of the 2.5D case with shear flow formulae from the 3D case

I will now come back to the 2.5D case with shear flow. The transformation equation (6.12) for the z-coordinate implies that

$$\frac{\partial \mathbf{X}}{\partial z} = (0, 0, 1)\,. \tag{6.25}$$

Using Eq. (6.21), the z-component of the magnetic field for the 2.5D case with shear is given by

$$\begin{aligned} B_z(x,y,t) &= \left(\frac{\partial Y}{\partial x}\frac{\partial \bar{Z}}{\partial y} - \frac{\partial \bar{Z}}{\partial x}\frac{\partial Y}{\partial y}\right) B_{0x}\left(\mathbf{X}\right) \\ &\quad + \left(\frac{\partial \bar{Z}}{\partial x}\frac{\partial X}{\partial y} - \frac{\partial X}{\partial x}\frac{\partial \bar{Z}}{\partial y}\right) B_{0y}\left(\mathbf{X}\right) \\ &\quad + \left(\frac{\partial X}{\partial x}\frac{\partial Y}{\partial y} - \frac{\partial Y}{\partial x}\frac{\partial X}{\partial y}\right) B_{0z}\left(\mathbf{X}\right). \end{aligned} \tag{6.26}$$

The last term of Eq. (6.26) is identical to the 2.5D solution for B_z without shear flow given in Eq. (6.10). The other two terms represent the extra possibility of turning B_x or B_y flux into B_z flux and vice versa.

The velocity field can be determined by using the transformation equations for the 2.5D case with shear flow in Eq. (6.23). This gives the components of the velocity as

$$v_x = \left(-\frac{\partial X}{\partial t}\frac{\partial Y}{\partial y} + \frac{\partial X}{\partial y}\frac{\partial Y}{\partial t}\right)\left(\frac{\partial X}{\partial x}\frac{\partial Y}{\partial y} - \frac{\partial Y}{\partial x}\frac{\partial X}{\partial y}\right)^{-1}, \tag{6.27}$$

$$v_y = \left(-\frac{\partial X}{\partial x}\frac{\partial Y}{\partial t} + \frac{\partial X}{\partial t}\frac{\partial Y}{\partial x}\right)\left(\frac{\partial X}{\partial x}\frac{\partial Y}{\partial y} - \frac{\partial Y}{\partial x}\frac{\partial X}{\partial y}\right)^{-1} \text{ and} \tag{6.28}$$

$$\begin{aligned} v_z &= -\frac{\partial \bar{Z}}{\partial t} - \left[\frac{\partial \bar{Z}}{\partial x}\left(-\frac{\partial X}{\partial t}\frac{\partial Y}{\partial y} + \frac{\partial X}{\partial y}\frac{\partial Y}{\partial t}\right)\right. \\ &\quad \left. + \frac{\partial \bar{Z}}{\partial y}\left(-\frac{\partial X}{\partial x}\frac{\partial Y}{\partial t} + \frac{\partial X}{\partial t}\frac{\partial Y}{\partial x}\right)\right]\left(\frac{\partial X}{\partial x}\frac{\partial Y}{\partial y} - \frac{\partial Y}{\partial x}\frac{\partial X}{\partial y}\right)^{-1}. \end{aligned} \tag{6.29}$$

Again, the electric field can be calculated from Ohm's law (6.1), once the velocity field and the magnetic field are known. The electric field in the invariant direction is

$$E_z = \frac{(\frac{\partial X}{\partial y}\frac{\partial Y}{\partial t} - \frac{\partial Y}{\partial y}\frac{\partial X}{\partial t})(\frac{\partial X}{\partial x}B_{0y} - \frac{\partial Y}{\partial y}B_{0x}) - (\frac{\partial Y}{\partial x}\frac{\partial X}{\partial t} - \frac{\partial X}{\partial x}\frac{\partial Y}{\partial t})(\frac{\partial Y}{\partial x}B_{0x} - \frac{\partial X}{\partial y}B_{0y})}{\frac{\partial Y}{\partial x}\frac{\partial X}{\partial y} - \frac{\partial X}{\partial x}\frac{\partial Y}{\partial y}}. \tag{6.30}$$

Electric fields in the x and y directions can also be calculated, but produce more complicated expressions.

6.3 Illustrative Examples of Collapsing Trap Models

I shall discuss some simple illustrative examples of CMTs in 2.5D with shear flow and in 3D. The main purpose here is to compare some of the features of these extended models with the results found by Giuliani et al. (2005) for 2D models. Therefore, I shall use one of the transformations used by Giuliani et al. (2005). It is not suggested that these examples can be regarded as realistic models of a flare, but they offer some insight into the basic features of 2D and 3D collapsing trap models.

6.3.1 An illustrative example for a 2.5D CMT model with shear flow

Firstly, a shear flow is added to the main example presented in Giuliani et al. (2005) and discussed in section 2.2. The 2D magnetic field is generated using the flux function

$$A_0 = c_1 \arctan\left(\frac{y_0 + d/L}{x_0 + 1/2}\right) - c_1 \arctan\left(\frac{y_0 + d/L}{x_0 - 1/2}\right), \tag{6.31}$$

as before. This represents a loop between two line currents at $x_0 = \pm L/2$, i.e. separated by a distance L and placed at a distance $y_0 = -d$ below the photosphere. The magnetic field generated by the flux function (6.31) is potential if regarded as a function of x_0 and y_0. This potential field is the final field to which the CMT relaxes as $t \to \infty$. In the model presented in this section, the magnetic field in the z-direction is set to zero, $B_z = 0$, as $t \to \infty$.

At other times, the magnetic field will be non-potential and I shall choose a coordinate transformation which gives an initially sheared magnetic field, i.e. with $B_z \neq 0$. To ensure continuity from the model of Giuliani et al. (2005) to this model the transformations of the x- and y-coordinates are the same as in their paper and chapter 2,

$$x_0 = x, \tag{6.32}$$

$$y_0 = (at)^b \ln\left[1 + \frac{y}{(at)^b}\right]\left\{\frac{1 + \tanh[(y - L_v/L)a_1]}{2}\right\} + \left\{\frac{1 + \tanh[(y - L_v/L)a_1]}{2}\right\} y, \tag{6.33}$$

i.e. Eqs. (2.19) and (2.19) from before. The same parameter values mentioned in Sect. 2.2 are also reused. For simplicity, the transformation depends on time only through the function $y_0(y, t)$. This time-dependence lets the field collapse to the final field described above as for $t \to \infty$, y_0 tends to y. Other important features of the transformation are that the foot points of magnetic field lines do not move during the collapse because on $y = 0$, $y_0 = 0$ for all t.

The important difference to the model used by Giuliani et al. (2005) is that I introduce an additional

transformation for the z-coordinate which produces a shearing flow as discussed above. The transformation for the z-coordinate is chosen as

$$z_0 = z + \delta\,[y_0(y,t) - y]\,\frac{x}{a_{2.5\mathrm{D}}^2 + x^2}, \tag{6.34}$$

where δ and $a_{2.5\mathrm{D}}$ are parameters that are explained later. This transformation induces an x- and y-dependent shear motion. The reasoning behind choosing the transformation as given is as follows:

1. the shear flow should be anti-symmetric with respect to x and vanish as $|x| \to \infty$, which is achieved in a simple way by the x-dependence of the transformation and controlled by the parameter $a_{2.5D}$;
2. the shear flow should vanish at the photosphere (no foot point motion) and be of noticeable strength only in the stretched area of the magnetic field and it should also vanish as $t \to \infty$; this is achieved in a simple way by the y-dependence of the transformation;
3. it should be possible to control the magnitude of the shear flow, which is done by the parameter δ.

An example of the effect of the transformation on the magnetic field is shown in Figs. 6.1 to 6.3 for two different times (in the normalisation here these are $t = 1.05$ s and $t = 50.8$ s). In these plots the values $\delta = 1$ and $a_{2.5\mathrm{D}} = 1$ have been used. The initial shear and stretching as well as the collapse and unshearing of the field are obvious when comparing the plots of the magnetic field for the two different times.

6.3.2 An illustrative example for a 3D CMT model

To generate an example model for a 3D CMT, two magnetic point sources are placed at positions $(-L/2, -d, 0)$ and $(L/2, -d, 0)$, so the sources are located at depth $y = -d$ under the photosphere ($y = 0$), and they are separated by a distance L. The potential magnetic field generated by these sources is then given by

$$\begin{aligned}\mathbf{B_0} \;=\; & c_1 \frac{\left[\left(x_0 + \frac{L}{2}\right)\mathbf{e}_x + (y_0 + d)\,\mathbf{e}_y + z_0\,\mathbf{e}_z\right]}{\left[(x_0 + L/2)^2 + (y_0 + d)^2 + z_0^2\right]^{(3/2)}} \\ & - c_1 \frac{\left[\left(x_0 - \frac{L}{2}\right)\mathbf{e}_x + (y_0 + d)\,\mathbf{e}_y + z_0\,\mathbf{e}_z\right]}{\left[(x_0 - L/2)^2 + (y_0 + d)^2 + z_0^2\right]^{(3/2)}}.\end{aligned} \tag{6.35}$$

The value of c_1 is chosen so that the maximum value of the magnetic field on the photosphere is around 0.01 T (100 G). The value of c_1 is chosen to be negative so that the magnetic polarity

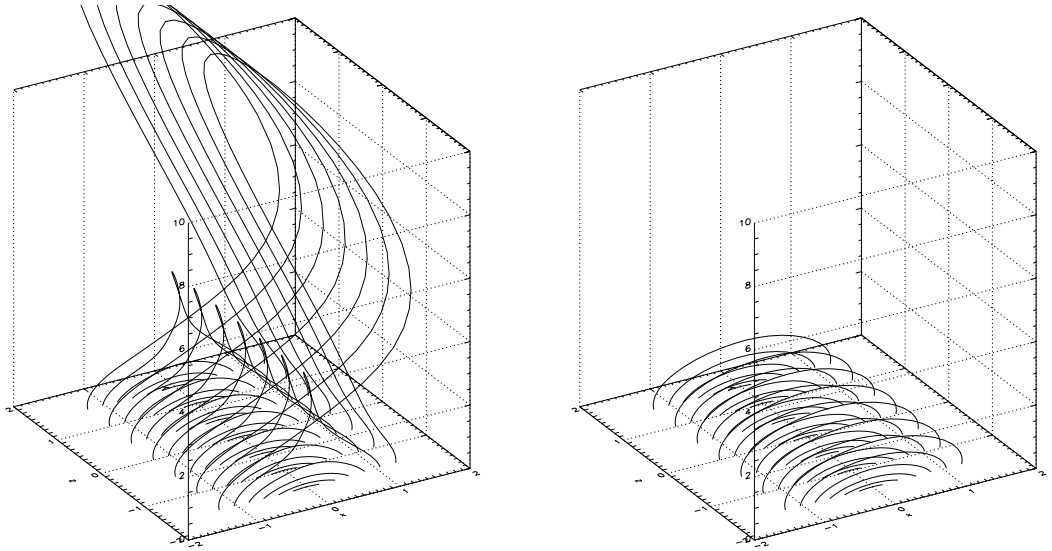

Figure 6.1: Field lines in the example 2D case with shear flow. Lengths are normalised to $L = 10$ Mm. The left plot shows the magnetic field at 1.05 s, the right plot shows it at 50.8 s. The collapse of the field lines in the y-direction is obvious. Note the difference in scale between the x-z-plane and the y-direction.

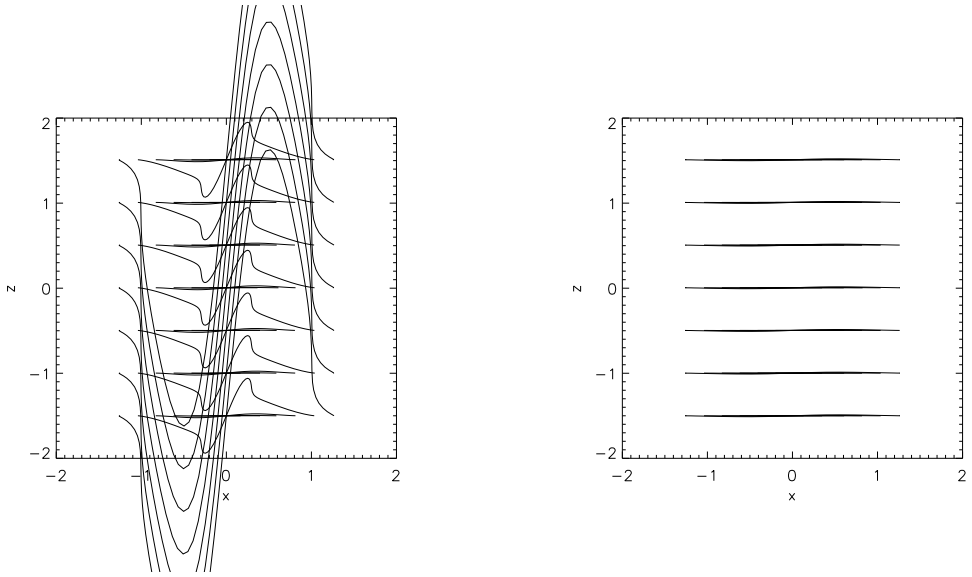

Figure 6.2: Top views of the field shown in Fig. 6.1, again at t=1.05 s and 50.8 s. These plot show more clearly how the magnetic field unshears.

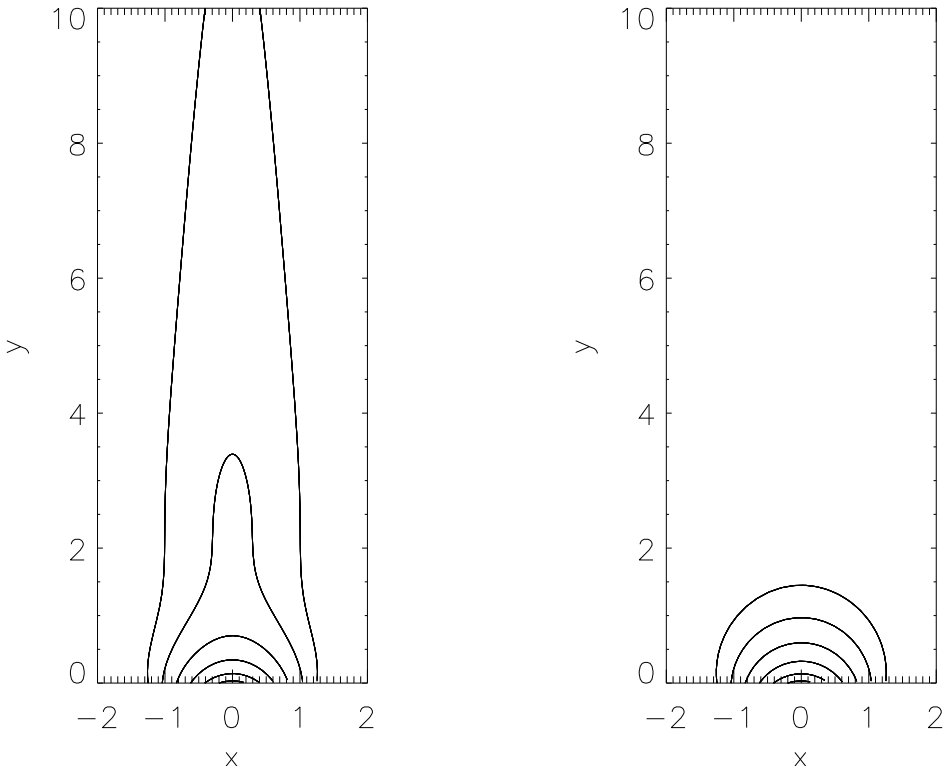

Figure 6.3: Side views of the field shown in Fig. 6.1 at t=1.05 s and 50.8 s. One can clearly see the collapse of the field lines in the CMT.

is negative for x_0 positive. As in the previous 2D case, I use $d = L$ and the same normalisation $L = 10^7$ m. As in the 2D case with shear flow, this potential field is the final field to which the CMT relaxes as $t \to \infty$. It can be considered as a 3D generalisation of the 2D magnetic field used by Giuliani et al. (2005) and in the present chapter in Sect. 6.3.1.

For this 3D example I choose a transformation which initially twists the field lines around the y-axis above a given height and for a given distance from the y-axis, as well as stretching them in the y-direction as in Giuliani et al. (2005). The time-dependence of the transformation then untwists the field while it relaxes. To achieve this feature, both the x-coordinate and z-coordinate are transformed, while keeping the transformation for y as given in Eq. (6.33) to make this illustrative example more easily comparable to the work by Giuliani et al. (2005) and the 2.5D case with shear flow described above.

The general structure of the x- and z-transformations is similar to the 2.5D case, with the difference that the x-transformation now also depends on z, while the z-transformation depends on x as follows:

$$x_0 = x - \delta \left(y_0(y,t) - y\right) \frac{z}{a_{3\mathrm{D}}^2 + x^2 + z^2}, \tag{6.36}$$

$$z_0 = z + \delta \left(y_0(y,t) - y\right) \frac{x}{a_{3\mathrm{D}}^2 + x^2 + z^2}. \tag{6.37}$$

The y-dependence has the same effect as for the 2.5D case with shear flow, whereas parameters δ and $a_{3\mathrm{D}}$ control the amount of twist and the distance from the y-axis for which there is twisting. The form of the transformation ensures that field lines which pass through the region where the transformation deviates noticeably from the identity transformation are twisted in the counterclockwise direction apart from being stretched in the y direction.

An example with parameter values of $\delta = 0.001$ and $a_{3\mathrm{D}} = 1$ is shown in Figs. 6.4, 6.5 and 6.6. Figure 6.4 shows how field lines relax between the initial time (1.05 s in the normalisation used for this example) and a later time (50.8 s). Apart from the collapse built into the example by the y-transformation (see Fig. 6.6) the effects of field line twisting through the x- and z-transformations can be seen, in particular in Fig. 6.5.

6.4 Test Particle Orbits

I present a couple of example calculations of particle orbits for the CMT models presented above to compare them to the case studied in Giuliani et al. (2005). As the gyroperiod and gyroradius of electrons are far smaller than the typical time and length scales of the collapsing traps, guiding centre theory can be used to determine the particle trajectories as discussed in earlier chapters.

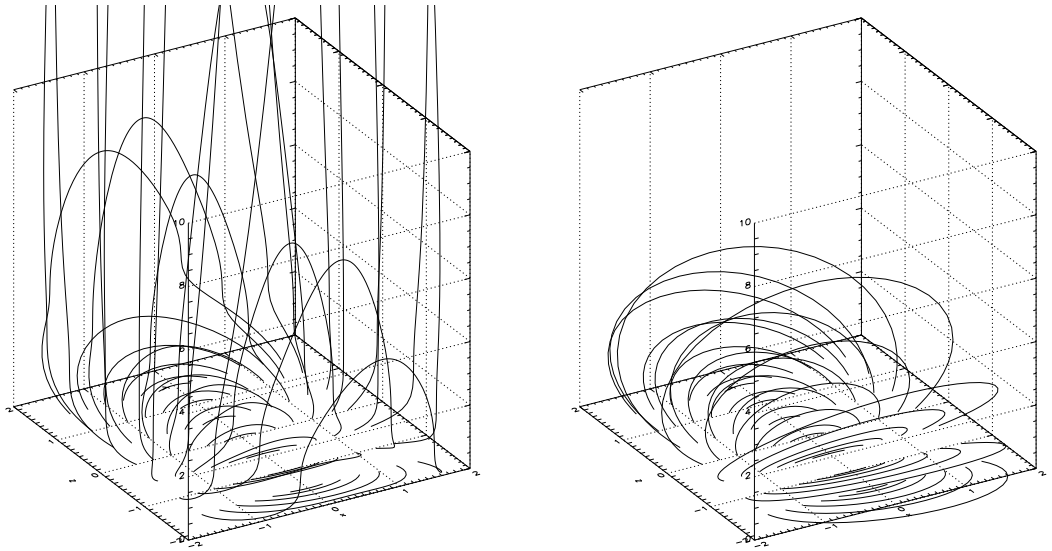

Figure 6.4: Field lines for the 3D example case. Lengths are normalised to $L = 10$ Mm. Left image shows the trap at 1.05 s, right shows once it has collapsed at 50.8 s. There is difference in scale between the y-direction, extending from 0 to $10L$ in the plot, and the x-z-plane which extends between $-2L$ and $2L$ in both directions.

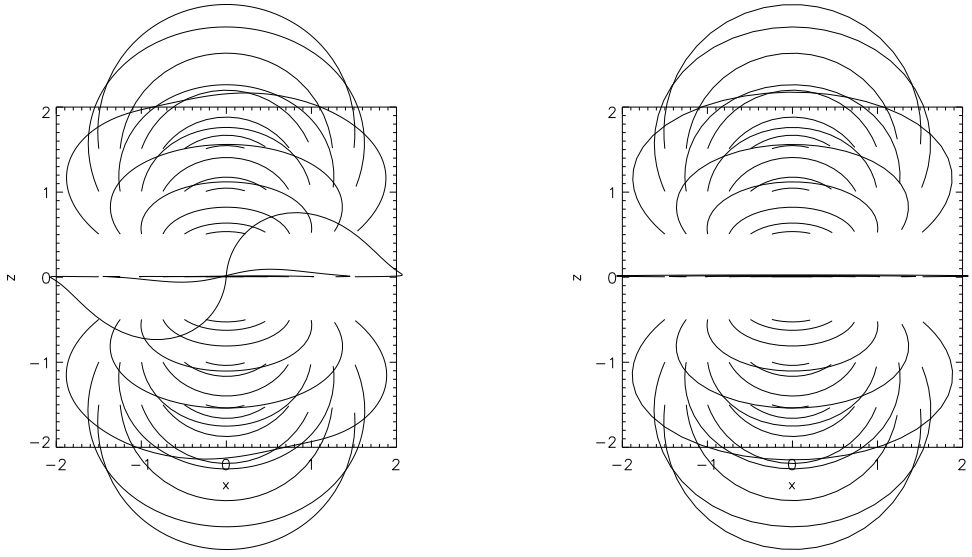

Figure 6.5: Top views of the field shown in Fig. 6.4, again at t=1.05 s and 50.8 s. These plots show more clearly how the magnetic field unshears.

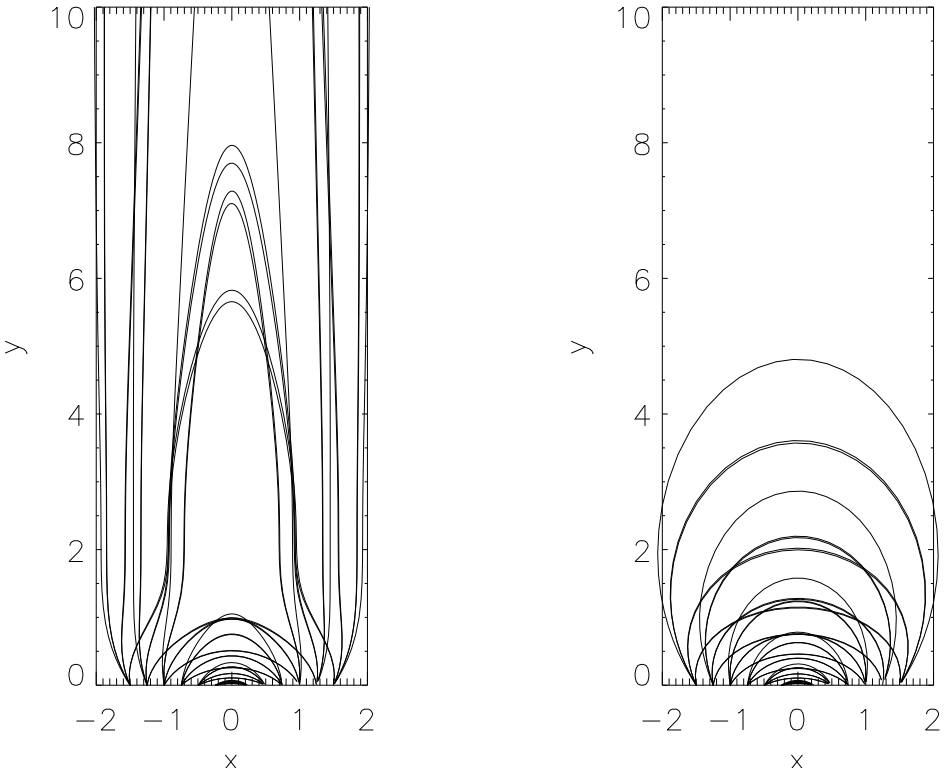

Figure 6.6: Side views of the field shown in Fig. 6.4, again at t=1.05 s and 50.8 s. The collapse of the magnetic field lines in the CMT model is obvious.

Initial conditions for the test particles for both the 2D example with shear flow and 3D example were chosen to be comparable to those studied in Giuliani et al. (2005), i.e. the particles start at the point $x = 0.1$, $y = 2.0$, $z = 1.25 \times 10^{-6}$ in normalised coordinates. For the 2D case the z-value is of course irrelevant due to the invariance in the z-direction, but is chosen to be small, but non-zero, for the 3D case to avoid creating a non-generic orbit.

The value for the magnetic moment was also kept the same as in Giuliani et al. (2005). Because the magnetic fields at the starting positions are now different, keeping the magnetic moment the same means the initial energy of the particles is different to the 6.5keV used by Giuliani et al. (2005). The values of the new magnetic fields at this starting point do not differ significantly, so the initial energies are of a similar magnitude to the previous work.

Figure 6.7 shows the particle orbit for an electron in the 2D fields with shear flow. The particle follows the untwisting field lines, and this can be seen clearly in the projections of the trajectory onto the coordinate planes, which are shown on the sides of the box. The orbit looks otherwise similar to the 2D case without shearing as examined by Giuliani et al. (2005).

The kinetic energy of the particle as it travels through the trap is shown in Fig. 6.8. As in the 2D case, the energy gained initially is mainly due to the effects of terms associated with the field line curvature in the parallel equation of motion, whereas in later stages the betatron effect is stronger. The particle starts with an energy of 6.5 keV. After 95 seconds the particle energy has increased by a factor of about 6 to 38.0 keV. This is a similar gain to that seen by Giuliani et al. (2005) using the stretched field without shear flow to accelerate an electron with initial energy of 6.5 keV to 37.3 keV.

The particle orbit in the 3D collapsing trap is shown in Fig. 6.9. This shows the effect of the untwisting field lines on the particle trajectory. A notable difference from the 2D CMT with shear flow is the asymmetric projection of the orbit onto the x-z- and y-z-planes, whereas in the x-y-plane the orbit looks very similar to the orbit in Giuliani et al. (2005).

The energy of the electron in the 3D example is plotted in Fig. 6.10. As the 3D magnetic field decreases faster with height than the 2D field, the initial particle energy is lower for the same magnetic moment than in the 2D case with shear flow. However, the energy gain is slightly weaker. The initial energy is about 3 keV and increases to about 16 keV after 95 seconds, which corresponds to an increase by a factor 5, whereas in the 2D cases there was an increase by a factor of just short of 6.

For both examples presented here, I have not yet tried to find initial conditions which give rise to higher energy gains than the rather modest ones that have given in the examples. As shown in chapter 2, a more systematic investigation of the 2D CMT of Giuliani et al. (2005) shows that much larger energy gains are possible with increases of a factor 50 or more. It is reasonable to

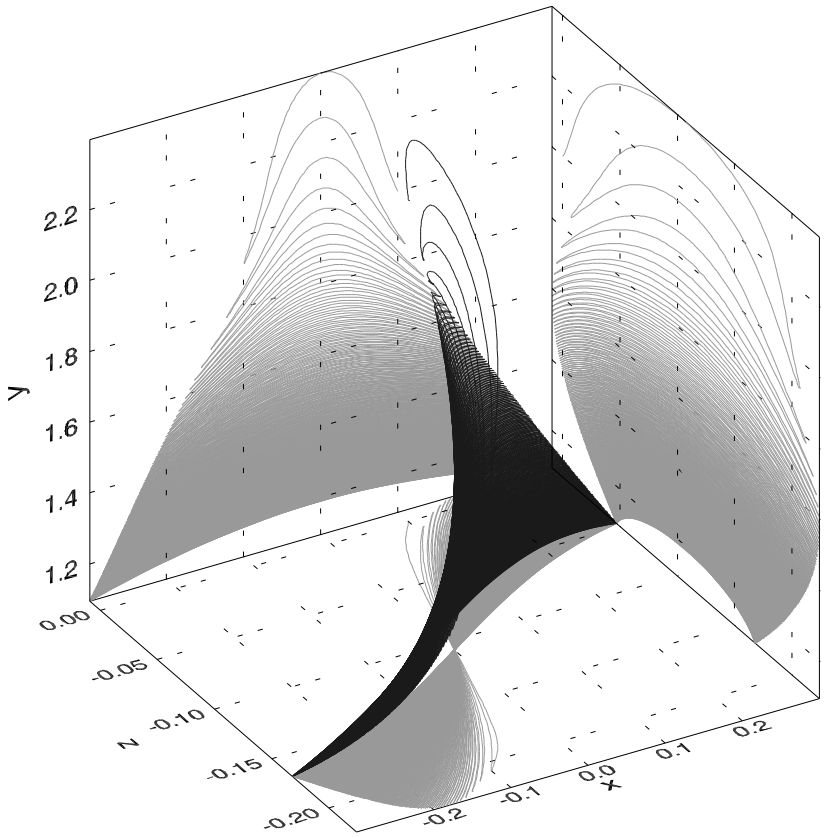

Figure 6.7: Particle orbit in the 2D CMT with shear flow. Projections of the trajectory onto the coordinate planes are shown on the sides of the box.

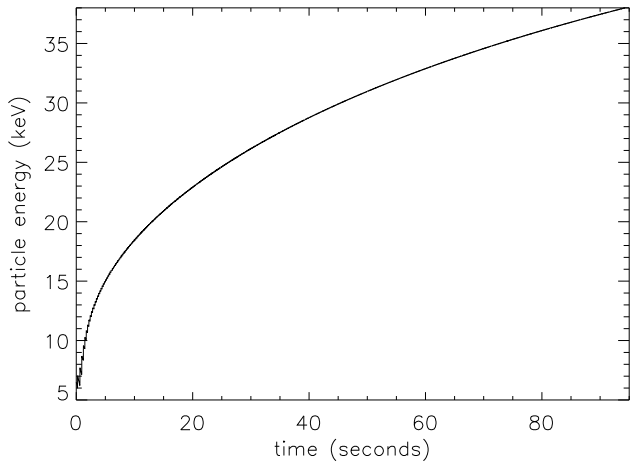

Figure 6.8: Time evolution of the particle energy in the 2D CMT with shear flow. This evolution is very similar to the orbit discussed by Giuliani et al. (2005).

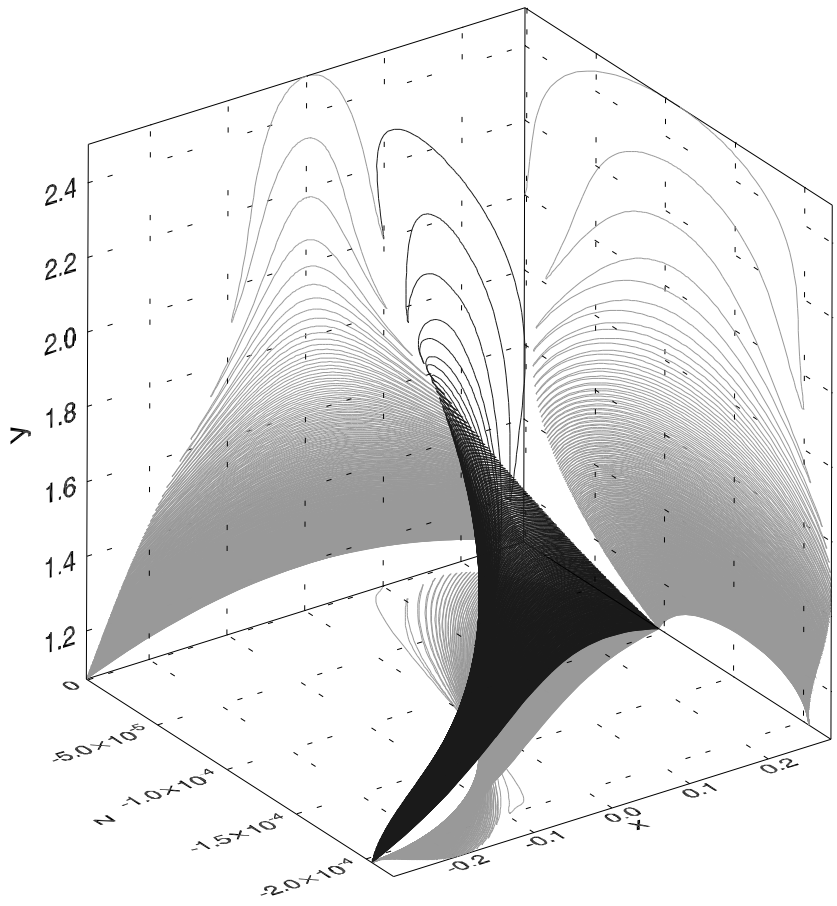

Figure 6.9: Particle orbit in the 3D CMT model.

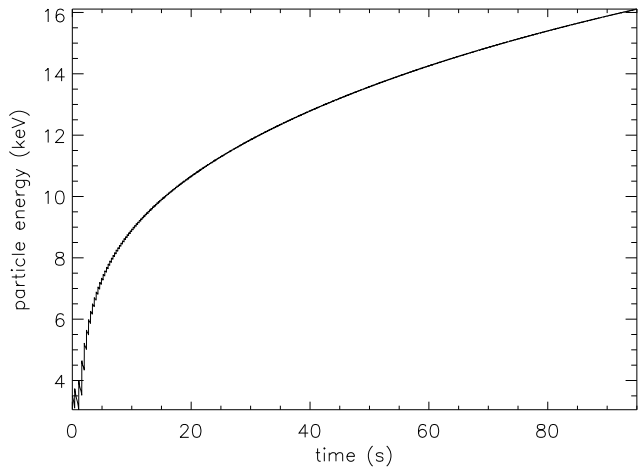

Figure 6.10: Energy gain of the particle in the 3D CMT model.

expect similar energy gains to be possible for the cases presented here. Another reason for the rather modest increase in energy is that assumptions about the maximum magnetic field strength on the photosphere have been very conservative, about 100 G. A factor 5 to 10 increase of the photospheric field strength in some places seems reasonable, in particular for flaring regions, and this could have a significant effect on energy gain so would also be a good area for future investigation.

6.5 Summary and Conclusions

I have developed a fully analytical model for kinematic time-dependent, 2D and 3D collapsing magnetic traps. This kinematic approach has the advantage that it allows full control over all the features of the model, but has the disadvantage that the modelling of the plasma system is not self-consistent.

In this chapter, I have shown how to build kinematic CMT models using the magnetic field directly, rather than using a flux function or Euler potentials. This is much easier and more straightforward to use, especially in 3D, than the theory presented in Giuliani et al. (2005).

I have given illustrative examples of collapsing traps with transformations that give rise to a shear flow in 2D and magnetic twist in 3D. I have calculated particle orbits for these new CMT models using guiding centre theory. For those orbits, the CMT models were found to give similar relative energy gains as with the 2D CMT without shearing. The particle orbits are different from the 2D CMT model by Giuliani et al. (2005) despite starting from the same initial position due to the differences in field line motion caused by the shear flow in 2D and by the twisting motion in 3D. The examples shown in this chapter have been chosen specifically to be comparable with the example shown in Giuliani et al. (2005). Different CMT models could allow for higher energy gains and should be considered in future work. There are also many other possible combinations of initial positions, initial particle energy and pitch angles, as well as investigating proton/ion orbits as well as electron orbits. In previous chapters, a systematic investigation for the 2D model of Giuliani et al. (2005) has shown that energy gain factors of order 50 or higher are possible for that model. A similar investigation could be conducted in the future for 2D with shear flow CMTs and 3D CMTs using the theory presented in this chapter.

Chapter 7

Summary and Future Work

How particles can be accelerated in a solar flare has been a big question for solar physics for some time. There have been many possible particle acceleration methods suggested, one of which is the collapsing magnetic trap.

The collapsing trap model has been discussed in solar physics literature for several years (e.g. Somov and Kosugi 1997; Giuliani et al. 2005) and even before this was the idea of particles being trapped in some magnetic field (Brown and Hoyng 1975). There are also close parallels with work in the Earth's magnetosphere (e.g. Birn et al. 1997, 1998, 2004; Reeves et al. 2008).

Work published by Giuliani et al. (2005) considered a 2.5D model for the magnetic and electric field to describe a straightforward theoretical model to study a collapsing trap. There were several improvements and further study of the fields and particles in these fields that are the main focus of this thesis.

Firstly, Giuliani et al. (2005) only considered a single particle in the trap. This was improved upon in Chapter 2 of this thesis. In this chapter, different values of initial condition were tested: the position, pitch angle and particle energy were all adjusted.

It was found that initial energy of a particle had little effect on its energy gain. The initial position of the particle was important, especially as moving from region of lower magnetic field strength to a stronger magnetic field causes an increase in the kinetic energy due to the betatron effect. Particles starting towards the trap centre were more likely to be trapped for longer and thus gain more energy. Particles starting away from the trap centre could also gain some energy, even if they escaped through the photosphere in a few seconds, well before the trap had collapsed.

In all the models in this thesis, the highest energy particles were found at the loop top once the trap had collapsed. This could be related to loop top sources that are observed in flares, although

the physics would have to be looked at in more detail.

The initial pitch angle of a particle was found to be very important for the particle to gain energy. Particles with pitch angles close to 90° were trapped for longer and gained more energy. Evidence throughout this thesis suggests that for these particles most of the energy was gained through betatron acceleration.

In general, the energy gain is lower for particles with initial pitch angles further from 90°. However, looking at the pitch angle initial condition closer to 0° or 180°, some particles gain slightly more energy than with pitch angles closer to 90°. These particles may be being accelerated by Fermi acceleration.

Particles that have initial pitch angle close to 0° or 180° are usually in the loss cone, which means they escape the trap because they have more of their velocity along the field lines and would require a stronger magnetic field to be reflected.

The relationship between pitch angle and energy gain processes was further examined in section 2.4, by looking at two particles where the only difference between the initial conditions is the pitch angle (same initial position and energy). As the particles start from the same position, they remain on the same field line[1] thus passing through the same magnetic fields at the trap centre. The particle with pitch angle close to 90° will stay close to the trap centre, whereas the particle with pitch angle close to 180° moves closer to the footpoints, where the magnetic field is stronger. Hence, the particles pass through the same minimums of magnetic field. The differences in perpendicular energy for these particles is due to them having different magnetic moments ($E_\perp = \mu B$), but the lower envelope of both perpendicular energy graphs have the same shape.

The acceleration processes for particles is not purely betatron acceleration. One effect this has is that the energy of escaped particles estimated by the formula in Bogachev and Somov (2005, see also Eq. 1.35) only provides an approximate lower bound for the final particle energy.

The bounce lengths of particles was also considered. From the longitudinal invariant[2] this suggested that Fermi acceleration was also a factor in energy gain, but only in an average sense, as the parallel velocity increases close to the centre of the trap.

There are several orders of terms in the guiding centre equations of motion. In section 2.4.3, three cases are considered: including higher order terms in both the parallel and perpendicular equations of motion; including higher order terms in the parallel equation only; and using lowest order terms only in both equations. This showed that the higher order terms are important in the parallel equation of motion but are not required in the perpendicular equation. These important

[1] Due to the $\mathbf{E} \times \mathbf{B}$-drift being the most significant term in the guiding centre equations of motion and on a larger scale, the frozen-in condition.

[2] $J = \oint m v_\parallel \mathrm{d}s \approx m v_\parallel 2l$ where the integral is calculated over a round trip and l is distance between bounce points.

terms relate to the field line curvature.

Going back to the magnetic and velocity field used by Giuliani et al. (2005), there were some changes that could be made to build towards a slightly more realistic model of a collapsing trap in a solar flare.

In chapter 3, a guide magnetic field is added in the z direction. For the modest guide fields considered, there was not much difference in particle energy gain. As the magnetic field lines are pushed in the z direction, particle orbits also did this.

The Giuliani et al. (2005) fields are created by placing two magnetic monopoles (of opposite polarity) at the same distance below the Corona to produce a symmetric trap. By altering the height of one of the monopoles the trap can be made asymmetric, as considered in chapter 4. This makes the field at one of the footpoints stronger, so particles mirror higher up at the stronger side. Additionally, this has the effect that more particles escape the trap by going through the side with the weaker field. The trap centre is more difficult to define in this case as it will be more towards one side. Many of the effects found for the symmetric case were also found for this asymmetric trap; e.g. effect of pitch angle on energy gain. By carefully considering the orbit of a particle in the asymmetric trap whilst at the same time considering its energy, it was found that the particle gains energy in a step when passing through the trap centre, and loses (less) energy more slowly when heading toward the bounce points. The particle spends more time in the side where the magnetic field is weaker. Despite this, the particle still loses less energy at this side than the other side.

There are other ways to model the fields required for a trap and for more insight into trapping in flares this is considered in chapter 5. Minoshima et al. (2010) use a 2D time dependent flux function. This is rather different from Giuliani et al. (2005) models as the flux function prescribes both magnetic and electric fields and the velocity field is found from the ideal Ohm's Law. In this case the field is an X-point and the region of interest is below the X-point, between it at the photospheric boundary. At the side, field lines can be thought of as open. One particle starting on an open field line is discussed and the point when the field line crosses the separatrix into the closed region can be clearly seen. However, the particles in the closed region are of more interest and are considered in a similar way to those in other traps. Again, particles starting close to the trap centre and with pitch angles close to 90° gain the most energy. Also, particles that have the highest energy are trapped at the loop tops.

Even in simple 2.5D models of solar flares we could expect the magnetic field in the invariant direction to decrease with time. To allow this in the model an unshearing velocity with a component in the invariant direction has to be introduced. Therefore, a velocity in the invariant direction is added to the Giuliani et al. (2005) model in chapter 6. In the same chapter, a method of building kinematic MHD models using the magnetic field directly is presented. This is a step towards the fully 3D models also discussed in that chapter that is more straightforward than the theory presen-

ted in Giuliani et al. (2005). In both these cases all the fields can be worked out analytically. The example particle orbits allow energy gain etc. to be compared with the other traps in this thesis, but a systematic investigation of the effects of initial conditions of particles in these traps, similar to the work in chapter 2 for the trap with 2D fields, still has to be carried out.

An important point regarding the findings of Giuliani et al. (2005) and in this thesis is that only a very moderate field strength of the CMT (of the order of 20 G) is considered. For solar flares, much higher field strengths are not uncommon and this may put into perspective that the initial energies used in this thesis and in Giuliani et al. (2005) are relatively high (5 - 6 keV) and that the time scale for the CMT collapse and hence for the energization is relatively long. For higher magnetic field strengths it would be expected that even particles with lower initial energies could be accelerated to the energies found here and that particles with higher initial energies might end up with final energies well into the relativistic regime. One would also expect that the time scale for energization would be shorter, as the associated electric fields would be larger for larger magnetic field strength. As particle kinetic energies get closer to the rest mass (511 keV for electrons), the relativistic equations of motion should be used. This is an issue that should be investigated in the future.

Obviously, like many other models, the CMT model used in this thesis is highly simplified. Firstly, the plasma has been assumed to be collisionless in all the models considered in this thesis. An improvement would be to include collisions with a thermal background plasma. Throughout this thesis, the flow field associated with CMT models is usually assumed to be laminar. It is, however, highly unlikely that a violent event such as a solar flare will give rise to such regular behaviour. A possible improvement for future CMT models might be to add turbulent motion (and the corresponding electromagnetic fields) onto the overall laminar motion associated with the collapse. A possible way of dealing with this is to add stochastic scattering terms to the equations of motion, similar in principle, but different in detail, to a Coulomb collision term. There are several interesting questions that arise in connection with such an approach, for example: How would the particle energization in a turbulent CMT change compared to a laminar CMT? How would the energy density associated with the turbulent flow and EM fields evolve in a CMT? Another interesting aspect of such models would be that they could provide a link between stochastic particle acceleration models (e.g. Miller et al. 1997) and the standard flare scenario in a similar way as proposed by e.g. Hamilton and Petrosian (1992), Park and Petrosian (1995), Petrosian and Liu (2004) and more recently by Liu et al. (2008).

Appendix A

Detailed calculation for the 3D case using Euler potentials

The following gives all of the steps required to model a magnetic trap in 3D using Euler potentials, although Euler potentials are not required, as discussed in Chapter 6.

For the following derivation I use a notation which allows certain groups of scalar quantities to be used as vectors or rows or columns of tensors. Firstly, the derivatives of the Clebsch variables, $\bar{\alpha}$ and $\bar{\beta}$, with respect to the transformed coordinates are required:

$$\begin{aligned}\frac{\partial\bar{\alpha}}{\partial\mathbf{X}} &= \left(\frac{\partial\bar{\alpha}}{\partial X},\frac{\partial\bar{\alpha}}{\partial Y},\frac{\partial\bar{\alpha}}{\partial Z}\right),\\ \frac{\partial\bar{\beta}}{\partial\mathbf{X}} &= \left(\frac{\partial\bar{\beta}}{\partial X},\frac{\partial\bar{\beta}}{\partial Y},\frac{\partial\bar{\beta}}{\partial Z}\right),\end{aligned}$$

which is basically the usual gradient with respect to X, Y and Z. The transformation differentiated with respect to the original Eulerian coordinates is also required,

$$\begin{aligned}\frac{\partial\mathbf{X}}{\partial x} &= \left(\frac{\partial X}{\partial x},\frac{\partial Y}{\partial x},\frac{\partial Z}{\partial x}\right),\\ \frac{\partial\mathbf{X}}{\partial y} &= \left(\frac{\partial X}{\partial y},\frac{\partial Y}{\partial y},\frac{\partial Z}{\partial y}\right),\\ \frac{\partial\mathbf{X}}{\partial z} &= \left(\frac{\partial X}{\partial z},\frac{\partial Y}{\partial z},\frac{\partial Z}{\partial z}\right).\end{aligned}$$

Now consider each component of Eq. (6.13), starting with the x-component

$$B_x = \frac{\partial\alpha}{\partial y}\frac{\partial\beta}{\partial z} - \frac{\partial\alpha}{\partial z}\frac{\partial\beta}{\partial y}. \tag{A.1}$$

With the coordinate transformation, Eqs. 6.16 and (6.17), and using the chain rule this becomes

$$B_x = \left(\frac{\partial\bar{\alpha}}{\partial\mathbf{X}}\cdot\frac{\partial\mathbf{X}}{\partial y}\right)\left(\frac{\partial\bar{\beta}}{\partial\mathbf{X}}\cdot\frac{\partial\mathbf{X}}{\partial z}\right) - \left(\frac{\partial\bar{\alpha}}{\partial\mathbf{X}}\cdot\frac{\partial\mathbf{X}}{\partial z}\right)\left(\frac{\partial\bar{\beta}}{\partial\mathbf{X}}\cdot\frac{\partial\mathbf{X}}{\partial y}\right). \tag{A.2}$$

Applying the well-known vector identity

$$(\mathbf{A}\cdot\mathbf{C})(\mathbf{B}\cdot\mathbf{D}) - (\mathbf{A}\cdot\mathbf{D})(\mathbf{B}\cdot\mathbf{C}) = (\mathbf{A}\times\mathbf{B})\cdot(\mathbf{C}\times\mathbf{D}) \tag{A.3}$$

to Eq. (A.2) gives the magnetic field in the x-direction as

$$B_x = \left(\frac{\partial\mathbf{X}}{\partial y}\times\frac{\partial\mathbf{X}}{\partial z}\right)\cdot\mathbf{B}_0\left(\mathbf{X}\right), \tag{A.4}$$

because the initial magnetic field is

$$\mathbf{B}_0(\mathbf{X}) = \frac{\partial\bar{\alpha}}{\partial\mathbf{X}}\times\frac{\partial\bar{\beta}}{\partial\mathbf{X}} \tag{A.5}$$

by construction. Similarly one finds that

$$B_y = \left(\frac{\partial\mathbf{X}}{\partial z}\times\frac{\partial\mathbf{X}}{\partial x}\right)\cdot\mathbf{B}_0\left(\mathbf{X}\right), \tag{A.6}$$

$$B_z = \left(\frac{\partial\mathbf{X}}{\partial x}\times\frac{\partial\mathbf{X}}{\partial y}\right)\cdot\mathbf{B}_0\left(\mathbf{X}\right). \tag{A.7}$$

Appendix B

Fortran particle orbit codes listings

The Fortran code is a Runge-Kutta 5th order stepper with adaptive step size controlled by the error from the 4th order Runge-Kutta step. The stepper and internal codes were written by P. Giuliani and P. Wood, based on codes from Press et al. (1986), to run single test particle experiments.

The `rkck_mod`, `rkqs_mod` and `products_mod` files have not been functionally changed since I received them, although some code that produced extra files has been removed. However, the `lognew` has been changed to allow for different test particle initial conditions and looping over them; recording different data in multiparticle files and/or RV files. The `derivs_mod` file was changed for some of the experiments in section 2.4.3 when the guiding centre equations of motion used had to be altered to remove the higher order terms. The `rkdrive_mod` file was modified so that the RV data files would be written only when the `writervs` variable is 1 (set in `lognew`) and to set a filename for the RV file based on the `uniqueparticleid` variable. The `global_mod` and `fields_mod` have to be changed for different trap fields. The `global_mod` file contains the normalisation for the quantities.

Output files are `multipar_fmt_t**.dat`, each having initial and final (the time of the file) conditions for each particle (one particle per line); and `RV********.dat` each having particle orbit data (time, position, velocity and energies) for a single particle.

Table B.1 shows the form of the `RV********.dat` output files, and B.2 shows the data fields in the `multipar_fmt_t**.dat` files.

IDL	Fortran	Name	Formula in code	Normalisation	Description/Notes	
0	1	T	`Tscl*(T-T1)`	In seconds, starting at 0	Time	
1	2	X	`R`	In units of 10Mm (e.g. 2=20Mm)	Position	
2	3	Y				
3	4	Z				
4	5	VPAR	`VPAR`	$Vscl = (10\mathrm{Mm}/100\mathrm{s} = 10\mathrm{Mm/s} = 10^5\mathrm{m/s}$		
5	6	VPERP2	`MU*sqrt(dot(B,B))`	$\frac{1}{2}Vscl^2 = 5 \times 10^9 \mathrm{m}^2/\mathrm{s}^2$		
6	7	VDRIFT2	`sum((DRDT-VPAR*bb)**2)`	$\frac{1}{2}Vscl^2 = 5 \times 10^9 \mathrm{m}^2/\mathrm{s}^2$		
7	8	EL1	`Vscl*B0*E`	V/m	Electric field (in x, y, z)	
8	9	EL2				
9	10	EL3				
10	11	B1	`B0*B`	T	Magnetic field (in x, y, z)	
11	12	B2				
12	13	B3				
13	14	E1	`e1=efct*0.5*M*(Vscl*Vpar)**2&eV`	eV	$mv_\parallel^2/2$	parallel energy
14	15	E2	`e2=efct*M*(Vscl**2)*MU*sqrt(dot(B,B))`		μB	perpendicular energy
15	16	E3	`e3=efct*0.5*M*dot(UE,UE)`		$mu_E^2/2$	energy due to $\mathbf{E} \times \mathbf{B}$ drift
16	17	ET	`e1+e2+e3`		Total E_k	
17	18	RHS1	`efct*Q*E0*(L/Tscl)*dot(DRDT,E)`		Energy budget. See Giuliani et al. (2005), Eq. (47) & Northrop (1963), Eq. (1.28)	
18	19	RHS2	`efct*(M*Vscl*Vscl/Tscl)*` `MU*dot(B,DBDT)/sqrt(dot(B,B))`			
19	20	Vfx	`Vscl*Vf`	m/s	velocity field	
20	21	Vfy				
21	22	Vfz				
22	23	H			stepsize	

note: `UE=(E0/B0)*cross(E,B)/dot(B,B)`

Table B.1: Data output into the 'RV' files. Each line in the file is the values at a timestep. Each file is the complete particle orbit.

The codes shown here are for the trap discussed in chapter 5. The normalisation, magnetic fields, velocity fields (or coordinate transformations) and their derivatives would be different for the models discussed in other chapters.

Real numbers are made double precision and some code optimisations are made using compiler flags. The command to compile the code using ifort is:

```
ifort -r8 -fast -O3 -parallel -o a.exe global_mod.f90 \
 products_mod.f90fields_mod.f90 derivs_mod.f90 rkck_mod.f90 \
 rkqs_mod.f90 rkdrive_mod.f90 lognew.f90
```

and the code can then be executed with the command
`a.exe`

B.1 global_mod.f90

Parameters and global variables, accessible to any subroutines in the code.

```
MODULE global

IMPLICIT NONE

!note normalisations are for Minoshima et al. fields.
!in Giuliani et al. code the L=1d7, Tscl=100., B=0.01
!and other values are as mentioned in the chapters.

!number of steps to keep and run before giving up
   Integer, Parameter     :: NKEEPMAX =1000001
   Integer, Parameter     :: NSTPMAX  = 2*10**9

!when to store step quantities calculated
!(i.e. store every nstore'th step)
   Integer, Parameter     :: NSTORE =1

!Electron charge and mass
   Real, Parameter        :: Q = - 1.6022d-19
   Real, Parameter        :: M = 9.1095d-31

!Normalisations
   Real, Parameter        :: L =  15.*1d6   ! 15 Mega meters
   Real, Parameter        :: Tscl = 1. ! 1 second
   Real, Parameter        :: Vscl = L/Tscl
   Real, Parameter        :: B0 = 0.013593d0 !so x=0,y=0,z=0,t=0 gives B=100G
```

IDL	Fortran	Name	Normalisation to MKS, eV, degrees	Description and Notes
0	1	xstart	`xstart*L`	initial postion
1	2	ystart	`ystart*L`	
2	3	zstart	`zstart*L`	
3	4	tstart	`tstart*T0`	initial time
4	5	ekinstart	`ekinstart*EkinScl`	initial total kinetic energy
5	6	alphastart	`alphastart*!RaDeg`	initial pitch angle
6	7	eperpstart	`eperpstart*EkinScl`	initial perpendicular energy
7	8	eparstart	`eparstart*EkinScl`	initial parallel energy
8	9	vtotstart	`vtotstart*Vscl`	initial particle speed
9	10	vperpstart	`vperpstart*Vscl`	initial perpendicular speed
10	11	vparstart	`vparstart*Vscl`	initial parallel speed
11	12	Exstart	`Exstart*E0`	initial electric field
12	13	Eystart	`Eystart*E0`	
13	14	Ezstart	`Ezstart*E0`	
14	15	Bxstart	`Bxstart*B0`	initial magnetic field
15	16	Bystart	`Bystart*B0`	
16	17	Bzstart	`Bzstart*B0`	
17	18	BStart	`BStart*B0`	initial magnetic field strength ($\|\mathbf{B}\|$)
18	19	mu	`mu*M*Vscl^2/B0`	particle magnetic moment (constant for each particle)
19	20	xend	`xend*L`	final position
20	21	yend	`yend*L`	
21	22	zend	`zend*L`	
22	23	tend	`tend*T0`	final time (i.e collapse or particle escape time)
23	24	ekinend	`ekinend*EkinScl`	final total kinetic energy
24	25	alphaend	`alphaend*!RaDeg`	final pitch angle
25	26	eperpend	`eperpend*EkinScl`	final perpendicular energy
26	27	eparend	`eparend*EkinScl`	final parallel energy
27	28	vtotend	`vtotend*Vscl`	final particle speed
28	29	vperpend	`vperpend*Vscl`	final perpendicular speed
29	30	vparend	`vparend*Vscl`	final parallel speed
30	31	Exend	`Exend*E0`	final electric field experienced
31	32	Eyend	`Eyend*E0`	
32	33	Ezend	`Ezend*E0`	
33	34	Bxend	`Bxend*B0`	final magnetic field experienced
34	35	Byend	`Byend*B0`	
35	36	Bzend	`Bzend*B0`	
36	37	Bend	`Bend*B0`	final magnetic strength

Table B.2: Data output into the 'multipar' files. Each line in the file is the start and end conditions for a particle.

```
   Real, Parameter        :: E0 = Vscl * B0

!parameters for the Giuliani et al. fields
   Real, Parameter        :: d=L      ! depth of monopoles
   Real, Parameter        :: Lv = L   ! Height where stretching starts
   Real, Parameter        :: Bzfinal =  0d0!.1426754410
   Real, Parameter        :: esp=1.d0  ! exponent in log transformation
   Real, Parameter        :: cc=0.4d0  ! coeff in log transformation
   Real, Parameter        :: c1=-0.15d6   ! Magnetic Charge

!Parameters for the Minoshima et al. field
   Real, Parameter        ::tp=5.0d0
   Real, Parameter        ::tau=1.77d0
   Real, Parameter        ::vp=6d4
   Real, Parameter        ::xf0=0.5558823530D0

!Global variables to track if RV is being written
!and what particle is being currently calculated
!
!These need to be accessable to any subroutine without being explicitly passed
!but change throughout the code, so are not parameters

   integer :: uniqueparticleid
   integer :: writervs

END MODULE global
```

B.2 newinput.dat

This file contains the initial conditions as a maximum, minimum and number of steps to take for each of energy, position (x,y,z) and the number of steps to take in pitch angle. Pitch angles can either go from 0° to 90° or from 0° to 180° depending on `fullangle`. In past versions of the code the start and end time of the orbit was also stored in this file, but later specified directly in the lognew file.

```
&inputdata

T1=0.
T2=10.

H1=0.00001
EPS=1.0E-15

AlphaSteps=21
FullAngle=1
```

```
R1(1)=0.0E7
R2(1)=1.05E7
RSTEPS(1)=10

R1(2)=1.0E7
R2(2)=1.0E7
RSTEPS(2)=1

R1(3)=0.0E7
R2(3)=1.35E7
RSTEPS(3)=10

EkinLow=0.5e3
EkinHigh=102.2e3
EkinSteps=10/
```

B.3 lognew.f90

This is the main program. This reads in the initial conditions from `newinput.dat` loops over each particle, and has variables to set if the multipar and RV files should be written. Quantities are normalised in this program before being passed on to the subroutines in other files.

```
PROGRAM SINGLE

USE GLOBAL
USE M_DRIVER

IMPLICIT NONE

 INTEGER :: NOK, NBAD
 REAL, DIMENSION(3) :: RSTART, RSTARTKEEP, R1, R2
 REAL :: T1, T2, H1, EPS, VPARSTART,MU,VPARSTARTKEEP
 INTEGER :: pos_no_x,pos_no_y,pos_no_z,pos_no_alpha,pos_no_ekin
 INTEGER :: EKinSteps, AlphaSteps, FullAngle !, itts
 INTEGER,DIMENSION(3) :: RSteps, pos_no_r
 REAL, DIMENSION(NKEEPMAX) :: TT
 REAL, DIMENSION(NKEEPMAX,3) :: S, TOTAL
 INTEGER :: I,NKEEP,time_no,maxtime
 REAL :: Ekin, alpha, Ekinlow,Ekinhigh,T1Keep,T2Keep
 REAL, PARAMETER :: Pi=3.1415926535


!maximum time to go to
maxtime=10

!loop for each multipar file we want to make
```

```
!this is the lazy way to make several multipar files
!from one code (although the code will be slower than
!some smarter ways)
DO time_no = 0,maxtime,1

OPEN (UNIT = 19, FILE = 'multipar.dat')

!Work out values of positions to start on.

!read the max/min and number of values for
!initial position,energy and pitch angle
CALL read_param2

!adjust T2 to use loop value (i.e. ignore value in newinput.dat)
T2=time_no*1.0

T1Keep=T1
T2Keep=T2

!itts=RSTEPS(1)*RSTEPS(2)*RSTEPS(3)*AlphaSteps*EkinSteps
!PRINT*,"Total Number of Particles to be calculated",itts

!give each particle an integer to identify it. useful for deciding
!which RV*.dat files to output and also for splitting up programs
!to run several at once e.g. use
!'IF uniqueparticleid .le. 100 and uniqueparticleid .gt. 200 THEN CYCLE'
!inside the following loops to only run particles 100 to 200.
uniqueparticleid=0

!note that y (or z) starts at 1 as usually only have one value
!alpha starts at 1 because don't want alpha=0 so code cant calculate mu
do pos_no_x = 0,RSTEPS(1),1
do pos_no_y = 1,RSTEPS(2),1
do pos_no_z = 0,RSTEPS(3),1
do pos_no_alpha =1,AlphaSteps,1
do pos_no_ekin = 0,EkinSteps,1

 uniqueparticleid=uniqueparticleid+1

!decide if we want to record the full orbit for this particle.
!at the moment, this records every 1009th particle, only if the
!time_no loop is on it's final go, i.e. running for the full time
 if (time_no .eq. maxtime .and. mod(uniqueparticleid,1009) .eq. 0) then
  writervs=1
 else
  writervs=0
 endif
```

```
!calculate the position, pitch angle and energy of this particle using
!the values from the loop and the bounds from newinput.dat
 pos_no_r=(/ pos_no_x,pos_no_y,pos_no_z /)
 RSTART=R1+(R2-R1)*(((pos_no_r)*1.0d0)/RSteps)
 alpha=pos_no_alpha/(AlphaSteps*1.0d0+FullAngle*1.0d0)* &
         ((1+FullAngle)*Pi/2.0d0)
 Ekin=EKinLow+ (EKinHigh-EKinLow)*(pos_no_ekin)/(EkinSteps*1.0d0)

!alpha is pi/(no of steps+1) if fullangle is 1
!(ie, steps from >=0 to >Pi (but not including Pi))

!alpha is pi/2/(no of steps) if fullangle is 0
!(steps from 0 to Pi/2 inclusive)

!want to keep starting values (so we can record them at the end)
 T1=T1Keep
 T2=T2Keep
 VPARSTARTKEEP=VPARSTART
 RSTARTKEEP=RSTART

!normalise the values
 RSTART=RSTART/L
 RSTARTKEEP=RSTARTKEEP/L
 T1=T1/Tscl
 T2=T2/Tscl
!convert energy to joules
 Ekin=Ekin*abs(Q)
!and normalise
 Ekin=Ekin/M/Vscl**2

!call the subroutine that works out mu (as used in the code)
!from the values of Ekin, alpha and B (via RSTART)
 CALL CALC2_MU(mu,vparstart,Ekin,alpha,RSTART,T1)

!Call the RK sophisticated driver, which then works out the arrays for the
!time steps and positions.

 CALL RKDRIVE(RSTART,VPARSTART,MU,T1,T2,EPS,H1,NOK,NBAD,TT,S,TOTAL)

!number of data points
 NKEEP=(NOK+NBAD)/NSTORE

!call the subroutine that writes out to the multipar file
CALL WRITE_ENDTIME(RSTART,T2,MU,VPARSTART)

end do
end do
end do
```

```
end do
end do

!close the multipar file
 CLOSE(19)

!because the multipar file is output at different points with
!unspecified formatting we best make this into a nicer to read
!file, with one particle's data per line and give the file
!a unique name
CALL MAKEFILE(time_no)

end do

!*********************************************************************
 Contains
!*********************************************************************

 Subroutine read_param2
!read in the newinput.dat file
 Namelist/inputdata/T1,T2,H1,EPS,AlphaSteps,FullAngle,R1,R2, &
    RSteps,EkinLow,EkinHigh,EkinSteps

 open(20,file='newinput.dat',status='unknown')
 read(20,nml=inputdata)
 close(20)

!check FullAngle is 0 or 1
IF (FullAngle .LT. 0 .OR. FullAngle .GT. 1) THEN
  PRINT*,'FullAngle must be 0 or 1. Check newinput.dat'
  STOP
ENDIF

 End Subroutine read_param2

!*********************************************************************
 SUBROUTINE CALC2_MU(mu,vparstart,Ekin,alpha,RSTART,T1)
!calculate the mu and vparstart given the
!total initial energy and pitch angle.

  REAL, DIMENSION(3),INTENT(IN) :: RSTART
  REAL, INTENT(IN) :: T1, Ekin, alpha
  REAL, INTENT(OUT) :: mu,vparstart
  REAL, DIMENSION(3) :: B ,El,a2,a3,a4,a5,a6,a7,a8,a9,a10,ue
  REAL :: magB,vtot,vperp


!need B to calculate mu given the perpendicular energy (Eperp=mu*B)
```

```
!calculate B at this point/time:
!don't care about the derivatives so they're called a2...a10
  CALL FIELDS(RSTART,T1,El,B,a2,a3,a4,a5,a6,a7,a8,a9,a10)

  !calculate magnitude of B
  magB=B(1)**2+B(2)**2+B(3)**2
  magB=magB**(0.5)

!energy due to ExB drift
  ue=cross(El,B)/dot(B,B)

!particle speed ignoring ExB drift
  vtot=sqrt(2.0*Ekin-dot(ue,ue))
!split this into parallel and perpendicular parts
  vparstart=vtot*cos(alpha)
  vperp=vtot*sin(alpha)

  !calculate mu
 mu=vperp**2/magB/2d0

!output starting data to the multipar.dat file
 WRITE (19,*) RStart,T1,Ekin,alpha, mu*magB, 0.5*vparstart**2
 WRITE (19,*) vtot,vperp,vparstart,El,B,magB,mu
 END SUBROUTINE

SUBROUTINE WRITE_ENDTIME(RSTART,T2,MU,VPARSTART)
!write data to the multipar file at the end of the particle's run
    REAL,DIMENSION(3), INTENT(IN) :: RSTART
    REAL, INTENT(IN) :: T2, MU, VPARSTART
    REAL, DIMENSION(3) :: B ,El,a2,a3,a4,a5,a6,a7,a8,a9,a10,ue
    REAL :: EKin,magB,Epar,Eperp,vperp,vtot

!write position and time
  WRITE(19,*) RSTART, T2
!  WRITE(19,*) "RSTART,T2"

!calculate magnetic and electric fields
CALL FIELDS(RSTART,T2,El,B,a2,a3,a4,a5,a6,a7,a8,a9,a10)
  magB=B(1)**2+B(2)**2+B(3)**2
  magB=magB**(0.5)
  ue=cross(El,B)/dot(B,B)
  Ekin=mu*magB+0.5*vparstart**2+0.5*dot(ue,ue) !addition of UE
  alpha=acos(vparstart/(sqrt(2*Ekin-dot(ue,ue))))
  EPar=0.5*vparstart**2
  EPerp=mu*magB
  vperp=sqrt(2.0d0*Eperp)
  vtot=sqrt(2.0*Ekin-dot(ue,ue))
```

```
WRITE(19,*) Ekin,alpha,Eperp,Epar,vtot,vperp,vparstart
WRITE(19,*) El, B, magB
END SUBROUTINE

SUBROUTINE MAKEFILE(time_no)
!reform the multipar.dat file into a multipar_fmt_t**.dat file
!this gives it a header so it's easier to read
!and puts one particle's data on each line.
!This subroutine is very fragile because different compilers will output
!data to files in different line lengths unless the formatting is explicit
!(i.e. not PRINT*,...). However, it still must be read in one line at a time
!This code works for the version of the ifort compiler used.

 INTEGER :: stat,timefile
 REAL,DIMENSION(3) :: a,b,d,e,f,h,j,k,m,n
 REAL,DIMENSION(2) :: c,g
 REAL ::              i,l,o
 CHARACTER(LEN=65) :: h1
 CHARACTER(LEN=63) :: h2
 CHARACTER(LEN=61) :: h3
 CHARACTER(LEN=42) :: h4
 CHARACTER(LEN=41) :: h5
 CHARACTER(LEN=264) :: header_str
 CHARACTER(LEN=29) :: fnameout
 INTEGER, INTENT(IN) :: time_no

!reopen the multipar.dat file so it can be read
 OPEN (UNIT = 19, FILE = 'multipar.dat', FORM="FORMATTED", &
        STATUS="OLD", ACTION="READ")

!choose a sensible filename, based on the final time being recorded
timefile=time_no
WRITE(fnameout,"('multipar_fmt_t',I2,'.dat')"),timefile

OPEN(UNIT=8,FILE=fnameout,FORM="FORMATTED",ACTION="WRITE")

!Write header for formatted file
h1='xstart ystart zstart t1 EKinStart alphaStart EperpStart EparStart'
h2=' vTotStart vPerpStart vParStart ExStart EyStart EzStart BxStart'
h3=' ByStart BzStart BStart mu xEnd yEnd zEnd t2 EKinEnd alphaEnd'
h4=' EperpEnd EparEnd vTotEnd vPerpEnd vParEnd'
h5=' ExEnd EyEnd EzEnd BxEnd ByEnd BzEnd BEnd'
!   12345678901234567890123456789012345678901234567890123456789012345678
!            10        20        30        40        50        60

header_str=h1 // h2 // h3 // h4 // h5
```

```
WRITE(UNIT=8,FMT='(A264)') header_str

DO

READ(UNIT=19,FMT=*,IOSTAT=stat) a
!if the input file is finished then we are done in the loop
IF (stat .lt. 0) EXIT
READ(UNIT=19,FMT=*) b
READ(UNIT=19,FMT=*) c
READ(UNIT=19,FMT=*) d
READ(UNIT=19,FMT=*) e
READ(UNIT=19,FMT=*) f
READ(UNIT=19,FMT=*) g
READ(UNIT=19,FMT=*) h
READ(UNIT=19,FMT=*) i
READ(UNIT=19,FMT=*) j
READ(UNIT=19,FMT=*) k
READ(UNIT=19,FMT=*) l
READ(UNIT=19,FMT=*) m
READ(UNIT=19,FMT=*) n
READ(UNIT=19,FMT=*) o

!if it's OK, write the line out to the new file
IF (stat .eq. 0) THEN
  WRITE(UNIT=8,FMT='(37D23.15)') a,b,c,d,e,f,g,h,i,j,k,l,m,n,o
ELSE
  PRINT*, "file status was",stat
  EXIT
END IF

END DO

!close both files
CLOSE(8)
CLOSE(19)
END SUBROUTINE

END PROGRAM SINGLE
```

B.4 products_mod.f90

Functions for the cross and dot products, used frequently when calculating fields and derivatives.

```
Module M_products

 Implicit None
```

```
 Contains

FUNCTION CROSS(A,B)

 IMPLICIT NONE
 REAL,DIMENSION(3) :: A,B,CROSS

  CROSS(1) = A(2)*B(3) - A(3)*B(2)
  CROSS(2) = A(3)*B(1) - A(1)*B(3)
  CROSS(3) = A(1)*B(2) - A(2)*B(1)

END FUNCTION CROSS

FUNCTION DOT(A,B)

 IMPLICIT NONE
 REAL, DIMENSION(3) :: A,B
 REAL :: DOT

 DOT = A(1)*B(1) + A(2)*B(2) + A(3)*B(3)

 END FUNCTION DOT

End Module M_products
```

B.5 fields_mod.f90

The `fields_mod` file is quite different for the 2D Giuliani et al. (2005) and Minoshima et al. (2010) fields, so both are included here. First, for the Giuliani et al. (2005) based traps:

B.5.1 fields_mod.f90 for 2D Giuliani et al. (2005) traps

```
Module M_fields

  Use global
  Use M_products
  Implicit None

  Contains

SUBROUTINE FIELDS(R,T,E,B,DBDX,DBDY,DBDZ,DBDT,DEDX,DEDY,DEDZ,DEDT,Vf)
!Given the position (R) and time (T), output the magnetic and
!electric fields and their derivatives and the velocity field
```

```
 REAL, DIMENSION(3), INTENT(OUT) :: B,E
 REAL, DIMENSION(3), INTENT(OUT) :: DBDX,DBDY,DBDZ,DBDT,DEDX,DEDY,DEDZ,DEDT
 REAL, INTENT(IN) :: T

 REAL, DIMENSION(3), INTENT(IN) :: R
 REAL :: X0,Y0,dX0dX,dX0dY,dY0dX,dY0dY,dX0dt,dY0dt
 REAL :: d2X0dXdY,d2X0dYdX,d2X0dX2,d2X0dY2, &
         d2Y0dXdY,d2Y0dYdX,d2Y0dX2,d2Y0dY2
 REAL :: d2X0dtdX, d2X0dXdt, d2X0dtdY, d2X0dYdt
 REAL :: d2Y0dtdX, d2Y0dXdt, d2Y0dtdY, d2Y0dYdt
 REAL :: d2X0dt2, d2Y0dt2
 REAL :: dA0dX0, dA0dY0
 REAL :: d2A0dx02,d2A0dy02,d2A0dx0dy0,d2A0dy0dx0
 REAL  :: DETERMINANT,der_det,xder_det,yder_det,zder_det
 REAL, DIMENSION(3)  :: Vf,dVfdt,dVfdx,dVfdy,dVfdz

 !!!!! Notice that X0 and Y0 and T represent dimensionless variables !!!!

  CALL SUB1_X0Y0(R,T,X0,Y0,dX0dX,dX0dY,dY0dX,dY0dY,dX0dt,dY0dt)
  CALL dA0 (X0,Y0,dA0dX0, dA0dY0)

 B(1) = (1./L) *  ( dA0dX0 * dX0dY + dA0dY0 * dY0dY )
 B(2) = (1./L) * ( -(dA0dX0 * dX0dX + dA0dY0 * dY0dX) )
 B(3) =  dY0dY * Bzfinal


B=B/B0  !B is made dimensionless

! Velocity field is also in dimensionless units
! Notice the factors L/T/Vscl
 DETERMINANT = dX0dX * dY0dY - dX0dY * dY0dX
 Vf(1)= (L/Tscl/Vscl) * ( -dX0dt*dY0dY + dX0dY*dY0dt )/DETERMINANT
 Vf(2)= (L/Tscl/Vscl) * ( -dY0dt*dX0dX + dY0dX*dX0dt )/DETERMINANT
 Vf(3)= 0.

E = -CROSS(Vf,B)   ! This electric field is dimensionless

!!!! Notice that the dimensionless electric field E(3) can also be calculated
!!!! as
! E(3) = -(1.0/Tscl)*(dA0dX0*dX0dt + dA0dY0*dY0dt)/(Vscl*B0)

!call subroutines that calculate the derivatives
CALL SUB2_X0Y0 &
(R,T,d2X0dXdY,d2X0dYdX,d2X0dX2,d2X0dY2,d2Y0dXdY,d2Y0dYdX,d2Y0dX2,d2Y0dY2)

CALL SUB3_X0Y0(R,T,d2X0dtdX,d2X0dXdt,d2X0dtdY,d2X0dYdt, &
                   d2Y0dtdX,d2Y0dXdt,d2Y0dtdY,d2Y0dYdt, &
```

```
                                        d2X0dt2,d2Y0dt2 )

CALL ddA0(X0,Y0,d2A0dx02,d2A0dy02,d2A0dx0dy0,d2A0dy0dx0)

!We calculate here time derivative of Velocity field

!!! derivative of DETERMINANT is done with respect to normalised time !!!
 der_det=d2X0dtdX*dY0dY+dX0dX*d2Y0dtdY - d2X0dtdY*dY0dX-dX0dY*d2Y0dtdX

xder_det=d2X0dX2*dY0dY+dX0dX*d2Y0dXdY-d2X0dXdY*dY0dX-dX0dY*d2Y0dX2

yder_det=d2X0dXdY*dY0dY+dX0dX*d2Y0dY2-d2X0dY2*dY0dX-dX0dY*d2Y0dXdY

zder_det=0.

!!! Time derivatives of dimensionless Vf with respect to dimensionless time!!
 dVfdt(1)= (L/Tscl/Vscl) * ( &
(-d2X0dt2*dY0dY-dX0dt*d2Y0dtdY+d2X0dtdY*dY0dt+dX0dY*d2Y0dt2)/DETERMINANT+ &
( -dX0dt*dY0dY + dX0dY*dY0dt )*(-der_det/DETERMINANT/DETERMINANT) &
)
dVfdt(2)=(L/Tscl/Vscl) * ( &
(-d2Y0dt2*dX0dX-dY0dt*d2X0dtdX+d2Y0dtdX*dX0dt+dY0dX*d2X0dt2)/DETERMINANT+ &
( -dY0dt*dX0dX + dY0dX*dX0dt )*(-der_det/DETERMINANT/DETERMINANT) &
)
dVfdt(3)= 0.
!---- SPACE DERIVATIVES: dimensionless quantities
dVfdx(1)= (L/Tscl/Vscl) * ( &
(-d2X0dXdt*dY0dY-dX0dt*d2Y0dXdY+d2X0dXdY*dY0dt+dX0dY*d2Y0dXdt)/DETERMINANT+ &
( -dX0dt*dY0dY + dX0dY*dY0dt )*(-xder_det/DETERMINANT/DETERMINANT) &
)
dVfdx(2)=(L/Tscl/Vscl) * ( &
(-d2Y0dX2*dX0dX -dY0dX*d2X0dX2 + d2Y0dX2*dX0dt + dY0dX*d2X0dXdt)/DETERMINANT+&
(-dY0dt*dX0dX + dY0dX*dX0dt )*(-xder_det/DETERMINANT/DETERMINANT) &
)
dVfdx(3)= 0.
!----
dVfdy(1)= (L/Tscl/Vscl) * ( &
(-d2X0dYdt*dY0dY-dX0dt*d2Y0dY2+d2X0dY2*dY0dt+dX0dY*d2Y0dYdt )/DETERMINANT+ &
( -dX0dt*dY0dY + dX0dY*dY0dt )*(-yder_det/DETERMINANT/DETERMINANT) &
)

dVfdy(2)=(L/Tscl/Vscl) * ( &
( -d2Y0dYdt*dX0dX -dY0dt*d2X0dYdX +d2Y0dYdX*dX0dt +dY0dX*d2X0dYdt) &
 /DETERMINANT + &
( -dY0dt*dX0dX + dY0dX*dX0dt )*(-yder_det/DETERMINANT/DETERMINANT) &
)
dVfdy(3)= 0.
!----
```

```
dVfdz(1)= 0.

dVfdz(2)= 0.

dVfdz(3)= 0.

!!!! Magnetic field derivatives in dimensional form !!!
!dBxdx
dBdx(1)=(1./L/L)*( (d2A0dx02*dx0dx+d2A0dy0dx0*dy0dx)*dx0dy +  &
dA0dx0*d2x0dxdy + (d2A0dx0dy0*dx0dx + d2A0dy02*dy0dx)*dy0dy + &
   dA0dy0*d2y0dxdy )

!dBxdy
dBdy(1)=(1./L/L)*( (d2A0dx02*dx0dy+d2A0dy0dx0*dy0dy)*dx0dy + &
dA0dx0*d2x0dy2 + (d2A0dx0dy0*dx0dy + d2A0dy02*dy0dy)*dy0dy + &
dA0dy0*d2y0dy2 )

!dBxdz
dBdz(1) = 0.

!dBydx
dBdx(2)=-(1./L/L)*( (d2A0dx02*dx0dx+d2A0dy0dx0*dy0dx)*dx0dx + &
dA0dx0*d2x0dx2 + (d2A0dx0dy0*dx0dx + d2A0dy02*dy0dx)*dy0dx + &
dA0dy0*d2y0dx2 )

!dBydy
dBdy(2) =-(1./L/L)*( (d2A0dx02*dx0dy+d2A0dy0dx0*dy0dy)*dx0dx + &
dA0dx0*d2x0dydx + (d2A0dx0dy0*dx0dy + d2A0dy02*dy0dy)*dy0dx + &
dA0dy0*d2y0dydx )

!dBydz
dBdz(2) = 0.

!dBzdx
dBdx(3)= (1./L)*d2y0dydx * Bzfinal

!dBzdy
dBdy(3)= (1./L)*d2y0dy2 *Bzfinal

!dBzdz
dBdz(3)= 0.


!dBxdt
dBdt(1)=(1./Tscl/L)*(d2A0dx02 * dx0dt * dx0dy + d2A0dy0dx0 * dy0dt *dx0dy + &
                     d2A0dx0dy0 * dx0dt * dy0dy + d2A0dy02 * dy0dt* dy0dy +  &
                     dA0dx0 * d2x0dtdy + dA0dy0 * d2y0dtdy)
```

```
!dBydt
dBdt(2)=-(1./Tscl/L)*( d2A0dx02 * dx0dt * dx0dx + d2A0dy0dx0 * dy0dt *dx0dx +&
                    d2A0dx0dy0 * dx0dt * dy0dx + d2A0dy02 * dy0dt* dy0dx +   &
                    dA0dx0 * d2x0dtdx + dA0dy0 * d2y0dtdx)

!dBzdt
dBdt(3)= (1./Tscl) * d2y0dtdy *Bzfinal

!! Make derivatives dimensionless !!!!
DBDX = (L/B0) * DBDX
DBDY = (L/B0) * DBDY
DBDZ = (L/B0) * DBDZ
DBDT = (Tscl/B0) * DBDT

!!! The dimensionless dEdt is !!
dEdt=-(cross(dVfdt,B)+cross(Vf,DBDT))

!!! The dimensionless dEdx is !!
dEdx=-(cross(dVfdx,B)+cross(Vf,DBDX))

!!! The dimensionless dEdy is !!
dEdy=-(cross(dVfdy,B)+cross(Vf,DBDY))

!!! The dimensionless dEdz is !!
dEdz=-(cross(dVfdz,B)+cross(Vf,DBDZ))

END SUBROUTINE FIELDS
!*********************************************
SUBROUTINE SUB1_X0Y0(R,T,X0,Y0,dX0dX,dX0dY,dY0dX,dY0dY,dX0dt,dY0dt)
 REAL, DIMENSION(3), INTENT(IN) :: R
 REAL, INTENT(IN)  :: T
 REAL, INTENT(OUT) :: X0, Y0, dX0dX, dX0dY, dY0dX, dY0dY, dX0dt, dY0dt
 REAL :: a=0.9,b=0.9

 X0=R(1)

If ( (1.+(R(2)/((cc*T)**esp))) .le.0.) then
!If this happens we'll have problems taking the logs below!
print*, '(1.+(R(2)/((cc*T)**esp)))=',(1.+(R(2)/((cc*T)**esp)))
print*, 'R(2)=',R(2)
print*,'T=',T
End if

 Y0=(cc*T)**esp*log (1.+(R(2)/((cc*T)**esp)))*  &
      (1.+tanh((R(2)-Lv/L)*a))*(1./2.) +           &
       (1.-tanh((R(2)-Lv/L)*b))*(1./2.)*R(2)

 dX0dX=1.
```

```
 dX0dY=0.
 dY0dX=0.
 dY0dY=1./2.*(1.+tanh((R(2)-Lv/L)*a))/(1.+R(2)/(cc*T)**esp)+         &
      1./2.*(cc*T)**esp*log(1.+R(2)/(cc*T)**esp)*                 &
      (1.-tanh((R(2)-Lv/L)*a)**2)*a-1./2.*                          &
      (1.-tanh((R(2)-Lv/L)*b)**2)*b*R(2)+1./2.-1./2.*tanh((R(2)-Lv/L)*b)

dX0dt=0.
dY0dt=1./2.*(cc*T)**esp*esp*log(1.+R(2)/(cc*T)**esp)*           &
      (1.+tanh((R(2)-Lv/L)*a))/T-1./2.*R(2)*esp*                    &
      (1.+tanh((R(2)-Lv/L)*a))/(T*(1.+R(2)/(cc*T)**esp))


END SUBROUTINE SUB1_X0Y0
!*********************************************************************
SUBROUTINE SUB2_X0Y0(R,T,                                       &
                     d2X0dXdY,d2X0dYdX,d2X0dX2,d2X0dY2, &
                     d2Y0dXdY,d2Y0dYdX,d2Y0dX2,d2Y0dY2)

REAL, DIMENSION(3), INTENT(IN) :: R
 REAL, INTENT(IN)  :: T
 REAL, INTENT(OUT) :: d2X0dXdY,d2X0dYdX,d2X0dX2,d2X0dY2
 REAL, INTENT(OUT) :: d2Y0dXdY,d2Y0dYdX,d2Y0dX2,d2Y0dY2
 REAL              :: y
 REAL              :: a=0.9,b=0.9

!because I used maple to calculate these, easier
!to call R(2) y then use that.
y=R(2)

d2y0dy2= -0.1e1 / (0.1e1 + y / (cc * t) ** esp) ** 2 * (0.1e1 + tan&
     &h((y - Lv/L) * a)) / (cc * t) ** esp / 0.2e1 + 0.1e1 / (0.1e1 + y /&
     & (cc * t) ** esp) * (0.1e1 - tanh((y - Lv/L) * a) ** 2) * a - (cc&
     &* t) ** esp * log(0.1e1 + y / (cc * t) ** esp) * tanh((y - Lv/L) * a&
     &) * (0.1e1 - tanh((y - Lv/L) * a) ** 2) * a ** 2 + tanh((y - Lv/L)&
     &* b) * (0.1e1 - tanh((y - Lv/L) * b) ** 2) * b ** 2 * y - (0.1e1&
     &- tanh((y - Lv/L) * b) ** 2) * b

d2x0dxdy = 0.

d2x0dydx = 0.

d2x0dx2 = 0.

d2x0dy2 = 0.


d2y0dxdy = 0.
```

```
d2y0dydx = 0.

d2y0dx2 = 0.

END SUBROUTINE SUB2_X0Y0

!*********************************************************************
SUBROUTINE SUB3_X0Y0(R,T,d2X0dtdX,d2X0dXdt,d2X0dtdY,d2X0dYdt, &
                         d2Y0dtdX,d2Y0dXdt,d2Y0dtdY,d2Y0dYdt, &
                                             d2X0dt2,d2Y0dt2 )
 REAL, DIMENSION(3), INTENT(IN) :: R
 REAL, INTENT(IN)  :: T
 REAL, INTENT(OUT) :: d2X0dtdX,d2X0dXdt,d2X0dtdY,d2X0dYdt
 REAL, INTENT(OUT) :: d2Y0dtdX,d2Y0dXdt,d2Y0dtdY,d2Y0dYdt
 REAL, INTENT(OUT) :: d2X0dt2, d2Y0dt2
 REAL              :: y
 REAL :: a=0.9

y=R(2)

d2x0dtdx =0.
d2x0dxdt=d2x0dtdx

d2x0dtdy =0.
d2x0dydt =d2x0dtdy

d2y0dtdx =0.
d2y0dxdt=d2y0dtdx

d2y0dtdy = 0.1e1 / (0.1e1 + y / (cc * t) ** esp) ** 2 * (0.1e1 + tanh &
     ((y - Lv/L) * a)) * y / (cc * t) ** esp * esp / t / 0.2e1 + (cc * &
     t) ** esp * esp / t * log(0.1e1 + y / (cc * t) ** esp) * (0.1e1 - &
     tanh((y - Lv/L) * a) ** 2) * a / 0.2e1 - y * esp / t / (0.1e1 + y &
     / (cc * t) ** esp) * (0.1e1 - tanh((y - Lv/L) * a) ** 2) * a / 0.2e1

d2y0dydt=d2y0dtdy

d2x0dt2 = 0.

d2y0dt2 = (cc * t) ** esp * esp ** 2 / t ** 2 * log(0.1e1 + y / (cc &
      * t) ** esp) * (0.1e1 + tanh((y - Lv/L) * a)) / 0.2e1 - (cc * t) ** &
      esp * esp / t ** 2 * log(0.1e1 + y / (cc * t) ** esp) * (0.1e1 +  &
      tanh((y - Lv/L) * a)) / 0.2e1 - esp ** 2 / t ** 2 * y / (0.1e1 + y  &
      / (cc * t) ** esp) * (0.1e1 + tanh((y - Lv/L) * a)) / 0.2e1 + y *   &
     esp / t ** 2 / (0.1e1 + y / (cc * t) ** esp) * (0.1e1 + tanh((y -  &
     Lv/L) * a)) / 0.2e1 - y ** 2 * esp ** 2 / t ** 2 / (0.1e1 + y / (cc  &
      * t) ** esp) ** 2 * (0.1e1 + tanh((y - Lv/L) * a)) / (cc * t) **    &
```

```
     esp / 0.2e1

END SUBROUTINE SUB3_X0Y0

!*****************************************************
SUBROUTINE dA0 (X0,Y0,dA0dX0, dA0dY0)

 REAL, INTENT(IN)  :: X0,Y0
 REAL, INTENT(OUT) :: dA0dX0, dA0dY0

!Derivatives of the flux function at final time,
!i.e. the magnetic field in y and x to within a sign!

 dA0dX0 = 32*c1*(Y0*L+d)*L**3*X0/  &
 ((4*L**2*X0**2-4*L**2*X0+L**2+4*Y0**2*L**2+8*Y0*L*d+4*d**2)* &
 (4*L**2*X0**2+4*L**2*X0+L**2+4*Y0**2*L**2+8*Y0*L*d+4*d**2))

dA0dY0 = 4*c1*L**2*  &
 (-4*L**2*X0**2+L**2+4*Y0**2*L**2+8*Y0*L*d+4*d**2)/  &
 ((4*L**2*X0**2-4*L**2*X0+L**2+4*Y0**2*L**2+8*Y0*L*d+4*d**2)*  &
 (4*L**2*X0**2+4*L**2*X0+L**2+4*Y0**2*L**2+8*Y0*L*d+4*d**2))

END SUBROUTINE dA0
!*****************************************************************
SUBROUTINE ddA0 (X0,Y0,d2A0dx02, d2A0dy02, d2A0dx0dy0, d2A0dy0dx0 )

!second derivatives of flux function (first derivs of magnetic field)

 REAL, INTENT(OUT) :: d2A0dx02, d2A0dy02, d2A0dx0dy0, d2A0dy0dx0
 REAL, INTENT(IN)  :: X0,Y0

 d2A0dx02 = 32 * c1 * (y0 * L + d) * L ** 3 / (4 * L ** 2 * x0 ** 2 - &
     4 * L ** 2 * x0 + L ** 2 + 4 * y0 ** 2 * L ** 2 + 8 * y0 * L * d + &
      4 * d ** 2) / (4 * L ** 2 * x0 ** 2 + 4 * L ** 2 * x0 + L ** 2 +  &
     4 * y0 ** 2 * L ** 2 + 8 * y0 * L * d + 4 * d ** 2) - 32 * c1 * (y&
    &0 * L + d) * L ** 3 * x0 / (4 * L ** 2 * x0 ** 2 - 4 * L ** 2 * x0 &
      + L ** 2 + 4 * y0 ** 2 * L ** 2 + 8 * y0 * L * d + 4 * d ** 2) ** &
      2 / (4 * L ** 2 * x0 ** 2 + 4 * L ** 2 * x0 + L ** 2 + 4 * y0 **  &
     2 * L ** 2 + 8 * y0 * L * d + 4 * d ** 2) * (8 * L ** 2 * x0 - 4 * &
      L ** 2) - 32 * c1 * (y0 * L + d) * L ** 3 * x0 / (4 * L ** 2 * x0 &
      ** 2 - 4 * L ** 2 * x0 + L ** 2 + 4 * y0 ** 2 * L ** 2 + 8 * y0 * &
      L * d + 4 * d ** 2) / (4 * L ** 2 * x0 ** 2 + 4 * L ** 2 * x0 + L &
      ** 2 + 4 * y0 ** 2 * L ** 2 + 8 * y0 * L * d + 4 * d ** 2) ** 2 * &
      (8 * L ** 2 * x0 + 4 * L ** 2)

d2A0dy02 = 4 * c1 * L ** 2 * (8 * y0 * L ** 2 + 8 * L * d) / (4 * L &
     ** 2 * x0 ** 2 - 4 * L ** 2 * x0 + L ** 2 + 4 * y0 ** 2 * L ** 2 + &
      8 * y0 * L * d + 4 * d ** 2) / (4 * L ** 2 * x0 ** 2 + 4 * L ** 2 &
```

```
      * x0 + L ** 2 + 4 * y0 ** 2 * L ** 2 + 8 * y0 * L * d + 4 * d ** &
     2) - 4 * c1 * L ** 2 * (-4 * L ** 2 * x0 ** 2 + L ** 2 + 4 * y0 ** &
      2 * L ** 2 + 8 * y0 * L * d + 4 * d ** 2) / (4 * L ** 2 * x0 ** 2 &
      - 4 * L ** 2 * x0 + L ** 2 + 4 * y0 ** 2 * L ** 2 + 8 * y0 * L *  &
     d + 4 * d ** 2) ** 2 / (4 * L ** 2 * x0 ** 2 + 4 * L ** 2 * x0 + L &
      ** 2 + 4 * y0 ** 2 * L ** 2 + 8 * y0 * L * d + 4 * d ** 2) * (8 * &
      y0 * L ** 2 + 8 * L * d) - 4 * c1 * L ** 2 * (-4 * L ** 2 * x0 ** &
      2 + L ** 2 + 4 * y0 ** 2 * L ** 2 + 8 * y0 * L * d + 4 * d ** 2)  &
     / (4 * L ** 2 * x0 ** 2 - 4 * L ** 2 * x0 + L ** 2 + 4 * y0 ** 2 * &
      L ** 2 + 8 * y0 * L * d + 4 * d ** 2) / (4 * L ** 2 * x0 ** 2 + 4 &
      * L ** 2 * x0 + L ** 2 + 4 * y0 ** 2 * L ** 2 + 8 * y0 * L * d +  &
     4 * d ** 2) ** 2 * (8 * y0 * L ** 2 + 8 * L * d)

d2A0dx0dy0 = 32 * c1 * L ** 4 * x0 / (4 * L ** 2 * x0 ** 2 - 4 * L ** &
     2 * x0 + L ** 2 + 4 * y0 ** 2 * L ** 2 + 8 * y0 * L * d + 4 * d ** &
      2) / (4 * L ** 2 * x0 ** 2 + 4 * L ** 2 * x0 + L ** 2 + 4 * y0 ** &
      2 * L ** 2 + 8 * y0 * L * d + 4 * d ** 2) - 32 * c1 * (y0 * L + d &
     ) * L ** 3 * x0 / (4 * L ** 2 * x0 ** 2 - 4 * L ** 2 * x0 + L ** 2 &
      + 4 * y0 ** 2 * L ** 2 + 8 * y0 * L * d + 4 * d ** 2) ** 2 / (4 * &
      L ** 2 * x0 ** 2 + 4 * L ** 2 * x0 + L ** 2 + 4 * y0 ** 2 * L **  &
     2 + 8 * y0 * L * d + 4 * d ** 2) * (8 * y0 * L ** 2 + 8 * L * d) - &
      32 * c1 * (y0 * L + d) * L ** 3 * x0 / (4 * L ** 2 * x0 ** 2 - 4  &
     * L ** 2 * x0 + L ** 2 + 4 * y0 ** 2 * L ** 2 + 8 * y0 * L * d + 4 &
      * d ** 2) / (4 * L ** 2 * x0 ** 2 + 4 * L ** 2 * x0 + L ** 2 + 4  &
     * y0 ** 2 * L ** 2 + 8 * y0 * L * d + 4 * d ** 2) ** 2 * (8 * y0 * &
      L ** 2 + 8 * L * d)

d2A0dy0dx0 = -32 * c1 * L ** 4 * x0 / (4 * L ** 2 * x0 ** 2 - 4 * L ** &
      2 * x0 + L ** 2 + 4 * y0 ** 2 * L ** 2 + 8 * y0 * L * d + 4 * d ** &
      2) / (4 * L ** 2 * x0 ** 2 + 4 * L ** 2 * x0 + L ** 2 + 4 * y0 **&
      2 * L ** 2 + 8 * y0 * L * d + 4 * d ** 2) - 4 * c1 * L ** 2 * (- &
     4 * L ** 2 * x0 ** 2 + L ** 2 + 4 * y0 ** 2 * L ** 2 + 8 * y0 * L  &
     * d + 4 * d ** 2) / (4 * L ** 2 * x0 ** 2 - 4 * L ** 2 * x0 + L ** &
      2 + 4 * y0 ** 2 * L ** 2 + 8 * y0 * L * d + 4 * d ** 2) ** 2 / (4 &
      * L ** 2 * x0 ** 2 + 4 * L ** 2 * x0 + L ** 2 + 4 * y0 ** 2 * L **&
      2 + 8 * y0 * L * d + 4 * d ** 2) * (8 * L ** 2 * x0 - 4 * L ** 2 &
     ) - 4 * c1 * L ** 2 * (-4 * L ** 2 * x0 ** 2 + L ** 2 + 4 * y0 **  &
     2 * L ** 2 + 8 * y0 * L * d + 4 * d ** 2) / (4 * L ** 2 * x0 ** 2  &
     - 4 * L ** 2 * x0 + L ** 2 + 4 * y0 ** 2 * L ** 2 + 8 * y0 * L * d &
      + 4 * d ** 2) / (4 * L ** 2 * x0 ** 2 + 4 * L ** 2 * x0 + L ** 2  &
     + 4 * y0 ** 2 * L ** 2 + 8 * y0 * L * d + 4 * d ** 2) ** 2 * (8 *  &
     L ** 2 * x0 + 4 * L ** 2)

END SUBROUTINE ddA0

END MODULE M_fields
```

B.5.2 fields_mod.f90 for Minoshima et al. (2010) traps

The way magnetic and electric fields are prescribed in the Minoshima et al. (2010) paper is different to the Giuliani et al. (2005) paper. This means that the coordinate transformation is not required. The following is `fields_mod.f90` for the work discussed in chapter 5.

```
Module M_fields

  Use global
  Use M_products

  Implicit None

  Contains

SUBROUTINE FIELDS(R,T,E,B,DBDX,DBDY,DBDZ,DBDT,DEDX,DEDY,DEDZ,DEDT,Vf)


 REAL, DIMENSION(3), INTENT(OUT) :: B,E
 REAL, DIMENSION(3), INTENT(OUT) :: DBDX,DBDY,DBDZ,DBDT,DEDX,DEDY,DEDZ,DEDT
 REAL, INTENT(IN) :: T
 REAL, DIMENSION(3), INTENT(IN) :: R
 REAL, DIMENSION(3),INTENT(OUT) :: Vf


 REAL :: x,y,z,a,xf,dxfdt,dadt,dadxf
 REAL,DIMENSION(3) :: dBda,dEda

x=R(1)
y=R(2)
z=R(3)

!easiest to work out these in MAPLE and paste here
!(after using the convert,fortran function in MAPLE)

dxfdt = vp / vscl * exp(-(t - tp) ** 2 / tau ** 2 / 0.2D1)
xf = 0.1D1 / vscl * vp * sqrt(0.3141592654D1) * sqrt(0.2D1) * tau *  &
 erf(sqrt(0.2D1) / tau * t / 0.2D1 - tp / tau * sqrt(0.2D1) / 0.2D1) / &
 0.2D1 + xf0 + 0.1D1 / vscl * vp * sqrt(0.3141592654D1) * sqrt(0.2D1) * &
 tau * erf(tp / tau * sqrt(0.2D1) / 0.2D1) / 0.2D1
a = (dble(xf) + sqrt(dble(xf ** 2 + 1))) * dble(xf)
dadxf = dble((1 + (xf ** 2 + 1) ** (-0.1D1 / 0.2D1) * xf) * xf) + &
 dble(xf) + sqrt(dble(xf ** 2 + 1))

b(1) = -(x ** 2 - (z + 1) ** 2) / (x ** 2 + (z + 1) ** 2) ** 2 - &
 1 / (a + 1) ** 2
b(2) = 0
b(3) = -2 * x * (z + 1) / (x ** 2 + (z + 1) ** 2) ** 2
```

```
dbdx(1) = -2 * x / (x ** 2 + (z + 1) ** 2) ** 2 + 4 * &
 (x ** 2 - (z + 1) ** 2) / (x ** 2 + (z + 1) ** 2) ** 3 * x
dbdx(2) = 0
dbdx(3) = -2 * (z + 1) / (x ** 2 + (z + 1) ** 2) ** 2 + &
8 * x ** 2 * (z + 1) / (x ** 2 + (z + 1) ** 2) ** 3

dbdy(1) = 0
dbdy(2) = 0
dbdy(3) = 0

dbdz(1) = -(-2 * z - 2) / (x ** 2 + (z + 1) ** 2) ** 2 + &
 2 * (x ** 2 - (z + 1) ** 2) / (x ** 2 + (z + 1) ** 2) ** 3 * (2 * z + 2)
dbdz(2) = 0
dbdz(3) = -2 * x / (x ** 2 + (z + 1) ** 2) ** 2 +  &
 4 * x * (z + 1) / (x ** 2 + (z + 1) ** 2) ** 3 * (2 * z + 2)

dbda(1) = 2 / (a + 1) ** 3
dbda(2) = 0
dbda(3) = 0

e(1) = 0
e(2) = 2 * dxfdt * (2 * xf + (2 * xf ** 2 + 1) * &
 (xf ** 2 + 1) ** (-0.1D1 / 0.2D1)) * z / (a + 1) ** 3
e(3) = 0

dedx(1) = 0
dedx(2) = 0
dedx(3) = 0

dedy(1) = 0
dedy(2) = 0
dedy(3) = 0

dedz(1) = 0
dedz(2) = 2 * dxfdt * (2 * xf + (2 * xf ** 2 + 1) * &
 (xf ** 2 + 1) ** (-0.1D1 / 0.2D1)) / (a + 1) ** 3
dedz(3) = 0

deda(1) = 0
deda(2) = -6 * dxfdt * (2 * xf + (2 * xf ** 2 + 1) * &
 (xf ** 2 + 1) ** (-0.1D1 / 0.2D1)) * z / (a + 1) ** 4
deda(3) = 0

!other bits we need, easier to put here than working out in maple
dadt=dadxf*dxfdt

dBdt=dBda*dadt
```

```
dEdt=dEda*dadt

!can only calculate vf parallel to field
vf=cross(E,B)/(B(1)**2+B(2)**2+B(3)**2)

END SUBROUTINE FIELDS
!*******************************************

END MODULE M_fields
```

B.6 derivs_mod.f90

This uses the time, particle position, magnetic moment and parallel velocity to calculate the time derivatives of vpar and guiding centre position using the guiding centre equations from Northrop (1963).

```
Module M_derivs

 Use Global
 Use M_fields

 IMPLICIT NONE

CONTAINS

 SUBROUTINE DERIVS (T, R, DRDT, VPAR, DVPARDT,MU)

 !This part of the program simply works out the right hand side of the 6
 !coupled ODEs. The values of q, m, and the electromagnetic field are to
 !be included in the code.


 IMPLICIT NONE
 REAL, INTENT(IN) :: T,MU
 REAL, INTENT(IN) :: VPAR
 REAL, INTENT(OUT) :: DVPARDT
 REAL, DIMENSION(3), INTENT(IN) :: R
 REAL, DIMENSION(3),INTENT(OUT) :: DRDT

 REAL, DIMENSION(3) :: B,E,Vf
 REAL, DIMENSION(3) :: DBDX,DBDY,DBDZ,DBDT,DEDX,DEDY,DEDZ,DEDT
 REAL, DIMENSION(3) :: GRADB,DBETADT,DBETADX,DBETADY,DBETADZ
 REAL, DIMENSION(3) :: EDRIFT, DUEDX,DUEDY,DUEDZ,DUEDT
 REAL :: MODB, DMODBDS, EPAR,GRADBT
 REAL, DIMENSION(3) :: GRADDRIFT,DBETADS,UEGRADB,UEGRADUE,DUEDS
 REAL, DIMENSION(3) :: ACCDRIFT, OTHERS
```

```
 REAL, DIMENSION(3) :: SCRAE

 CALL FIELDS(R,T,E,B,DBDX,DBDY,DBDZ,DBDT,DEDX,DEDY,DEDZ,DEDT,Vf)
 MODB = SQRT(B(1)**2 + B(2)**2 + B(3)**2)

 EPAR = (DOT(E,B))/MODB

 GRADB(1) = (DOT(B,DBDX))/MODB
 GRADB(2) = (DOT(B,DBDY))/MODB
 GRADB(3) = (DOT(B,DBDZ))/MODB
 GRADBT = (DOT(B,DBDT))/MODB

!We'll call Bx/B BETAX. Got to call it something.
!So these are arrays of three (BETAX,BETAY,BETAZ)

 DBETADX = DBDX/MODB - B*GRADB(1)/MODB**2
 DBETADY = DBDY/MODB - B*GRADB(2)/MODB**2
 DBETADZ = DBDZ/MODB - B*GRADB(3)/MODB**2
 DBETADT = DBDT/MODB - B*GRADBT/MODB**2

 EDRIFT = (CROSS(E,B))/(MODB**2)

 DUEDX = (CROSS(DEDX,B) + CROSS(E,DBDX) - 2.*EDRIFT*DOT(B,DBDX))/(MODB**2)
 DUEDY = (CROSS(DEDY,B) + CROSS(E,DBDY) - 2.*EDRIFT*DOT(B,DBDY))/(MODB**2)
 DUEDZ = (CROSS(DEDZ,B) + CROSS(E,DBDZ) - 2.*EDRIFT*DOT(B,DBDZ))/(MODB**2)
 DUEDT = (CROSS(DEDT,B) + CROSS(E,DBDT) - 2.*EDRIFT*DOT(B,DBDT))/(MODB**2)

 DMODBDS=dot(B,B(1)*DBDX+B(2)*DBDY+B(3)*DBDZ)/(MODB**2)

 GRADDRIFT = CROSS(B,GRADB)/(MODB**2)

 DBETADS = (B(1)*DBETADX + B(2)*DBETADY + B(3)*DBETADZ)/(MODB)

 UEGRADB = (EDRIFT(1)*DBETADX + EDRIFT(2)*DBETADY + EDRIFT(3)*DBETADZ)

 DUEDS = (B(1)*DUEDX + B(2)*DUEDY + B(3)*DUEDZ)/(MODB)

 UEGRADUE = (EDRIFT(1)*DUEDX + EDRIFT(2)*DUEDY + EDRIFT(3)*DUEDZ)

!All the acceleration drift terms, to be crossed with B
 ACCDRIFT = VPAR*DBETADT + (VPAR**2)*DBETADS + VPAR*UEGRADB + DUEDT &
    & + VPAR*DUEDS + UEGRADUE

!all the terms that make up the last bit of the parallel equation
 OTHERS = DBETADT + VPAR*DBETADS + UEGRADB

!The equations of motion
```

```
 DVPARDT = ((Q*L*(B0**2))/(M*E0))*EPAR - MU*DMODBDS + DOT(EDRIFT,OTHERS)

 DRDT = EDRIFT + ((M*E0)/(Q*L*B0**2))*(MU*GRADDRIFT + &
  CROSS(B,ACCDRIFT)/(MODB**2)) + VPAR*(B/MODB)

 END SUBROUTINE DERIVS

End Module M_derivs
```

B.7 rkdrive_mod.f90

This subroutine has a loop that runs the RK stepper for the particle until it has either escaped the trap or the trap has collapsed (final time reached).

```
Module M_driver
    Use global
    Use M_derivs
    Use M_rkqs
 Implicit None

  Contains

  Subroutine RKDRIVE(RSTART,VPARSTART,MU,T1,T2,EPS,H1,NOK,NBAD,TT,S,TOTAL)
 !#####################################################################
 !Description from P. Giuliani:
 !Driver routine with adaptive stepsize control. It goes from T1 to
 !T2 with accuracy eps. Hmin is the minimum allowed stepsize. nok and
 !nbad are the number of good and bad (i.e. retried) steps. RSTART is
 !replaced by the end values.
!#####################################################################

 IMPLICIT NONE

 INTEGER :: NOK, NBAD
 REAL, INTENT(IN) :: EPS, H1,MU
 REAL, INTENT(INOUT) :: T1,T2
 REAL, INTENT(INOUT), DIMENSION(3) :: RSTART
 REAL,PARAMETER :: TINY=1.0e-20
 INTEGER :: I, J,NSTP
 REAL :: H, HDID, HNEXT, T
 REAL, DIMENSION(3) :: DRDT, R
 REAL :: VPAR, VPARSTART, DVPARDT

 REAL, DIMENSION(3) :: E,B,DBDX,DBDY,DBDZ,DBDT,DEDX,DEDY,DEDZ,DEDT,Vf
 REAL, DIMENSION(3) :: bb
```

```
 REAL :: efct,e1,e2,e3
 REAL, DIMENSION(4) :: RSCAL

 REAL, DIMENSION(NKEEPMAX) :: TT
 REAL, DIMENSION(NKEEPMAX,3) :: S, TOTAL
 REAL, DIMENSION(3) :: ENERGY
 REAL, DIMENSION(3) :: UE

  CHARACTER(LEN=14) :: rvfilename

 T=T1
 TT(1) = T1
 H=SIGN(H1,T2-T1)
 NOK = 0
 NBAD = 0
 DO I = 1,3
   R(I) = RSTART(I)
   S(1,I) = RSTART(I)
 ENDDO
   VPAR = VPARSTART
   DO I=1,3
   TOTAL(1,I) = 0.
   END DO

 efct=1./abs(Q)

!make a unique name for the file if it will be written
if (writervs .eq. 1) WRITE(rvfilename,"('RV',I8.8,'.dat')"),uniqueparticleid
if (writervs .eq. 1)  open(29,file=rvfilename,recl=1024,status='unknown')


 CALL DERIVS (T, R, DRDT, VPAR, DVPARDT,MU)
 CALL FIELDS(R,T,E,B,DBDX,DBDY,DBDZ,DBDT,DEDX,DEDY,DEDZ,DEDT,Vf)
 bb=B/sqrt(dot(B,B))
 UE=(E0/B0)*cross(E,B)/dot(B,B)


!output the initial conditions to the RV***.dat file
  e1=efct*0.5*M*(Vscl*Vpar)**2
  e2=efct*M*(Vscl**2)*MU*sqrt(dot(B,B))
  e3=efct*0.5*M*dot(UE,UE)
if (writervs .eq. 1)   write(29,*)Tscl*(T-T1),                          &   !1
             R,                                    &   !2,3,4
             VPAR,                                 &   !5
             MU*sqrt(dot(B,B)),                    &   !6
             sum((DRDT-VPAR*bb)**2),               &   !7
             Vscl*B0*E,                            &   !8,9,10
             B0*B,                                 &   !11,12,13
```

```
             e1,                                      &   !14
             e2,                                      &   !15
             e3,                                      &   !16
             e1+e2+e3,                                &   !17
             efct*Q*E0*(L/Tscl)*dot(DRDT,E),          &   !18
             efct*(M*Vscl*Vscl/Tscl)*MU*dot(B,DBDT)/sqrt(dot(B,B)), & !19
             Vscl*Vf,                                 &   !20,21,22
             H                                            !23

!***************************** Main Time-Loop Starts **************

 DO NSTP = 1, NSTPMAX
   CALL DERIVS (T, R, DRDT, VPAR, DVPARDT,MU)

   DO I = 1,3       !Scaling used to monitor accuracy
     RSCAL(I) = ABS(R(I))+ABS(H*DRDT(I)) + TINY
  ENDDO
     RSCAL(4)=ABS(VPAR)+ABS(H*DVPARDT) + TINY

    RSCAL =1


    IF((T+H-T2)*(T+H-T1) > 0.) THEN
       H=T2-T   !if stepsize can overshoot, decrease
    END IF

!update values using RK method
    CALL RKQS(R,DRDT,VPAR,DVPARDT,T,H,MU,EPS,RSCAL,HDID,HNEXT)

    IF (HDID == H) THEN
      NOK = NOK+1
    ELSE
      NBAD = NBAD+1
    ENDIF

!This is for storing every NSTORE step
  IF (MOD(NSTP,NSTORE)==0) THEN
    TT((NSTP/NSTORE)+1) = T

 CALL DERIVS (T, R, DRDT, VPAR, DVPARDT,MU)
 CALL FIELDS(R,T,E,B,DBDX,DBDY,DBDZ,DBDT,DEDX,DEDY,DEDZ,DEDT,Vf)
 bb=B/sqrt(dot(B,B))
 UE=(E0/B0)*cross(E,B)/dot(B,B)

      ENERGY(1)=VPAR**2
      ENERGY(2)=MU*sqrt(dot(B,B))
      ENERGY(3)=sum((DRDT-VPAR*B/sqrt(dot(B,B)))**2)
```

```
    DO I = 1,3
      S((NSTP/NSTORE)+1,I) = R(I)
    TOTAL((NSTP/NSTORE)+1,I) = ENERGY(I)
    ENDDO

  e1=efct*0.5*M*(Vscl*Vpar)**2
  e2=efct*M*(Vscl**2)*MU*sqrt(dot(B,B))
  e3=efct*0.5*M*dot(UE,UE)

!output the points from this step
  if (writervs .eq. 1)  write(29,*)Tscl*(T-T1),     &   !1
             R,                                     &   !2,3,4
             VPAR,                                  &   !5
             MU*sqrt(dot(B,B)),                     &   !6
             sum((DRDT-VPAR*bb)**2),                &   !7
             Vscl*B0*E,                             &   !8,9,10
             B0*B,                                  &   !11,12,13
             e1,                                    &   !14
             e2,                                    &   !15
             e3,                                    &   !16
             e1+e2+e3,                              &   !17
             efct*Q*E0*(L/Tscl)*dot(DRDT,E),        &   !18
             efct*(M*Vscl*Vscl/Tscl)*MU*dot(B,DBDT)/sqrt(dot(B,B)), & !19
             Vscl*Vf,                               &   !20,21,22
             H                                          !23

ENDIF


    IF((T-T2)*(T2-T1) >= 0.) THEN         !Are we done?
      DO I = 1,3
        RSTART(I)=R(I)
      ENDDO
      VPARSTART = VPAR
      RETURN                             !normal exit
    ENDIF



!there is also chance to put code in here to stop if the particle
!escapes the bottom of the trap (to the footpoints) similar to below:

!Particle leaves the box if y value is too big
! IF(R(2) <= 0.) THEN
!    DO I = 1,3
!        RSTART(I)=R(I)
!     ENDDO
!    T2 = T
```

```
!     VPARSTART = VPAR
!      RETURN
!     ENDIF


     H=HNEXT


 ENDDO !if we get to nstpmax...
 PRINT *, 'too many steps in odeint'
 STOP
!Note: this point was never reached for any particle discussed in this thesis
!(nstpmax was always sufficient for the particle to escape the trap or the
!trap to collapse)
 RETURN

 End Subroutine RKDRIVE

End Module M_driver
```

B.8 Runge-Kutta stepper

B.8.1 RKQS

The `rkqs` subroutine is based on the adaptive step size Runge-Kutta 4th/5th order code from Press et al. (1986). The subroutine is called by
`RKQS(R,DRDT,VPAR,DVPARDT,T,HTRY,MU,EPS,RSCAL,HDID,HNEXT)`
and the variables passed to this subroutine have the following meaning.

Variable	in/output	Description
R	in & out	Input and output variables. R and DRDT have dimension 3.
DRDT		
VPAR		
DVPARDT		
T		
HTRY	in	Step size to try first
MU	in	Particle magnetic moment. Constant for a particle so not updated
EPS	in	required accuracy for all values
RSCAL	in	required accuracy of R and VPAR (dimension 4; 3 for R, 1 for VPAR)
HDID	out	step size that was actually used
HNEXT	out	step size for next step

The RKQS routine returns one step that has an error that is acceptably small. This means that several step sizes may have been tried. The main purpose of the RKQS routine is to control the step size. The step size is made smaller if the error is too large, and made bigger if the error is small (to save taking unnecessary steps).

There is a limit on how small the step size can get. This is required because as the particle comes towards a turning point smaller steps become necessary and the code would keep trying a smaller step until it had reached machine precession.

If the step size becomes too small, the code fails with a message. This is triggered if the variable T is the same before and after taking a step.

The actual RK step is done in another subroutine, RKCK, called from within RKQS.

B.8.2 RKCK

This subroutine is called using

```
RKCK(R,DRDT,VPAR,DVPARDT, T,H,MU,ROUT,VPAROUT,RERR)
```

This takes one Runge-Kutta step, given R and VPAR and their time derivatives at time T. The stepsize is H so the new variables are calculated for time T+H. It calculates a fifth and fourth order solution and gives the difference (error) as RERR. RERR has dimension 4, 3 for the error in DRDT and 1 for the error in VPAR. ROUT and VPAROUT are the newly calculated values at time T+H.

Appendix C

IDL routines

These are a selection of IDL routines I wrote to help with some of the data analysis and visualisation. There are many modifications that could be made to make these better (e.g. colpoints has a loop that is not necessary to plot individual points as the 'color' can be an array of values).

Some of these are fudges to get around the way IDL works (e.g. unique & plot_big3dbox).

C.1 colpoints.pro

This procedure draws a plot with coloured points representing different values. A small modification can be made to make the plotting area 3D. By default this uses the 'nicect' colour table, a short procedure that loads a colour table with black and white at the start and end respectively.

Required Arguments:	
xdata,ydata	x and y data to plot
colordata	data to use for colours
Optional Arguments:	
xtitle,ytitle	x and y titles
title	title for plot
coltitle	title above colourbar
psym	symbol to plot with, defaults to 3, dot
fillsq	use a filled square to plot
collog	use a logarithmic scale for colour
reloadct	colour table number to load after outputting background
noctload	use the current colourtable, not nicect

```
pro colpoints,xdata,ydata,colordata, xtitle=xtitle,ytitle=ytitle,title=title,$
```

```
  coltitle=coltitle, psym=psym, fillsq=fillsq,collog=collog,$
  reloadct=reloadct, charsize=charsize, _Extra=extra

if not keyword_set(noctload) then begin ;load the nice colour table
tvlct,rstore,gstore,bstore,/get
nicect
endif

plot,[1],[1],psym=3,xtitle=xtitle,ytitle=ytitle,title=title, $
  xrange=[min(xdata),max(xdata)], yrange=[min(ydata),max(ydata)],$
  Position=[0.15,0.15,.75,.95],/nodata,charsize=charsize,_Extra=extra

IF keyword_set(reloadct) then loadct,reloadct

;use linear or log colourbar?
IF keyword_set(collog) then begin
 zcolors=BytScl(alog10(colordata),Top=!D.Table_Size-3)+1b
 Colorbar, /YLOG, Range=[min(colordata),max(colordata)],  /Vertical, $
    Position=[0.85,0.15,0.90,0.95],Format='(E12.2)',Title=coltitle,$
    bottom=1b,ncolors=!D.Table_size-3,charsize=charsize
endif else begin
 zcolors=BytScl(colordata,Top=!D.Table_Size-3)+1b
  ;(remove 1 for 0 index, 2 for black/white bg/fg colours)
 Colorbar,Position=[0.85,0.15,0.90,0.95], $
    Range=[min(colordata),max(colordata)],$
    /Vertical,Format='(E12.2)',Title=coltitle,bottom=1b,$
    ncolors=!D.Table_size-3,charsize=charsize
endelse

IF not keyword_set(psym) then psym=3 ;default to dot

IF keyword_set(fillsq) then begin
  psym=8
  usersym,[-1,-1,1,1,-1],[-1,1,1,-1,-1],/fill
endif

for j=0L,(n_elements(xdata)-1L) DO BEGIN
  plots,xdata[j],ydata[j],psym=psym,color=zcolors[j]
endfor

;reload previous colour table if required
if not keyword_set(noctload) then tvlct,rstore,gstore,bstore

end
```

C.2 localmax.pro

This returns the indices of local maximums in data, by considering the values immediately before and after. Used in this thesis to find turning points for particles. Could be used to find minimums in array x, say by using `localmax(-x)`, or both maximums and minimums using `localmax(abs(x))`.

Required Argument:

arrvals array to search.

```
function localmax,arrvals

;returns array positions of local maxima of arrvals

madearray=0

for i=1L,n_elements(arrvals)-2 do begin
 if arrvals[i] gt arrvals[i-1] and arrvals[i] gt arrvals[i+1] then begin
  if madearray eq 0 then begin
   maxs=i
   madearray=1
  endif else maxs=[maxs,i]
 endif
endfor

return, maxs

end
```

C.3 unique.pro

This is an easier to use and remember form of the `uniq` function. This returns an array of all the unique values in an array. Works nicely for printing out unique values, e.g. `print,unique(x)`.

Required Argument:

array array to search through

Optional Argument:

index used for returning the indexes of the first appearance of each of the unique values

```
FUNCTION unique,array,index=index
;returns the unique values in the array (via sort and uniq).
;Optional value index gives the indices of these (as uniq)

  index=UNIQ(array, SORT(array))
  unique=array[index]
```

```
return,unique

END FUNCTION unique

end
```

C.4 plot_big3dbox.pro

The `plot_3dbox` has a maximum number of data it can handle. This procedure gets around it by only plotting the extremes of data with `plot_3dbox` (so 6 points) then overplotting with `plots`. Arguments are the same as `plot_3dbox` as everything is passed onto this and the `plots` commands.

```
pro plot_big3dbox,xdata,ydata,zdata,psym=psym,_Extra=extra

t=max(xdata,maxpos1,subscript_min=minpos1)
t=max(ydata,maxpos2,subscript_min=minpos2)
t=max(zdata,maxpos3,subscript_min=minpos3)

points=[maxpos1[0],maxpos2[0],maxpos3[0],minpos1[0],minpos2[0],minpos3[0]]

plot_3dbox,xdata[points],ydata[points],zdata[points],/save,psym=3,_Extra=extra

if not keyword_set(psym) then psym=0

plots,xdata,ydata,zdata,/t3d,psym=psym,_Extra=extra

end
```

C.5 Plotting many graphs as one figure

This code plots several graphs next to each other. See Fig. 2.7 for an example of output.

Each graph represents one starting point (x,y) and the graph is of the energy ratio vs the initial pitch angle. Required variables are `xstart`, `ystart`, `alphastart`, `ekinend` and `tend`, which can all come from a multipar file that has been read into a structure `t` before running the code below.

If there are any particles that have escaped (i.e. the endtime is less than the maximum endtime for particles) then they are plotted in red.

Number of plots along and up the page can be set using `x_graphs` and `y_graphs` respectively. It is recommended that these match up with the number of unique x and y starting positions in multipar, but specific points could be selected first then used in this code, as done in some comments below with `selectedenergy`.

```
;selectedenergylist=unique(t.ekinstart)

set_plot,'PS'
device,/color,/encapsulated,bits=8

;loop to plot graphs with same initial energy
;for i=0,n_elements(selectedenergylist)-1 do begin
;selectedenergy=selectedenergylist[i]

xstart=t.xstart;[where(t.ekinstart eq selectedenergy)]
ystart=t.ystart;[where(t.ekinstart eq selectedenergy)]
alphastart=t.alphastart;[where(t.ekinstart eq selectedenergy)]
ekinend=t.ekinend/t.ekinstart;[where(t.ekinstart eq selectedenergy)]
tend=t.tend;[where(t.ekinstart eq selectedenergy)]

;number of graphs in x,y direction
x_graphs=8
y_graphs=11

;size of top/bottom space relative to size of height of one graph
topsize=0.1
bottomsize=0.5

;size of left/right space relative to length of one graph
leftsize=0.5
rightsize=0.2

;width/height of each graph
graphwidth=1.0/(x_graphs+leftsize+rightsize)
graphheight=1.0/(y_graphs+topsize+bottomsize)

uniquex=unique(xstart)
uniquey=unique(ystart)

xrange=[min(alphastart),max(alphastart)]
yrange=[min(ekinend),max(ekinend)]

;need to know maximum particle time so can see which have escaped
maxt=max(tend)

ctload,0;,/reverse
```

```
;use this to output to screen/JPG screen capture
;window,0,xsize=1280,ysize=1024

;or use EPS output
;device,filename=string('alpha_pos_ek',i,'.eps',format='(A,I3.3,A)')
device,filename='alpha_pos_ekratio.eps'


xyouts,(leftsize+x_graphs/2.)*graphwidth,bottomsize*graphheight*0.3, $
   "Pitch Angle (degrees)",alignment=.5,/normal,charsize=0.3*1.7
xyouts,leftsize*graphwidth*0.3,(bottomsize+y_graphs/2.)*graphheight, $
  "Ratio of final/initial energy",alignment=0.5,/normal,charsize=0.3*1.7, $
  orientation=90

;xyouts,0,0,string("Initial Energy = ",selectedenergy,format='(A,E10.4)'), $
;    /normal,charsize=0.3*2


;loop for each graph to draw
FOR thisx=0,x_graphs-1 do begin
  FOR thisy=0,y_graphs-1 do begin

;position of this plot
position=[(leftsize+thisx)*graphwidth,(bottomsize+thisy)*graphheight,$
  (leftsize+thisx+1.0)*graphwidth,(bottomsize+thisy+1.0)*graphheight]

if thisy eq 0 then begin
;bottom row, so let IDL control ticks on x axis
xtickname=''
;output a title for each column
xyouts,position[0]+graphwidth/2.0,bottomsize*0.6*graphheight, $
  string(uniquex[thisx],format='("x=",e8.2,"m")'),alignment=0.5, $
  /normal,charsize=0.3
endif else begin
;not the bottom row, so suppress IDL tick labels
xtickname=replicate(' ',30)
endelse

;as above for y instead of x!
if thisx eq 0 then begin
ytickname=''

xyouts,leftsize*0.5*graphwidth,position[1]+graphheight/2.0, $
  string(uniquey[thisy],format='("y=",e8.2,"m")'),alignment=0.5, $
  /normal,orientation=90,charsize=0.3
endif else begin
ytickname=replicate(' ',30)
endelse
```

```
;select only the relevent data to plot
selected=where(xstart eq uniquex[thisx] and ystart eq uniquey[thisy])
;and for the particles that escape the trap
selected_escaped=where(xstart eq uniquex[thisx] and ystart eq uniquey[thisy] $
   and tend lt maxt)

; ;to highlight a box, use this section before plot. (not used in thesis)
; if thisx eq 3 and thisy eq 2 then begin ;choose box to highlight here
; polyfill,position[[0,0,2,2]],position[[1,3,3,1]],color=100,/normal
; endif

;check we've got some data to plot
if (n_elements(selected) gt 1) then begin

  plot,alphastart[selected],ekinend[selected],position=position,/noerase, $
    xtickname=xtickname,ytickname=ytickname,xstyle=1,ystyle=1,psym=3, $
    xrange=xrange,yrange=yrange,charsize=0.3

;if there are escaped particles then plot them in red

  if (selected_escaped ne [-1L]) then oplot,alphastart[selected_escaped], $
     ekinend[selected_escaped],color=getcolor('red',3),psym=3

endif else begin
; no data to plot, so make an empty graph and write text in it.
  plot,xrange,yrange,position=position,/noerase,xtickname=xtickname, $
    ytickname=ytickname,xstyle=1,ystyle=1,psym=3,xrange=xrange,yrange=yrange,$
    /nodata,charsize=0.3
  xyouts,position[0]+graphwidth/2.0,position[1]+graphheight/2.0, $
    'Outside!Cregion',charsize=0.3*2,alignment=0.5,/normal
endelse



endfor
endfor

;close EPS file
device,/close_file

;JPG screen capture
;write_png,string('alpha_pos_ek',i,'.png',format='(A,I3.3,A)'),tvrd(/true)

;endfor

end
```

Appendix D

Replacement images for online version

Some images from other authors and publishers could not be given adequate copyright clearance to be used in the online version. The replacement images are shown below.

Figure of Layers of the sun, not shown for copyright reasons.

Descriptions: Solar structure indicated by concentric circles

Layer	Radius/ Thickness	Temperature	Density	Other Features
Core		1.5E7	1.6E5	Energy generated
	0.25R	8E6		
Radiative Diffusion				
	0.7R	5E5		
Convection zone				Granulation from convection cells
	1R	6600	8E5	Radiation emitted
Photosphere	0.5Mm	4300		Waves
Chromosphere	2.5Mm			
		1E6	1E-11	Solar wind
Corona				

Figure D.1: Replacement for Fig. 1.1.

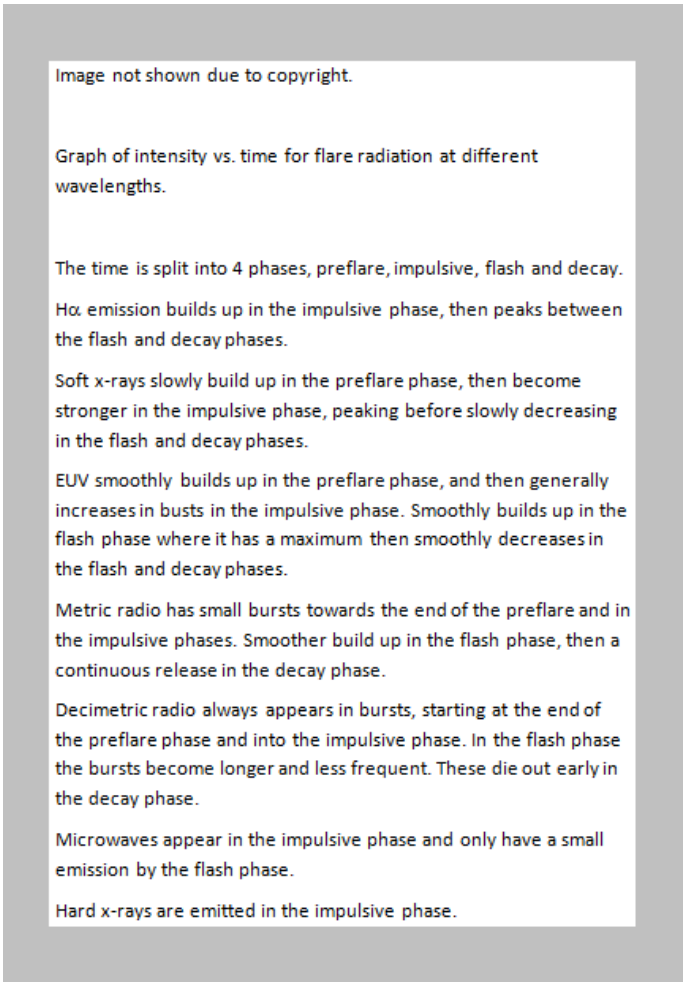

Figure D.2: Replacement for Fig. 1.7.

Bibliography

Aschwanden, M. J. (2002). Particle acceleration and kinematics in solar flares A Synthesis of Recent Observations and Theoretical Concepts (Invited Review). *Space Science Reviews*, 101:1–227.

Aschwanden, M. J. (2004). Pulsed Particle Injection in a Reconnection-Driven Dynamic Trap Model in Solar Flares. ApJ, 608:554–561.

Aschwanden, M. J. (2009). New aspects on particle acceleration in solar flares from RHESSI Observations. *Asian J. Phys.*, 17:423–444.

Benz, A., editor (2002). *Plasma Astrophysics*. Astrophysics and Space Science Library. Kluwer Academic Publishers, Netherlands.

Benz, A. O. (2008). Flare Observations. *Living Reviews in Solar Physics*, 5:1–+.

Bhatnagar, A. and Livingston, W. (2005). *Fundamentals of Solar Astronomy*. World Scientific, Singapore.

Birn, J., Thomsen, M. F., Borovsky, J. E., Reeves, G. D., McComas, D. J., Belian, R. D., and Hesse, M. (1997). Substorm ion injections: Geosynchronous observations and test particle orbits in three-dimensional dynamic MHD fields. J. Geophys. Res., 102:2325–2342.

Birn, J., Thomsen, M. F., Borovsky, J. E., Reeves, G. D., McComas, D. J., Belian, R. D., and Hesse, M. (1998). Substorm electron injections: Geosynchronous observations and test particle simulations. J. Geophys. Res., 103:9235–9248.

Birn, J., Thomsen, M. F., and Hesse, M. (2004). Electron acceleration in the dynamic magnetotail: Test particle orbits in three-dimensional magnetohydrodynamic simulation fields. *Phys. Plasmas*, 11:1825–1833.

Bogachev, S. A. and Somov, B. V. (2001). Acceleration of Charged Particles in Collapsing Magnetic Traps During Solar Flares. *Astronomy Reports*, 45:157–161.

Bogachev, S. A. and Somov, B. V. (2005). Comparison of the Fermi and Betatron Acceleration Efficiencies in Collapsing Magnetic Traps. *Astronomy Letters*, 31:537–545.

Bogachev, S. A. and Somov, B. V. (2009). Effect of Coulomb collisions on the particle acceleration in collapsing magnetic traps. *Astronomy Letters*, 35:57–69.

Boyd, T. J. M. and Sanderson, J. J. (1969). *Plasma dynamics*. Nelson, London.

Brown, J. C. and Hoyng, P. (1975). Betatron acceleration in a large solar hard X-ray burst. ApJ, 200:734–746.

Carrington, R. C. (1859). Description of a Singular Appearance seen in the Sun on September 1, 1859. MNRAS, 20:13–15.

Cary, J. R. and Brizard, A. J. (2009). Hamiltonian theory of guiding-center motion. *Reviews of Modern Physics*, 81:693–738.

Chamberlain, J. W. (1964). *Motion of charged particles in the earth's magnetic field*. Gordon & Breach, New York.

Clark, S. (2009). *The Sun Kings: The Unexpected Tragedy of Richard Carrington and the Tale of How Modern Astronomy Began*. Princeton University Press.

Drake, J. F., Shay, M. A., Thongthai, W., and Swisdak, M. (2005). Production of Energetic Electrons during Magnetic Reconnection. *Physical Review Letters*, 94(9):095001.

Emslie, A. G., Dennis, B. R., Holman, G. D., and Hudson, H. S. (2005). Refinements to flare energy estimates: A followup to "Energy partition in two solar flare/CME events" by A. G. Emslie et al. J. Geophys. Res., 110(A9):11103–+.

Emslie, A. G., Kucharek, H., Dennis, B. R., Gopalswamy, N., Holman, G. D., Share, G. H., Vourlidas, A., Forbes, T. G., Gallagher, P. T., Mason, G. M., Metcalf, T. R., Mewaldt, R. A., Murphy, R. J., Schwartz, R. A., and Zurbuchen, T. H. (2004). Energy partition in two solar flare/CME events. J. Geophys. Res., 109(A18):10104–+.

Fermi, E. (1949). On the Origin of the Cosmic Radiation. *Physical Review*, 75:1169–1174.

Fitzpatrick, R. (2008). The physics of plasmas. http://farside.ph.utexas.edu/teaching/plasma/plasma.html. [Online; accessed 23-Nov-2010].

Fletcher, L. (1995). On the generation of loop-top impulsive hard X-ray sources. A&A, 303:L9+.

Fletcher, L. and Martens, P. C. H. (1998). A Model for Hard X-Ray Emission from the Top of Flaring Loops. ApJ, 505:418–431.

Forbes, T. G. and Acton, L. W. (1996). Reconnection and Field Line Shrinkage in Solar Flares. ApJ, 459:330–341.

Freidberg, J. (2008). *Plasma Physics and Fusion Energy*. Cambridge University Press.

Giuliani, P., Neukirch, T., and Wood, P. (2005). Particle Motion in Collapsing Magnetic Traps in Solar Flares. I. Kinematic Theory of Collapsing Magnetic Traps. ApJ, 635:636–646.

Grady, K. J. and Neukirch, T. (2009). An extension of the theory of kinematic MHD models of collapsing magnetic traps to 2.5D with shear flow and to 3D. A&A, 508:1461–1468.

Hamilton, R. J. and Petrosian, V. (1992). Stochastic acceleration of electrons. I - Effects of collisions in solar flares. ApJ, 398:350–358.

Helioviewer Project (2011). http://helioviewer.org/. [Online; accessed 8-Jun-2011].

Hesse, M., Forbes, T. G., and Birn, J. (2005). On the Relation between Reconnected Magnetic Flux and Parallel Electric Fields in the Solar Corona. ApJ, 631:1227–1238.

Hesse, M. and Schindler, K. (1988). A theoretical foundation of general magnetic reconnection. J. Geophys. Res., 93:5559–5567.

Hodgson, R. (1859). On a curious Appearance seen in the Sun. MNRAS, 20:15–16.

Holman, G. D. (1985). Acceleration of runaway electrons and Joule heating in solar flares. ApJ, 293:584–594.

Hoshino, M., Mukai, T., Terasawa, T., and Shinohara, I. (2001). Suprathermal electron acceleration in magnetic reconnection. J. Geophys. Res., 106:25979–25998.

Karlický, M. and Bárta, M. (2006). X-Ray Loop-Top Source Generated by Processes in a Flare Collapsing Trap. ApJ, 647:1472–1479.

Karlický, M. and Kosugi, T. (2004). Acceleration and heating processes in a collapsing magnetic trap. A&A, 419:1159–1168.

Kovalev, V. A. and Somov, B. V. (2002). On the Acceleration of Solar-Flare Charged Particles in a Collapsing Magnetic Trap with an Electric Potential. *Astronomy Letters*, 28:488–493.

Kovalev, V. A. and Somov, B. V. (2003a). Role of Anisotropy of the Initial Particle Distribution in the Acceleration in Collapsing Solar-Flare Traps. *Astronomy Letters*, 29:111–115.

Kovalev, V. A. and Somov, B. V. (2003b). The Role of Collisions in the Particle Acceleration in Solar-Flare Magnetic Traps. *Astronomy Letters*, 29:409–415.

Krucker, S., Battaglia, M., Cargill, P. J., Fletcher, L., Hudson, H. S., MacKinnon, A. L., Masuda, S., Sui, L., Tomczak, M., Veronig, A. L., Vlahos, L., and White, S. M. (2008). Hard X-ray emission from the solar corona. A&A Rev., pages 8–+.

Landau, L. D. and Lifshitz, E. M. (1993). *Mechanics*. Butterworth-Heinemann, Oxford.

Lang, K. R. (2001). *The Cambridge Encyclopedia of the Sun*. Cambridge University Press.

Lin, J., Forbes, T. G., Priest, E. R., and Bungey, T. N. (1995). Models for the Motions of Flare Loops and Ribbons. Sol. Phys., 159:275–299.

Litvinenko, Y. E. (1996). Particle Acceleration in Reconnecting Current Sheets with a Nonzero Magnetic Field. ApJ, 462:997–+.

Liu, W., Petrosian, V., Dennis, B. R., and Jiang, Y. W. (2008). Double Coronal Hard and Soft X-Ray Source Observed by RHESSI: Evidence for Magnetic Reconnection and Particle Acceleration in Solar Flares. ApJ, 676:704–716.

Longair, M. S. (1981). *High Energy Astrophysics: Volume 2: Stars, the Galaxy and the interstellar medium*. Cambridge University Press, Cambridge.

Masuda, S., Kosugi, T., Hara, H., Tsuneta, S., and Ogawara, Y. (1994). A loop-top hard X-ray source in a compact solar flare as evidence for magnetic reconnection. Nature, 371:495–497.

Maxwell, J. C. (1861). On physical lines of force. http://en.wikisource.org/wiki/On_Physical_Lines_of_Force. Philosophical Magazine, 21 & 23. [Online; accessed 28-Nov-2011].

Melnikov, V. F., Shibasaki, K., and Reznikova, V. E. (2002). Loop-Top Nonthermal Microwave

Source in Extended Solar Flaring Loops. ApJ, 580:L185–L188.

Miesch, M. S. (2005). Large-scale dynamics of the convection zone and tachocline. *Living Reviews in Solar Physics*, 2(1).

Miller, J. A., Cargill, P. J., Emslie, A. G., Holman, G. D., Dennis, B. R., LaRosa, T. N., Winglee, R. M., Benka, S. G., and Tsuneta, S. (1997). Critical issues for understanding particle acceleration in impulsive solar flares. J. Geophys. Res., 102:14,631–14,659.

Miller, J. A., Larosa, T. N., and Moore, R. L. (1996). Stochastic Electron Acceleration by Cascading Fast Mode Waves in Impulsive Solar Flares. ApJ, 461:445–+.

Minoshima, T., Masuda, S., and Miyoshi, Y. (2010). Drift-kinetic Modeling of Particle Acceleration and Transport in Solar Flares. ApJ, 714:332–342.

Moffatt, H. K. (1978). *Magnetic field generation in electrically conducting fluids*. Cambridge, England, Cambridge University Press, 1978. 353 p.

Neukirch, T. (2005). Theory of Energy Storage and Release in the Solar Corona. In *The Dynamic Sun: Challenges for Theory and Observations*, volume 600 of *ESA Special Publication*.

Neukirch, T., Giuliani, P., and Wood, P. D. (2007). Particle acceleration in flares: Theory. In Birn, J. and Priest, E., editors, *Reconnection of Magnetic Fields*, pages 281–291. Cambridge University Press.

Northrop, T. (1963). *The Adiabatic Motion of Charged Particles*. Interscience Publishers, Inc, New York.

Park, B. T. and Petrosian, V. (1995). Fokker-Planck Equations of Stochastic Acceleration: Green's Functions and Boundary Conditions. ApJ, 446:699–+.

Petrosian, V. and Liu, S. (2004). Stochastic Acceleration of Electrons and Protons. I. Acceleration by Parallel-Propagating Waves. ApJ, 610:550–571.

Pitjeva, E. V. and Standish, E. M. (2009). Proposals for the masses of the three largest asteroids, the Moon-Earth mass ratio and the Astronomical Unit. *Celestial Mechanics and Dynamical Astronomy*, 103:365–372.

Platt, U. and Neukirch, T. (1994). Theoretical study of onset conditions for solar eruptive processes: Influence of the boundaries. Sol. Phys., 153:287–306.

Press, W. H., Flannery, B. P., and Teukolsky, S. A. (1986). *Numerical recipes. The art of scientific computing*. Cambridge University Press.

Priest, E. (2000). *Solar Magneto-Hydrodynamics*. D. Reidel Pub. Co, Dordrecht.

Reeves, K. K., Seaton, D. B., and Forbes, T. G. (2008). Field Line Shrinkage in Flares Observed by the X-Ray Telescope on Hinode. ApJ, 675:868–874.

Rohde, R. A. (2006). Sunspot numbers. http://www.globalwarmingart.com/wiki/File:Sunspot_Numbers_png. [Online; accessed 26 Apr 2011].

Romeou, Z. and Neukirch, T. (1999). Self-consistent Models of Solar Magnetic Structures in Three Dimensions. In Wilson, A. and et al., editors, *Magnetic Fields and Solar Processes*,

volume 448 of *ESA Special Publication*, pages 871–+.

Romeou, Z. and Neukirch, T. (2002). On the application of numerical continuation methods to the calculation of magnetostatic equilibria. *Journal of Atmospheric and Solar-Terrestrial Physics*, 64:639–644.

Scharmer, G. and Langhans, K. (2003). Small regular spot. http://www.solarphysics.kva.se/gallery/images/2003/. Image processing: Mats Löfdahl. [Online; accessed 28 Aug 2011].

Secchi, A. (1875). *Le Soleil*. Gauthier-Villars, Paris.

Selkowitz, R. and Blackman, E. G. (2004). Stochastic Fermi acceleration of subrelativistic electrons and its role in impulsive solar flares. MNRAS, 354:870–882.

Somov, B. (1992). *Physical Processes in Solar Flares*, volume 172 of *Astrophysics and Space Science Library*. Kluwer Academic Publishers.

Somov, B. V. and Bogachev, S. A. (2003). The Betatron Effect in Collapsing Magnetic Traps. *Astronomy Letters*, 29:621–628.

Somov, B. V. and Kosugi, T. (1997). Collisionless Reconnection and High-Energy Particle Acceleration in Solar Flares. ApJ, 485:859–868.

Stern, D. P. (1970). Euler Potentials. *American Journal of Physics*, 38:494–501.

Stern, D. P. (1987). Tail modeling in a stretched magnetosphere. I - Methods and transformations. J. Geophys. Res., 92:4437–4448.

Tsuneta, S. and Naito, T. (1998). Fermi Acceleration at the Fast Shock in a Solar Flare and the Impulsive Loop-Top Hard X-Ray Source. ApJ, 495:L67+.

Veronig, A. M., Karlický, M., Vršnak, B., Temmer, M., Magdalenić, J., Dennis, B. R., Otruba, W., and Pötzi, W. (2006). X-ray sources and magnetic reconnection in the X3.9 flare of 2003 November 3. A&A, 446:675–690.

List of Figures

List of Tables